UNIVERSITY OF LIVERPOOL

School of Engineering

PhD Thesis

Experimental Studies on Ultrafast Laser-Materials Micro-Structuring with Phase Only Spatial Light Modulators

Thesis submitted in accordance with the requirements of
The University of Liverpool for the degree of
Doctor in Philosophy

By

Guangyu Zhu

Jan 2018

Guangyu Zhu
Laser Group
School of Engineering
The University of Liverpool
Liverpool, UK
L69 3GH
Email: psgzhu@liverpool.ac.uk
Web: www.lasers.org.uk

Abstract

The thesis presents a comprehensive study of ultrafast laser-materials micro-structuring with a phase only spatial light modulator.

Internal inscription was carried out in organic and hybrid composite materials using fs pulses with wavelengths (λ) from the NUV, visible and NIR, 387.5 $\leq \lambda \leq$ 1480nm and NA in the range 0.01 – 1.3. In the polymer, Polymethyl Pentene (PMP), NA ~0.4 inscription at λ = 387.5nm resulted in a much higher refractive index modulation, $\Delta n \sim 2.3 \times 10^{-3}$. Volume Bragg Gratings inscribed at 387.5nm with 200 l/mm and 200μm thick demonstrated a high first order diffraction efficiency, $\eta_1 > 68.5\%$, the highest observed to date in this material.

Multi-photon induced photochemical reduction of silver doped polyvinyl alcohol (PVA) in silica was demonstrated with 1kHz, NUV femtosecond laser irradiation. The regions of two-photon absorption are distinguished by a yellow/amber colour of the silver nanoparticles which agglomerate and formed at pulse energy E_p = 2.0μJ, λ= 387.5nm, NA~0.1. The study improves the viability of 3D nanoscale fabrication in bulk transparent composites.

New spatial complex structures are constructed within bulk polymer using a femtosecond vortex beam. It is observed that critical powers for self-focusing (SF) with spiral beams scale linearly with topological charge m and linearly polarised spiral beams always couple more strongly than circular during inscription due to polarisation dependent self-focusing. With high states of orbital angular momentum, complex filamentary structures converging to the focus are observed which collapse to multiple filaments, in accord with theoretical expectations. Clear rotation of these filaments is detected near the focal plane due to the twisting wavefronts. This study open a new route to create complex 3D microstructure within transparent material.

The thermal and optical phase response of liquid cooled spatial light modulators to high average laser power exceeding $\langle P \rangle = 200$W at 1064nm with picosecond pulses were measured for the first time. SLM chip temperature rise was limited by efficient cooling to 5°C with $\langle P \rangle$ =220W incident, with a clear temperature gradient and thermal response time of 1-2 seconds Numerical modelling of the thermal and optical response gave excellent agreement with experiment. The optical phase response with incident power approaches 2π radians with average power up to $\langle P \rangle$ =140W, while above $\langle P \rangle$ = 200W, liquid crystal thickness variations limit phase response to just over π radians while the degree of polarization remains relatively high. With this knowledge, high throughput parallel beam ablation on stainless steel at 4mm^3/sec and thin film ablation of Aluminium on PET at a rate of 80cm^2s^{-1} was demonstrated.

Declaration

I hereby declare that all of the work contained within this dissertation has not been submitted for any other qualification.

Signed:

Date:

Acknowledgements

I would like to thank everyone who encouraged and supported me during the time of my PhD.

Sincere acknowledge goes to my academic supervisors, Dr Stuart Edwardson and Prof Geoff Dearden, who always give me encouragement, help, advice and guidance through the ups and downs of my research. I would like to thank my technical supervisor, Dr Walter Perrie, for his invaluable advice, endless patience and support. Without their dedication, this work would not have been possible. I am very grateful to everyone from the department of mechanical, materials and aerospace engineering of the University of Liverpool who was involved in my research, in particular, Dr Richard Potter, Mr Dave Atkinson, Ms Jones Andrea and Mr Andy Snaylam.

I thank Dr Bryce Dorin, Dr Patrick Parkinson, Dr Patricia Scully, Dr David Whitehead, Dr Oliver Allegre and Prof Lin Li, from university of Manchester for providing kind help and advice for this research. I also acknowledge Prof Miles Padgett at the University of Glasgow for providing the hologram calculation software used for this research.

Finally, I would like to sincerely acknowledge my beloved wife, Ms Lan Shen, for her constant support and understanding. I would like to thank to my parents: Ms Xinhua Liu and Prof Zhenghe Zhu for providing financial supports and unwavering faith throughout my study.

List of publications to date

Journal papers:

1. B. Dorin*, **G. Zhu**, P. Parkinson, W. Perrie, M. Benyezza and P. Scully, "Characterization of a silica-PVA hybrid for high density and stable silver dissolution"- on Materials Chemistry and Physics (Volume 177, 1 July 2016, Pages 19–24) - **Second author**.

2. G. Zhu, D. J. Whitehead, W. Perrie*, O. J. Allegre, V. Volle, Q. Li, Y. Tang, K. Dawson, Y. Jin, and S. P. Edwardson, "Investigation of the thermal and optical performance of a Spatial Light Modulator with high average power picosecond laser exposure for Materials Processing Applications," J. Phys. D (2018) " – **First author.**

3. **G. Zhu, B.** Dorin, W. Perrie*, P. Scully, P., Parkinson, D. Liu, S. P. Edwardson and G. Dearden, "Femtosecond Inscription inside Poly-Methyl Pentene with Numerical Aperture, Wavelength and with Polarised Helical Beams carrying Orbital and Spin Angular Momentum" – **First author** and the paper has been fully completed and will be submitted in Aug. 2018.

Conference contributions:

1. G. **Zhu*, L.** Ye, W. Perrie, Z. Zai, O. J. Allegre, E. Fearon, S. P. Edwardson and G. Dearden**,** "Filamentation in PMMA with linear, circular, Radial and Azimuthal polarisations with Vortex wavefronts" - Photon 14 (IPO publication).

2. G. **Zhu**, W. Perrie*, O. J. Allegre, Y. Jin, S. P. Edwardson and G. Dearden**, "**On femtosecond laser inscription inside PMMA using a spatial light modulator" - in a conference, 6th European Conference on Applications of Femtosecond Lasers in Materials Science March 16-17, 2015, Mautherndorf Castile, Nauterndorf, Salzburg, Austria.

3. G. **Zhu***, W. Perrie W., Y. Tang, Y. Jin, S. P. Edwardson and G. Dearden, "Femtosecond laser inscription inside Polymethyl Pentene with vector optical fields"- Photon 16 (IPO publication).

4. G. **Zhu***, W. Perrie, Y. Tang, Y. Jin, S. P. Edwardson and G. Dearden, **"**Internal 3D inscription of semi-crystalline polymer using multimode beams" - ILAS 2017.

5. G. **Zhu*,** B. Dorin, W. Perrie, S. P. Edwardson and G. Dearden "Femtosecond laser inscription inside Poly-Methyl Pentene with polarised helical beams carrying orbital and spin angular momentum" – MATADOR 2017

6. G. **Zhu**, W. Perrie*, D. Whitehead, O. J. Allegre, S. P. Edwardson and G. Dearden, "Investigation of the thermal and optical performance of a spatial light modulator (SLM) with 220W of picosecond laser exposure for material processing applications" – LASERTAGUNG 2017.

7. Q. Li, **G. Zhu**, W. Perrie, S. P. Edwardson, G. Dearden "Investigation of PEEK ablation with femtosecond laser pulses" – MATADOR 2017

Table of contents

List of figures	XI
List of symbols	XX
List of abbreviations	XXII

Chapter 1 Introduction	1
1.1 Theme and motivation	1
1.2 Industrial relevance	1
1.3 Aim and objectives	3
1.4 Overview of this thesis	5

Chapter 2 Theories and literature reviews	7
2.1 Introduction	7
2.2 Natural phenomena generated by femtosecond pulses	7
2.2.1 Filamentation	7
2.2.2 The third order susceptibility ($\chi^{(3)}$)	10
2.2.3 Multi-photon absorption (MPI)	11
2.2.4 Supercontinuum	12
2.2.5 Interaction mechanism	13
2.3 Photons with orbital angular momentum	15
2.3.1 orbital angular momentum and spin orbital momentum	15
2.3.2 Intensity profile of a beam carrying orbital angular momentum	17
2.3.3 OAM conservation	18
2.3.4 The propagation of optical vortex in transparent material	19
2.3.5 Spiral Microstructure	20
2.4 Optical polarization and vectored beam	21
2.4.1 Polarization states	21
2.4.2 Polarization sensitivity	24

2.5 Internal processing using femtosecond pulses 26
2.6 LCOS Spatial Light Modulator 30
2.7 Silver doped polyvinyl hybrid material 34
2.8 Summary 35

Chapter 3 Experiments and methodologies 37
3.1 Introduction 37
3.2 Internal modification using femtosecond pulses 37
3.2.1 Experimental setup 37
3.2.2 Clark MXR CPA 2010 37
3.2.3 Optical parametric converter – TOPAS C 40
3.2.4 Investigated materials 40
3.2.5 Focusing optics 42
3.2.6 Spectrometers 42
3.2.7 Spiricon SP620U 43
3.2.8 Inscription of volume Bragg gratings 44
3.2.9 Transmission diffraction efficiency measurement of A VBG 45
3.3 Using SLM to generate optical vortex and vector beam 46
3.3.1 SLM-and-PC setup 46
3.3.2 CGH-generating software: “Blue Tweezers” 48
3.3.3 Generation of optical vortex using a SLM 49
3.3.4 Vector-beams generation using a SLM 52
3.5 Vector beam built using S-waveplate 54
3.6 High power thermal tests and phase response of the cooled SLM 54
3.6.1 LCOS SLMs ((Hamamatsu X13139-03) 54
3.6.2 Edgewave, Innoslab laser, (*10*ps at *1064*nm) 55
3.6.3 Thermal and phase response test 57
3.6.4 Parallel processing 57
3.6 Summary 58

Chapter 4 Femtosecond laser 3D micromachining	59
4.1 Introduction	59
4.2 Supercontinuum (SC) generation of λ775 femtosecond pulses	59
4.2.1 Experimental setup	59
4.2.2 SC spectra for linear polarization and circular polarization	59
4.3 Inscription within poly methyl pentene (PMP)	66
4.3.1 Linear absorption	66
4.3.2 Filamentary inscription using VIS fs pulses	70
4.3.3 Filamentary length versus pulse energy	71
4.3.4 Low NA VBG inscription, NUV and visible region	73
4.3.5 Supercontinuum in PMP with Gaussian beam	75
4.3.6 Inscription with higher NA's	77
4.3.7 Raman spectroscopy	80
4.3.8 Discussion	82
4.4 Laser processing of Silver doped silica-PVA hybrid material	83
4.5 Pulses-and-medium interaction in Zinc Selenide	85
4.6 Summary	87
Chapter 5 Focusing of cylindrical vortex and vector beams	89
5.1 Introduction	89
5.2 Laser Beam with orbital angular momentum	89
5.2.1 Numerical study of the formation of helical phase fronts	89
5.2.2 Numerical study of intensity profile of laser beam with OAM	91
5.2.3 Harmonic orbital angular momentum conversion	93
5.2.4 Machining	96
5.3 Femtosecond vector beam	99
5.4 Bulky modification in PMP using Vortex beam	103
5.4.1 Effects of OAM on filamentation in PMP at low NA	103
5.4.2 Low NA inscription with spiral beams carrying both OAM	104

and SAM

5.4.3 High-NA inscription with high intensity spiral beams carrying OAM 108

5.5 Summary 113

Chapter 6 250W ultrafast pulse (ps) handling with a spatial light modulator 114

6.1 Introduction 114

6.2 Experimental Characterization 114

6.2.1 Thermal tests 114

6.2.2 Phase response 118

6.3 Modelling of observed thermal and phase response 124

6.3.1 Infrastructure of a liquid-cooled SLM 124

6.3.2 Simulated thermal response 125

6.3.3 Phase-response simulation 129

6.4 Laser-micromachining results 131

6.4.1 Parallel beam laser surface processing at $\langle P \rangle \leq 25$W 131

6.4.2 High power processing at $\langle P \rangle > 100$W 134

6.4.3 More complex phase CGH's 135

6.4.4 High speed surface micro-structuring 137

6.5 Discussion and summary 138

Chapter 7 Conclusions and future works 141

References 146

Appendix i

A1 Optical-vortex simulation in MatLab environment i

A2 Spatial-light-modulating method developing in LabVIEW environment vi

A3 Laser sources, optics and investigated materials xi

List of figures

Figure 2.1	Filamentation in air, courtesy to W. Pelletier (University of Michigan)	8
Figure 2.2	Objective lens and Self-guiding propagation	9
Figure 2.3	Jacobi Diagram of the multiphoton excitation of an electron in PMMA, ZnSe and PMP from the valence to the conduction band.	12
Figure 2.4	Optical Vortex for topological charge number (a) m=0, (b) m=1, (c) m= 2, and (d) m = 3. The schematic is courtesy to [89].	14
Figure 2.5	Azimuthal component of k vector. This schematic is courtesy to [89].	17
Figure 2.6	Spin angular momentum (circular polarization). The schematic is courtesy to [89].	17
Figure 2.7	Intensity profiles of a vortex beam (λ=1064) at focus plane outputs with topological charges m= 1and 2. The images are courtesy to [92].	18
Figure 2.8	Spatial intensity distribution of vortex beam with topological charge number: (a) m=3, (b) 5 and (c) 8; Yellow refers to high intensity and blue to low intensity. The figures are courtesy to [102].	20
Figure 2.9	AFM micrography of helical twist structure generated by CW green laser on the surface of azo-polymer. The AFM micrography is courtesy to [112].	21
Figure 2.10	Conventional laser beam with homogenous-polarization distribution. This photo is courtesy to [116].	22
Figure 2.11	Vector beams with homogenous-polarization distribution. This photo is courtesy to [116].	22
Figure 2.12	Spiral LIPSS pattern generated by vector beam (λ=1064nm, τ~5ps). The SEM microscopy is courtesy to [138].	25
Figure 2.13	Photograph of a lab-on-chip device micro reactor fabricated in photo-sensitive glass using fs pulses with post chemical etching. The work was courtesy to [160].	29
Figure 2.14	Schematic of a LCOS SLM device. The schematic is courtesy to HAMATSU [166].	30
Figure 2.15	Nematic alignment of liquid crystal layers. PA: parallel aligned.	31
Figure 2.16	(a) 8-bit phase depth phase pattern. (b) Designated vectored beam. The schematic is courtesy to [182].	36

Figure 3.1	Schematic of experimental set-up.	37
Figure 3.2	A femtosecond laser, Clark-MXR CPA 2010 system (*775*nm, *160*fs, *2*kHz, *1*mJ) is used. The peak powers are $3< P < 10$ MW are above the critical power for self- focusing in PMMA, Pc > 1.5MW.	38
Figure 3.3	Flow chart for synthesis of silica, Ag^{+} and PVA films using sol–gel method.	46
Figure 3.4	(a) Spiricon SP620U Beam Profiler; (b) BeamGage® Interface.	43
Figure 3.5	(a) Filamentary Structures induced by 170-fs pulse using singlet lens (NA <0.1) in transverse writing geometry. (b) A demonstration to construct 3-layer volume Bragg grating by offsetting scans along the optic axis.	44
Figure 3.6	Schematic of parallel display using two monitors.	46
Figure 3.7	Blazing function which shows the relationship of phase change and grey level.	46
Figure 3.8	(a) Interface module of "*Blue Tweezers*"; (b) 775-nm Correction field; (c) *"displayCombinedHologram U8"*.	47
Figure 3.9	Applying blazing function to correct phase modulation response to grey level in "*Blue Tweezer*".	48
Figure 3.10	8-bit bitmap for constructing a vortex beam with charge number m=1, where (a) is the spatial (spiral) wavefront and (b) is a 2D-bitmap CGH which would create the wavefront in (a).	49
Figure 3.11	The Module "interface" (a) the red rectangular (top) inputs field for topological charge number (m). A bottom switch is used to choose correction field "OFF" or "ON". The corresponding spiral CGH for m =3 is shown in (b) without flatness correction and (c), with correction added.	50
Figure 3.12	In the Module "interface" (a) the red square sets the input field for topological charge number (m) as 1.5. The CGH (b) with a 1.5 $\times 2\pi$ phase change around a circle is generated with upgrade version.	51
Figure 3.13	The optical setup of polarization modulation using a single phase SLM. Radial or azimuthal polarization with a vortex phase is tailored from incident linear polarization.	52
Figure 3.14	Set the L=2 in *Interface* (a). The CGH (b) is to generate radial polarization when I =1 while the CGH (c) is to generate azimuthal polarization when I =-1. Both carry a helical wavefront.	52

Figure 3.15	The experimental setup to generate vector beam (λ_{1064}),	53
Figure 3.16	(a) Photo of cooled SLM (Hamamatsu X13139-03) on mirror mount with liquid cooling connections to the Copper heat sink; (b) The controller board of the SLM; (c) a Koolance liquid pump (model EX2-755).	54
Figure 3.17	(a) EdgeWave Innoslab laser; (b) A digital waveform generator (Tektronix AFG 3021B 250ms/s 25MHz); (c) Lecroy WaveRunner 6100A 1GHz Oscilloscope showing pulse bursts; (d) Laser Control-software interface.	55
Figure 4.1	Transmitted SC spectra were obtained using fibre coupled spectrometer (Spectra Product SM-240).	60
Figure 4.2	Observed SC, Stokes and anti-stokes broadening Δλ vs pulse energy for linear TE polarization. Measured by Spectra Product SM-240.	61
Figure 4.3	Observed SC, Stokes and anti-stokes broadening Δλ vs pulse energy for linear TM polarization. Measured by Spectra Product SM-240.	61
Figure 4.4	Observed SC, Stokes and anti-stokes broadening Δλ vs pulse energy for circular polarizations. Measured by Spectra Product SM-240.	62
Figure 4.5	Linear fitting experiment spots of linear polarization with transverse electric field (TE). The determination coefficient of linear fitting is R^2 *=0.99*.	64
Figure 4.6	Linear fitting experiment spots of linear polarization with transverse magnetic field (TM). The determination coefficient of linear fitting is R^2 *=0.99*.	64
Figure 4.7	Linear fitting experiment spots of linear polarization with circular polarization. The determination coefficient of linear fitting is R^2 *=0.98*.	65
Figure 4.8	Optical setup of the observation of thermal effects.	66
Figure 4.9	(a) FLIR thermal imaging; (b) line heat source; (c) Visible filamentary line (d) SHG or THG of frequency-difference and frequency-summation signals.	67
Figure 4.10	External transmittance for PMP in thickness: 1.27mm, 2.54mm and 5.06m for near infrared light (940 -2850nm). This transmission spectrum is courtesy to Lytle et al [9].	68

Figure 4.11	External transmission of PMP measured with a sample thickness of 10 mm.	69
Figure 4.12	τ (full width at half maximum) corresponding to wavelength λ.	70
Figure 4.13	Microscopic structures generated by laser pulses τ~ *180*fs, *Ep = 1±0.073 μJ* (1σ) and λ = *550, 560 … and 680* nm in poly methyl pentene (PMP). The red arrow represents the propagation direction of incident beam.	71
Figure 4.14	(a) Δn modulation in bulk PMP and (b) measured filament length with power function fit shows the exponent = 0.53, close to theoretical value 0.5 of Zverev and Pashkov 's work [217].	72
Figure 4.15.	(a) 4 × 4 × 2mm thick VBG inscribed in PMP at λ= *387.5*nm and NA= 0.1 with RI modulation Δn ~1.10^{-4}, (b) first order diffraction at the Bragg angle for *1.5* mm thick, 10μm pitch VBG inscribed at λ = *670*nm reaching $\eta_{\pm 1}$ = *63%* with almost no coupling to minus first order.	73
Figure 4.16.	The first order DE with grating thickness in PMP and theoretical curve due to Kogelnick equation [158] based on Δn =1.0 x 10^{-4}. The absolute diffraction efficiency is saturated at 67.5% by scatter loss due to optical breakdown.	75
Figure 4.17.	Reflected SC spectral sampled by Andor Shamrock time-resolved spectrometer.	76
Figure 4.18.	Anti-stokes broadening spectrum generated by fs pulse with linear polarization (TE), λ= 387.5nm and Ep =1.5μJ. Measured by Andor Shamrock SR 303i.	77
Figure 4.19.	Optical images of RI modifications in PMP at NA = 0.25, (a) side view of 30micron thick VBG, (b) side view of a 4 layer VBG using 10% overlap rate, (c) front view of inscribed VBG filaments. Scan speed throughout s = 0.7mm/s.	78
Figure 4.20.	(a) Cross-sectional microscopic results of single layer, 5μm pitch VBG inscribed in PMP at λ = 387.5nm with NA = 0.4. Laser direction from left to right, (b) image of Bragg diffraction from the 200 l/mm grating at 532nm with DE η_1 = 0.47 inferring a Δn ~2.3×10^{-3}.	79
Figure 4.21.	Damage dots generated by optical breakdown which is induced by focused laser light (~180fs, 650nm and 0.15NA).	79
Figure 4.22.	Structure of poly methyl pentene (PMP) [219].	80
Figure 4.23.	Raman spectroscopy of laser filaments in PMP using 0.20 μJ and 0.35 μJ pulses is compared to a pristine PMP sample. Background	81

	subtraction was performed to remove the PL signal from the data. Inset: Comparison of pristine PMP with a 0.20 μJ filament without background subtraction	
Figure 4.24	Multi-photon absorption of 775 nm and 387 nm in PMP.	82
Figure 4.25	Silver doped silica-PVA hybrid material is processed at 1kHz by 170 fs, 387nm, NUV light using 0.49 μJ pulse energy, 1mm/s scan speed and focused using 0.45 N.A. objective.	84
Figure 4.26	Absorption spectral of composites sample processed using NUV femtosecond laser pulses with pulse energy 0, 0.26, 0.51, 1.0 and 2.0 μJ. The SPR peak of 0.26 μJ is coincide with Mie's theory guess. The colour of trace presents the processing peak energy and the dash trace is a theoretical guess (Mie's theory).	85
Figure 4.27	(a)Using femtosecond NIR pulses (τ ~170fs, λ=1.42μm) to test a piece of polycrystalline ZnSe substrate; (b) No thermal effect can be observed.	86
Figure 4.28	(a) Reflected-light spectrum generated by ZnSe, recorded by Andor Shamrock spectrometer; (b) Reflected-light spectrum generated by a BBO crystal, recorded by Andor Shamrock spectrometer.	86
Figure 4.29	The NUV pulse is characterized using an autocorrelator (Pulse Check) with (a) ZnSe and without (b) ZnSe.	87
Figure 5.1	3 plane-phase fronts (m=0) space with λ=775.	91
Figure 5.2	A vortex front with 3 spiral treads (m=3) over a period (λ).	92
Figure 5.3	Calculated intensity distributions for Gaussian and Vortex beams (W/cm^2) when a 1μJ/ 170fs pulse at 387.5nm is focused with a 50mm lens.	93
Figure 5.4	Optical vortex (m=3) exhibits helical wavefront.	95
Figure 5.5	Far field intensity distribution observed at *387.5* nm on Spricon camera. Ring structures are clear when $m_{2\omega}$ are integer, indicating conversion of angular momentum during SHG.	96
Figure 5.6	Optical micrograph of steel surface ablation (N=100 pulses/spot) at the focal plane of a 150mm focal length lens using spiral beam with $m_{2\omega}^{387.5}$ = *0.6, 1.0, 1.4, 2.0.*	96
Figure 5.7	Focusing of a cylindrical femtosecond laser beam with orbital angular momentum.	97

Figure 5.8	m = *0,2,4,6,8,10,12,14* and *16*. Material – stainless steel (S/S 321). Microscopic lens ~ 0.4 NA at λ_{387}. Ep =150±1mW, Exposure time 30s.	98
Figure 5.9	Large deviation regarding to m> 4 suggests high-order components were removed in second harmonic generation and the decrease of effective NA number.	99
Figure 5.10	Schematic presents the generation of vector beam using S-waveplate. A half waveplate is used to rotate incident linear polarization 45° in clockwise.	100
Figure 5.11	Optical set-up used to analysis polarization purity of vector beams generated by S wave plate. The entry direction of PA is put in horizontal or vertical directions.	101
Figure 5.12	Linear polarization purity of vector beam generated by S wave plate regarding to incident angle ranged from *0º* to *360º*.	101
Figure 5.13	Schematic presents only S-polarized light was profiled by a CCD camera.	102
Figure 5.14	Near-field intensity profiles for focused vector beams with radial (a) and azimuthal polarizations (b).	103
Figure 5.15	Optical images of LIPPS formation with the RP and AP beams when substrate translated through the focal plane.	103
Figure 5.16	(a) -45° and (b) +45°. Microscopic image of Plasmonic patterns structured with spiral vector fields when θ = -45° (a) and +45° (b) and 0.5 mm above focal plane.	104
Figure 5.17	Low NA transverse inscription at λ = 387.5nm with spiral beams carrying OAM, $m_{2\omega}^{387.5}$ = 1, 2, 4, 6 with constant pulse energy E_p = 2μJ.	105
Figure 5.18	Optical image of low NA filamentary in side view. There is no effect of coupling between OAM and SAM (RCP and LCP) at low NA but linearly polarised states (TE) couple stronger than circular (RCP and LCP), consistent with third order susceptibility higher with linear than circular polarisation.	106
Figure 5.19	Typical SC spectrum (bluish continuum) excited at λ = 387nm covering the NUV to the visible with $m_{2\omega}$ = 4.	107
Figure 5.20	SC spectra for spiral beams with $2 \leq m_{2\omega} \leq 8$ over 350-400nm and expanded detail showing that the Anti-Stokes (and Stokes) intensity reduces with increasing $m_{2\omega}$, consistent with critical	107

power rising with $m_{2\omega}$.

Figure 5.21 Near threshold integrated continuum signal over *350-380*nm for linear polarized spiral beams with $m_{2\omega}$ = 2,4,6,8. Linear scaling is clear indicating that critical power rises linearly with $m_{2\omega}$, showing a difference in coupling due to polarisation dependent self-focusing, independent of the total angular momentum, orbital plus spin. 108

Figure 5.22 Transmission optical image of observed side view of ring structures inscribed transversely in PMP. Focus distance below surface ~400µm. 109

Figure 5.23 Complex filamentation with twisted beam carrying high OAM, $m_{2\omega}$ =10 when varying pulse energy from 1-5µJ 110

Figure 5.24 (a) Cross sections along optic axis of the filamentary modification in exposed PMP at 0.4NA showing multiple filaments near focus (b) rotation of the two strongest filaments counter-clockwise with increasing depth, relative to (a). 111

Figure 5.25 (a) Microscope image of modification cross section in PMP with OAM beams, $m_{2\omega}$ =10 while varying pulse energy from *0.3-0.5*µJ, exposure time = *50*ms, NA *=0.7*, (b) expanded image from (a) with E_P = *0.5* µJ showing multiple guiding regions. Surrounding rings are due to WL diffraction around the core. 112

Figure 5.26 (a) Optical image (transmission) of micro-structures inscribed longitudinally along optic axis when $m_{2\omega} = \pm 10$, and longitudinal scan speed was 0.5mm/sec, (b) expanded structure from (a) with $m_{2\omega}$ = 10, (c) expanded structure from (a) with $m_{2\omega}$ = - 10. The structure with $m_{2\omega}$ = - 10 shows a clockwise spiral, not apparent with the opposite helicity in (b). 113

Figure 6.1 Schematic of experimental set-up for high power thermal tests of cooled SLM (Hamamatsu X13139-03). 116

Figure 6.2 Measured temperature variation of device -01 to incident picosecond pulses with repetition of 404 kHz and up to 140W average power. Measured thermal response coefficient (m_0) is 0.041°C/W. Errors represent 1σ and fit is least squares with high 117

confidence, R=0.99.

Figure 6.3 Measured temperature variation of device 02 response to incident picosecond pulses with repetition of 1MHz. Measured thermal response coefficient (m_0) is 0.026°C/W, significantly lower than device -01. Errors represent 1σ and fit is least squares with high confidence, R = 0.99. 118

Figure 6.4 Infrared image of device 2 with increasing incident average power (a) P = 0, (b) $\langle P \rangle$ = 44W, (c) $\langle P \rangle$ = 118W, (d) $\langle P \rangle$ = 172W (e) $\langle P \rangle$ =215W, showing evidence of laser spot near the centre of chip, (f) $\langle P \rangle$ = 215W showing spot temperature T = 26.6°C. Note that there was some off axis low intensity scatter from the laser beam reaching the surrounding enclosure (matt black) hence showing a slight temperature rise above and below on this highly absorbing surface. Room temperature is ~ 20°. 119

Figure 6.5 Optical set-up used to determine phase response of cooled SLM using polarisation modulation induced by Grey Level (GL) phase maps applied to the SLM. 120

Figure 6.6 Grey-level (GL) adjustment using *"displayCombinedHologram U8"*. 120

Figure 6.7 Phase changes of Device-01 response to incident power less than 132.5W. The phase response is stable up to average power $\langle P \rangle$ = 37.8W but begins to deviate slightly above 80W while a significant deviation occurs at 132.5W, reaching just over a π phase shift instead of the desired 2π. 123

Figure 6.8 Phase modulation of Device-02. The phase response can engage 2π change which is satisfactory at laser power up to $\langle P \rangle$ = 109W but begins to deviate at 160W and above, reaching just over a π phase shift instead of the desired 2π. 124

Figure 6.9 Schematic of a liquid-cooled LCOS SLM. Inset illustrates the schematic of the incident of picosecond pulses and LC layer. Temperature response on silicon substrate and phase response with temperature are modelled. 125

Figure 6.10 Thermal response as boundaries without water-cooling function. 127

Figure 6.11	Thermal response as boundaries with water-cooling function.	127
Figure 6.12	Thermal responses of silicon (centre) with absorbed power, ranged from 0 – 10W.	128
Figure 6.13	Simulated temperature profile at silicon front surface when thermal equilibrium is built.	129
Figure 6.14	Normalized transmitted power and compared to experiment at <P> = 26.2W (a) and at <P> = 160W (b).	132
Figure 6.15	(a) Optical micrograph of three parallel tracks ($\pm1^{st}$ order and 0^{th} order) machined at 2W, 10 kHz and 250 mm/s. (b) Optical micrograph of 3 spot processing with 25W/404kHz exposure with 1000 mms^{-1} scan speed and offset hatch spacing of 460μm, overlapping the $\pm1^{st}$ orders. (c) SEM image of the stainless-steel machining in (b) clearly showing the overlapping $\pm1^{st}$ orders and zero order in between.	133
Figure 6.16	(a) Macroscopic image of surface texturing ($1cm^2$) on a stainless steel sample using diffractive 3-spot patterns. Laser exposure was 25W, 404 kHz with 3 m/s scan speed, minimizing pulse overlap. (b) SEM image indicates LIPSS with 1-μm periodicity (c) High resolution SEM image showing nanostructures within the LIPSSs.	134
Figure 6.17	Macroscopic image of three beam parallel processing. The asymmetrical pattern persists.	135
Figure 6.18	SEM images of parallel processing with 3 spots at 160W, 3000 mm/s and 1 scan. (a) is similar to asymmetrical pattern of low power cases. (b) The overlap of $\pm1^{st}$ orders.	136
Figure 6.19	(a) Spot pattern set representing the letter M (b) resulting complex phase CGH created by the lens and gratings algorithm (b) observed intensity pattern at far field, showing even distribution.	137
Figure 6.20	Optical images of surface patterning (letter "M") on polished brass plate with increasing laser powers. (a) <P> = 90W, 30ms, (b)<P> = 120W, 30ms, (c) <P> = 60W, 10ms, (d) <P> =250W, 10ms. Diffraction efficiency drops above <P> = 120W as expected	138
Figure 6.21	Thin film patterning of flexible Al/PET with 97W/404kHz using 9-spot parallel processing with ~ 50% pulse overlap and fluence F ~ $0.4J/cm^2$. The total removal rate was $90cm^2/s$.	139

List of symbols

S.I. Units

Symbol	Description
C_p	Specific heat capacity J/(kg·K)
e	Euler's number 2.718
E_b	Bandgap energy eV
E_p	Peak energy J
f	Lens focal length mm
h	Planck constant 6.62606×10^{-34} m^2·kg/s
$\hbar$	Reduced Planck constant $h/2\pi$ m^2·kg/s
I	Intensity (W/cm^2)
k	Wave number rad/cm
ℓ	Angular momentum number n/a
L	Grating thickness mm
m	Orbital angular momentum number n/a
m	Mass kg
NA	Numerical aperture n/a
n_0	Refractive index n/a
n_2	Nonlinear refractive index cm^2/W
Δn	Refractive-index modulation n/a
P	Power W
P_c	Threshold of filamentation W
s	Spin angular momentum number n/a
t	Time s
T	Temperature K
v	Velocity mm/s
$\eta_{\pm1}$	First order diffraction efficiency %
θ_B	Bragg angle degree or radian
λ	Wavelength nm

$\Delta\lambda$	Spectral bandwidth nm
Λ	Grating period μm
ρ	Mass density kg/m^3
τ_p	Pulse Duration fs/ps
φ	Phase of complex field rad
$\chi^{(3)}$	The third order susceptibility e.s.u

List of abbreviations

BBO	Beta Barium Borate
CCD	Charge Coupled Device
CPA	Chirped Amplification
DE	Diffraction Efficiency
DOEs	Diffractive Optic Elements
FL	Filamentation
EM	Electromagnetic
FWHM	Full Width of Half Maximum
GLV	Grating Light Valve
GVD	Group Velocity Dispersion
HG	Hermite-Gaussian
KTP	Potassium Titanyl Phosphate
LBO	Lithium Triborate
LCOS SLMs	Liquid-Crystal-On-Silicon Spatial Light Modulators
LG	Laguerre-Gaussian
LIPSS	Laser Induced Periodic Surface Structures
MOEMS	Micro-Opto Electromechanical System
MPA	Multi-Photon Absorption
MPI	Multi-Photon Ionisation
MWD	Molecular Weight Distribution
NL	Nonlinear
NUV	Near Ultraviolet
NIR	Near Infrared
OPA	Optical Parametric Amplifier
PA	Parallel-Aligned
PEO	Poly Ethylene Oxide
PL	Photoluminescence
PMMA	Poly(Methyl) Methracylate
PMP	Poly Methyl Pentene
PVA	Poly Vinyl Alcohol

PVP	Poly Vinyl Pyrrolidone
RI	Refractive-Index
ROI	Region of Interest
OAM	Orbital Angular Momentum
SC	Supercontinuum
SEC	Size Exclusion Chromatography
SF	Self-Focusing
SPR	Surface Plasmon Resonance
VI	Visible Irradiation
WLC	White-Light Continuum

Chapter 1

Introduction

1.1 Theme and motivation

This PhD thesis is a report on the research studies undertaken, with emphasis on ultrafast laser sources combined with adaptive optics which have great application potential. The problems studied, deal with three topics: (i) Internal modification in dielectrics with femtosecond pulses; (ii) Structured vortex and vector beams and their microstructural properties, (iii) High average power picosecond pulse handling of a liquid crystal on silicon (LCOS) spatial light modulator (SLM). Although the general theme is determination of engineering applicability, certain scientific investigations in this thesis pursue production-throughput and efficiency-and-quality improvement. The motivating theme of any laser engineering technique in this thesis is applicability. Whether the techniques are internal modification that changes material properties, the complex optical field that twists material, or the high average and giant peak power handling that use for parallel fast processing application is essential.

1.2 Industrial relevance

In the field of non-linear optics, self-focusing and observation of filamentation accompanied by supercontinuum are amongst some of the most interesting non-linear (NL) phenomena. The earliest reports on self-trapped filaments and observation of both Self Phase Modulation (SPM) and 4 wave mixing in solids was reported by Alfano and Shapiro in 1970 using high energy picosecond pulses excitation in glasses and crystals [1]. While spectral broadening in liquids was reported earlier [2]., supercontinuum generation in high pressure gases was observed much later [3] while stable self guiding or filamentation in air over many metres, termed optical bullets was demonstrated and attributed to the balance between self-focusing and plasma defocusing. Conical emission around the filament core, surrounding the thite light continuum is also observed in the forward direction in dielectrics [1,2] and in air [4]. Focusing ultrahigh intensity, fs laser pulses inside transparent dielectrics induces multi-photon absorption and can result in permanent structural modifications or chemical changes.

This is now a route to inscribing 2D/3D photonic components in glasses and polymers [5, 6]. Filamentation or self guiding requires low NA focusing optics and can create relatively deep modifications well exceeding the Rayleigh length due to the balance of SF with plasma defocusing.

Undoped polymers are attractive bulk substrates for femtosecond laser inscription due to their low cost and excellent optical transparency. For example, Poly(methyl) methracylate (PMMA) has been widely used for inscription of waveguides and Volume Bragg Gratings, (VBG's) [7]. Poly (methyl) Pentene (PMP, TPX Mitsui Corporation) is a very low-density polymer ($\rho = 0.83 g/cm^3$) with wideband transmission from the UV to the MIR with transmission windows even in the FIR. The material has stable dielectric properties. It can be extruded by injection moulding and has a relatively high melting point of 240°C, excellent chemical resistance, high gas permeability. Its structure, however, unlike PMMA is semi-crystalline which results in a slight haze. Applications of PMP include use as a release film, LED moulds and sterilisation case, blood test cells, medical instruments, and blood transfusion equipment [8]. A throughout study of the optical transmission properties of TPX from 0.4 – 40 µm was carried out by Lytle et al [9] to help optical designers and fabricators considering replacing expensive, glass optical components with cheaper and lighter modulable polymers.

A wide range of insulators exist that are capable of storing large amounts of metal ions. If the concentration of metal ions is below the saturation point of the host insulator, they can be dissolved without drastically changing the material's mechanical, optical, or electrical properties. These solid solutions form an interesting class of materials for creating metal-insulator composites. Materials with dissolved metal ions provide designers freedom to create unique metal structures embedded within host solids. In addition, femtosecond laser pulses can selectively precipitate metal particle [10, 11]. The controlled precipitation of silver nanoparticles in 3-demnsions using femtosecond laser irradiation is an industrially viable method to create precise conductive structure embedded within insulating material.

Typically a vortex beam has a helical phase front and rim-mode intensity distribution with a dark centroid. In theoretical explanation, photons in a vortex beam possess orbital angular momentum. Orbital angular momentum is a new eigenstate of photons which is of great interest in foundational research. It is very interesting that even in the macro-scale this kind of beam can introduce mechanical torque to material. Padgett in 2014 [12] theoretically outlined how to convert OAM to mechanical torque. Recently, Ambrosio *et al* [13] has used

vortex beams to generate spiral structures at the surface of dye doped azo-polymer films. In contrast to vortex beams, the beam with azimuthal or radial polarizations, the beams may not have a helical phase front but the orientation of electric field can be radial, azimuthal or spiral. Such beams, called vector beams, show great potential to build novel material or geometrical structures but the research for the application of this beam is on the way. These kinds of beams have space-variant polarization instead of homogeneous polarization. Vortex-and-vector beam technology has resulted in advances in many applications, including microscopy [14], optical tweezer [15], and electron acceleration [16].

McKnight *et al.* (1989) described a SLM device with a 50×50-pixel nMOS array [17] on an active silicon backplane combined with a nematic liquid crystal (LC). Within five years, a 250×250-pixel device was designed and constructed [18] and commercial development of LC SLMs has been rapid ever since by companies such as Holoeye (Germany) Boulder Systems (USA) and Hamamatsu (Japan). Phase only SLMs (spatial light modulators) have been used for a wide range of both scientific and industrial applications such as: wavefront correction in astronomy [19]; the creation of spiral laser beams carrying orbital angular momentum (OAM) [20], clarifying the relationship of OAM to spin angular momentum (SAM) [21]; static and dynamic parallel beam processing with ultrafast lasers [22]; and dynamic polarisation control for surface micro-patterning [23].

1.3 Aim and Objectives

The single aim of this work is to develop micro-processing technology of ultrafast laser using spatial-light-modulating technology. The objectives of this thesis are:

1) To study femtosecond inscription inside polymer materials with numerical aperture, wavelength and increase the amount of refractive-index change an order high than previous work in PMMA and construct volume Bragg gratings.

2) To study 3-dimentional writing in silver-doped silica and polyvinyl alcohol (PVA) using NUV femtosecond pulses.

3) To explore twist structures inside transparent material using femtosecond beams carrying orbital and spin angular momentum.

4) To investigate the thermal and optical performance of a spatial light modulator with 250W of picosecond laser exposure for materials processing applications.

In the area of femtosecond modification, low NA – 0.13, 120 fs /800nm/400nm inscription of VBG's in a range of polymers with different densities can be carried out with highest diffraction efficiency $\eta_1 = 45\%$ observed in PMP, an order of magnitude greater than in the other polymers and attribute to its very low density [24, 25]. Such a low-density material with a large free volume may contract more than a denser material, increasing local density and hence Δn. This argument was also supported by both optical images and TEM of modified regions in PMP, showing higher contrast than in other polymers with RI modulation estimated to be $\Delta n \sim 5\times10^{-4}$ [24].

A silver-doped silica and polyvinyl alcohol (PVA) material is an attractive material for developing silver-insulator composites which can host a high density of silver ions. The gel mixer can be cast into thin films, which was homogenous. Thermal dynamic analyses can be engaged to characterize the composite and it was observed that the silver ions remain stable in the material over time and at temperature of *100* °C, which represents a remark improvement over previous solid solutions of silver [26]. Silver ions in the films can be activated in 3-dimentional geometries using femtosecond pulses.

Employing an optical vortex, especially in fs regime, is an interesting technique and can be created from a Gaussian beam using a phase only SLM. Optical orbital angular momenta (OAM), different from the intrinsic spin angular momentum (SAM), associated with circular polarizations. At this stage, there is little knowledge about the internal interaction of vortex beams within dielectrics. It is interesting to carry out an experimental investigation on the transfer of momentum between dielectrics and optical OAM. Absorption of photons carrying high levels of OAM can generate a torque on the surrounding material, which has been investigated here.

There is great interest in ultrahigh throughput precision laser-materials micro-structuring. New powerful ultrafast lasers on the market can now produce average powers of several hundred Watts and with peak powers exceeding 150GW [27], presenting a challenge for SLM devices. The power-handling level of SLMs has been limited to < 15W restricting industrial applications severely. Very recently, Klerks and Eifel (Pulsar Photonics GmbH)

demonstrated laser processing with up to <P> = 60W (404kHz/6ps) of laser radiation at 515nm on a cooled SLM in a fully integrated flexible beam shaping system with active cooling of the SLM chip [28]. There is a significant achievement, but is still somewhat limited, therefore, high-power tests at P >100W are of great interest for industrial and scientific applications.

1.4 Overview of this thesis

This thesis consists of 7 chapters and 3 appendixes.

Chapter 1 is the introduction of this thesis. In this chapter, the motivation, industrial relevance, aim and objectives are presented, followed with a discussion of aim and objectives.

Chapter 2 commence with a comprehensive literature review. This chapter presents knowledges of internal modifications, optical vortex-and-vector beams and details of liquid-cooled LCOS spatial light modulators. A synopsis for the state of arts is also given.

Chapter 3 is the experimental schemes and setups. This chapter introduce laser systems, spatial light modulators and related apparatus used in experiments. The fabrication of volume Bragg gratings and the assessment of their working diffraction efficiency are introduced. The approach to generate computer-generated hologram (CGH) is introduced.

Chapter 4 focuses on internal inscription. Microscopic results of structural changes of investigated materials are presented, supplemented with supercontinuum spectral and Raman spectral analysis.

Chapter 5 focuses on optical vortex and vector beams. This chapter is focused on the processing using fs pulses with tailored complex amplitudes – and-phase vortex and vectored beam. A numerical study about phase front and intensity profile is presented and followed with experimental investigations.

Chapter 6 focuses on high-power tests on liquid-cooled LCOS SLMs. The experimental results of thermal response and phase response are reported. This chapter also report practical tests of the two SLM device exposures to picosecond pulse with average power from a few Watts to 250W in parallel processing micromachining.

Finally, Chapter 7 summarises the results and conclusions of the individual chapters, and suggests potential improvements and ideas for future work. In appendix, MATLAB codes to simulate 3D spatial structure and LABVIEW program upgrades work to refine CGH are presented. In addition, the transmittance spectra of investigated materials are also presented.

Chapter 2

Theories and literature reviews

2.1 Introduction

Today ultrafast-laser technology continues to develop very quickly. Advanced ultrafast laser systems can provide femtosecond pulses with pulse duration <10fs, high repetition rates >1GHz and average power P > 300W. Commercial development of liquid crystal on silicon spatial light modulators (LCOS SLMs) has been rapid. The newest technology opens the possibility of using an integrity system to fabricate complex and accurate products with high production throughput and promised quality. This chapter provides a technical view of the field concerning innovative techniques of ultrafast laser machining and will review the state of the art of mechanisms and models of nonlinear interaction, internal femtosecond-laser microstructure, advanced photonic-and-optical technology: orbital angular momentum (OAM) and vector beam, and advanced diffractive optics: liquid-crystal-on-silicon LCOS spatial light modulators (SLMs).

2.2 Natural phenomena generated by femtosecond pulses

2.2.1 Filamentation

Laser beam with ultrahigh intensity could lead to filamentation in a dielectric medium. Filamentary structures are formed by the competition between self-focusing and plasma defocusing effects [29]. Figure 2.1 illustrates filamentation or self-guiding generated by terawatt femtosecond pulses in air.

Using a Gaussian beam, optical energy is confined in a volume with a symmetrically cylindrical envelope with a diameter close to beam waist at the focal plane [30]. Self-focusing critical power is given as, [31]

$$P_c = \left[\frac{\pi(0.61)^2\lambda_0^2}{8n_0n_2}\right] \quad (2.1)$$

where n_0 is refractive index, n_2 is the non-linear (NL) refractive index and λ_0 is wavelength in vacuum.

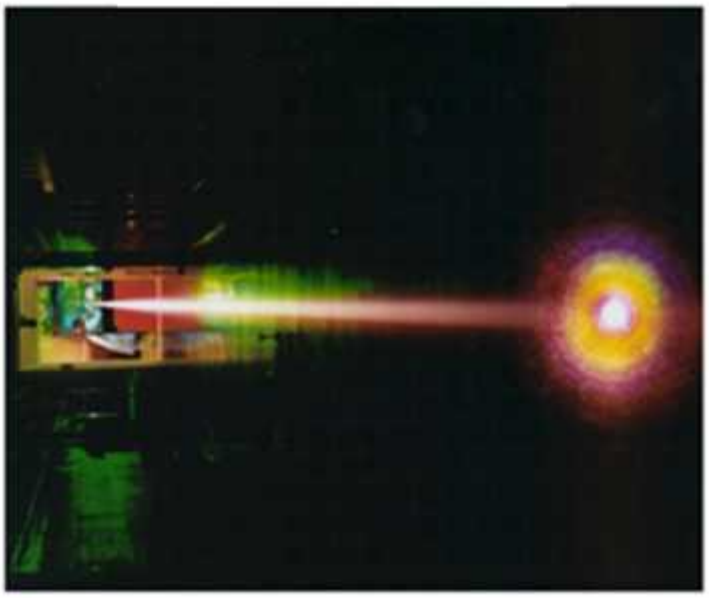

Figure 2.1. Filamentation in air, courtesy to W. Pelletier (University of Michigan)

When peak power is above a critical value (material dependent), self-focusing (SF) occurs, creating a positive lens with refractive index

$$n = n_0 + n_2 I \quad (2.2)$$

where n_2 is the NL refractive index. The increase of intensity excites seed electrons in the conduction band through nonlinear multi-photon ionisation (MPI), followed by electron avalanche, producing a weak free electron plasma of density $\rho_e(t)$ which rises exponentially with the peak at the centre, creating a negative lens. Consequently, the rising of electron plasma density can defocus the beam. The balance of these two effects results in filamentation, self-guiding over distances much greater than the Rayleigh length. Figure 2.2 illustrates that the focused beam does not defocus after the focus plane, instead of forming cylindrical volume, coloured with cyan region, along the propagation of light. The formation of weak plasma in filamentation, caused by multiphoton absorption of electrons is well confined in the filamentation, leading to a uniform and long volume. The confined energy can be used to modify physical or chemical properties of materials.

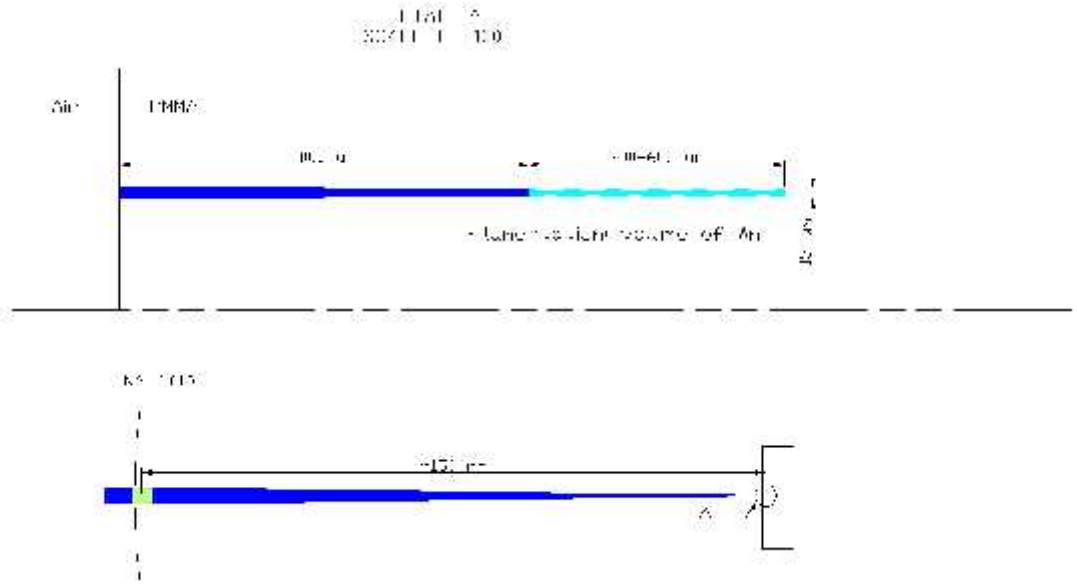

Figure 2.2. Objective lens and Self-guiding propagation

Zverev and Pashkov's work [32] theoretical explain filament length related to beam intensity and critical power, which is given by

$$l_f \propto \sqrt{\left(\frac{n_2}{n_0}\right)(P - P_C)} \quad (2.3).$$

The cross section of filaments, which is the region coloured with cyan in Figure 2.2, has a radius not just the beam waist of focused Gaussian beam and was experimentally determined.

It is notable that the induced wave-front curvature brings the focal point nearer the laser source so that the geometrical focus and self-focusing focus are at different points. This means the leading edge of filamentation is moving to the incident surface related to beam intensity (P) and the critical power (P_C) is given by [33]

$$z_f = \frac{0.3 \quad ka^2}{\left\{\left[\left(\frac{P}{P_C}\right)^{1/2} - 0.8\right]^2 - 0.0\right\}^{1/2}} \quad (2.4)$$

where z_f is the depth from the front face.

2.2.2 The third order susceptibility ($\chi^{(3)}$)

Filamentation is a third-order nonlinear optical effect. Third-order nonlinear effects are physical mechanisms of some important applications, such as phase modulation, nonlinear refraction and mixing and nonlinear absorption. Interaction of femtosecond laser pulses and medium induce polarization which is nonlinear with the optical electric field [34]. The induced polarization can be expressed by a Taylor series expansion as:

$$P_i = \varepsilon_0 \chi_{ij} E_j + 2d_{ijk} E_j E_k + 4\chi_{ijkl} E_j E_k E_l + \cdots \quad (2.5)$$

in which χ_{ij} is the linear susceptibility, d_{ijk} and χ_{ijkl} are nonlinear optical susceptibilities respectively. The second order term is responsible for the second harmonic generation, parametric amplification and oscillation while the third order term is responsible for filamentation, supercontinuum and multi-photon absorption. These are all related and the coefficient $\chi_{ijkl} \overset{\text{def}}{=} \chi^{(3)}$.

The third-order susceptibility is theoretically described by a complex number, $\chi^{(3)}$. The real and imaginary parts of $\chi^{(3)}$ are the important physical parameters that contain the information of high-order electromagnetic response of materials which can be used in ultrafast switching [35], high-speed decoding [36]. The real part of $\chi^{(3)}$ can be obtained via experimental methods. The unit of the real part is not explicitly sated while it is given in "e.s.u." (electrostatic unit). For Gaussian unit:

$$[\chi^{(3)}] = \frac{c^2}{s^2} \quad (2.6)$$

and

$$1 \text{ statvolt} = 300 \text{ v} \Rightarrow \chi^{(3)}\left(\frac{c}{v^3}\right) = \frac{4\pi}{(3\times 10^4)^2}\chi^{(3)} \text{ e.s.u} \quad (2.7)$$

$\chi^{(3)}$ is a polarisation-dependent tensor which scale linearly with wavelength [37]. In addition, the nonlinear refractive index n_2 with units cm^2W^{-1} is given by, [38]

$$n_2\left(\frac{c^2}{W}\right) = \frac{2}{n_0^2} \times 10^4 \times \chi^{(3)}\left(\frac{m^2}{V^2}\right) = \frac{80}{n_0^2} \times \chi^{(3)} \text{ (e.s.u.)} \quad (2.8)$$

When $\chi^{(3)} > 0$, the medium is termed a self-focusing material [39]. The $\chi^{(3)}$ of optical materials is in the range of 10^{-13} – 10^{-14} e.s.u. [40]. In table 2.1, $\chi^{(3)}$ coefficients of materials concerned in this work are presented.

Table 2.1 shows measured values of the third order susceptibility from previous literature.

Table 2.1: $\chi^{(3)}$ (10^{14} e.s.u.) of investigated solid material.

Material	**λ**	**Sort**	$\chi^{(3)}$	**References**
PMMA	1500 nm	amorphous	3.0	[41]
Fused Silica	1064 nm	amorphous	3.8	[42]
ZeSe	1064 nm	crystalline	440	[43]
Sapphire	-	crystalline	6.2	[37]

2.2.3 Multi-photon absorption (MPA)

During internal inscription, the structural changes are produced directly through photonic modification. The photon absorption is nonlinear because of the short time duration and high irradiance [44]. The electric-field strength of constrained electrons in the valence band which is of the order of 10^7 Vcm^{-1}, has the same order of the electric field strength of irradiance 5×10^{16} Wcm^{-2} [45]. Few thermal mechanisms play direct roles because the coupling time between two temperatures: electrons and lattice is typically greater than 1ps, absorbed optical energy is directly deposit in a confined volume, similar to an adiabatic processing. Table 2.2 shows measured values of the band gap from previous literature.

Table 2.2: Optical band gap of investigated solid materials.

Material	**Band Gap (eV)**	**References**
PMMA	4.58	[46]
PMP	6.2	[9]
Fused Silica	8.9	[47]
ZeSe	2.82	[48]
Sapphire	10	[49]

Below the picosecond timescale, the electrons from the valance band can be directly ionized by laser pulses with ultrahigh intensity. The excitation is driven by multi-photon ionization (MPI) or tunnelling ionization [50]. The photoionization rate depends strongly on laser intensity and the rate is given by

$$P(I)_M = \sigma_k I^k \quad (2.9)$$

where σ_k is the multphoton absorption coefficient for absorption of k photons [51].

For explaining the MPI, a Jacoby's diagram, illustrated in Figure 2.3, is used. The photon energy makes critical roles on the order of multi-photon absorption. For example, the optical bandgap of PMMA which is *4.58*eV, is the minimum energy to excite an electronic transition from the valence band (VB) to the conduction band (CB). In addition, the bandgap energy of poly methyl pentene (PMP) is *6.2* eV. Therefore, it requires 2-photon and 4-photon coupling respectively for 387-nm and 775-nm photons in PMP to generate free electrons.

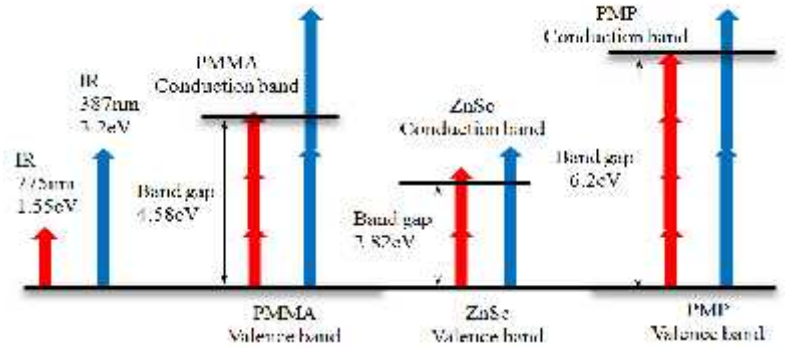

Figure 2.3. Jacobi Diagram of the multiphoton excitation of an electron in PMMA, ZnSe and PMP from the valence to the conduction band.

In the case of tightly focused beam, MPA can be overrode by avalanche ionization [52], also called as impact ionization [53]. The dense plasma around geometrical focus can lead to optical breakdown (OB) damaging materials. The damages can be vacancy, dislocation for crystalline materials, or just carbon debit for polymers. The occurrence of OB or FL depends on the plasma density in which pulse duration and external focusing condition play critical roles in the case.

2.2.4 Supercontinuum

One of the remarkable phenomena associated with self-focusing (SF) at low NA is the generation of supercontinuum (SC) which is useful for many important applications. Because SC is a wideband light source, techniques based on SC serve as optical frequency combs [54], tuneable coherent source [55], nonlinear microscopy [56] and optical coherence tomography (OCT) [57].

Alfano and Shapiro (1970) reported a spectral super-broadening, which covered from 400 to 700 nm, of the generated light in BK7 glass using ultrafast pulses (τ = 5ps, λ=530nm and Ep=

5mJ) [58], in which notable that the super-broadening spectra were 10-times wider than previous reports. When using NIR fs pulses, the anti-Stokes continuum results in well-known white light [59]. Hence supercontinuum is also called as white-light continuum. Conical emission around the filament core, surrounding the white light continuum is also observed in the forward direction in dielectrics [60] and in air [61].

The threshold for SC generation is the threshold for self-focusing (SF) [62, 63, 64]. Bloembergen proposed the connection between supercontinuum and filamentation and he used the hypotheses to explain the supercontinuum generated by picosecond pulses as a form of self-phase modulation generated in self-focusing and plasma defocusing [65]. The increasing spectral bandwidth of self-phase modulation is due to the temporal change of refractive index δn/δt. Then at higher intensities, this is enhanced by avalanche ionization, SF/WLC (white-light continuum) with much higher bandwidths. In addition, it is notable that SC generation has material dependence, which requires that the material bandgap $E_b > 2.8eV$ [66]. In most media a threshold peak power P_{th}^{s} for supercontinuum can be found in the order of 10^6 Watt [67].

2.2.5 Interaction mechanism

Femtosecond pulses could produce defects [68] and colour centres [69] in transparent dielectrics. The defects and colour centre lead to significant change in refractive index. The change resulted in colour centre is not permanent and by annealing method, the changes is reversible. It was suggested that the laser field (loosely focused and 1-μJ) could directly drive structural rearrangement [70] and trap stress around the focal region. Morikawa *et al*. (2010) reported that birefringence in fused silica is observed in processing region using loosely focused laser pulses with 1μJ energy which is evidence of trapped stress [71]. The structure exhibited birefringence features against the incident linear-polarized beam and had a positive refractive-index change ($\Delta n \approx 10^{-3}$). A photon-induced structural transition and defect formation are likely responsible for the change of refractive index. It is notable that Cerullo et al (2002) reported that weak plasma induced by low energy pulses under tight-focusing conditions can produce small irreversible refractive-index changes ($\Delta n \approx 10^{-4}$ to 10^{-2}) [72].

Femtosecond pulse, especially with high repetition rate, may change the phase of material [73]. Material could be melted by the rise of temperature and re-solidified, causing material

phase changes. In addition, Chan *et al* (2001) reported that femtosecond laser pulses could directly densify materials [74]. Rising temperature can increase density of fused silica to the maximum magnitude and then quenching fused silica from *1800* K can form higher-density structures. Schaffer *et al*., (2003) used Raman spectrum analysis characterized densifying structures in fused silica after damaged with tightly focused femtosecond pulses [75]. However, Saeta *et al* argued that in some cases, the density drops along with the rise of temperature [76]. In addition, heavy exposure in bulk glass with high-repetition pulses could cumulatively produce positive index modulation [75], which can be used to write waveguides in glasses.

For polymers, chemical mechanisms play critical role. Baum *et al.* suggested focused 170fs NUV (λ=387nm) pulses lead to photochemical degradation of PMMA in focused volume and the highest refractive-index changes is 1×10^{-4} and concluded that 2-photon absorption in PMMA at 387nm, 3-photon absorption at 775nm absorption requires short pulses <120fs with higher peak power to excite the transition [77]. They suggested that the multi-photon absorption in filamentation results in photochemical modification and leads to cleavage of the polymer chains and the formation of monomers. Baum *et al.* (2008) supplemented that using Size Exclusion Chromatography (SEC) comparing Polymer Molecular Weight Distribution (MWD) after exposure - the peak broadens and shifts to lower molecular weight values with rising laser fluence, indicating the scission of the polymer backbone [78]. These results suggest the increased refractive index change is due to the two underlying processes, firstly the UV- densified C=C bonds generated by the chain scission in the polymer end groups and secondly, thermoplastic deformation. Note that the monomer MMA release is possibly undesirable for the in-vivo application as MMA is toxic in bio systems.

Heating [79] or laser irradiation with pulse lengths ranging from nanoseconds to femtoseconds [80] can activate the silver in transparent host material. These processes cause chemical and structural changes in the host insulator, which produce free electrons that reduce the metal ions. The formation of metallic particle has size of nanometre scale. A key example of this technique is the production of embedded metal nanoparticles, where the host material is responsible for the reduction of the metal ions to atoms, and stabilization of the resulting nanoparticles. The technology of surface plasmon resonance (SPR) is employed on these encapsulated nanoparticles [81]. Some applications were developed, including micro-polarizers [82], optical sensors [83], and 3D optical storage units [84].

Note the remarkable NL response of Zinc Selenide, two orders of magnitude larger than other materials, shown in Table 2.1. It means that Zinc Selenide is interest nonlinear material. Research interests include lasing, spatial stretching of pulse width and second harmonic conversion. In addition, Zinc Selenide is transparent to mid-infrared light which can be used to produce diffractive optics or simply a lens. The most important is that is Zinc Selenide is attractive host material for solid-state infrared lasers. Cr^{2+}: ZnSe has enormous gain bandwidth which gives the availability to generate infrared pulses with extreme short duration in a few cycles. The mode-locked implementation using Cr^{2+}: ZnSe (850 nm FWHM) to generate sub 100fs pulses was reported in previous works [85]. In addition, using Er-dopped fiber laser (CW, λ=1.16μm) to pump multi-crystalline Cr^{2+}: ZnSe can generate femtosecond frequency combs with a central wavelength λ=2.45 μm [86]. Femtosecond frequency combs can provide higher resolution for optical interferometer and precise spectroscopy. Especially, femtosecond comb operated in mid-infrared region can be used to detect molecular due to the particular absorption features [87]. In addition, the comb is used to harness the phase of the electric field in such attosecond pulses [87].

2.3 Photons with angular momentum

2.3.1 Orbital angular momentum and spin angular momentum

Light possessing helical phase front which shown in Figure 2.4 is called an optical vortex. Optical vortex beams carry angular momentum. The helical structures are illustrated in Figure 2.3. The spiral phase front of a vortex beam revolving about the propagation can be geometrically characterized by an integer number (m). In a polar coordinate system m determines the number of how many revolving azimuthal phase, φ varying from 0 to 2π. The topological number (m) defines the OAM carried by each photon is equal to $\pm m\hbar$ [88].

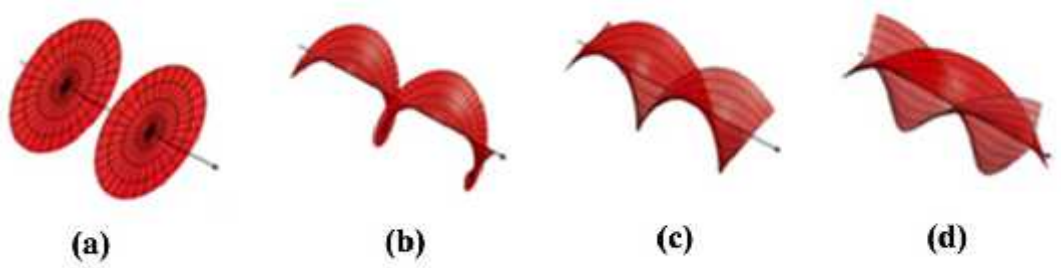

Figure 2.4. Optical Vortex for topological charge number (a) m=0, (b) m=1, (c) m= 2, and (d) m = 3. The schematic is courtesy to [89].

Theoretical understand of orbital angular momentum due to the azimuthal component is presented. According to Yao and Padgett [89], the k vector is normal to the helical face, shown in Figure 2.5, and consequently an azimuthal component is acquired. The linear momentum of a photon is $\hbar k$. The deviation of the tangential angle of the helical face of a point on the wavefront is,

$$\frac{m}{2\pi r} = m/k_{\perp} r \quad (2.10),$$

where r is the radius to the optical axis. The photon gets an angular momentum as

$$\hbar k \times m \times r = m\hbar \quad (2.11).$$

Each photon carries an OAM $\pm m\hbar$ while a beam carries a flux of OAM: $\pm N \hbar$, where $N = W/\hbar\omega$ and W is intensity.

Besides OAM, photons can also carry spin angular momentum (SAM) which is related to their polarization states, shown in Figure 2.6. A beam with circular polarization carries SAM of magnitude $\pm\sigma\hbar$ per photon, where ± regards to two different the polarization chirality. Then the total angular momentum of a photon is $(m\pm\sigma)\hbar$.

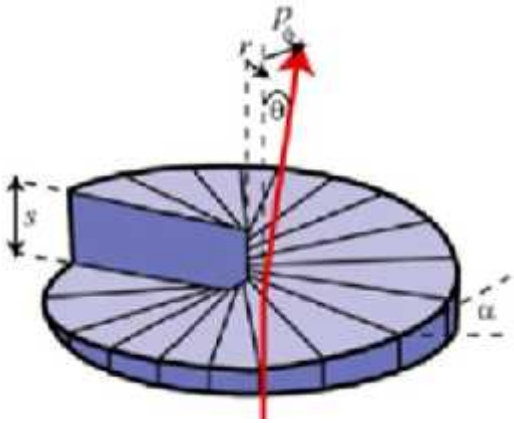

Figure 2.5. Azimuthal component of k vector. This schematic is courtesy to [89].

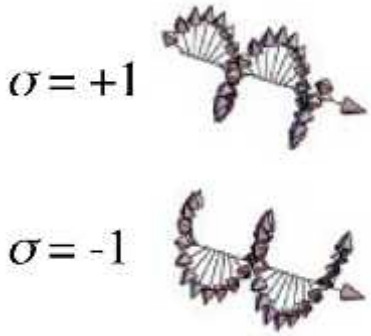

Figure 2.6. Spin angular momentum (circular polarization). The schematic is courtesy to [89].

2.3.2 Intensity profile of a beam carrying orbital angular momentum

The mode of a laser beam carrying OAM is Laguerre Gaussian which characterizes with annular intensity distribution [90], shown in Figure 2.7. Harris *et al.* described that the constructive interference of two beams with Hermite-Gaussian modes results in this annular distribution where the dark centroid is called as phase singularity [91]. It is interesting that the geometrical size of the singularity can be beyond diffraction limitation.

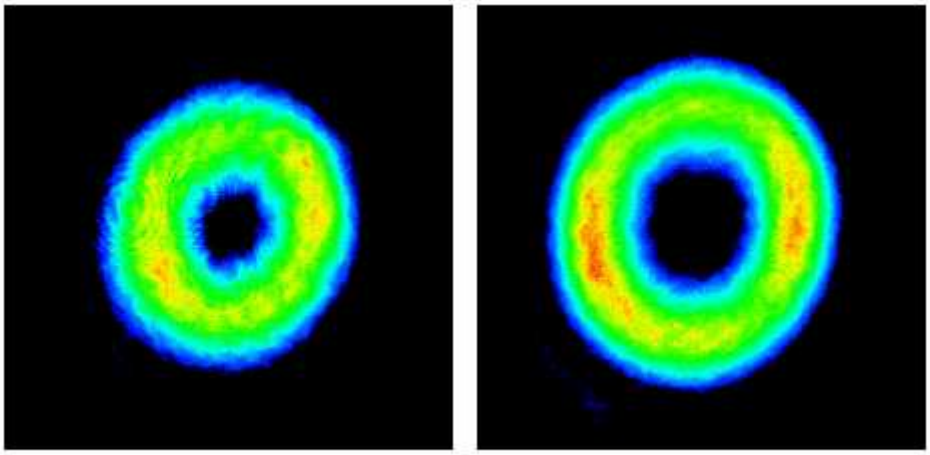

Figure 2.7. Intensity profiles of a vortex beam (λ=1064) at focus plane outputs with topological charges m= 1and 2. The images are courtesy to [92].

The electric field of spiral beams can be described theoretically by the following equation [93] for the electric field amplitude. In equation 2.12, the r_0 applies to radius to $1/e^2$ of the peak (Gaussian mode).

$$E(r,\theta) = E_0 \frac{1}{\sqrt{m!}} \left(\frac{\sqrt{2}r}{r_0}\right)^m e \quad \left(-\frac{r^2}{r_0{}^2}\right) \exp(i \quad) \qquad (2.12)$$

and hence intensity given by

$$I(r,m) = E^* \cdot E \qquad (2.13).$$

2.3.3 OAM conservation

The experimental study of OAM conservation yields more physic knowledges about OAM such as atom physics [94], nonlinear optics [95] and quantum optics [96]. It is notable that in recent using a spatial light modulator to construct vortex beams are very popular however short wavelength UV light could degrade the liquid crystal material via photonic disassociation [97]. Using a SLM device to modulate light in NIR region then doubling to NUV region is a good solution.

Using phase matching in a non-linear crystal such as BBO can apply a frequency doubling on the signal and generate light with shorter wavelength. It is interesting that the OAM number maintain conservation in frequency doubling, presented as

$$m_{2\omega} = 2m_{\omega} \quad (2.14)\ [89]$$

Previously it was believed that the direction of Poynting vector keeps the same in the case of frequency doubling. However, Desyatnikov, Kivshar, and Torner (2005) observed that the phase-matching condition for a vortex beam is different from the one for a plane wave in experiments [98].

For higher order mode (m>0), the intensity distribution has a multiple-ringed pattern [99]. The problem becomes more difficult. The divergence of intensity distribution becomes much larger, due to the frequency-doubling process. The mode is not a pure Laguerre-Gaussian mode, which can be explained as a superposition of several LG modes corresponding to different p but same l [100]. The mode-order difference leads to difference in Gouy phase [89]. Consequently, there is a spatial difference upon the superposition in propagation. In addition, Miao *et al.* (2016) suggest that SAM and OAM are independently conserved when propagating in homogenous, isotropic, non-dispersive transparent medium, however, in anisotropic or inhomogeneous materials, spin and orbital momentum can swap [101].

2.3.4 The propagation of optical vortex in transparent material

Employing an optical vortex, especially in fs regime, is an interesting technique. At this stage, there is little knowledge about the internal interaction of vortex beams within dielectrics, hence an ideal area in which to carry out an experimental investigation on the transfer of momentum between dielectrics and optical OAM. The propagation of a vortex beam in nonlinear media appears very different from that of Gaussian beam [102]. The propagation of vortex beam could be self-guided similar as guidance by waveguides [103, 104, 105]. Due to the self-guidance propagation, the annular intensity of a vortex beam can lead to the rising of refractive index in a hollowed cone volume and give a rise of a secondary beam along the hollowed cone structure [106]. Vortex beams can be viewed as a series of inclined plane waves and the developing directions of solitons are tangential to the initial ring because of the conservation of original angular momentum (OAM) [107] and [108]. Apart from the secondary beam, the annular ring can be distorted and self-focused to “hot spots” by the

asymmetry feature of the system, and broken into individual transverse solitons [89]. Figure 2.8 (a), (b) and (c) respectively modelled intensity distribution of vortex beam with m = 3, 5, and 8, showing solitons at yellow region.

The most recent literature shows that the filamentation of vortex beam can be manipulated and the amount of filaments can be predicted" (Ju *et al.*, 2016). Presently soliton theory provides new insight on the study the OAM of light [102].

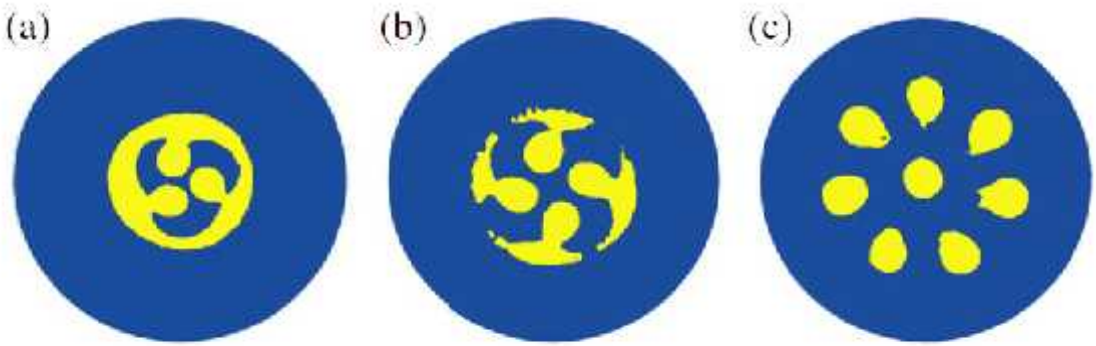

Figure 2.8. Spatial intensity distribution of vortex beam with topological charge number: (a) m=3, (b) 5 and (c) 8; Yellow refers to high intensity and blue to low intensity. The figures are courtesy to [102].

2.3.5 Spiral microstructure

The study of optical vortex is significant. experimental study and theoretical studies show the great prospect on many important applications and deep knowledge on fundamental science. For example, the study of momentum transfer between photons and matter reveals "the geometrical Berry phase" [109], "spin Hall effect" [110] and "OAM conservation in SHG" [111].

Ambrosio et al. observed spiral structures during exposure of azo-polymer to spiral beams where the spiral direction reversed with beam helicity using CW laser [112], shown in Figure 2.9. The origin of the mass transport-driving mechanism is unclear. Padgett and Bowman (2011) outlined how to convert OAM to mechanical torque [113]. Previously, proposed models share a common element: the light-induced mass-transport action is linked to the

optical field via its intensity gradients. The relationship is vectoral, as the mass transport appears to occur preferentially in the direction of the electric field [114]. Recently Barada *et al*. theoretically explain the radiation force driving azo-polymer film and claim observed the formation of the twisted structures requires both spin and orbital angular momentum [115].

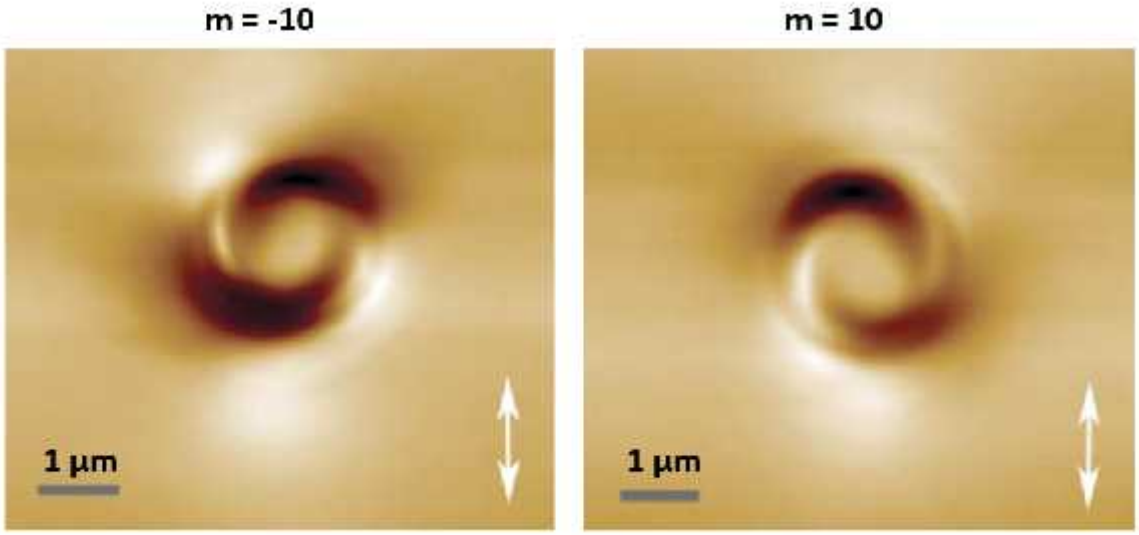

Figure 2.9. AFM micrography of helical twist structure generated by CW green laser on the surface of azo-polymer. The AFM micrography is courtesy to [112].

2. 4 Optical polarization and vectored beam

2.4.1 Polarization states

Conventional states include linear horizontal polarization (T), linear vertical (T) and circular polarization. For these states, the electric field has same direction in cross section, which is shown in Figure 2.10.

In recent years, vector beams in which electric-field distribution is inhomogeneous become very interesting because of the great applicable prospect. Two eigenmodes are radial and azimuthal polarized beams, shown in Figure 2.11. In addition, there is intermediate state of azimuthal and radial state. The intermediate state is the superposition of these two eigenmodes. The two eigenmodes with same amplitude generate the superposition pattern which consists of a series of logarithmic spirals.

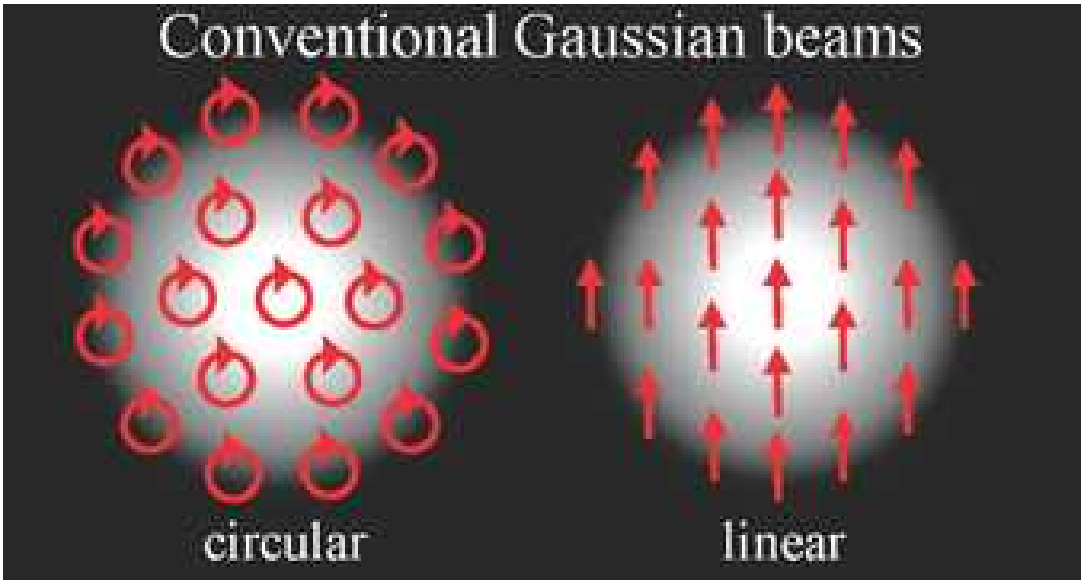

Figure 2.10. Conventional laser beam with homogenous-polarization distribution. This photo is courtesy to [116].

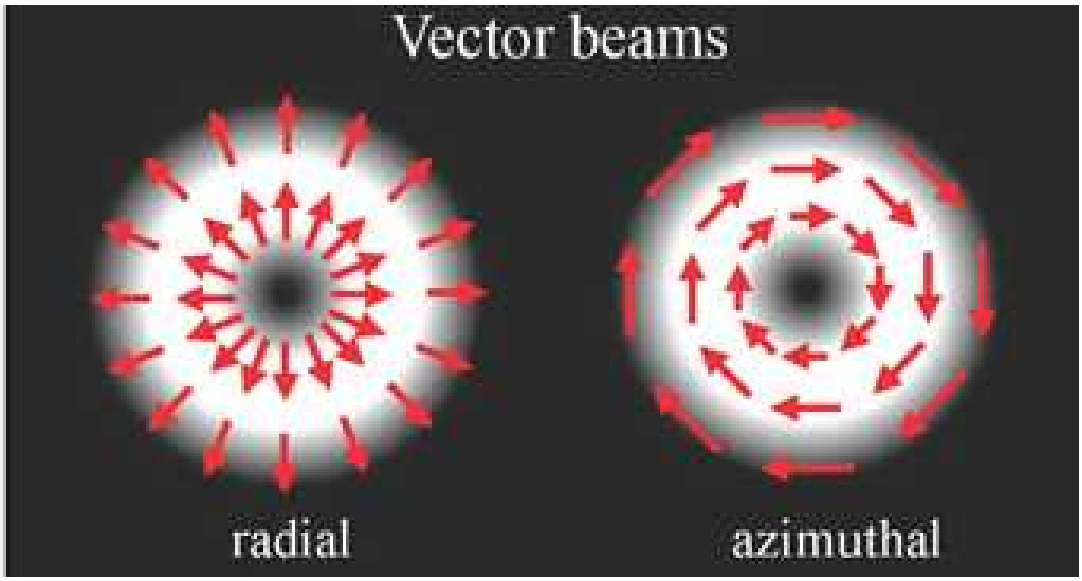

Figure 2.11. Vector beams with homogenous-polarization distribution. This photo is courtesy to [116].

For simplicity, the polarization state can be denoted as Ket notation, $|\mathrm{P}\rangle$. The polarization states associated in this thesis are listed in Table 2.3.

Table 2.3: Polarization states

Ket notation	J_p	Notation
$\|\mathrm{H}\rangle$	$\begin{bmatrix}1\\0\end{bmatrix}$	Horizontal Linear
$\|\mathrm{V}\rangle$	$\begin{bmatrix}0\\1\end{bmatrix}$	Vertically Linear
$\|\mathrm{R}\rangle$	$\begin{bmatrix}0\\-i\end{bmatrix}$	Right-handed Circular
$\|\mathrm{L}\rangle$	$\begin{bmatrix}0\\i\end{bmatrix}$	Left-handed Circular
$\|\mathrm{A}\rangle$	$\begin{bmatrix}\cos\phi\\s\end{bmatrix}$	Azimuthally Axial Symmetry, Ref.1
$\|\mathrm{R}\rangle$	$\begin{bmatrix}-\sin\phi\\\cos\phi\end{bmatrix}$	Radial Axial Symmetry , Ref.1

(Notes: ϕ is the anticlockwise angle to the positive x-axis [117].)

2.4.2 Intensity profile of vectored beams

The intensity distribution of pure vector beam has a donut-like pattern, known as a Laguerre Gaussian (LG) mode. The dark area at centre for pure vector beams is called as polarization singularity. Vector beams has great application prospect and resulted in advanced applications such as microscopy [118], optical trapping [119] and electron acceleration [120]. The singularity of polarization has zero intensity can construct nanostructures or produce nanoparticles.

In a cylindrical coordinate system, the scalar electric field can be described by [121]:

$$E(r,\phi) = E_0\sqrt{\rho}e^{-\rho/2}e^{\pm i\phi} \quad (2.15)$$

where r and ϕ are the radial and azimuthal cylindrical coordinates ($\rho = \frac{2r^2}{w^2}$, w is the beam waist and ± sign is the spiral sense. Hence, intensity is given by,

$$I(r,\phi) = [E]^2 = E^*E = I_0\rho e^{-\rho} \quad (2.16).$$

A donut intensity with zero intensity on centre. The L $(0,1)^*$ spiral mode can be defined by a superposition of two orthogonal harmonic functions;

$$E_x(r,\phi) = E_0\sqrt{\rho}e^{-\rho/2}\cos(\phi) \quad (2.17)$$

$$E_y(r,\phi) = E_0\sqrt{\rho}e^{-\rho/2}\sin(\phi) \quad (2.18)$$

Radial polarization can consequently be explained by a vector sum, given by,

$$E(r,\phi) = E_0\sqrt{\rho}e^{-\rho/2}\cos(\phi)\overrightarrow{e_x} + E_0\sqrt{\rho}e^{-\rho/2}\sin(\phi)\overrightarrow{e_y} \quad (2.19)$$

where $\overrightarrow{e_x}$ and $\overrightarrow{e_y}$ are the unit vectors in the x and y directions.

Consequently, the intensity distribution,

$$I(r,\phi) = E^*E = I_0\rho e^{-\rho}\cos^2\phi + I_0\rho e^{-\rho}\sin^2\phi = I_0\rho e^{-\rho} \quad (2.20).$$

Vice Versa for AP mode:

$$E(r,\phi) = E_0\sqrt{\rho}e^{-\rho/2}\sin(\phi)\overrightarrow{e_x} + E_0\sqrt{\rho}e^{-\rho/2}\cos(\phi)\overrightarrow{e_y} \quad (2.21)$$

$$I(r,\phi) = E^*E = I_0\rho e^{-\rho}\sin^2\phi + I_0\rho e^{-\rho}\cos^2\phi = I_0\rho e^{-\rho} \quad (2.22).$$

2.4.3 Polarization sensitivity

Polarization plays critical role in the linear interaction of ultrafast pulses with material. For instance, surface ablation with ultrafast pulses [123], Fresnel reflection [124], Zeeman effect [125] all exhibit significant polarization sensitivity. For nonlinear interaction, self-focusing, filamentation [126] and multi-photon ionization (MPI) in atoms [127], molecules [128] and solids [129] are sensitive to polarization state of incident beam. Gawelda *et al.* observed distinct polarization-dependent filamentation in doped phosphate glass through the studying of transient plasma in self-guiding [130].

Theoretically for isotropic material nonlinear refractive index ratio of n_2^{ll} and n_2^{c} is 1.5 because the numbers of components in the third-order susceptibility $\chi^{(3)}$ are 2 (linear) and 1 (circular) respectively [131]. For the effect of nonlinear (NL) order on the ratio of these transition probabilities (δ) for circular polarisation (CP) at low n, CP dominates over linear polarisation, but at higher n > 4 linear polarisation couples more strongly. In experimental studies, the relation between transition coefficient δ_{3c} and δ_{3l} in 3-photon ionization of Cesium, respectively corresponding to circular and linear polarization, was given by δ_{3c} =

(2.15 ± 0.4) δ_{3l} [132] however this transition ratio become reversed when MPI is at higher order (n > 4) [133]. Carman and Compton confirmed the ratio of $\left(\frac{\sigma_6^{li}}{\sigma_6^{c}}\right)$ ~2.9 in 6-photon (N=6) resonance-enhanced MPI, in the NO molecule [134]. Furthermore, Temnov *et al*. measured $\left(\frac{\sigma_6^{li}}{\sigma_6^{c}}\right)$ ~3.7, in fused silica using laser pulses (50fs, 800nm, peak intensities I_p ~ 10-20 TW cm^{-2}) [132]. Quantum selection rules contributes the difference. In addition, polarization can also affect the efficiency and quality of process, such as refractive index modulation, surface structuring. The isotropic properties of circular polarization are applied in the case of multi-direction processing [135] but there is a compromise on the processing efficiency and quality [136, 137].

Laser induced periodic surface structures (LIPSS) have been found on surface-processing region. LIPSS appears as orientated ripples with a period close to incident wavelength and the orientation is perpendicular to the polarization of the incident electric field of light. Since LIPSS is controllable, LIPSS processing is an important technique to change surface morphology controlling the physical or chemical properties of a solid product. Figure 2.12 presents spiral LIPPS pattern generated by vector beam with orthogonal superposition of two eigen sates: azimuthal and radial polarizations. LIPPS processing can be used to many applications including to photonics, security, biomedicine, wettability, tribology and others.

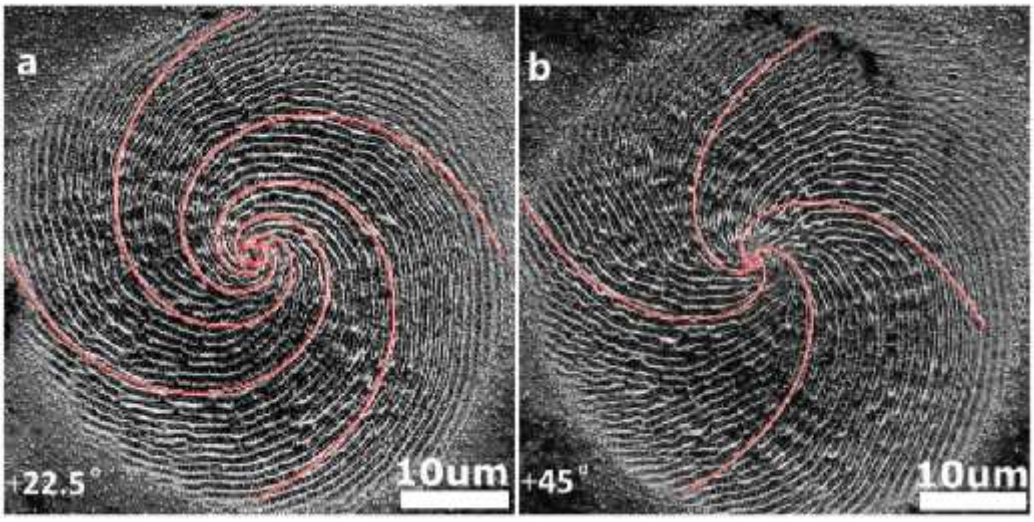

Figure 2.12. Spiral LIPSS pattern generated by vector beam (λ=1064nm, τ~5ps). The SEM microscopy is courtesy to [138].

The mechanism of LIPSS formation is not yet firmly established. Bonse, Rosenfeld and Krüger assumed that there is an electromagnetic wave excited on surface when ablation is made [139]. It is explained that the interference between surface plasmon wave and incident beam for the LIPPS formation. It is argued that surface wave or acoustic wave was excited by surface plasma [140]. Whatever, LIPSS can be used to characterize polarization states of incident light, certainly on surfaces.

Shimotsuma and Kazansky (2003) first reported periodic structures observed inside silica glass after exposure of tightly focused 800-nm, 150-fs pulses (NA= 0.95) [141]. This observation created a new technique for nanoscale dielectric modification. In consequent work, the technique was used to for inscription using birefringent dots in 3D for data storage and nanoscale gratings.

2.5 Internal processing using femtosecond pulses

Multi-photon absorption is the ideal absorption mechanism which can homogenously change refractive index of material. Self-focusing threshold $P_{cr.}$ can be estimated by SC spectral analysis. The third order susceptibility ($\chi^{(3)}$) can be derived from P_{cr}. The minimum bandgap for Self-focusing is ~2.8 eV [142]. The mechanism of refractive-index change may come from densification when high NA is applied. The feature of low density is expected to result in high Δn modification hence speed fabrication of diffractive components.

Pulse duration (τ) plays critical roles in filamentary inscription. Experiments carried out by Du *et al*. (1994) on fused silica (SiO_2) using the pulse duration ranging from 10ps to 150fs report the dependence of the fluence threshold on pulse duration, showing an increasing of threshold with decreasing pulse duration [142]. For filamentary inscription, the threshold value would be above 10^8 V/cm, at the order of magnitude at which tunnelling ionization makes a key role [142]. Baum *and* co-workers studied the pulse-duration effects on refractive-index modulation in PMMA, with pulse durations from 45-210fs at 800nm (*45*, *60*, *90*, *120*, *150* and *210* fs) [143]. They found that the strongest refractive-index change comes from the shortest pulses (45fs) whereas at the duration of 210 fs, RI change was very low combined with lower damage threshold. Hence pulse duration is critical to achieving the highest index change, especially for long wavelength. For longer pulses, free electrons interact with the ongoing pulse, lead to impact ionization and optical breakdown.

High repetition rates can significantly reduce the intensity threshold for Δn processing, opening the door to modulate refractive index for difficult-processing materials such as sapphire. For example, Schaffer *et al.* used *1.4*-NA focusing of an f_{rep} =*25*MHz, *800*nm femtosecond pulse train to write single-mode waveguide in glass [144]. The mechanism leading to refractive-index modulation is thermal accumulation while energy coupling is nonlinear. Cumulative heating mechanism can be used for accurately thermal energy depositing in sub-microscale volume. The deposited energy in given volume and hence the magnitude of the refractive-index modulation is related to total exposure. By adjusting the number of laser pulses, the amount of thermal energy deposited per unit volume can be precisely controlled to nanojoule resolution. In addition, the high repetition rate increases the inscription speed due to the high scan speeds required. The scan speed is two or three orders of magnitude higher than that accomplished with 1kHz rate.

High NA objectives manifest a very narrow processing window for filamentary processing. Femtosecond pulse train can reduce the peak energy threshold of inscription. The modification regime is based on plasma formation. Strong plasma formation is caused by optical breakdown, whereas the weak plasma formation is caused during filamentation. To implement filamentary inscription, a laser beam is weakly converged using an objective lens with low numerical aperture, N.A. < 0.2. The use of high NA objectives establishes a strong geometrical convergence of the beam which is likely to increase the rate of impact and avalanche ionization. Hence the electron density in the CB can reach 10^{18} -10^{21} cm^{-3} [145]**.** The self-guidance propagation does not necessarily happen in high NA, tight-focused case [146]. Bloembergen and his co-workers used tightly focused beam to achieve breakdown threshold but avoiding the filamentation. If the beam is tightly focused to radius r_0, $r_0 \ll (P_c / I_b \pi)^{1/2}$, where P_c is the critical power for self-focusing and I_b is the intensity threshold of breakdown, the converged beam cannot form filamentation. Since the focusing spot is in very small size, the nonlinear absorption is confined within the focal volume, leading to a very small Δn modulated volume which is as small as *0.008* μm^2 [147]. The peak energy for irreversible damage related to high NA and fluence has been estimated, [145] as:

$$E = \frac{I_t^2}{0.9}\left[2\pi\frac{N^2}{1-N^2} + \frac{I_\lambda^2}{P_c}\right]^{-1} \quad (2.23).$$

When filamentation occurs at low NA, this is accompanied by the appearance of super-continuum which is a useful diagnostic. Ashcom, *et al.* (2006) observed that when N.A. >

0.25, there is no supercontinuum and the spectral-signal intensity is thus changed. However, when 0.05 < N.A. < 0.15, supercontinuum is often observed [146].

It is noteable that the objective is designated for operating with UV light. Optics are coated with a dielectric film to enhance the transmission of UV light. It is notable that for internal inscription the choice of objective lens is critical. A microscopic objective might cause the stretching of the pulse duration leading to breakdown. However, the optic is possibly made of several materials. The problem of stretching pulse duration by 'group velocity dispersion (GVD) [148] is considerable. This is a challenge when engaging inscription with transmission objectives. In contrast, reflecting objective is better than transmission objective.

There are many reports using this technique to fabricate waveguides in a wide variety of glasses. Du *et al*. firstly demonstrated using femtosecond pulses to change refractive index of fused silica [142]. Miura *et al.* constructed optical waveguides in various glasses [149]. Watanabe, *et al.* (2006) used femtosecond pulse to write symmetric waveguides in bulk PMMA [150]. Okhrimchuk *et al* (2012) constructed waveguides in a Nd:YAG single crystal for active waveguide lasers [151]. Chen and Aldana used femtosecond pulses write 4 types of waveguides [152].

Volume Bragg Gratings (VBGs) are essential for certain high-cost optical integrity systems, such as thermal-image cameras [153] and astronomical telescopes [154]. In transmitted method, the light pass these layers with an angle θ, the VBG become a spectral-bandwidth filter [155], which is a critical component in advanced astronomical telescopes with high spectrum resolution measuring photometric redshifts and spectral emission line comparisons. In addition, VBGs are used as stretchers and compressors of a chirped pulse amplification (CPA) femtosecond lasers. This technique avoids damage to the expensive laser crystal and other optical components in the cavity by reducing peak powers well below the threshold for self-phase modulation, SFM and SF [156]. For example, the laser seed has large bandwidth, 100fs, 10nm bandwidth at *800*nm [157], VBGs act as diffraction gratings to stretch or chirp pulses. A VBG constitutes of a series of Δn layers with a given pitch, Λ. The diffractive beam can be shifted between 0 order, 1^{st} order, 2^{nd}. order etc. By carefully designing the length of Δn layer, the first order diffraction efficiency can theoretically achieve to 100%.

Diffraction efficiency is the ratio of the 1^{st} order diffraction intensity to the 0^{th} order intensity when no modulation is performed. The actual light utilisation efficiency depends on the amount of diffraction loss caused by the pixelated structures and the device reflectivity,

which is affected by readout light wavelength. The first-order diffraction efficiency, η, for a VBG is defined by the following relationship:

$$\eta = I_{+1}/(I_{-1} + I_{0} + I_{+1}) \quad (2.24)$$

where I_{+1} and I_{-1} is a first diffraction intensity and I_{0} a reflected intensity. The first order diffraction efficiency is the function of wavelength, and described by [158],

$$\eta_{\pm 1} = \sin^2\left(\frac{\pi \Delta n}{\lambda \cos\theta_B}\right) \quad (2.25)$$

where Δn is refractive index modulation of the grating plane, L is the grating thickness λ is the wavelength of incident light and θ_B is the Bragg angle.

The advantage of using fs pulses is that the processing structure is more convenient than conventional photo-modification UV treatment which requires multi-step procedure. In addition, the modification is ascribed to nonlinear absorption. The intrinsic nonlinear features make the processing area more precise with less thermal effects and 3D capability. This technique has many important applications and has been widely studied, such as photochromism [159], lab-on-chip [160], and 3D optoelectronics devices [161]. The using fs pulses to form silver particles with post thermal treating is especially interesting in this study. Figure 2.13 show a lab-on-chip device.

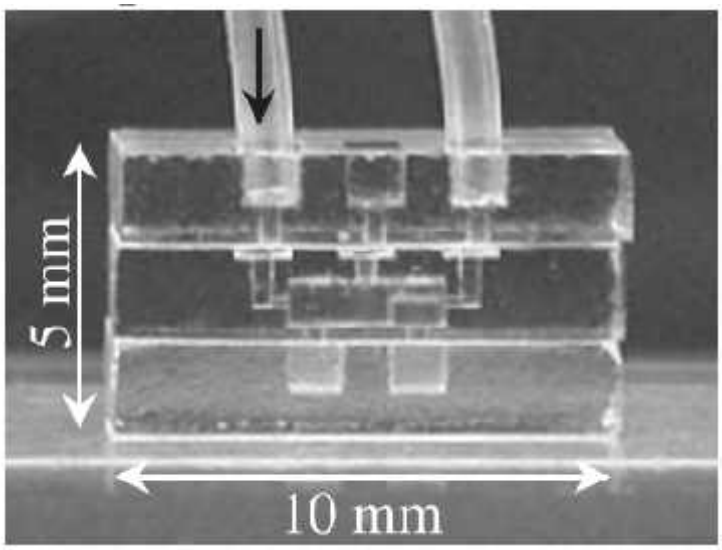

Figure 2.13. Photograph of a lab-on-chip device micro reactor fabricated in photo-sensitive glass using fs pulses with post chemical etching. The work was courtesy to [160].

Using femtosecond pulse can inscribe 3D optical memory by the measure of optical damaging of a polymer in the region of focus of laser irradiation by micro explosion [162]. Optical memory is an application to create three-dimensional (3D) structures for recording In recent, the processing is also used to produce advanced birefringence waveplates: phase and polarization vortex waveplate [163]. More recent research has seen emphasis on developing meta materials. For example, Rapp *et al* (2015) used ultrafast pulses (*170* fs, *790* nm) with fluence of a few mJ/cm^2 focused by a high numerical aperture (NA =*1.45*) objective to induce micro-explosion and a dramatic quenching rate of up to 10^{14} °K/sec at the interface of single-crystal SiO_2 and silicon substrate, to synthesis meta material [164].

Finally, it is notable that a very low-density polymer PMP has hitherto had little study hence of great interest for fs inscription and is the focus of this thesis for modification at both low and high NA and with various polarisations. short pulse duration minimises impact ionisation, improving inscription.

2.6 LCOS Spatial Light Modulator

Figure 2.14 illustrate a schematic of LCOS SLM. It includes CMOS chip, parallel-aligned crystal layer, pixel electrode, transparent electrode and glass substrate. The alignment of liquid crystal is pixelated to the CMOS chip via pixel electrode and transparent electrode. The transparent electrode is possible a thin ITO layer [165].

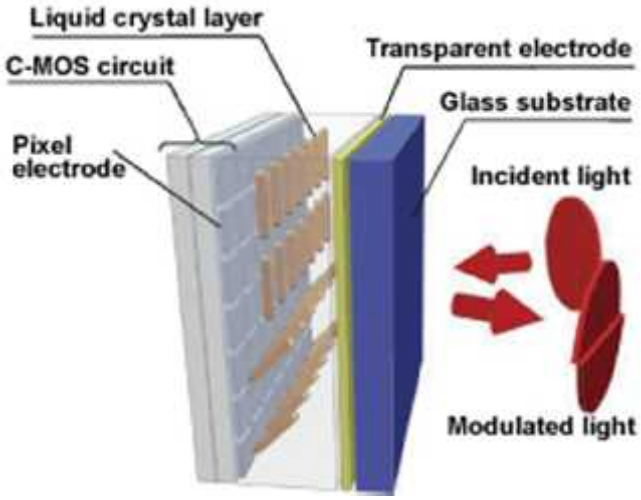

Figure 2.14. Schematic of a LCOS SLM device. The schematic is courtesy to HAMATSU [166].

The optical and electrical properties of liquid crystal are anisotropic. The liquid crystal consists of a thin layer typically a few microns thick and the cell pixels are birefringent. The birefringence liquid crystal optical axes of each cell are initially aligned as twisted, parallel or vertical orientation. For parallel-aligned and vertical aligned cells, shown in Figure 2.15, the optical axis of each liquid crystal cell is oriented in same direction.

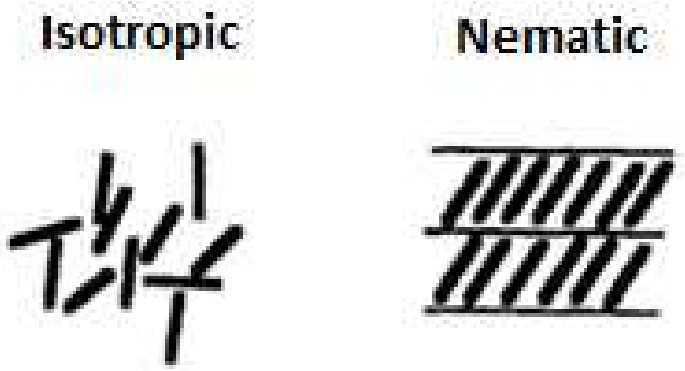

Figure 2.15. Nematic alignment of liquid crystal layers. PA: parallel aligned.

The parallel-aligned (PA) LC devices are more feasible to modulate phase or polarization. In addition, the polarization modulation is novel application. A Jones matrix is used to describe the effect of a liquid crystal device on incident polarized beam. For PA crystal, this Jones matrix is given by, [167]

$$W_{P\ -L} = \exp(-i\ ) \begin{pmatrix} \exp(-i\ ) & 0 \\ 0 & \exp(i\ ) \end{pmatrix} \quad (2.22)$$

in which β and ϕ are birefringent coefficient and phase shift respectively, given by

$$\beta = (n_e\ - n_0)\frac{\pi}{\lambda} \quad (2.26)$$

$$\phi == (n_e\ + n_0)\frac{\pi}{\lambda} \quad (2.27)$$

n_0 and n_e are two refractive indices of axes respectively and d is the thickness of liquid-crystal layer, λ is the wavelength. It is notable that one of E vector component in one axis cannot be changed [168]. The birefringent properties of liquid crystal are controlled via the voltage applied to the liquid crystal cells.

From equations 2.19 and 2.20, the PA LC device is a form of a switchable waveplate. The controllable axis of LC material is parallel to the fast axis. The retardation is a function of the voltage-controlled birefringence β. The PA LC device is more convenient to modulate phase of a linear polarized beam. For single phase modulation, the phase of incident beam can be modulated in continuous fashion between 0 and 2π [169]. The pixelized devices are controlled electronically via computers with application of CGH's.

For ultrafast pulses, the power-handling level of SLMs has been limited for many years to < 15W, restricting industrial applications severely however there is great interest in ultrahigh throughput precision laser-materials micro-structuring. High-power tests at P >100W are of great interest for industrial and scientific applications. Presently, average power handling of LCOS-SLM's have induced some worries with regards to likely damage levels. The first demonstration of power handling at 15W using a cooled SLM was by Duncan Hand [170]. Very recently, Klerks and Eifel demonstrated handling of 60W of picosecond laser radiation at 515nm along with laser material 2D surface patterning in a fully integrated flexible beam shaping system with active cooling of the SLM chip, a significant achievement [171].

There are other competing technologies. Fixed diffractive optic elements (DOEs) [172] based on precision etched surface profiles on fused silica are very robust, able to handle 10's of Watts but designed and fabricated for one particular function only, whether beam shaping or generating multi beams. A competing technology, termed a Grating Light Valve (GLV) is a diffractive Micro-Opto Electromechanical System (MOEMS) spatial light modulator, capable of high bandwidth (kHz) modulation of light with applications in high-resolution displays and computer-to-plate printing [172]. The average laser power handling capability of these devices is around 60W which is a impressive number compared with the capability of a few Watts to tens of Watt handled by most of type of LCOS SLM [173]. While in general, these devices can modulate only intensity, a recent experiment using a MOEMS device combined with polarizing crystals demonstrated high-bandwidth polarized vector field at 5 kHz [174]. In holographic technique, using SLM can reconstruct images.

One beam can be split to multi beams or diffractive spots (1^{st} order) using holographic techniques, called parallel processing [175]. The adapted algorithms to generate computer-generated hologram (CGH) can be lens and gratings [176] or Gerchberg-Saxton algorithms [177], depending on the balance of calculation efficiency or diffractive uniformity. The parallel processing can easily increase processing throughput gain 1 order of magnitude

higher. The designated 2D diffractive patterns in focus plane is a Fourier transform of the complex field image in hologram loaded by CGH to an incident beam. This technique has been well studied and applied in multi-beam optical trapping [178] and laser micro-machining [179]. The positions of these diffractive spots can be adjusted in real time by changing of the CGHs. Iterative Fourier transform is the common method, which has been well used in diffractive beam shaping technology. Liu *et al.* achieved 16 diffracted and addressed NIR beams focused simultaneously in bulk PMMA to create a series of 19 μm pitch volume Bragg gratings [180]. In addition, multi beams in NUV regime, using second harmonic generation in a BBO non-linear crystal placed after the SLM allowed fabrication of high quality VBG's with first order diffraction efficiency η_1 >70% [181].

The incident polarization can be modulated by a spatial light modulator incorporated with birefringent waveplates. Davis *et al* (2000) demonstrates the generation of vector beam by using SLM devices to convert a polarized light [182] in to a vector beam. Inserting a SLM between two ¼ λ waveplates can play a role as a polarization modulator. The Jones transformation matrix of the three devices is a rotation matrix and the rotation angle is controlled by the phase change introduced by the SLM. It is interesting that the polarization variation requires high polarization purity degree. This particular setup can create a laser beam with spatial variable polarization, such as azimuthal or radial polarization. Figure 2.16 (a) shows a CGH and (b) shows the designated vectored beam.

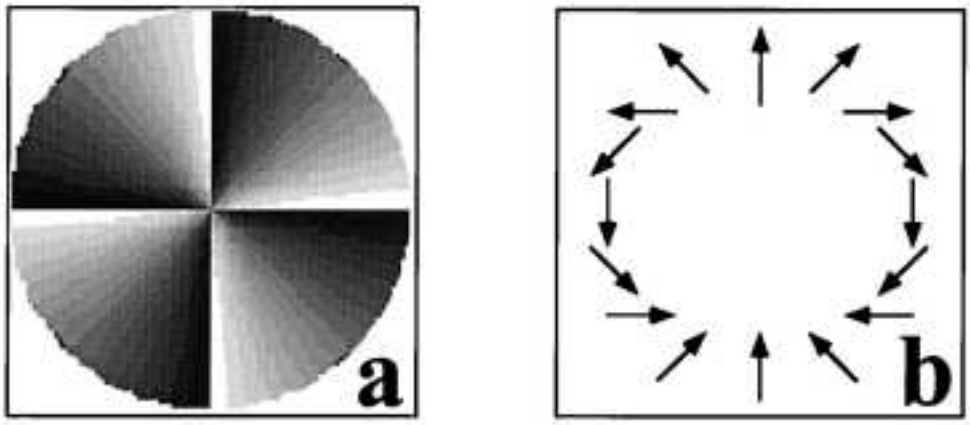

Figure 2.16. (a) 8-bit phase depth phase pattern. (b) Designated vectored beam. The schematic is courtesy to [182].

2.7 Silver doped polyvinyl hybrid material

For the interest to host metallic ions in insulator materials, solid solution, there are many choices. If the concentration of metal ions is below the saturation point, the properties, such as mechanical, optical, or electrical properties, are similar to host materials. The metal exists in form of ions dissolved in host medium. If the metal ion is active, materials with embedded metal nanoparticles can also reinforce the mechanic properties of host material [183] Conductive structures can be produced when high concentrations of metal ions are dissolved in the host material. These structures are often designed to function as 3D arrays [184], diodes [185], or switches [186].

Using solution processing, the production of silver-polymer composites also becomes relatively straightforward. Polymers can generally dissolve large quantities of silver, but they lack stability when compared to glass. Exposure to light and room temperatures can initiate the reduction of silver ions to solid metal in polymers, compromising the performance of the material. In most cases these are metals such as copper [187], gold [188] and silver [189] that are dissolved into insulating materials because of their high electrical conductivities. The host materials are often transparent dielectrics, which allow them to be used in optical applications. Common host materials include glasses [190] and polymers [191]. To activate the ions dissolved in an insulator and form a metal-insulator composite, the ions must first be reduced to atoms. The reduction can be carried out through electrical processes, where a current directly reduces the ions [192]. The most important characteristic of any metal ion host is a high saturation point at which the ion concentration at which the host material's properties begin to change. Stability of the metal ions over time and at moderate temperatures is also important to ensure silver is not activated spontaneously, which would compromise the performance of the composite. For many applications, such as those that require laser processing within the bulk [193], thick and mechanically robust films are an additional requirement. One of the first materials used to dissolve silver was silica glass. Glass is an attractive host as it can stabilize dissolved silver for long periods of time and at temperatures up to 400 ℃ [194].

Using solution processing, the production of silver-polymer composites also becomes relatively straightforward. Various polymers such as polyvinyl alcohol (PVA) [195], polyvinyl pyrrolidone (PVP) [196], polyethylene oxide (PEO) [197], and gelatin [198] have been used in the past as hosts for silver ions. Polymers can generally dissolve large quantities

of silver, but they lack stability when compared to glass. Exposure to light and room temperatures can initiate the reduction of silver ions to solid metal in polymers, compromising the performance of the material. A limited number of glass/organic hybrids have been developed to dissolve silver ions [199], yet these examples also lacked stability in ambient conditions. The insulating host must be capable of dissolving concentrations of silver ions that are comparable with the polymer and glass materials previously demonstrated [186].

Early attempts infused silver ions into the glass matrix through ion-exchange [189], which produced low silver concentrations (<1 wt. %) and very poor uniformity through the thickness of the glass. Ion concentrations were improved to ~4 wt.% using high voltages to induce ion-exchange, yet the ions were still confined to the surface of the sample [200]. Melt-quench techniques solved the problem of poor uniformity and have demonstrated silver concentrations of ~8 wt. % uniformly distributed in the glass [201]. However, fabricating these glasses requires very high processing temperatures, limiting the number of potential applications, for example for biomedical devices or polymers. Solution processing is a convenient way to homogeneously combine insulators and silver ions in high densities. Salts such as silver nitrate are readily soluble in many solvents. In addition, casting materials from solution allows one to create films and coatings without high temperatures. The sole-gel process is a well-studied method capable of synthesising silica from solution. This process has been exploited many times to uniformly dissolve silver in glass films, with concentrations as high as 8 wt. % [202]. However, the sol-gel process is not suited to producing crack-free films thicker than 1 mm [203].

Using sol-gel method could cast silver doped silica-PVA hybrids, but the stability of silver ion is unknown. Using focused fs pulse to active the silver ions inside the hybrids is possible while the processing map is far from clear. This technique is expected to construct 3D silver structure inside insulator.

2.8 Summary

This chapter review knowledge and development progress of laser micro engineering technology. It studies: the mechanisms of filamentary inscription, the theory, generating methods, characterization, photonic-particle interaction and present application of

vortex beam and vector beam and the infrastructure, working principle and some applications of spatial light modulators.

The effect of processing parameters: objective NA, polarisation state and laser pulse duration has been discussed. Optimised processing parameters can effectively increase production throughput and accuracy and reduce optical breakdown. Optical vortex and vector beam exhibits great application prospect but there is little knowledge in internal modification. Spatial light modulator is a mature technique which can use to increase production efficiency via parallel processing technique. The newest powerful ultrafast laser is a challenge to conventional SLM devices. This review is a guide to the further experimental works.

Chapter 3

Experiments and methodologies

3.1 Introduction

Good experimental design is the basis of understanding the solution of any given problem. Experimental methods for internal inscription, supercontinuum-spectra analysis, measurement of Volume Bragg Grating diffraction efficiency and thermal characterization are presented in this chapter. The approaches to generate optical vortex beams and vector beams are also presented along with an introduction to the software package, *"Blue Tweezer"* for the generation of computer-generated hologram (CGH).

3.2 Internal modification using femtosecond pulses

3.2.1 Experimental setup

A femtosecond laser source (Clark MXR CPA 2010) was used. The laser can provide *1* kHz pulses with wavelength λ=*775* nm. The pulse duration τ_p at the best performance is ~ *170* fs. Average intensity of the output beam is 1W while peak energy 1mJ. Figure 3.1 shows the main experimental setup which was set to a two-route arrangement. A sample was mounted securely and translated on a 3-axis micro-positioning stage (Aerotech). S represents a fast shutter with a ~3ms response time.

In route 1, the laser beam was attenuated using a diffractive optic attenuator (DOA) and then was incident to the SLM (Hamamatsu X10468-02). A pair of turning mirrors were used to keep the angle of incidence, AOI is less than 10° satisfying the requirement of manufacturer [166]. BBO crystal is used to convert the laser light from 775-nm wavelength to 387-nm wavelength in the method of frequency doubling, also called as second harmonic generation. In this case, the maximum conversion efficiency is 15% and the orientation of linear polarization changes from incident horizontal linear to vertical linear at 387nm. In principle, the best position of BBO crystal is as close as possible to the SLM however there is physical restriction - the laser beam will be blocked by the edge of the crystal mirror mount. A 4f system is followed with lenses L1 and L2. Just beyond the focal plane of lens L1, a fast

shutter, NEWPORT 846 HP, was installed. A periscope was used to raise the beam height from *110* mm *to 230* mm which is suitable for processing on a 3-axis motion control stage, Aerotech AC3200. It is notable that the optic setup allows inscription with λ_{775}, as well, providing the appropriate optics are chosen. In the case of λ_{775}, the BBO crystal should be taken out and the reflecting mirrors should be replaced to the ones with dielectric coating suitable for the wavelength λ_{775}.

In Route 2, an OPA oscillator (TOPAS-C) is pumped by the 1-Watt fundamental beam at 775nm. Tuneable output wavelength can span from *280* to *2600* nm. The beam diameter from TOPAS C is *~1.5*mm with Gigawatt-level peak intensity yielding high influence in collimated beam. The high influence could damage the following optics. Therefore a 5× beam expander is used to increase the beam size from 1.5 mm to 7mm diameter. In addition, the large beam diameter makes a smaller focus spot for higher accuracy. A routing mirror is used to direct the expanding beam to an attenuator, so that pulse energy is controllable, ranging from *0.2-12*μJ.

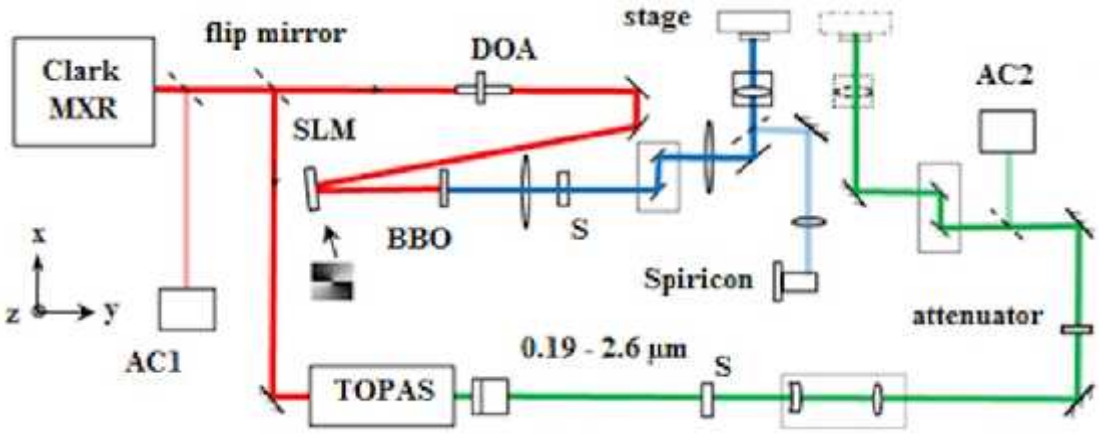

Figure 3.1. Schematic of experimental set-up.

3.2.2 Clark MXR CPA 2010

The Clark laser system, shown in Figure 3.2, consists of an optical oscillator, a neodymium-doped yttrium aluminium garnet (Nd-YAG) laser pump and a regenerative cavity. The optical oscillator, pumped by a diode pump, is a "mode-locked Ebrium-doped fibre" [204] laser which has a round trip period of 30ns and hence 33MHz rep. rate. The mode locked pulse train is indicated by a fast digital oscilloscope. The spaced pulses are a coherent seed which has *9*-nm bandwidth with central wavelength 1550nm, frequency doubled to 775nm in

periodically poled Lithium Niobate (LBO). A Faraday isolator is placed between seed oscillator and regenerative cavity to prevent back reflection. The regenerative amplifier uses chirped pulse amplification (CPA) [205]. Before injection, pulses are stretched using a pair of gratings. The lasing medium is a titanium-doped sapphire crystal which is embedded in a liquid cooling enclosure. Amplified pulses are compressed using a single transmission VBG using *4* passes, after regenerative amplification. The lasing pulses are then ejected from regenerative cavity in the method of the synchronized Q switching via KTP Pockels cell. A digital oscilloscope and fast photodiode showing the regenerative amplification process of a pulse in the cavity.

Figure 3.2. A femtosecond laser, Clark-MXR CPA 2010 system (*775*nm, *160*fs, *2*kHz, *1*mJ) is used. The peak powers are $3 < P < 10$ MW are above the critical power for self- focusing in PMMA, Pc > 1.5MW.

3.2.3 Optical parametric converter – TOPAS C

TOPAS C is a wavelength tuneable converter which employs optical parametric amplification (OPA) to generate coherent light with wavelength over the range *250* nm- *2400* nm. TOPAS C system is pumped by Clark system via a routing mirror. In TOPAS C, pumping beam is split into two beams. *10%* of energy is used to generate super-continuum seed in a sapphire disc. The seed is amplified in a first stage through a Lithium Triborate (LBO) crystal. The remaining *90*% of pump energy is used to amplify the weak signal in a second stage via a nonlinear (NL) crystal and generate signal and idler. Through two-stage amplification, the required signal and idler can be amplified out of noise by positive gain using phase matching method. Using an external frequency mixer, signal or idler beam also can also be frequency-doubled.

3.2.4 Investigated materials

Poly methyl pentene (PMP, TPX Mitsui Corporation) was provided as thermal-extruded rod with diameter ($\phi = 24$ mm), which may have residual stress, displaying birefringence features and pre-processing work. Substrates were sectioned and ground to rectangular shape with dimensions 18mm×20mm×10mm. Then the front and back faces are polished by hand on a glass pad (THORLABS CTG 913), using 4-level lapping sheet (THORLABS alumina oxide lapping sheets, *5*μm, *3*μm, *1*μm and *600*nm) under running water. The final polishing quality can achieve optical finishing grade.

PMMA (Poly methyl methacrylate) substrates, from Vista Optics (Vistracryl CQ^{TM}), without additives and trace impurities was used, with a refractive index n = 1.49 at 775 nm. The PMMA employed in the experiments is sectioned to a size (30×30 ×5 mm^3).

Silver doped silica-PVA film is prepared using Sol-gel method. Figure 3.3 shows a flow chart of the sol-gel method. It is noted that silica sol-gel solution was prepared by mixing tetraethyl orthosilicate (TEOS): ethanol: HNO_3 (0.2 mole /litre), respectively in volume ratios of 3:3:1 for [206]. The dilute acid was added, adjusting the pH to 2 for a more interconnected gel [207]. In addition, reference samples containing only PVA and silver nitrate were also cast. The weight ratio for these samples was 1:0.18 for PVA: Ag^+. Hybrid films without silver nitrate were used as a second set of reference samples, with the weight ratio 1:1 for SiO_2: PVA.

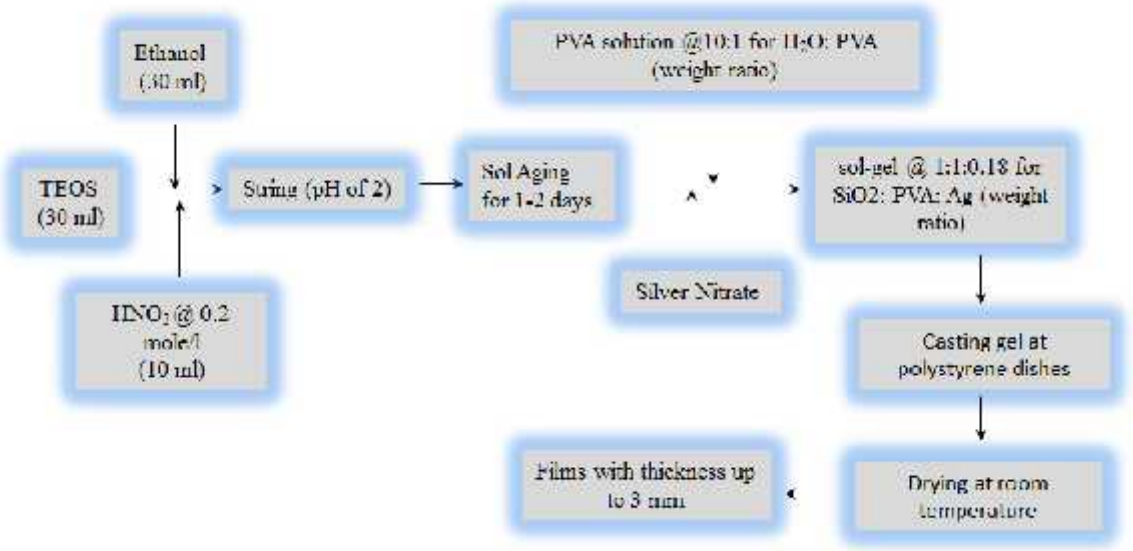

Figure 3.3. Flow chart for synthesis of silica, Ag^{+} and PVA films using sol–gel method.

Other investigated material includes crystalline Sapphire and poly crystalline Zinc Selenide and the known details of these materials are presented in Table 3.1.

Table 3.1: Target materials

Materials	**Manufacturer**	**Sort**
PMMA	VISTA OPTICS	Polymer
PMP	Goodfellow Cambridge Limited	Polymer
Silica-PVA hybrids	*	Composite
Sapphire	-	Dielectric
ZnSe	CRYSTRAN LIMITED	Poly Crystalline

3.2.5 Focusing optics

A series of objectives with N.A. number ranging from *0.01 – 1.2* is used in different experiments. Singlet lenses (N.A. < 0.1) are used to generate filamentation in polymers and study the dependence of polarization. Complicated microscopic objectives are used to inscribe volume Bragg gratings (Λ < 20μm). In addition, objectives (NA> 0.4) are used to generate twisted structures.

Because the investigated wavelength covers from NUV and MIR, the materials of objectives lens have been considered. For λ=387.5, a transmission microscopic (THORLABS LMU-20X-NUV) is used and 95% UV irradiation can pass the objective. In the visible range, a Nikon LU Plan 5×/0.15 was used. This objective lens has a broad transmission band. Singlet lens made of Zinc Selenide was used when the mid-infrared laser light was used. In some experiments, microscope objective were mounted in adapters of special design. In alignment, the crosshair technique is used to keep the optical axes collinear to optic axis. A short brief introduction of the specific and usage of objectives are presented in Table 3.2.

Table 3.2: Specifics of objectives

N.A	**λ (nm)**	**Notes**
< 0.1	387/775	Fused Silica / BK7/ CaF_2;
0.025	1400 - 1600	ZnSe
0.15	500 - 700	Nikon LU Plan 5x/0.15
0.25	387	Ealing 25-506-00 Reflecting Objective x 15
0.4	387	THORLABS (LMU-20X-NUV)
0.7	387	Mitutoyo M Plan APO 100x/0.70 ∞/0 f=200

3.2.6 Spectrometers

Spectrum-analysing technique is used in experiments for characterization of super continuum, fluorescence, illuminance and nonlinear optical effects. Two mobile spectrometers: SM240 and Andor Shamrock 303i are used in different experiments.

SM240 is a compact CCD Spectrometer for use with a PC. Based on optical bench design, it supports many different applications where spectra are required, including high dynamic

range applications. The SM240 accepts light via an optical fibre. The spectrometer is used to investigate wavelength effect in NIR regime and spectral response from 400-850nm.

In NIR, NUV and VIS regime, Andor Shamrock 303i wide-bandwidth spectrometer system is used. The advanced system is a research-grade, high performance and rugged platform designed for demanding low-light applications. This spectrometer is integrated with an intensified CCD (charge-coupled device) iStar camera. The wide measurable wavelength range can vary from UV to IR. (200-1300nm). Data collection was synchronised to 1kHz, TTL output on the DT505 Pockells cell driver of the femtosecond system. Operation of the spectrometer is not complex, as a friendly application software interface is provided. Interestingly, Andor system is a time-resolved spectrometer, and therefore the system can be used for example, for measuring upper state lifetimes and research on atomic physics. Table 3.3 presents briefly optimised setup parameters of the two spectrometers.

Table 3.3: Optimised setup parameters

Set-up	Shamrock SR 303i	SM240
Trigger Mode	external	live
Offset	6 nm	-
Slit	20.5μm	-
Accumulation	20	-
Exposure Time	0.022 ms	10ms-few secs

3.2.7 Spiricon SP620U

A silicon CCD profiler (Spiricon SP620U), shown in Figure 3.4(a), is used to analysis beam mode. Analysis software (BeamGage®), shown in (b), is used. The beam profiler is used to accurately measure the vortex beam modes in near and far field. In far-field measurement, this system needs to be used with beam attenuation. A set of ND filters (ND0.5, ND1 and ND2) are used to attenuate beam power lower than damage threshold of silicon CCD detector in beam profilers. ND filter also can reduce profile-sampling distortion attributed to nonlinear effects. In operation, the adjustment of exposure time and signal gain must be set carefully.

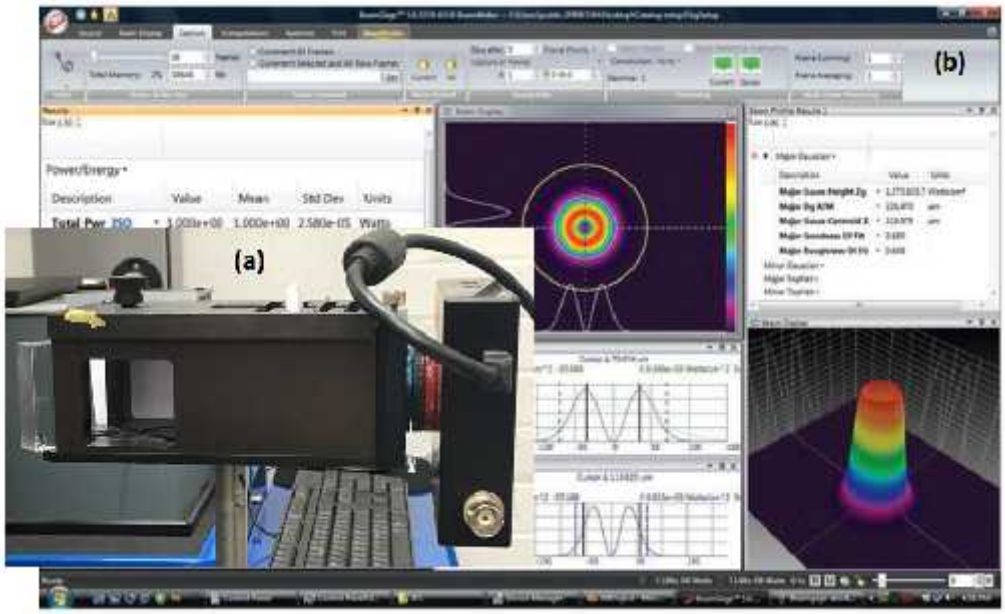

Figure 3.4. (a) Spiricon SP620U Beam Profiler; (b) BeamGage® Interface.

3.2.8 Inscription of volume Bragg gratings

Pulse duration of the femtosecond laser system (Clark-MXR CPA-2010) is optimised the shortest number which is ~170 fs. Figure 3.5(a) shows a schematic of low NA transverse writing of layer of Δn region in a transparent substrate Gratings with 40 lines / mm are processed by a *0.013*-NA singlet lens which is designated for operating with NIR light. To inscribe thick 3D gratings along the optic axis (x-direction), the beam was scanned layer by layer using stitching method. An overlap rate of each layer by distance of 10% of the filament length is set to keep continuity and uniformity. As the length of single process in X direction is 370μm, 333μm with 10% offset, along X direction was applied and a series of thick VBGs were created and the deepest layer is firstly scanned, shown in (b). In addition, a synchronized fast mechanical shutter is used to control exposure only on one scan direction to avoid "tilt of pulse front" [208].

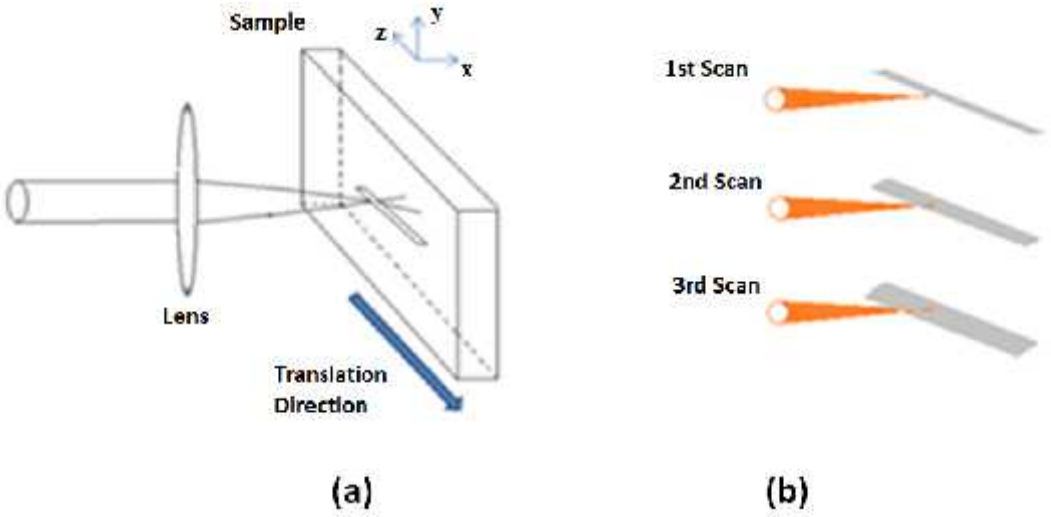

Figure 3.5. (a) Filamentary Structures induced by 170-fs pulse using singlet lens (NA <0.1) in transverse writing geometry. (b) A demonstration to construct 3-layer volume Bragg grating by offsetting scans along the optic axis.

3.2.9 Transmission diffraction efficiency measurement of A VBG

A picosecond laser (High Q), delivering *0.5*W at λ=*532*nm (SHG), was utilized for probing the volume gratings. The output from the laser was attenuated to ~ *400* μW, and then passed through a volume grating sample that was mounted on a precision rotation stage. A silicon detector with power meter (Coherent LM1/Fieldmaster) was placed a metre away from the grating to measure the transmitted power into each order. The schematic of optical setup is presented in Figure 3.6. Diffraction curves were measured by placing the detector in turn at the location of each diffracted order and rotating the grating from normal incidence. The first order diffraction efficiency, assuming a sinusoidal RI modulation, is introduced in chapter2, given by,

$$\eta_{\pm 1} = s \quad {}^{2}\left(\frac{\pi}{\lambda \quad \theta_B}\right) \quad (2.25)$$

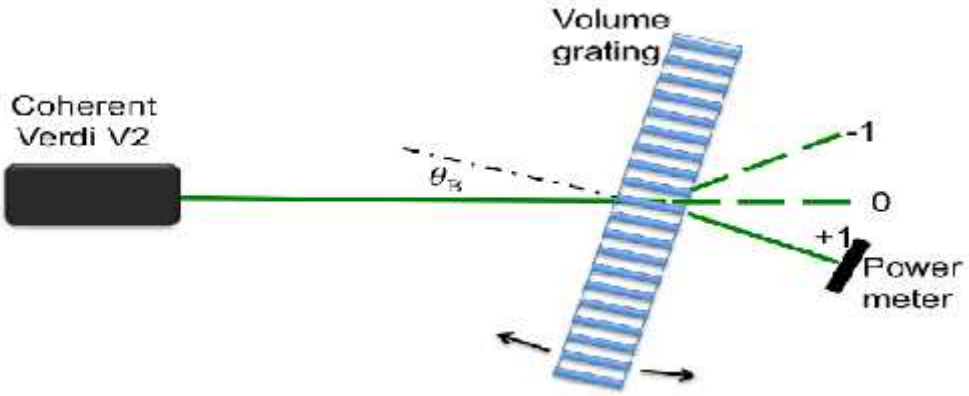

Figure 3.6. The $\eta_{\pm 1}$ is measured using 532-nm coherent light and a volume grating sample that was mounted on a precision rotation stage.

3.3 Using SLM to generate optical vortex and vector beam

3.3.1 SLM-and-PC setup

The SLM used (Hamamatsu X10468-02) is a commercial product, which is designed to handle NIR laser beam. This device is designed to be operated in reflective mode with reflectivity R > 95%. The SLM is controlled with a personal computer and SVGA digital interface (800 x 600). It is notable that the active pixel numbers of the effective area are 792 x 600. The surplus pixels are ignored and not illustrated. A short table of specific parameters for the SLM is presented in Table 3.4.

Table 3.4: Specification of SLM (Hamamatsu X10468-02)

Incident irradiation (W)	<5
Resolution (pixels)	800 x 600
Pixel Pitch (μm)	20
Effective Area (mm^2)	16 x 12
Readout Wavelength (nm)	775
Frame Rate (Hz)	60
Response Time (rise/fall ms)	25/65

The calculated bitmap was parallelly illustrated on a second monitor [209], shown in Figure 3.6. M1 and M2 are parallel monitors to set parameters in the software interface and to show CGH's respectively.

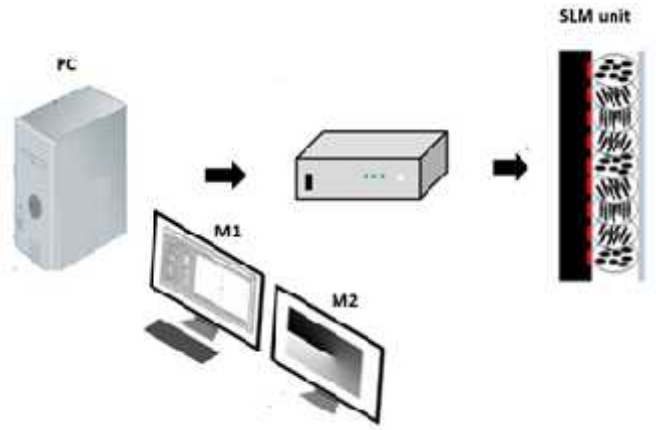

Figure 3.6. Schematic of parallel display using two monitors.

Computer-generated hologram (CGH) is an 8-bit grey level map. Phase modulation levels of 0 to 2π *radian* is converted into integer number in the range of 0 to 255 (8bit) via blazing function [166], shown in Figure 3.7. Each grey level represents voltage on each pixel via lookup table (LUT) [166].

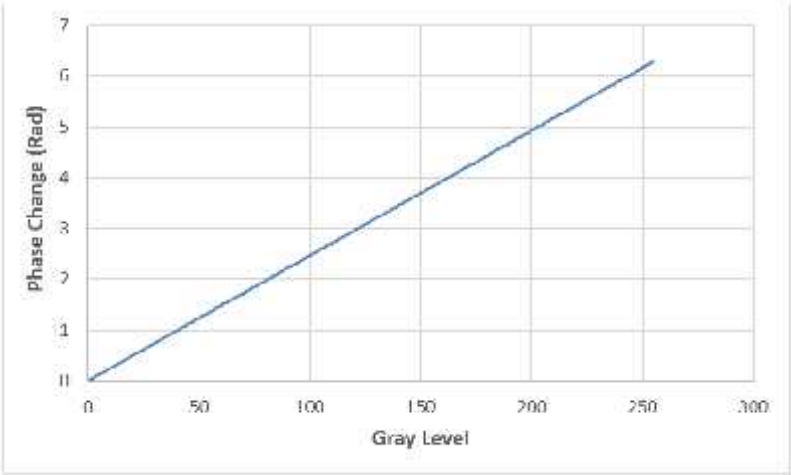

Figure 3.7. Blazing function which shows the relationship of phase change and grey level.

3.3.2 CGH-generating software: *"Blue Tweezers"*

The software package "*Blue Tweezers*", was the main approach to generate CGHs. The package includes an open graphic library (OpenGL) program to calculate bitmaps. "*Interface"* module is used to generate CGHs for phase gratings and optical vortex. The module also provides grating- algorithm choice and addition of the correction field, shown in figure 3.8(a). The correction-field bitmap, shown in (b) is used to fix the phase distortion attributed to flatness variation of parallel aligned (PAL) crystal layers [166]. The research module "*displayCombinedHologram U8*", presented in (c), offers powerful functions which include Zernike correction and blazing function.

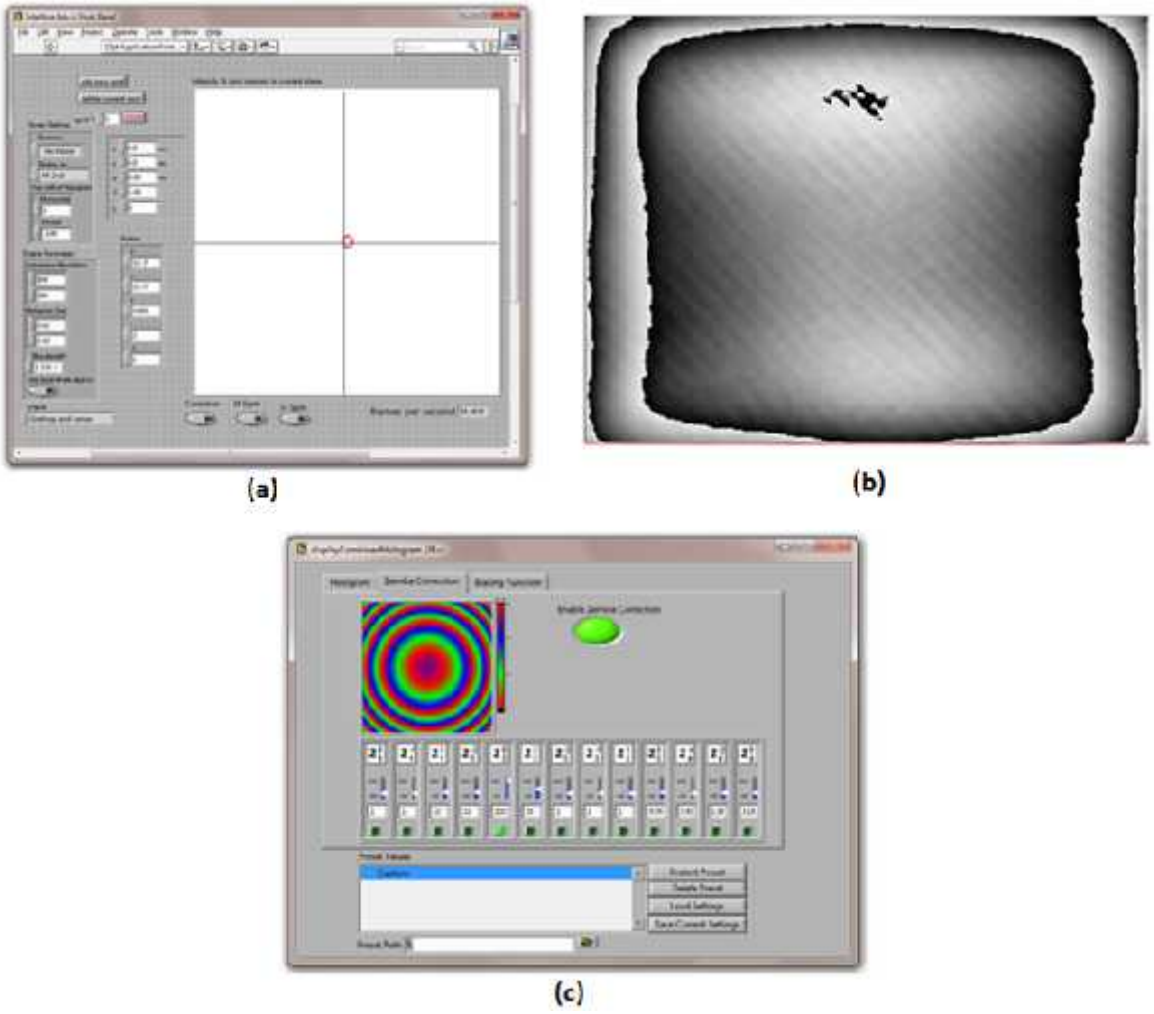

Figure 3.8. (a) Interface module of "*Blue Tweezers*"; (b) 775-nm Correction field; (c) "*displayCombinedHologram U8"*.

Zernike-correction can be used to fix the phase errors which are produced by alignment errors, instability of laser system or other system errors. It can be used to pre-compensate the phase error generated behind SLM as well. It is very interesting that the Zernike correction can be used to create beam shapes, such as Bessel beams. To apply a blazing function on CGH, the *"displayCombinedHologram U8"* can be used. Figure 3.9 shows the adjustment of grey level via blazing function.

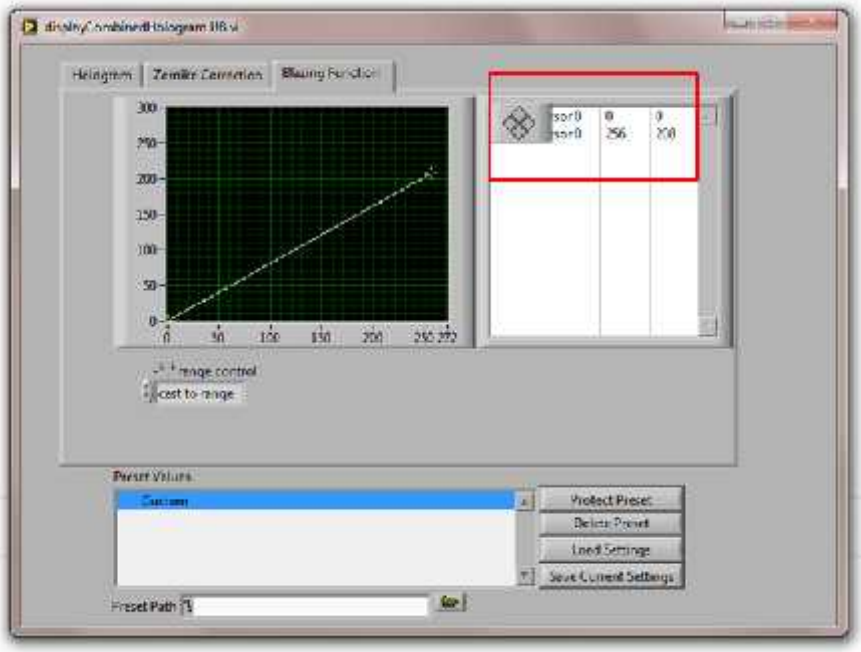

Figure 3.9. Applying blazing function to correct phase modulation response to grey level in "*Blue Tweezer*".

3.3.3 Generation of optical vortex using a SLM

A simple scheme, developed by Roichman *et al* [210], was used. The single-phase SLM is exposure to collimated beam with diameter ϕ ~ 8mm. The phase value of any points was modulated using computer-generated hologram (CGH). If the polarization term is ignored, a vortex beam can be explained as

$$A(r,t) = u(r)e^{i\phi(r)}e^{-i\omega t} \quad (3.1)\ [211]$$

where $u(r)$ is a real amplitude and $\phi(r)$ is a real phase (azimuthal phase) of a point in the cross-section of beam. Actually, the SLM is used to set $\phi(r)$ with the pixelated grey bitmap.

The black (0) corresponds to 0 modulation whie the white (255) corresponds to 2π modulation. Figure 3.10 illustrate a spiral phase front (a) regarding to the CGH (b). The 3D phase structure of a vortex beam was described using MATLAB. The details and codes are in Appendix 1. In addition, a new technique of yielding dynamic rotated spiral phase fronts has been developed out by an upgrades work in LABVIEW environment. If the reader is interested in the technique, please refer to Appendix 2.

Basic parameters, for example topological charge number (m) and application of the correction-field are set in module "*interface*", present in Figure 3.11 (a), the red circles represents the zero-order beam. If the circle is out of centroid, the circle then represents 1st order diffractive beam. In addition, the circle represents the positon but not the actual size. A toggle switch is used to make decision whether the wave-front correction is applied. (b) is a CGH to generate a vortex beam with m=3. (c) is the CGH superposited with a corrected bitmap. The correction bitmap is provided by HAMAMATSU. The correction is a solution to the flatness variation of liquid crystal layer in the SLM device.

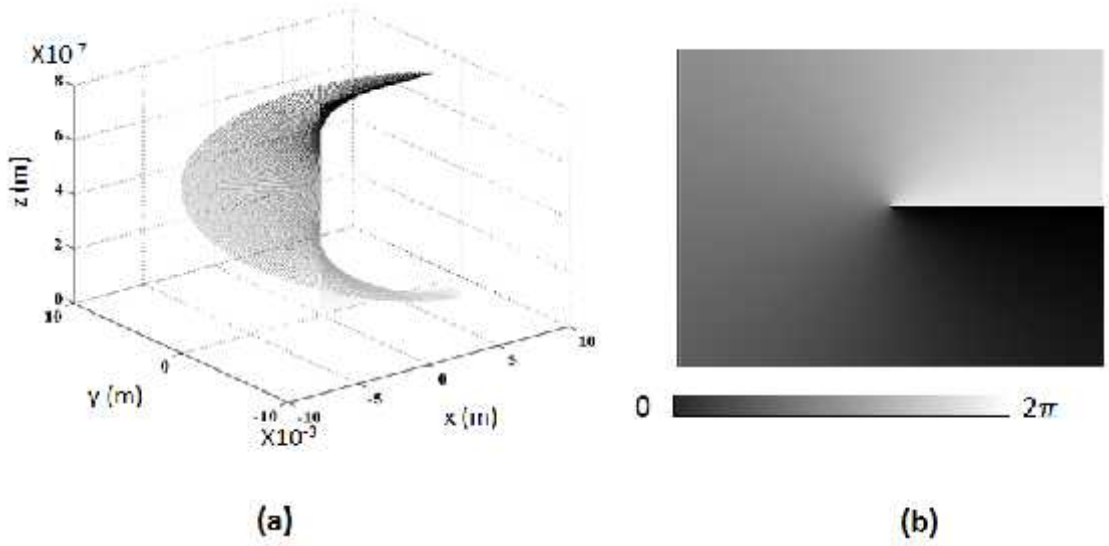

Figure 3.10. 8-bit bitmap for constructing a vortex beam with charge number m=1, where (a) is the spatial (spiral) wavefront and (b) is a 2D-bitmap CGH which would create the wavefront in (a).

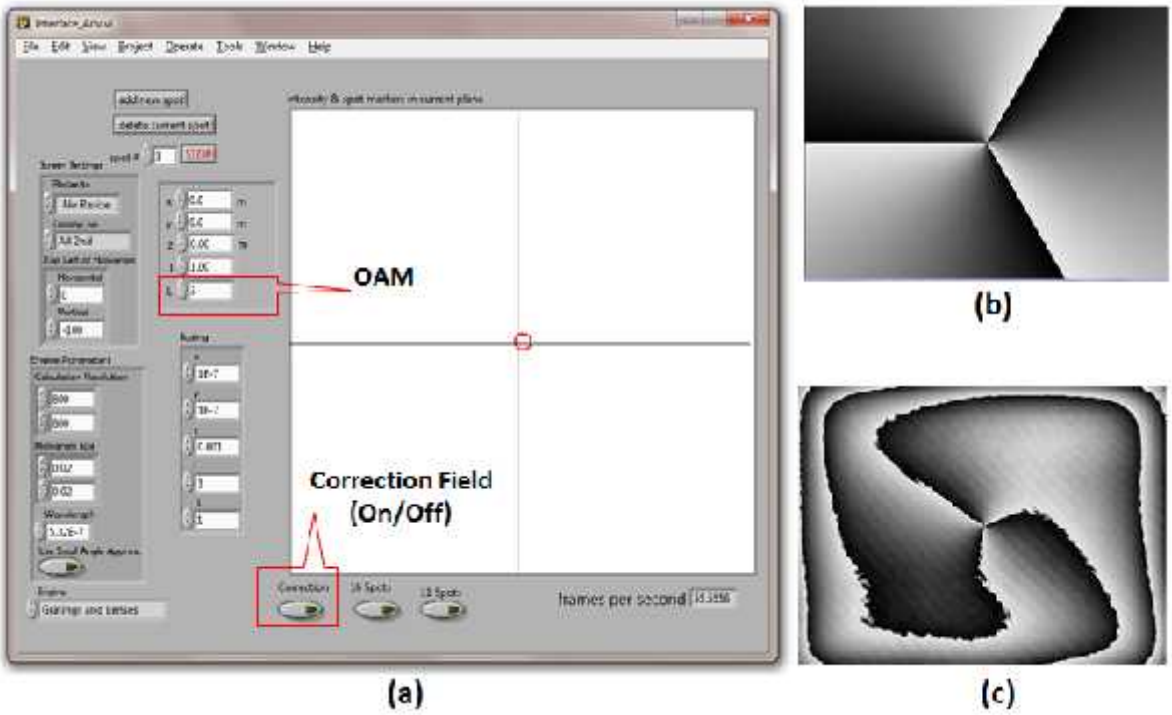

Figure 3.11. The Module "interface" (a) the red rectangular (top) inputs field for topological charge number (m). A bottom switch is used to choose correction field "OFF" or "ON". The corresponding spiral CGH for m =3 is shown in (b) without flatness correction and (c), with correction added.

Original "*Blue Tweezers*" provide solutions to generate vortex beam, the software conventionally set the topological number (m) as integral type. That means the phase change around a circle is the $n \times 2\pi$, where n is integral. Upgrade work has been done to develop "*Blue Tweezers*" and the OAM number can be fractional numbers, shown in Figure 3.12.

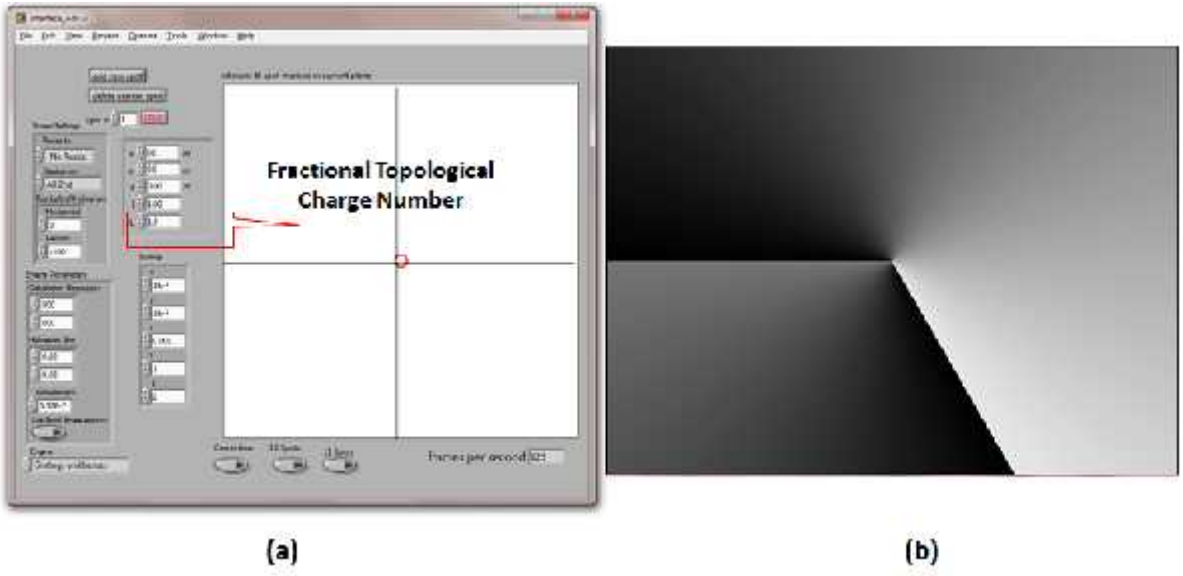

Figure 3.12. In the Module "interface" (a) the red square sets the input field for topological charge number (m) as 1.5. The CGH (b) with a 1.5 ×2π phase change around a circle is generated with upgrade version.

3.3.4 Vector-beams generation using a SLM

The optical setup is shown in Figure 3.13 in which a SLM is used to rotate vector fields along the optic axis, at 775-nm with spiral wave front. If the SLM director is in the horizontal, the phase of horizontal component of E can be modulated. A half waveplate was placed in front of the SLM, setting the incident linear polarisation orientation at 45º to the horizontal direction. When a CGH with m = 2 is applied, causing a 0 - 4π around a circle, a vortex beam with azimuthal or radial polarization can be generated. In addition, a ¼ λ waveplate is used to compensate phase shift (*π/4*) introduced by SLM. Figure 3.14 presents the setup in which the L number which is topological number "m" but represents as "L" in *Blue Tweezer* is set to 2 and I number is set to "+" or "–" 1, respectively for the azimuthal or radial polarization. In addition, vector beams built with a SLM is possible while the beam has helical wave front.

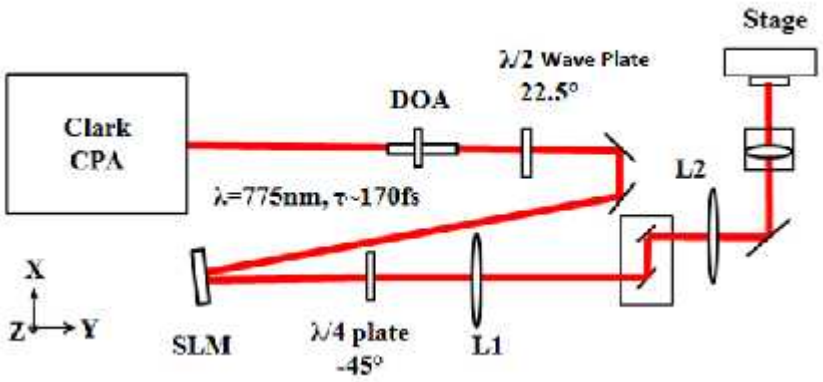

Figure 3.13. The optical setup of polarization modulation using a single phase SLM. Radial or azimuthal polarization with a vortex phase is tailored from incident linear polarization.

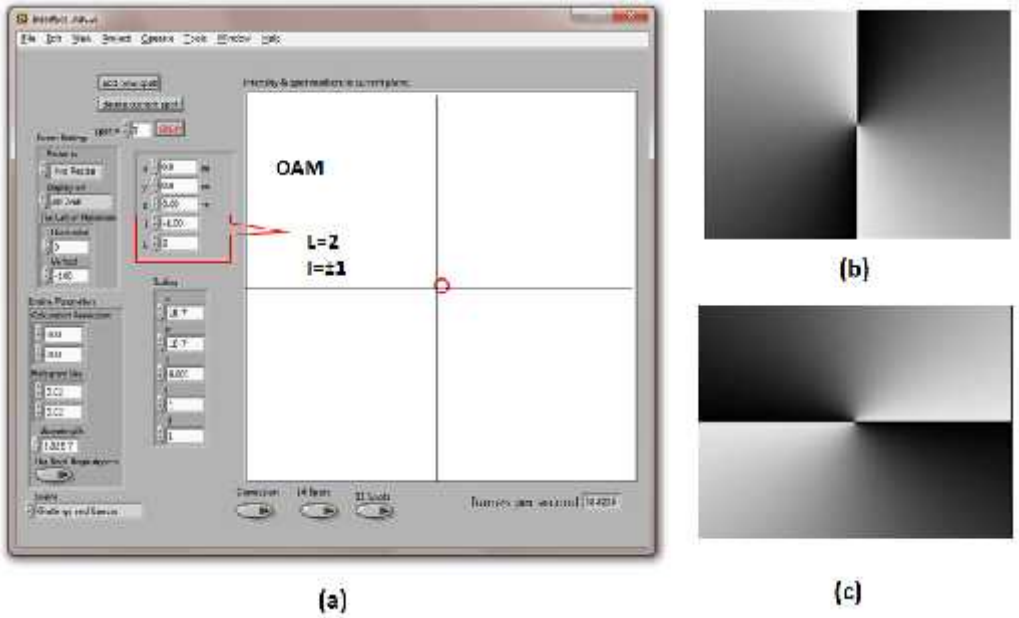

Figure 3.14. Set the L=2 in *Interface* (a). The CGH (b) is to generate radial polarization when I =1 while the CGH (c) is to generate azimuthal polarization when I =-1. Both carry a helical wavefront.

3.5 Vector beam built using S-waveplate

Figure 3.15 illustrates the optical setup of generating fs vector beam. Electric field is manipulated to radial/azimuthal polarization with plane wave front using a nanostructured wave plate (S - wave plate, Altechna RPC-1030-10-109). An OPA source (TOPAS C) is used to convert wavelength from 775 nm to 1064 nm because the wave plate is designed for wavelength at 1030 ± 35nm. This wave plate is made of a fused silica plate which is inscribed with a spatial birefringence nano-grating structure. Mirrors after S-waveplate are dielectric-coated devices for 1064-nm light. The advantage for the use of dielectric-coated mirror is the filtering of any unwanted wavelengths from the OPA.

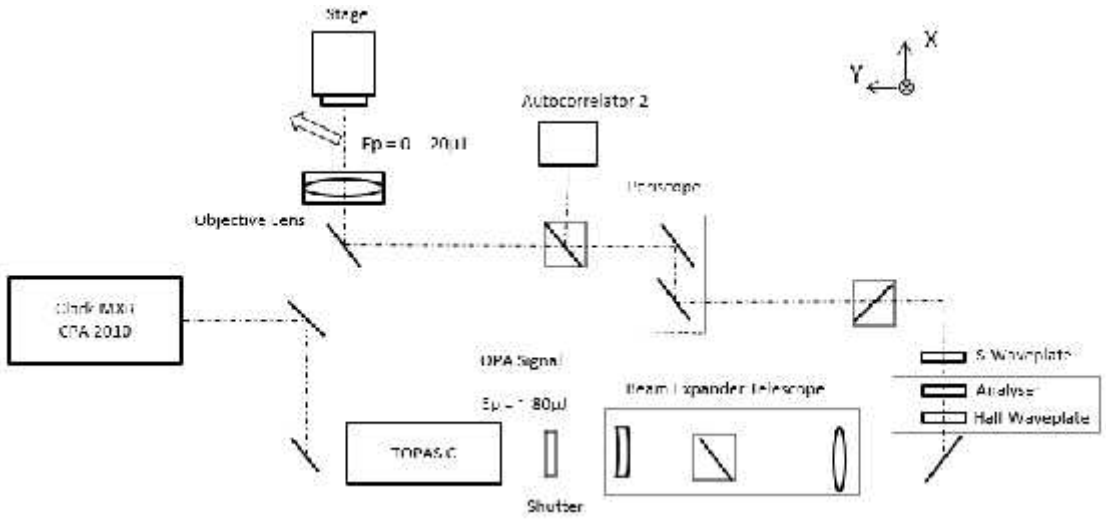

Figure 3.15 The experimental setup to generate vector beam (λ_{1064}),

3.6 High power thermal tests and phase response of the cooled SLM

3.6.1 LCOS SLMs ((Hamamatsu X13139-03)

Liquid cooled SLMs (Hamamatsu X13139-03), shown in Figure 3.16(a), were operated at wavelength 1064 nm (NIR) and exposed to high average laser powers. This SLM constitutes a novel upgrade product for which the pixelated resolution is higher, 1272 x1024 pixels with 12.5μm pitch. The SLM is addressed by a computer via SXGA digital interface, shown in (b). It is important that this device is liquid-cooling SLM and designed for handling high average

power, high peak power ultrafast pulses, shown in (c). The functional device is mounted on an engineered copper block, thermally connected to the rear of the silicon chip with copper tubes on the side for liquid cooling of the unit. The block has internally structured cooling channels and the circulating liquid was pumped and cooled by a Koolance (model EX2-755) liquid to air cooling unit rated for 500W.

Table 3.6: Specification of SLM (Hamamatsu X13139-03)

Incident irradiation (W)	<500W
Resolution (pixels)	1272 x 1024
Pixel Pitch (μm)	12.5
Effective Area (mm^2)	19.5 x 14.6
Readout Wavelength (nm)	1064
Frame Rate (Hz)	-
Response Time (rise/fall ms)	-

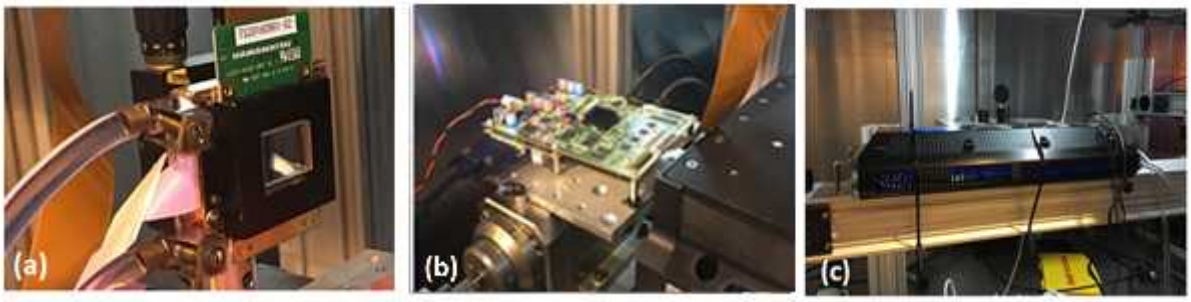

Figure 3.16. (a) Photo of cooled SLM (Hamamatsu X13139-03) on mirror mount with liquid cooling connections to the Copper heat sink; (b) The controller board of the SLM; (c) a Koolance liquid pump (model EX2-755).

3.6.2 Edgewave, Innoslab laser, (*10*ps at *1064*nm)

Edgewave, Innoslab laser, (*10*ps at *1064*nm) Model PX400-3-GH was used to test phase/temperature response (P>200W) of liquid cooled LCOS spatial light modulator (SLM). The laser system was located at Laser Process Research Centre (LPRC) of the University of Manchester. This system has turnkey function and can provide maximum average power of *300* W and *2* MHz rep. rate.

The laser can be operated in two trigger modes: internal trigger (low-power output) and external trigger (high-power output). A digital waveform generator (Tektronix AFG 3021B 250ms/s 25MHz) is used to check the internal trigger pulse for an optical gate in the laser. Another fast digital oscilloscope (Lecroy WaveRunner 6100A 1GHz Oscilloscope) is used to observe the modulated laser output. Using this setup, it is possible to generate high frequency pulse burts with kilo-Hz repetition rate. The irradiation power respect to system parameter setup is listed in Table 3.7.

Figure 3.17. (a) EdgeWave Innoslab laser; (b) A digital waveform generator (Tektronix AFG 3021B 250ms/s 25MHz); (c) Lecroy WaveRunner 6100A 1GHz Oscilloscope showing pulse bursts; (d) Laser Control-software interface.

Table 3.7: Irradiation power (watt.) of Laser Edgewave (1064nm).

	Int. Trig (kHz)			Ext. Trigger (kHz)
Freq.	10	20	30	404
30 %	1.5	3.5	5.2	20
40 %	2.5	5.4	8	33
50 %	3.6	7.5	11.2	47
60 %	4.7	10	14.9	62
70 %	5.6	12.2	18.2	76
80 %	6.4	13.7	21	87
90 %	7	14.8	22.5	94
100 %	7.1	15.2	23	97

The laser mode was an ellipse with dimensions of ~ 12mm × 7 mm with horizontal major axis, where eccentricity (e) is ~1.7. In the case of high power, the mode was investigated using a hand held NIR camera (Find-R-scope) which can observe the scattered infrared radiation from optics. The mode was elliptical as well.

3.6.3 Thermal and phase response test

A thermal camera (FLIR SC660) was used to analysis temperature response and a 4f system is built and a series of CGH's with grey level GL = *0-255*(*8*bit) is applied on the SLM to investigate phase response to average laser power. The detail of these experiments will be discussed in Chapter 7.

3.6.4 Parallel Processing

Ultrafast laser beam with average power from tens of watt to a few hundred of watt handling using LCOS SLM has engineering significance, for example parallel processing which is a diffractive multi-spot pattern in focus plane which could improve the production efficiency significantly however the phase response to these powerful ultrafast pulses are very unclear. This experiment will tell us the diffraction efficiency responding to laser beam with higher average power above to *230*W.

A 4f system was built with a pair of plano-convex lenses (anti-reflective coating) with focal length, F1 =*300* mm and F2 = *160* mm. The beam diameter was therefore reduced by × 0.53. The reduced beam size can help to resolve the problems of clips at the edge of following optics. The liquid cooling SLM was used to apply phase CGHs with diffractive patterns in front of the 4f system. The reflected beam from the SLM passed the 4f system and was directed after lens L2 to the input aperture (*14*mm) of a digital scanning galvo (Scanlab intelliScan 14/RTC-5 card) and focussed with *100*mm focal length tele-centric lens operating under Scaps GmbH scanner software. Later, a 250mm f-theta lens was also used for micro-machining.

The complex optical field applied at the SLM was re-imaged to the input aperture of the scanner. Samples were put on an adjustable lab jack for vertical control to bring the surface to the focal plane. Stainless steel substrate (60 x 60 x 3mm) with polish surface and brass coated

steel plates (80 x 80 x 2mm) were used to assess the machining quality. In order to get to precise phase modulation, it was necessory to apply the correct blazing function to fix the characteristic phase front error induced by the average power level. In LabView software, this can be directly adjusted by module *"displayCombinedHologram U8"*.

3.7 Summary

In this chapter, experiment setup, key equipment and software are introduced.

For internal inscription in polymer material, the main femtosecond system (Clark MXR) can provide *~170*-fs and *775*-nm pulses at 1kHz with 1W average power. The pulses could be used to pump the TOPAS C to generate light with wavelength range from *280* nm- *2400* nm. A hybrid setup is used to delivery laser pulses to substrates. SC spectra are obtained using setups using both reflectivity and transmission. Two spectrometers are used respectively for wavelength *387*nm and *775*nm. The inscription is carried out using objectives with 0.013 < NA< 1.3. Applications are Volume Bragg Gratings and Photonic crystal Fibres.

The spatial light modulator (Hamamatsu X10468-02) is used to modulate 775-nm pulses to generate vortex beams. A BBO crystal is used to generate vortex NUV 387.5-nm pulses. The main software to generate CGHs is "*Blue Tweezers*". In addition, the beam profiler (Spyricon) is used to monitor far-field beam mode. Vortex beams are used to generate filamentary structures and twisted structures in transparent materials.

Edgewave, Innoslab laser, (*10*ps at *1064*nm) Model PX400-3-GH was used to test phase/temperature response (P *>200*W) of two liquid LCOS spatial light modulator (Hamamatsu X13139-03) chips. The performance on handle handling high average power, picosecond pulses using the SLM was also tested by parallel processing on metallic substrates.

Chapter 4

Femtosecond laser 3D micromachining

4.1 Introduction

This chapter is concerned with new knowledge learning of the femtosecond laser direct writing in polymers: Poly methyl acrylate (PMMA) and Poly methyl pentene (PMP). The threshold for appearance of Super-continuum spectra is used to estimate the threshold peak power for self-focussing. Microscopic results of structural changes in PMP are investigated, supplemented with Raman spectral analysis. The microscopic results of femtosecond laser exposure of a silver doped polymer are presented and combined with a detailed discussion. In addition, experimental results of nonlinear interaction between femtosecond pulses and Zinc Selenide are also presented.

4.2 Supercontinuum (SC) generation of λ_{775} femtosecond pulses

4.2.1 Experimental setup

Collimated beam is focused by a singlet lens (NA < 0.1) ~ 0.5-mm underneath the front face of transparent poly methyl acrylate (PMMA) sample. The sample was translated in speed 7 - 10mm/s. Supercontinuum generation require the pulse duration short enough. Hence, the pulse duration is optimized to 0.269/1.5~ 170fs.

Figure 4.1 shows transmitted setup for measuring supercontinuum. A plano-convex lens with focal length 300 mm is used to collect SC signal in forward resultant beam [58]. An optical-density filter (OD1) is used to attenuate the foundational 775-nm light. It is notable that the focus plane of the sampled beam should be well out of fibre coupler to prevent from saturation or damage of spectrometer detector. A compact spectrometer (Spectra Product SM-240) is used to attain spectral signal in the region between 740nm and 800nm. The limited bandwidth in NIR region is due to ability of the spectrometer which cannot cover visible region. Because the laser beam is scanned in the substrate, detected curves varied along a circumference but less than *5%* which is within tolerance.

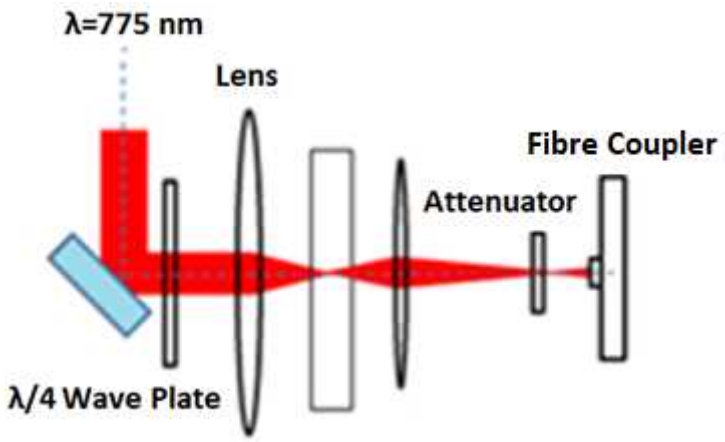

Figure 4.1. Transmitted SC spectra were obtained using fibre coupled spectrometer (Spectra Product SM-240).

4.2.2 SC spectra for linear polarization and circular polarization

Three-polarization states: transverse electric field (TE $|V\rangle$), transverse magnetic field (TM $|H\rangle$) and circular polarization (CP $|R\rangle$), are investigated. SC spectra were generated in an increasing peak-energy series. The spectra for each energy level will be measured for 5 times. Spectral results are respectively shown in Figure 4.1, 4.2 and 4.3 which present a spectrum with foundation peak centred at 775 nm.

Figure 4.2 present spectra for 0.18±0.01μJ, 0.67±0.02μJ and 1.00±0.03μJ with foundation peak centred at λ_{775}. It is satisfied to expect of an anti-stoke peak centred at λ_{758} at the left side of foundation peak is observed. Anti-Stoke broadening pattern is a characteristic of supercontinuum [58]. In addition, the tail on left side of foundation peak suggests anther nonlinear phenomena self-phase modulation which is likelihood due to impact ionization. For low peak energy input, the continua are general narrow with a steep edge at left side. The spectra exhibit the occurrence of strong self-phase modulation at pulse energy Ep > 0.6 μJ, inferring strong impact ionization [66]. The self-phase modulation usually generates a narrow continuum along the central laser wavelength [212].

Figure 4.3 presents the spectral results for TM polarization. It is observed that the signal for anti-Stoke (blue-broadening) component is slightly less than the one for TE linear polarization. It exhibits the stronger coupling efficiency of TE mode.

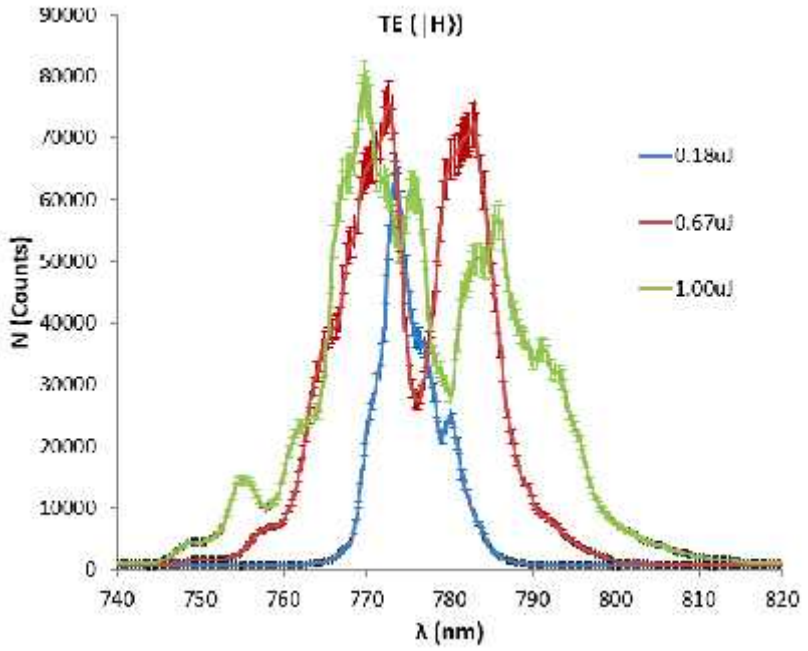

Figure 4.2. Observed SC, Stokes and anti-stokes broadening Δλ vs pulse energy for linear TE polarization. Measured by Spectra Product SM-240.

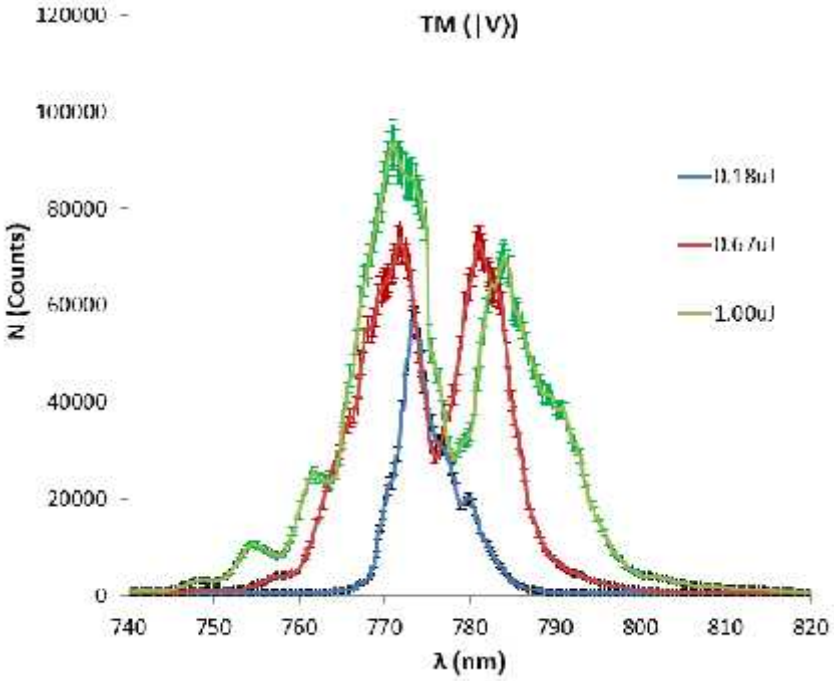

Figure 4.3. Observed SC, Stokes and anti-stokes broadening Δλ vs pulse energy for linear TM polarization. Measured by Spectra Product SM-240.

Spectra for the circular polarization (CP) are shown in Figure 4.4. There is less SC signal, compared with the two linear polarization modes. It suggests that processing threshold for circular polarization should be higher than the two linear cases. The anti-stoke broadening is not obvious even for Ep ~1μJ while the strong SPM was observed.

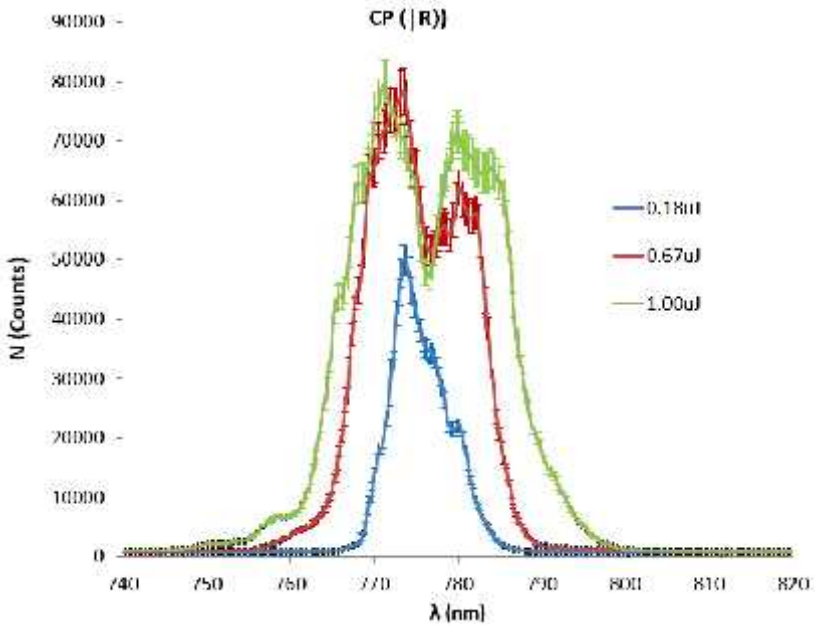

Figure 4.4. Observed SC, Stokes and anti-stokes broadening Δλ vs pulse energy for circular polarizations. Measured by Spectra Product SM-240.

4.2.3 Nonlinear-processing characterization

When peak intensity of femtosecond pulse is higher than a critical value, the filamentation could be built up. This critical value is the threshold of refractive-index change if filamentary inscription is wanted. As the peak intensity threshold of supercontinuum is the same as one for self-focusing, it is possible to get the critical value via measurement peak intensity threshold of SC. In this section, interpolation method is used to estimate peak power threshold of SC generation in PMMA. In addition, this critical number can be used to estimate two important nonlinear coefficients: n_2 - the nonlinear refractive index and $\chi^{(3)}$ - the third order of susceptibility.

Considering to the FWHM of the fundamental wavelength is ~10 nm and SC spectral trace of continuum is constituted of anti-Stokes components at left side of pump-beam wavelength

(775nm). The area of interest (AOI) is the integral between the trace of anti-Stokes components and horizontal axis between two λ coordinates, λ=*740* nm and λ=*770* nm.

$$a \quad = \int_{7}^{7} \quad I(\lambda)d \quad . \quad (4.1)$$

The lines were determined by the method of the least square fitting applied to the results obtained for the minium peak energy of SC generation which is the peak energy threshold of SC generation. The integral signal of AOI increases exponentially with the peak energy. It is possible to change the complex form to linear form if take logarithm on both side as equation (2.1). The least square fitting equation is given as

$$\ln(a \quad) = a \quad (E_p) + b. \quad (4.2)$$

The threshold peak power for SF is given by the equation,

$$P_c \quad = \left[\frac{\pi(0.6\ )^2 \lambda_0^{\ 2}}{8 n_0 n_2}\right] \qquad (2.1).$$

The relation between n_2 and $\chi^{(3)}$ is given by

$$n_2 \left(\frac{c}{w}^{2}\right) = \frac{0.0}{n_0^{\ 2}} \times \chi^{(3)} \text{ (e.s.u.)} \quad (2.8)$$

This infers a third order susceptibility $\chi^{(3)}_{775}$ proportional to the nonlinear (NL) refractive index component n_2.

For laser irradiation with linear transverse electric polarization which means the electric field is along the scanning direction, the experimental points and the calculated curve are presented in Figure 4.5. The right 8 spots are fitted into a linear equation with determination coefficient R^2 =0.99 which presents the static confidence of interpolation point. Let us apply background signal as $\ln(a \quad) = 11.75$. The interpolation point of threshold value is $E_{th,TE}$ = 0.51±0.02μJ, inferring to $P_{th,TE}$ = 3.00 ± 0.05MW. Using equation 2.1 and 2.2, the calculated $n_2^{775,TE}$ =*1.96* ×*10*$^{-16}$ cm^{2}W^{-1} and $\chi^{(3)}_{775,TE}$ ~ *1.10* ×*10*$^{-14}$ esu which are in agreement with experiment figures in [213].

For laser irradiation with linear transverse magnetic polarization which means the electric field is orthogonal to the scanning direction, the experimental points and the calculated curve are presented in Figure 4.6. The right 8 spots are fitted into a linear equation with determination coefficient R^2 =*0.99* which presents the static confidence of interpolation point.

The interpolation point of threshold value is $P_{th,TM}$ = *6.24* ï *0.05* MW with $E_{th,TM}$ = *3.15*ï*0.05*μJ, near Gaussian pulses, inferring to $n_2^{775,TM}$ =*1.88*×*10*$^{-16}$ cm^{2}W^{-1} and $\chi^{(3)}_{775,TM}$ ~ *1.05* ×*10*$^{-15}$ esu.

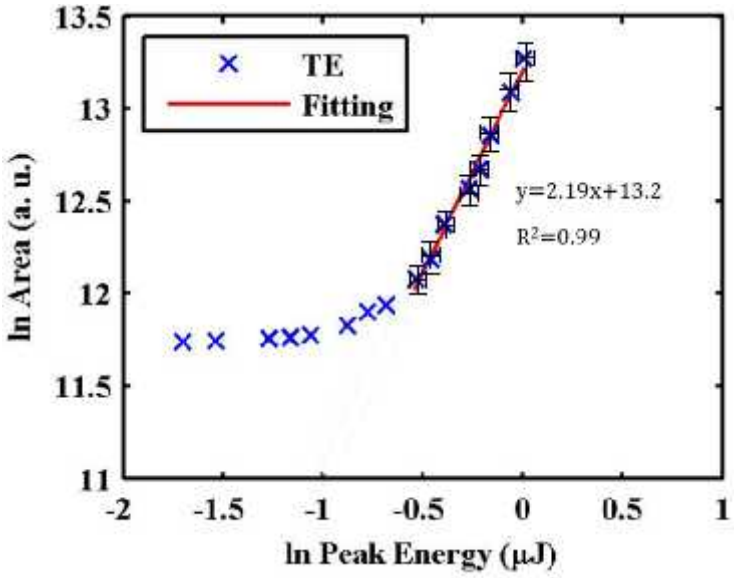

Figure 4.5. Linear fitting experiment spots of linear polarization with transverse electric field (TE). The determination coefficient of linear fitting is R^2 =*0.99*.

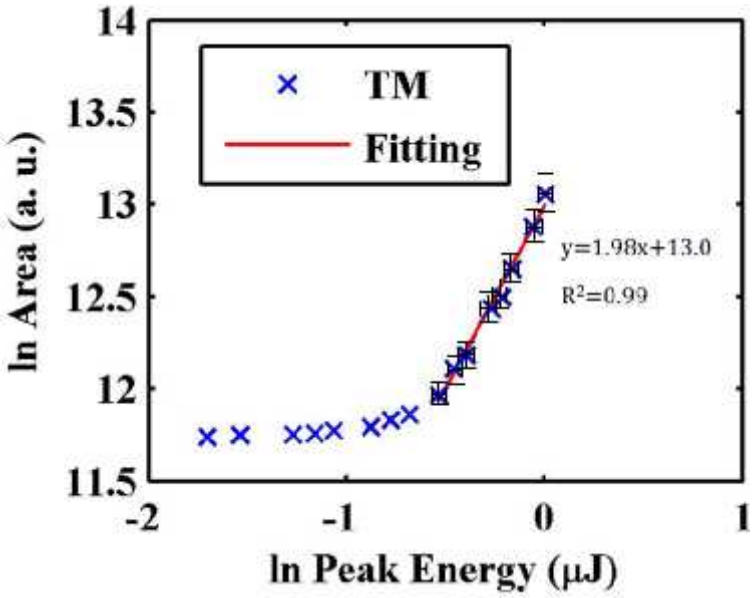

Figure 4.6. Linear fitting experiment spots of linear polarization with transverse magnetic field (TM). The determination coefficient of linear fitting is R^2 =*0.99*.

For laser irradiation with circular polarization, the experimental points and the calculated curve are presented in Figure 4.7. The right 5 spots are fitted into a linear equation with determination coefficient R^2 =*0.99* which presents the static confidence of interpolation point. The interpolation point of threshold value is $P_{th,CP}$ =*4.02* ï *0.05*MW with $E_{th,CP}$ = *0.68*ï*0.02*µJ, near Gaussian pulses, inferring to $n_2^{775,CP}$ =*1.46*×*10*$^{-16}$ cm^2W^{-1} and $\chi^{(3)}_{775,CP}$ ~ *8.21* ×*10*$^{-15}$ esu.

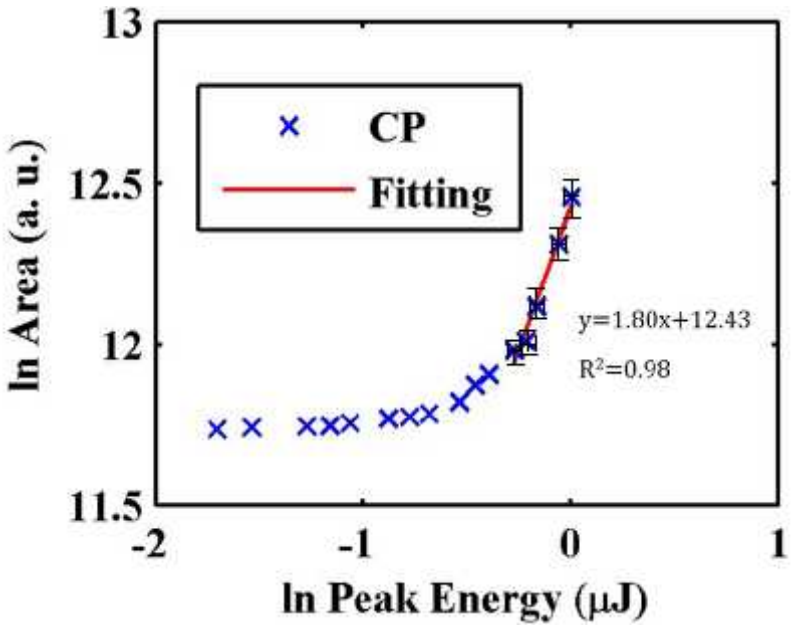

Figure 4.7. Linear fitting experiment spots of linear polarization with circular polarization. The determination coefficient of linear fitting is R^2 =*0.98*.

This investigation revealed that continuum generation depends on the polarization state of the incident light linear (TE and TM) and circular polarization (C) exhibit a difference which indicates that the ratio of critical powers P_C^C / P_C^{ll} >1. It is observed stronger coupling and higher refractive-index modulation with linear polarization, especially for linear TE polarization (evidence reference). From the measured threshold energies for SC, ~0.51µJ (linear) and ~0 .69µJ *(circular)*, the polarization dependent peak powers is ~*1*.35. The result is close to the theoretical result: 1.5 [131].

The band gap of PMMA is 4.58 eV [46] while photon energy of 775 nm light is 1.55 eV. Hence the multi-photon ionization is triggered by 3-photon absorption. In addition, the pulse duration is ~170 fs, leading to significant impact ionization. Electron density in weak plasma may reach to $10^{19}cm^{-3}$, leading to permanent refractive-index modulation.

4.3 Inscription within poly methyl pentene (PMP)

4.3.1 Linear absorption

PMP has a semi-transparent window for ~10μm MIR light which allows thermal effects observed by a FLIR camera. Optical setup is shown Figure 4.8 and Figure 4.9(a). The optical setup is shown in Figure 4.8. 5-mm collimated OPA beam with signal (*1064* nm) and idler (*2869* nm) with average power P~*50* mW is focused by a ZnSe lens below the surface of a PMP substrate. A calibrated thermal camera (model FLIR SC660, sensitive from 8μm-15μm, mid-wave infrared) was used to detect IR signals in thermal imaging to analyse the thermal effects during internal inscription. This camera was placed on a tripod at distance of *~1* m from the investigated targets and later brought closer to within *~0.4* m for higher resolution images. It was possible also to take real time videos with this camera. Another NIR camera (Find-R-scope) is used to watch the scatter light from optic.

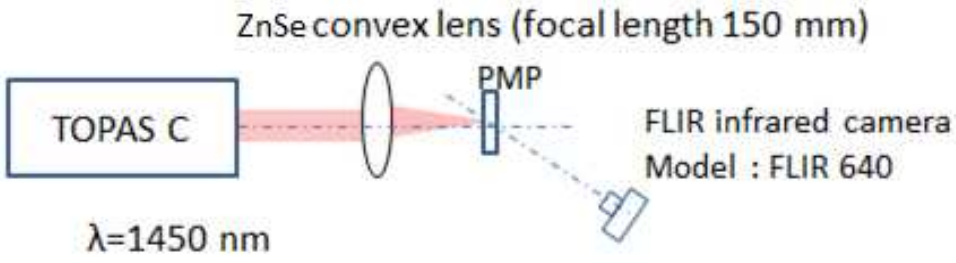

Figure 4.8. Optical setup of the observation of thermal effects.

A thermal-diffusion study was carried out. The PMP exhibited high or reasonable transmission in MIR region. The centre temperature achieved to saturation within 6s, shown in Figure 4.9(b). By naked eyes, clear super-continuum phenomenon which is accompanied with filamentation, is observed, shown in (c), because the beam is invisible. It has been observed that the OPA beam consists of other 3 visible components, shown in shown in (d). Two visible components are respectively the signal of second harmonic component (532nm: green) of signal (1064nm), the third harmonic component (λ_{601}: red) of frequency difference of idler (*2869*nm) and signal (*1064*nm). The source of blue component is unknown. The three visible components are all weak. They have less chance to ignite strong filamentation and white continuum signal. It concludes that nonlinear coupling does happen. Consequently, nonlinear absorption combined with linear absorption happen in the case.

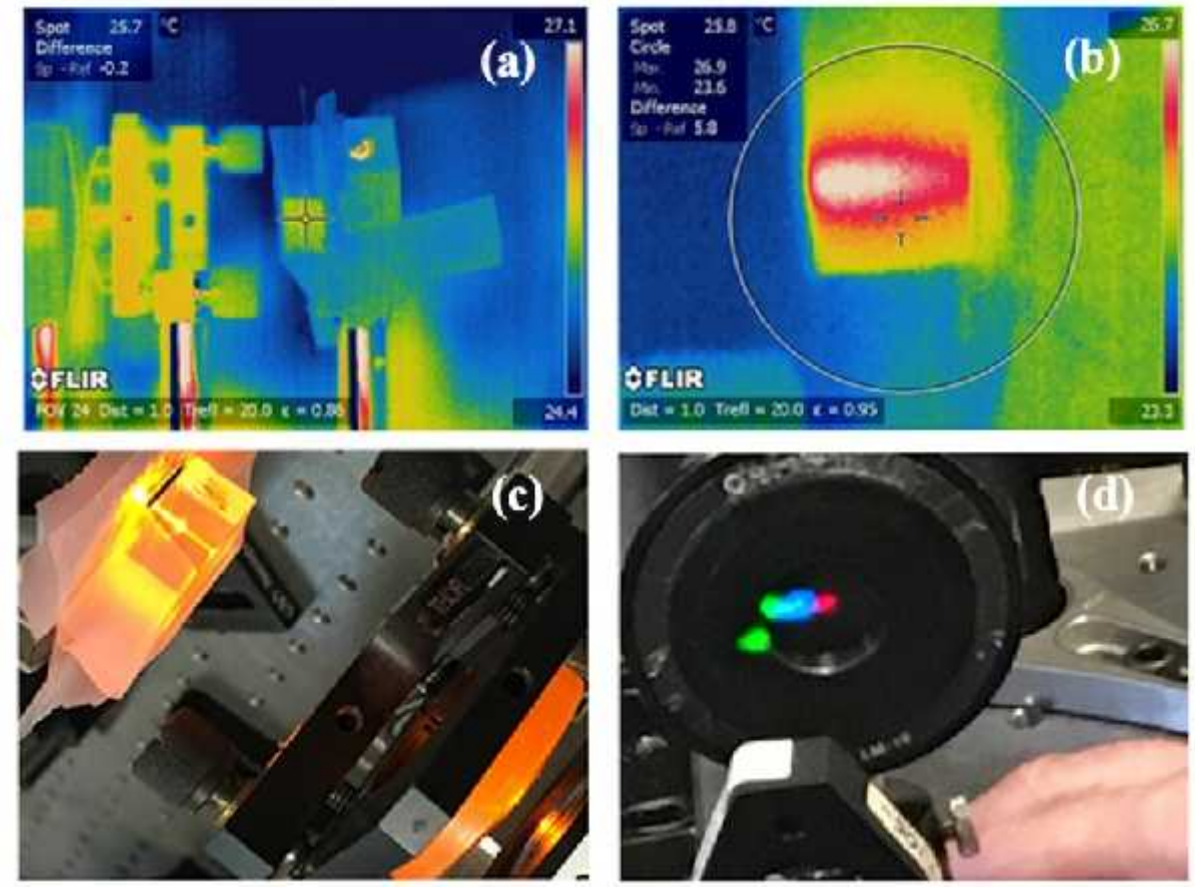

Figure 4.9. (a) FLIR thermal imaging; (b) line heat source; (c) Visible filamentary line (d) SHG or THG of frequency-difference and frequency-summation signals.

Notably PMP is not completely transmitted for NIR light and the external transmittance for PMP is shown in Figure 4.10. PMP has an absorption band between *1.1* μm -*1.3* μm and in the NIR band the transmittance rate drops from *97%* to *45%* [9]. Inscription with NIR fs pulse, it is arguable that interacting mechanism for lattice vibration induced by EM wave cannot be ignored. Linear absorption may cause heat effect, which leads to the processing becoming uncontrollable. For undirected bandgap material, coupling can generate phonons which can also lead to thermal effect.

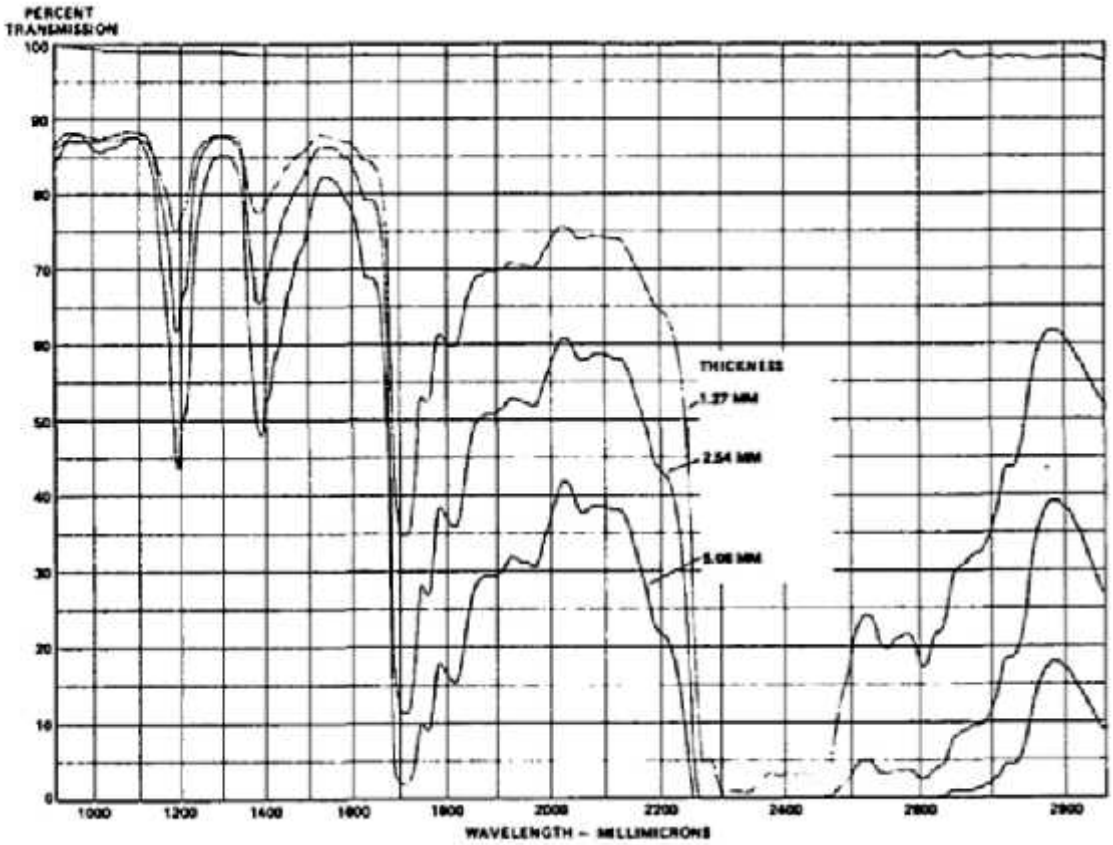

Figure 4.10. External transmittance for PMP in thickness: 1.27mm, 2.54mm and 5.06m for near infrared light (940 -2850nm). This transmission spectrum is courtesy to Lytle et al [9].

Hence for, the absorption at 1140 nm is chosen for studying and at this wavelength PMP is nearly half transmission. Transmission (T_{1140nm}) at is measured at ~ *0.5*. Beer Lambert law is applied [34].

$$T_{1\quad n} = (1-R)^2 e^{-\alpha} = 0.5 \quad (4.3)$$

and

$$R = \frac{(n_0-1)^2+K^2}{(n_0+1)^2+K^2} \quad (4.4)\ [34]$$

In addition,

$$\alpha = \left|\frac{4\pi}{\lambda}\right| \quad (4.5)$$

where $n_0 = 1.423$ and K is a complex number. To solve the equation 4.3. Linear absorption coefficient (α) is derived as ~ *0.61* cm^{-1}, which exhibits that linear absorption is significant.

Lytle et al investigated the external transmittance of PMP in a viable wavelength range but in the case of a light source of a 2700-K tungsten lamp. This kind of light source couldn't generate nonlinear effects. To supplement more knowledge for femtosecond laser pulse, external transmission rates of a *10*-mm thick sample corresponding to collimated beam (~5mm and 170fs) with wavelength ranged *470* nm -*750* nm are measured. from Figure 4.11 shows coincidence of two sets of results with *500* m- *700* nm while the transmission rate for fs pulse is slightly less than previous one [9]. The comparison suggests transmission rate for the two lights is almost same. For a collimated beam, the filamentation is not obvious due to the short optical length in the PMP. The built-in temperature field in neighbourhood of geometrical focus provide clues of mechanisms.

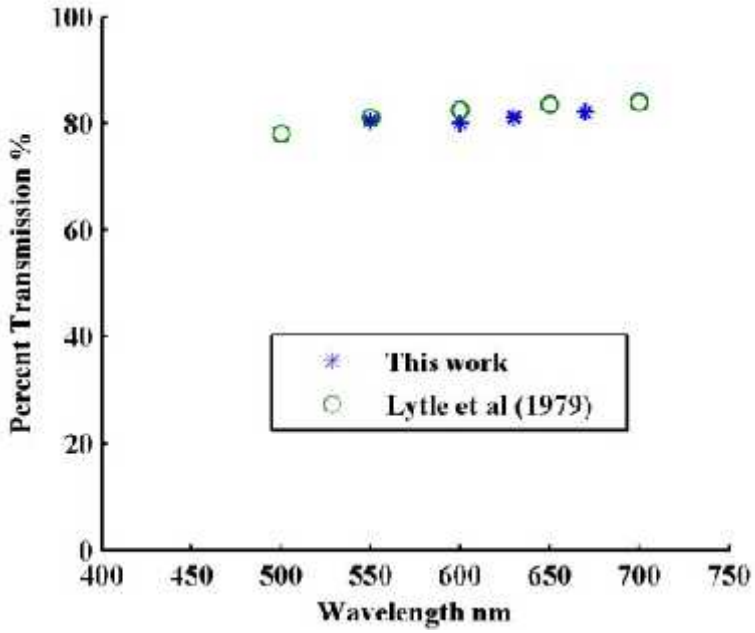

Figure 4.11. External transmission of PMP measured with a sample thickness of 10 mm.

4.3.2 Filamentary inscription using VIS fs pulses

The pulse duration versus wavelength of the OPA beam is presented in Figure 4.12. Optimisation in the Clark MXR compressor was also required to optimise pulse length. The minimum pulse length of 150fs was observed at 600nm output which minimises optical breakdown. In supplement, supercontinuum spectra were used as diagnostic signal using the wideband spectrometer (Andor Shamrock).

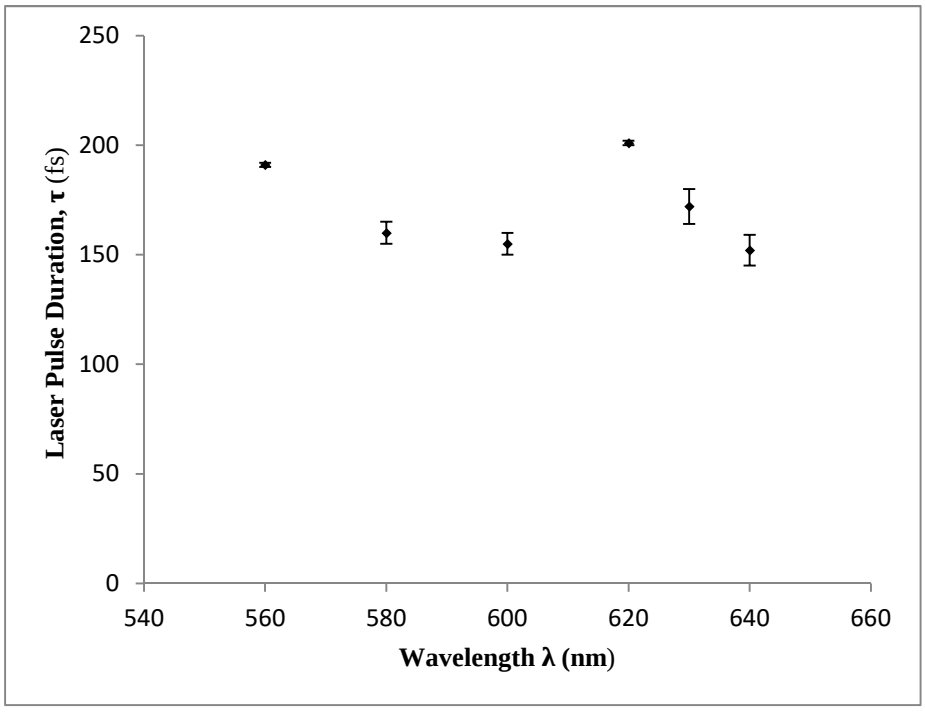

Figure 4.12. τ (full width at half maximum) corresponding to wavelength λ.

A set of filamentary strucures, presented in Figure 4.10, were inscribed using a single-beam low NA inscription at different wavelength with a pulse energy $Ep = 1 \pm 0.073\ \mu J$ (1σ) and transverse scan speed of 1 mm/sec. The breakdown failure is more serious in long wavelength region. That means nonlinear coupling efficiency drops when the wavelength is rising. Another notable manifestation is the beginning of these filamentary structures is moving to the front surface, accompanied with the accompanied with the drop of the wavelength and the fitting function is quadratic rather than linear shift.

It is seen that the breakdown failure is more serious in long wavelength region. That means nonlinear coupling efficiency drops when the wavelength is rising. Another notable

manifestation is the beginning of these filamentary structures is moving to the front surface, accompanied with the accompanied with the drop of the wavelength and the fitting function is quadratic rather than linear shift. The result is coincidence to [214].

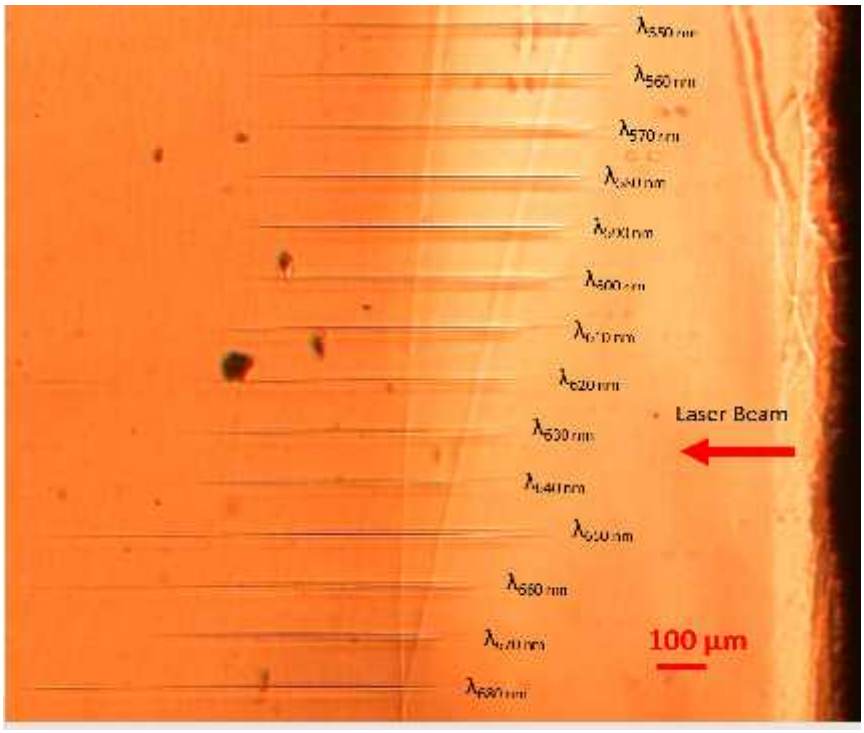

Figure 4.13. Microscopic structures generated by laser pulses τ~ *180*fs, *Ep = 1±0.073 µJ* (1σ) and λ = *550, 560 … and 680* nm in poly methyl pentene (PMP). The red arrow represents the propagation direction of incident beam.

4.3.3 Filamentary length versus pulse energy

This beam with 387 nm wavelength is focused by a NUV microscope objective with NA 0.4 (THORLABS LMU-20X-NUV). Optics are coated with an anti-reflection (AR) dielectric coating to enhance the transmission of UV light. Transmittance was measured to be 99%. It is notable that for internal inscription the choice of objective lens is critical. The microscope which is made of several optical materials can stretch of pulse duration. The problem of stretching pulse duration by 'group velocity dispersion (GVD)' [215] is considerable. In contrast, reflecting objectives avoid this problem. By transversely scanning with vertical polarization, a series of Δn layers are obtained, observed from side-view. The laser beam comes from right side and the start point is clearly in front of geometrical focus, moving

closer to the source with increasing energy, shown in Figure 4.14 (a). The result is satisfied to those observed by Sudrie *et al's* work [216]. In (b), the fitting equation has coincidence of the estimation of Zverev and Pashkov [217]. The Processing maximum length is Rayleigh length (R_L) of a focused Gaussian beam

$$R_L = \pi n_0 \frac{w_0^2}{\lambda} \quad (4.6),$$

where $2w_0$ is beam waist diameter and

$$2w_0 \sim \frac{1.2\ \lambda}{N} \quad (4.7),$$

NA is the effective number depending on the focusing optics.

Because the calculated beam waist ($2w_0$) is lower than diffractive limitation (1μm), the experimental measure data is applied. Therefor in linear case, processing length

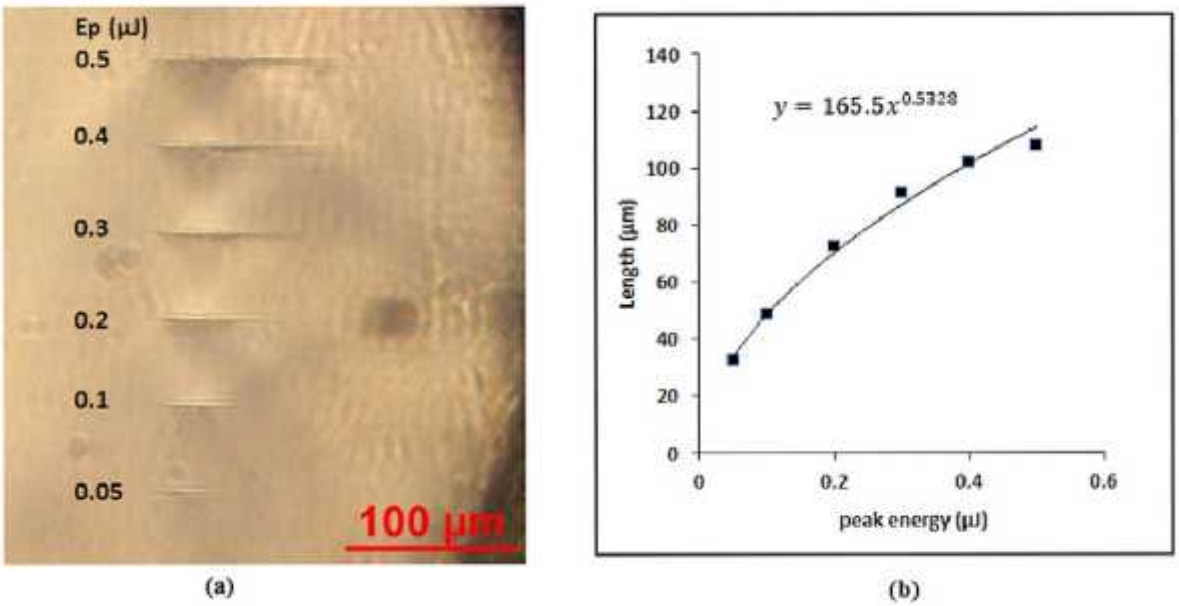

Figure 4.14. (a) Δn modulation in bulk PMP and (b) measured filament length with power function fit shows the exponent = 0.53, close to theoretical value 0.5 of Zverev and Pashkov 's work [217].

$$2R_L \approx 2 \times \pi n_0 \frac{w_0^2}{\lambda} \approx 32\ \mu m \ .$$

In contrast, the processing maximum length of filamentation, shown in the micrograph of Figure 4.14, is *107.9 μm >> 2R*$_L$ (*~32.0 μm*) . Actually, the shortest length is close to $2R_L$. That means filamentation mechanism can make processing length much longer.

4.3.4 Low NA volume Bragg gratings (VBGs) inscription

VBG's were fabricated using femtosecond pulses at two wavelengths, respectively generated using second harmonic generation (SHG) via BBO crystal and optical parametric amplification (OPA) via TOPAS-C. In each case, the Bragg diffraction efficiency (DE) for gratings of single layer was low. Gratings of *1 -30* layers and *0.3 – 2.5* mm thickness were created with stitching overlap method. The processing time costs 8 seconds per scan 400s per mm^2 (50 lines/mm). The total time to create VBG is *0.2 ~ 4* hours. Work performance of gratings fabricated with two wavelengths is respectively presented in Figure 4.15. For scan parameters, refer to Table 4.1 and Table 4.2.

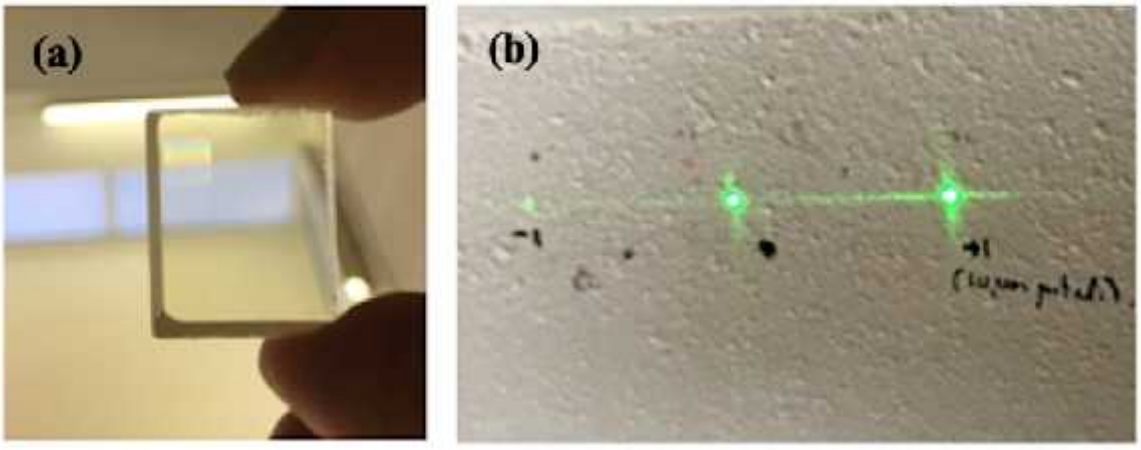

Figure 4.15. (a) 4 × 4 × 2mm thick VBG inscribed in PMP at λ= *387.5*nm and NA= 0.1 with RI modulation Δn *~1.10*$^{-4}$, (b) first order diffraction at the Bragg angle for *1.5* mm thick, 10μm pitch VBG inscribed at λ = *670*nm reaching $\eta_{\pm 1}$ = *63%* with almost no coupling to minus first order.

Notably, some residual scatter is apparent, attributable to a small contribution of dielectric breakdown. With 2-mm thick gratings, first order diffraction efficiency η_1 is higher than 60%. Using Kogelnik's equation [158],

$$\eta_1 = \sin^2(\pi \ \Delta n/\lambda \cos\theta_B) \quad (2.25)$$

we can infer $\Delta n \sim 1\times10^{-4}$, where L is the grating thickness, Δn is the RI modulation, λ (532nm) is the incident wavelength and θ_B is the Bragg angle. This Δn is a factor of 5 lower than observed in PMP by Mochizuki *et al* [218]. However, the quality appeared good with a relatively low level of light scatter.

Table 4.1: Processing parameter of low NA inscription

Nonlinear Method	SHG and OPA
NA	<0.18
Scan Speed	0.5 mm/s
Ep	0.5 μJ
τ	~170 fs

Table 4.2: DE and Δn of VBG fabricated with $\lambda = 387.5/670$ nm and τ_p~170fs.

Λ (nm)	NA	Thickness (mm)	ξ (l/mm)	η_1	Δn
387.5	0.08	2	100	> 60%	1.00×10^{-4}
670	0.15	1.5	100	~63%	1.03×10^{-4}

Figure 4.16 presents diffractive efficiency (DE) of volume Bragg gratings (VBGs) with thickness up to *2.5* mm. The gratings were fabricated using OPA beam with λ =*670* nm and τ_p~*170* fs. The measurement of theoretical and measured diffraction efficiencies is listed in Table 4.3. The limitation of absolute diffraction efficiency comes from an increasing level of scatter due to optical breakdown. The theoretical fit is due to equation 2.25 with $\Delta n = 1 \times 10^{-4}$.

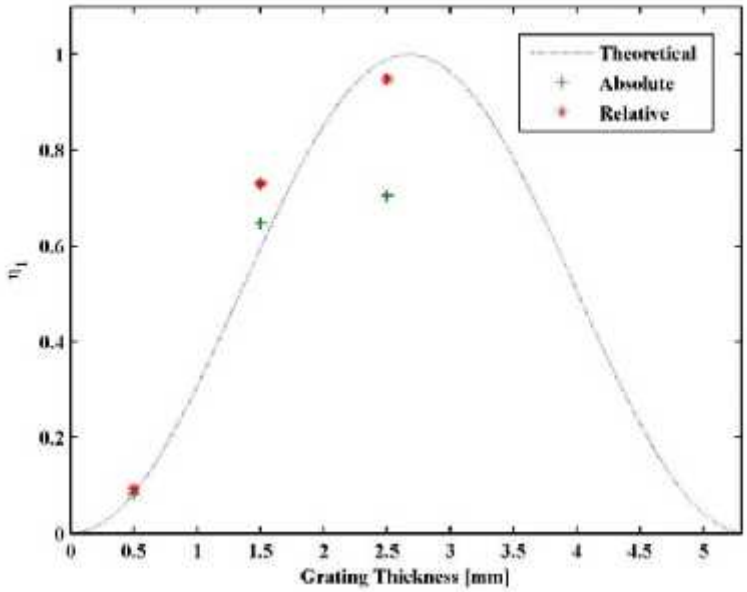

Figure 4.16. The first order DE with grating thickness in PMP and theoretical curve due to Kogelnick equation [158] based on $\Delta n = 1.0 \times 10^{-4}$. The absolute diffraction efficiency is saturated at 67.5% by scatter loss due to optical breakdown.

Table 4.3: Diffraction efficiency of 2.5 mm VBG, fabricated with λ =670 nm and τ_p~170fs

Relative diffraction efficiency	$\eta_1=I_{+1}/I_0$	95%
Absolute diffraction Efficiency	$\eta_1=I_{+1}/I_T$	67.5%

4.3.5 Supercontinuum in PMP

The experimental set-up used retro-reflection of the continuum from an aluminised mirror placed immediately behind the mounted PMP sample and optical setup is showing in Figure 4.17. This reflected light was transmitted through the NUV, dielectric coated, *45*î turning mirror which is just before the objective then focused into the fibre coupler and connected to the wideband spectrometer (Andor Shamrock). Data collection was synchronised to the laser source from the *1* kHz, TTL output on the DT505. Pockels cell driver of the femtosecond system.

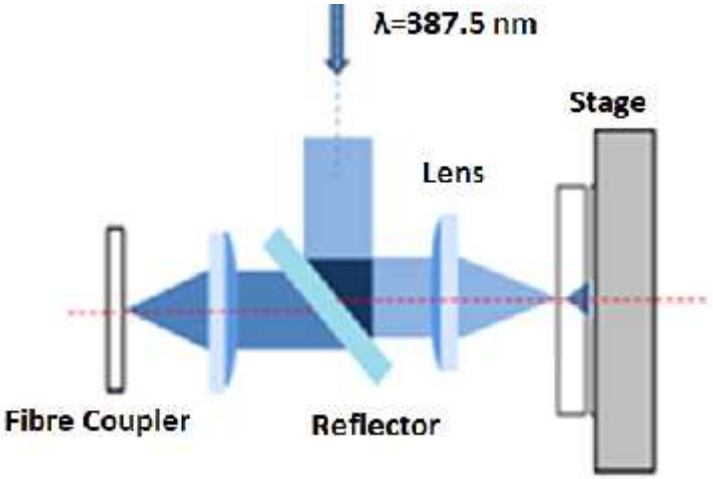

Figure 4.17. Reflected SC spectral sampled by Andor Shamrock time-resolved spectrometer.

The spectral result is shown in Figure 4.18. At low intensity, the laser bandwidth at 387.5nm was observed to be ~2.5nm, consistent with the 5nm laser bandwidth observed at 775nm. The threshold for supercontinuum generation, also the threshold peak power for SF was measured to be P_{th}^{0} = *2.2* ï *0.6*MW with E_{th} = *0.4*ï*0.1*µJ, *170* fs linearly polarised, near Gaussian pulses. This infers a third order susceptibility $\chi^{(3)}_{387}$ *~1.1x10*$^{-14}$esu hence NL refractive index component n_2^{387} = *2.10*$^{-16}$ cm^{2}W^{-1} in PMP. This compares with P_{th} = 1.1MW measured previously in PMMA where it is estimated n_2^{387} (PMMA) = *1.46*$^{-16}$ cm^{2}W^{-1} for TE polarization in section 4.2.2.

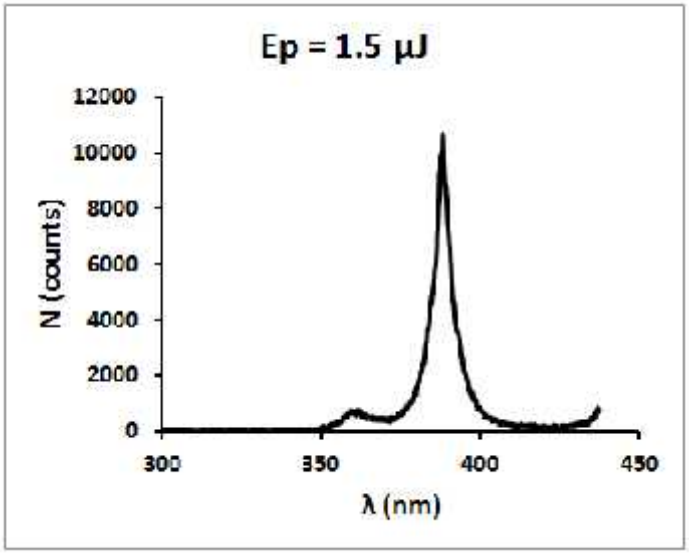

Figure 4.18. Anti-stokes broadening spectrum generated by fs pulse with linear polarization (TE), λ= 387.5nm and Ep =1.5µJ. Measured by Andor Shamrock SR 303i.

4.3.6 Inscription with higher NA's

A reflective microscopic objective (Schwarzchild Ealing, NA =*0.25*) was used to modify refractive index using λ = *387.5*nm. Optical images are presented in Figure 4.19. Tests with pulse energy in the range $0.05 \leq E_p \leq 0.3$µJ indicated filament length ~ 40µm with $E_p = 0.2$µJ. A single layer grating, inscribed at pulse energy *0.2*µJ, is shown with pitch Λ = *15*µm in Figure 4.15 (a) while a 4 layer VBG with 10% overlap offset, deepest layer first is shown in (b), inscribed at *0.2*µJ and transverse scan speed s = *0.7*mm/s. A front view of the grating is shown in (c).

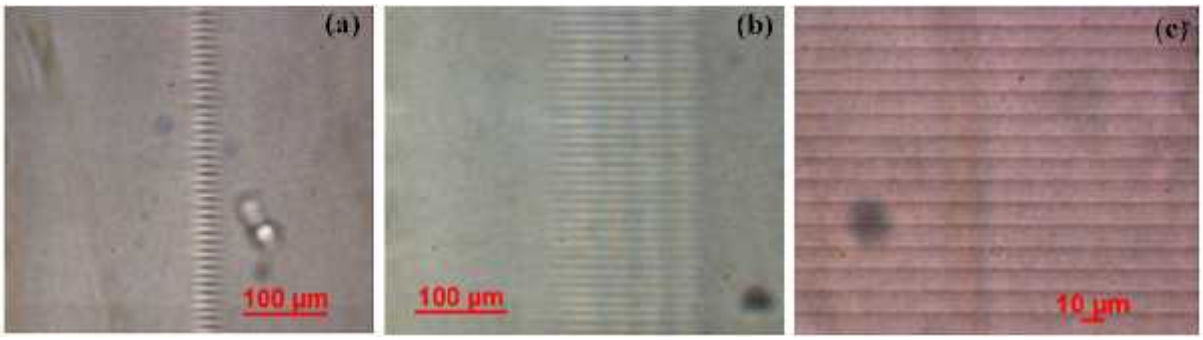

Figure 4.19. Optical images of RI modifications in PMP at NA = 0.25, (a) side view of 30micron thick VBG, (b) side view of a 4 layer VBG using 10% overlap rate, (c) front view of inscribed VBG filaments. Scan speed throughout s = 0.7mm/s.

Fabrication with a transmission microscopic objective at NA=0.4 (Thorlabs ×20 NUV) was investigated at λ = 387.5nm. The 4 layers, 120 µm thick grating exhibited high diffraction efficiency under illumination of white light. Cross-sectional optical results are shown in Figure 4.20(a) using E_P = 0.1µJ/pulse and transverse scan speed s = 0.5mm/s. Filament length and width was l ~ 40 µm and ϕ ~3µm respectively. A strong phase grating resulted and (b) indicates first order diffraction at 532nm from the single layer (40µm thick), Λ = 5µm pitch, VBG at the Bragg angle, with absolute DE, η_1 = 47%. This result inferred that the RI modulation Δn ~2.3 x 10^{-3}, an order of magnitude higher than achieved with low NA, indicating that NA is a significant variable in obtaining higher Δn modulation at 387.5nm and 170fs temporal pulse length. Surprisingly, there is also evidence here of low intensity coupling at pitch 2Λ. 3-layer gratings whose absolute DE should have approached unity, reached only η_{+1} ~ 70%, lower than expected, again due to continuous scatter observed between the orders due to voids.

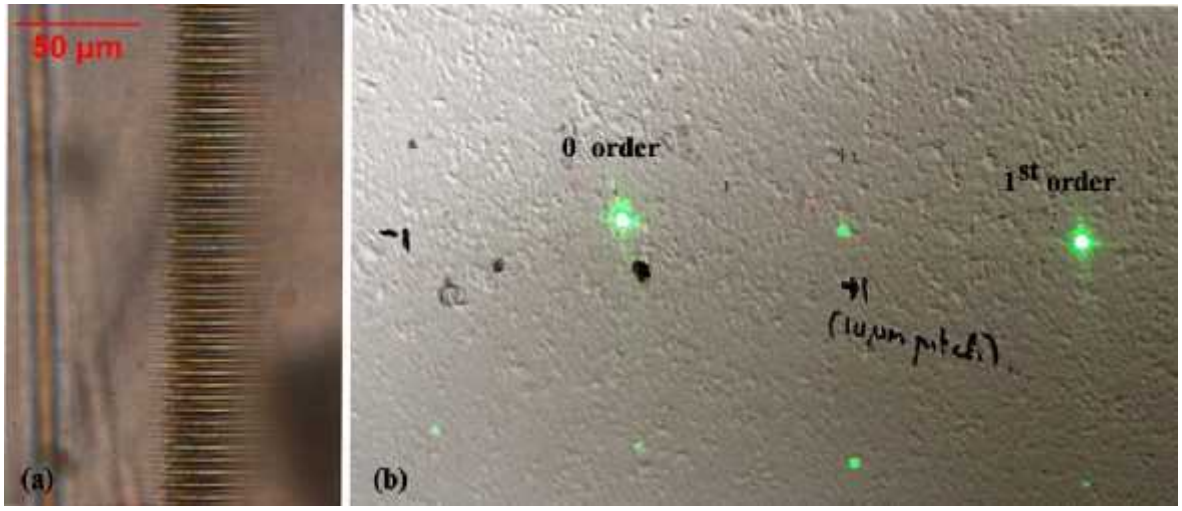

Figure 4.20. (a) Cross-sectional microscopic results of single layer, 5µm pitch VBG inscribed in PMP at λ = 387.5nm with NA = 0.4. Laser direction from left to right, (b) image of Bragg diffraction from the 200 l/mm grating at 532nm with DE η_1 = 0.47 inferring a Δn ~2.3×10^{-3}.

The occurrence of optical breakdown in filamentation will lead to damage spot in gratings. Figure 4.21 is a micrography of modification using femtosecond pulse Ep (*0.3 – 1.0* µJ), 0.18NA, λ=650nm and pulse duration ~180fs. The damage spot, black dots, are randomly distributed inside filamentary structures.

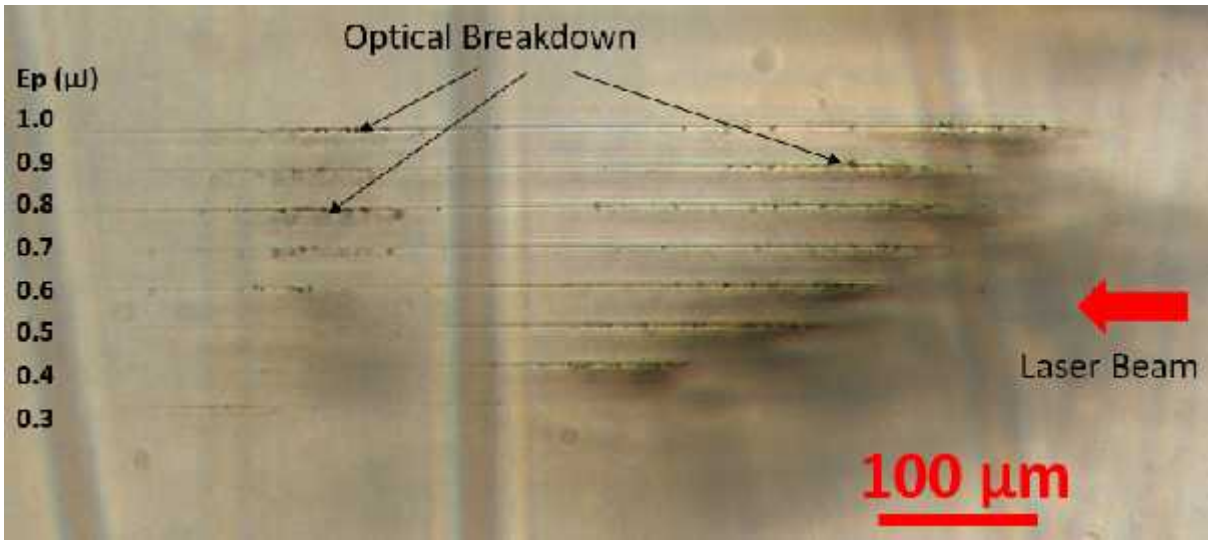

Figure 4.21. Damage dots generated by optical breakdown which is induced by focused laser light (~180fs, 650nm and 0.15NA).

4.3.7 Raman spectroscopy

The topological structure of poly methyl pentene is shown in Figure 4.22. Chemical changes during femtosecond exposure in polymers can lead to bond breaking and formation [143]. Raman spectroscopy was utilized to investigate the chemical changes to PMP following laser modification. The PMP was exposed with femtosecond pulses from a system operating at *400* nm wavelength, pulse length τ = 190fs, 30 kHz repetition rate and pulse energies of *0.20* and *0.35* µJ. The beam was focused 0.5 mm below the surface at 0.4NA and scanned transversely at *5*mm/s.

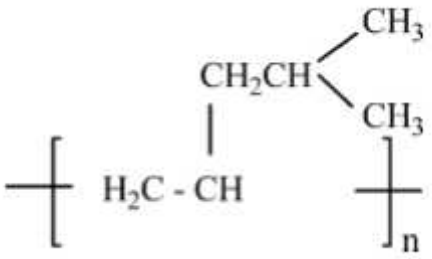

Figure 4.22. Structure of poly methyl pentene (PMP) [219].

A Renishaw 1000 Raman Microscope with a 514 nm Ar-ion laser focused through a 0.55 NA objective to a spot size <1µm was used to perform the measurements. A reference measurement of PMP was first taken, which returned very low fluorescence and clear peaks consistent with Samuel and Mohan's work [220]. The processing sample with processing gratings which is ~1mm below the surface. The material above processing layers is removed using a disk-polishing machine with diamond cream. The substrate was polished to allow direct measurement of the filaments inside of the PMP with the Raman microscope.

Raman peaks between 2800 and 3000cm^{-1} are due to backbone CH stretching and CH_3 asymmetric stretching while those between 750 and 1500cm^{-1} are due mainly to CH_3 rocking and twisting vibrational modes [221]. The peaks corresponding to spatial assignment are presented in Table 4.4. Comparing the Raman spectra of clean PMP sample to irradiated PMP, it was observed that strong photoluminescence (PL) due to Raman scattering emerged in the filament regions. When this PL was removed from the data it became clear that the Raman peak height had decreased in the regions of filamentation. These observations match what has previously been seen in Raman spectra of laser modified PMMA [222]. The Raman

spectra presented in Figure 4.23, with background PL subtracted, demonstrate the decrease in the strength of all Raman peaks with increasing pulse energy. This trend suggests that depolymerisation and bond breakage is induced by femtosecond exposure. As this occurs consistently in all Raman peaks, this probably indicates that breakage is not localized to the polymer backbone or side chains, but instead occurs near uniformly throughout the material and energy loss due to photonic PL. In the inset of Figure 4.22, Raman spectra without background subtraction are presented for the reference PMP and the 0.2 µJ filament. Here the emergence of PL in the filament is clear, which is often associated with the generation of defects and free radicals by direct laser writing [223].

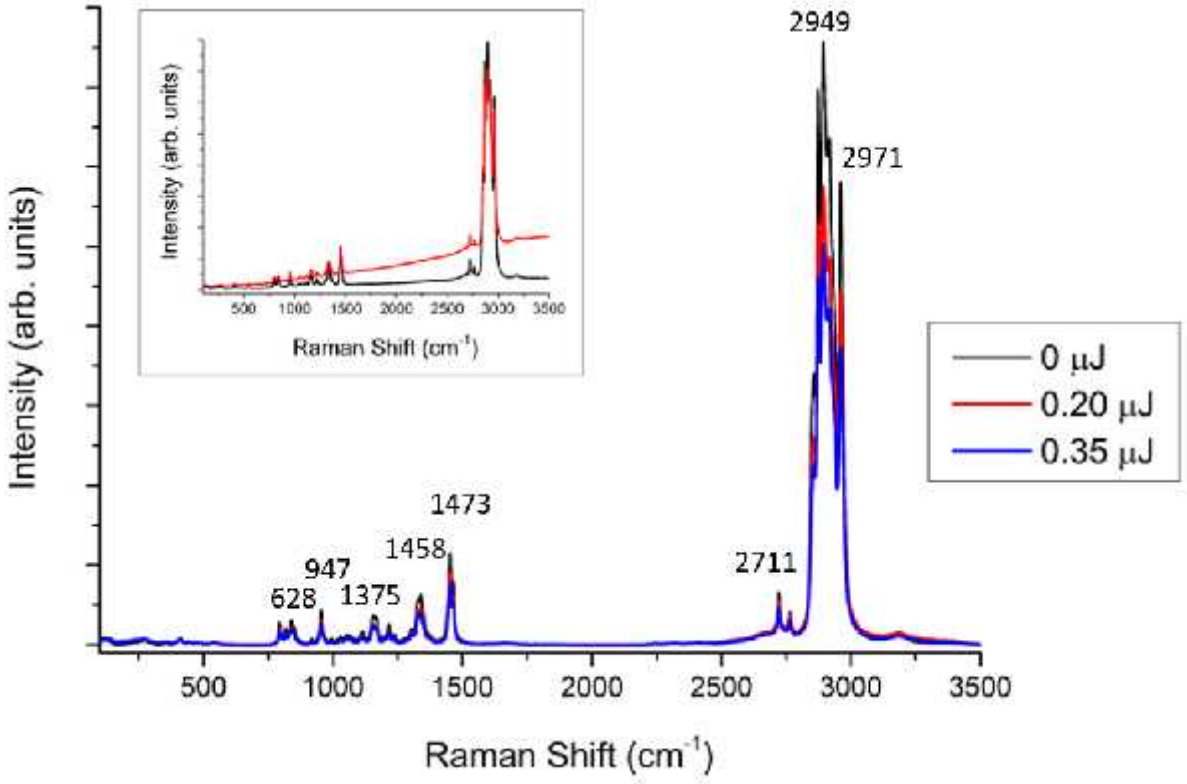

Figure 4.23. Raman spectroscopy of laser filaments in PMP using 0.20 µJ and 0.35 µJ pulses is compared to a pristine PMP sample. Background subtraction was performed to remove the PL signal from the data. Inset: Comparison of pristine PMP with a 0.20 µJ filament without background subtraction

Table: 4.4 Wave number (cm^{-1}) and Assignment of PMP [221].

Wave Number (cm^{-1})	Assignment
628	C-C in plane bending
947	C-C stretching
1375	CH_3 symmetric deformation
1458	CH_3 symmetric deformation
1473	CH symmetric deformation in CH_3/
2711	CH stretching
2949	CH asymmetric stretching in CH_3
2971	CH asymmetric stretching in CH_3

4.3.8 Discussion

Inscription of Δn employs multi-photon absorption (MPA), which is a nonlinear absorption mechanism. The nonlinear absorption is of importance for the uniformity of processing volume material [224]. In order to explain the MPA, a Jacoby's diagram illustrated in Figure 4.24 is used. Tt is 2-photon and 4-photon coupling respectively for 387-nm and 775-nm photons because of the band gap *6.2* eV.

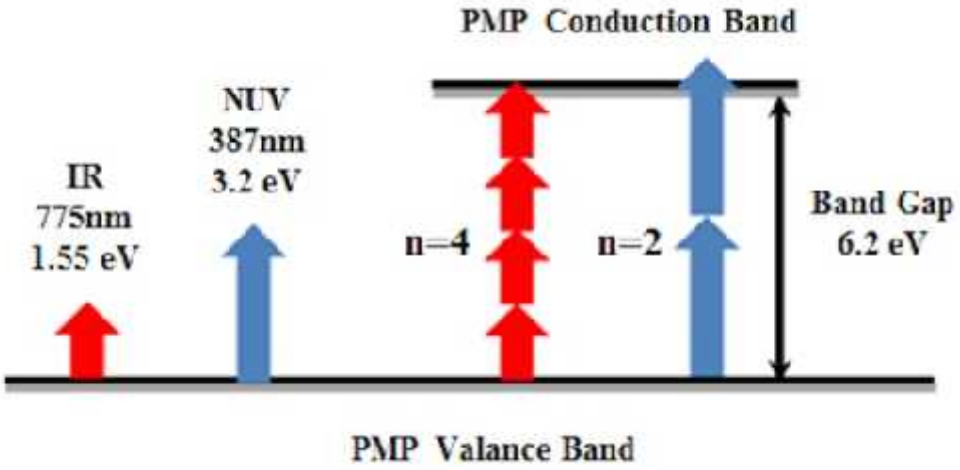

Figure 4.24. Multi-photon absorption of 775 nm and 387 nm in PMP.

Femtosecond laser inscription in Polymethyl Pentene in the NUV at λ = 387.5nm, at visible wavelengths 550 $\leq \lambda \leq$ 700nm has been carried out. Low NA ~0.08 inscription at all wavelengths resulted in a correspondingly low refractive index modulation, $\Delta n \sim 1.10^{-4}$ while higher NA ~0.4 inscription at λ = 387.5nm resulted in an order of magnitude increase in refractive index modulation, $\Delta n \sim 2.3 \times 10^{-3}$. Volume Bragg Gratings inscribed at 387.5nm with 200 lines/mm showed a first order diffraction efficiency η_1 = 68.5%, however, diffraction efficiency was limited by observed scatter due to some residual material breakdown at pulselength τ_p = 180fs, creating a low intensity background between orders. If the pulse duration is lower than 130fs, optical breakdown will be significant supressed and remove the breakdown damage.

4.4 Laser processing of Silver doped silica-PVA hybrid material

Using femtosecond laser can internally activate silver ion doped silica-PVA hybrid material. Figure 4.25 presents a set of cross-sectional results microscopic result. The length of modification volume is much longer than Rayleigh length, (~16 μm) which indicates the optical energy is clamped inside due to filamentation. At the geometrical focus position, the dark amber/yellow colour indicates concentration of silver particles and the light amber/yellow area shows the start of formation of silver particles. The unprocessed area shows bright and the yellow/amber region indicate the formation of nanoparticles and the dark area at the geometrical focus position shows particle aggregates. Processing layers is shifted forward and go through the substrate in 10 μm increments to show the selective capability of 3D construction.

Using absorption spectra to measure the formation of nanoparticles and the results are presented in Figure 4.26. The SPR peaks in absorption spectra indicate that more pulse energy leads to more particles concentration. The absorption is saturated at E_p = *2.0* μJ which means the agglomerates of silver particles [225]. It is notable that the peak of *0.26* μJ has good agreement with theoretical calculation according to Mie's SPR theory [226], in which the theoretical guess of SPR absorption peak corresponding to particles with 36nm diameter is plotted using a dashed line.

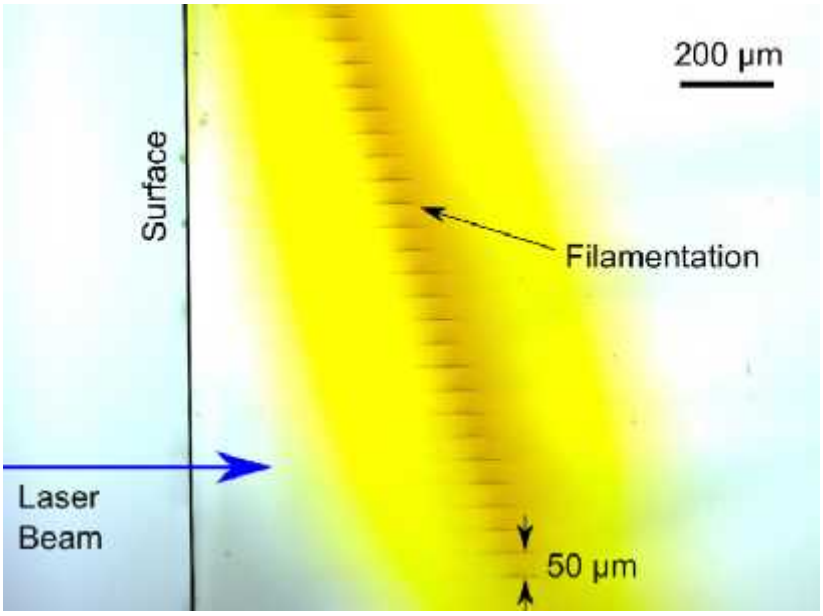

Figure 4.25. Silver doped silica-PVA hybrid material is processed at 1kHz by 170 fs, 387nm, NUV light using 0.49 μJ pulse energy, 1mm/s scan speed and focused using 0.45 N.A. objective.

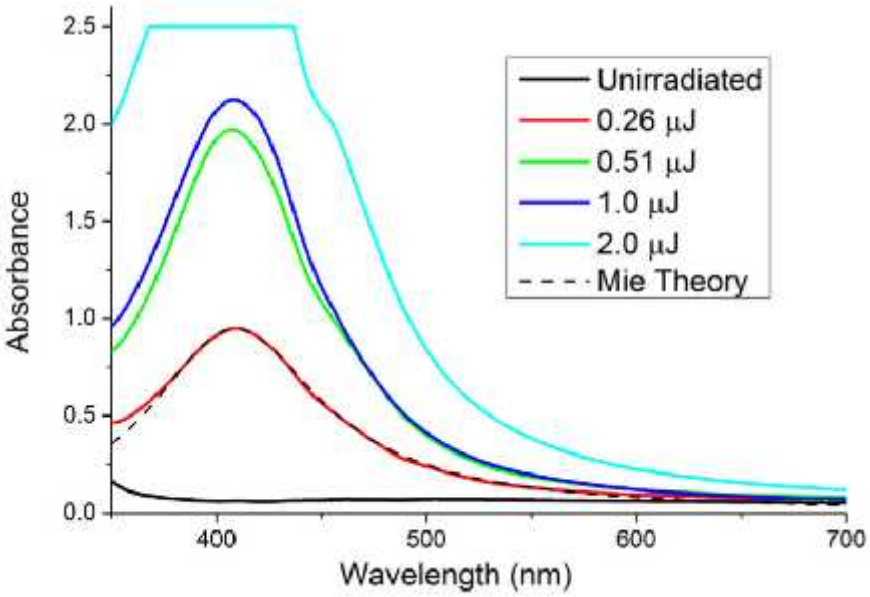

Figure 4.26. Absorption spectral of composites sample processed using NUV femtosecond laser pulses. The SPR peak of 0.26 μJ is coincide with Mie's theory guess. The colour of trace presents the processing peak energy and the dash trace is a theoretical guess (Mie's theory).

4.5 Pulses-and-medium interaction in Zinc Selenide

Zinc Selenide is a very interesting material which shows great application prospect. A few labs have been done on poly-crystalline Zinc Selenide substrates of 11mm thickness. The experimental setup for studying pulses-and-medium interaction is schematized in Figure 4.8. Femtosecond pulse ((λ=*1.26*μm) with E_p= *0.962* ± *0.089* expose the substrate. Figure 4.27 (a) shows clear blue light emitted from interface of air and ZnSe and filaments which emits visible light. The emitted bright blue light is supposed to origin from secondary harmonic generation. There is not obvious thermal effect, which is analysed using a thermal camera and the thermal analysis is illustrated in (b).

The incident beam is the reflected and attenuated to a spectrometer (Andor Shamrock). The spectrum, shown in Figure 4.28, has peak at *630*nm with FWHM *20* nm. At the same time, another interest point is noticeable. The 20-nm bandwidth is obviously wider than the one generated by BBO. Figure 4.23 shows the spectrum of SHG pulses generated by BBO crystal in which the FWHM is ~5nm which suggests lasing process involved.

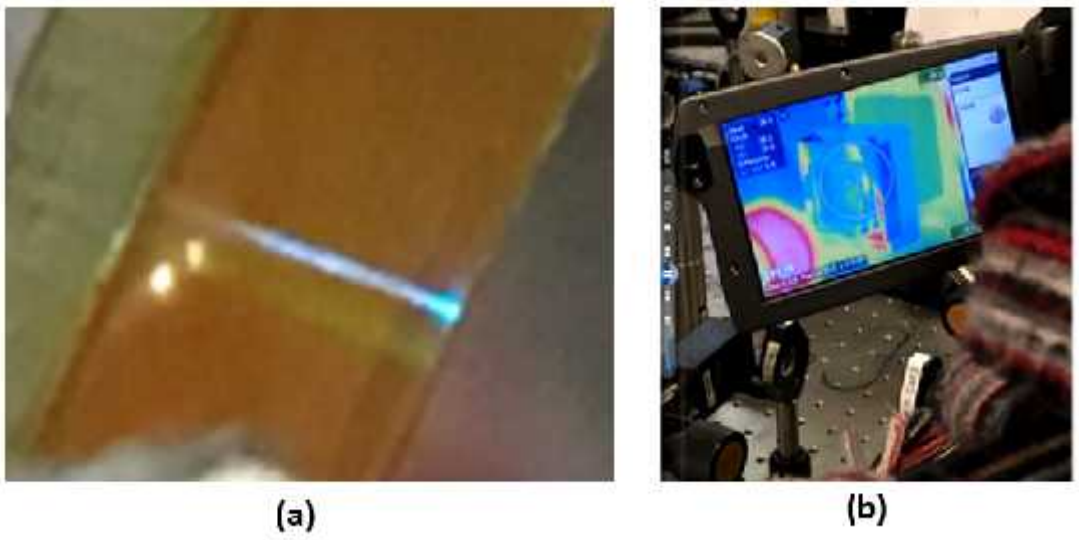

Figure 4.27. (a)Using femtosecond NIR pulses (τ ~170fs, λ=1.42μm) to test a piece of polycrystalline ZnSe substrate; (b) No thermal effect can be observed.

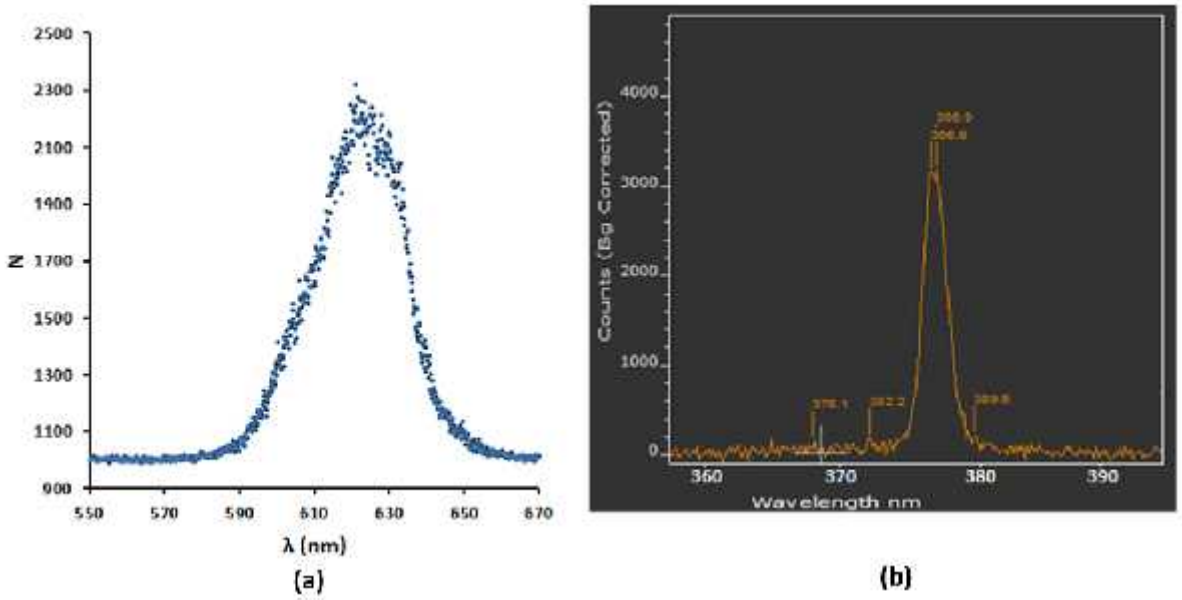

Figure 4.28. (a) Reflected-light spectrum generated by ZnSe, recorded by Andor Shamrock spectrometer; (b) Reflected-light spectrum generated by a BBO crystal, recorded by Andor Shamrock spectrometer.

In addition, the pulse has been obviously stretched from *0.19* fs to *0.50* ps, measured by autocorrelator (Pulse Check), shown in Figure 4.27. The pulse waveform is stretched due to positive group velocity dispersion (GVD). This result suggest ZnSe is a good nonlinear optical material which is likelihood used in chirped amplification (CPA), nonlinear crystal and lasing medium. A full set of quantitative study could be planned to study multi photon absorption, life time of exciting electrons and spectral features of ultrafast pulse interaction. The most interest point is to get distinct microscopic Δn changes inside the bulk material using fs MIR pulses. To further study, an autocorrelator was used to characterize the transmit femtosecond pulses. Figure 4.29 shows the wave form is significantly stretched when a piece of ZnSe substrate is insert. The possible source is positive group velocity dispersion (GVD).

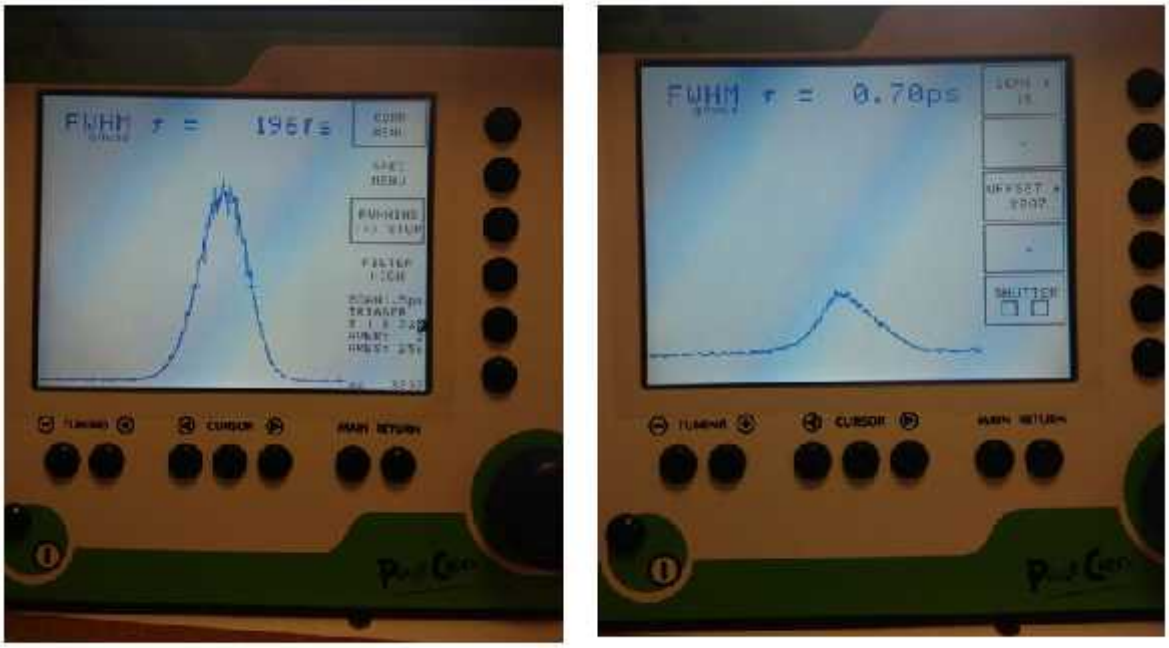

Figure 4.29. The NUV pulse is characterized using an autocorrelator (Pulse Check) with (a) ZnSe and without (b) ZnSe.

4.6 Summary

In this chapter we have discussed femtosecond inscription inside polymers with Gaussian beam. The main femtosecond system (Clark MXR CPA 2010) is the key laser source. Two nonlinear techniques for generating other wavelengths from the fundamental at *775*nm, OPA and SHG are used. The investigation λ covered from *387* nm to *1450* nm. The effect of polarization presented here considers only linear (TE and TM) and circular polarisation. Two kinds of modifications: refractive-index modulation and photo-chemical modification are studied. We conclude that:

1) The critical power threshold for supercontinum generation, also the critical power threshold for self-focussing, was measured in pure PMMA at λ = *775*nm with *170*fs pulses for all polarisations. The highest threshold for supercontinuum generation is observed with circular polarisations while the lowest threshold occurs with linear polarisation. The ratio $(P_{cr,circ}/P_{cr\,lin}) = 1.35$ experimentally, close to theoretically expected value of *1.50*.

2) Femtosecond laser inscription in poly methyl pentene (PMP) in the NUV at $\lambda = 387.5$nm, at visible wavelengths $550 \leq \lambda \leq 700$nm has been carried out. Low NA ~0.08 inscription at all wavelengths resulted in a correspondingly low refractive index modulation, $\Delta n \sim 1.10^{-4}$ while higher NA ~0.4 inscription at $\lambda = 387.5$nm resulted in an order of magnitude increase in refractive index modulation, $\Delta n \sim 2.3 \times 10^{-3}$. Volume Bragg Gratings inscribed at 387.5nm with 200lines/mm showed a first order diffraction efficiency $\eta_1 = 68.5\%$, however, diffraction efficiency was limited by observed scatter due to optical breakdown at pulselength $\tau_p = 180$fs, creating a low intensity background between orders. The critical power for self-focusing in PMP at 387.5nm, estimated from the threshold for supercontinuum was found to be $P_c^{387} = 2.2$MW ($0.4\mu J/170$fs) inferring that the non-linear refractive index of PMP at 387nm is $n_2^{387} = 2.10^{-16} cm^2W^{-1}$ and hence third order susceptibility $\chi^{(3)}$ ~ susceptibility $\chi^{(3)}_{387} \sim 1.1x10^{-14}$esu.

3) The fs pulse process is advantageous precisely control the precipitation of metal particles, such as silver in polymer composites. Femtosecond laser pulse can break PVA chemical bonds via nonlinear absorption. The scission of chemical bond yields free electrons to active doped silver ion. The result shows the 3-dimensional capability to construct silver metal structures selectively in the composites. The promised electronic-conductive feature is very attractive for creating 3D conductive circuits in micro or sub-micro scale as the silver atoms form Ag nanoparticles which could diffuse to form cluster if heat treatment is applied.

4) Using focused MIR beam (($\lambda=1.26\mu$m) to exposure polycrystalline zinc selenide was studied. There is not obvious thermal effect. Spectral analysis suggests sign of lasing, positive group velocity dispersion and second harmonic generation. Zinc selenide could be a very good material used for nonlinear crystal, lasing crystal and volume Bragg gratings (VBG) in mid-and far infrared region.

Chapter 5

Focusing of cylindrical vortex and vector beams

5.1 Introduction

This chapter is concerned with new knowledge learning of two photonic techniques: optical vortex and vector beams. Photons in macroscale with orbital angular momentum and spatial polarization are expected to exert forces and torques on matters. At this stage, there is little knowledge about the internal interaction of vortex beams within dielectrics, hence an ideal area for studying in experimental approaches. The study of the mechanic interaction between photons and matters can not only on matter but also and the applications of modern photonic device. Research in manipulation of optical field has also contributed new finds to spectral analysis, microscopic and quantum technologies.

5.2 Laser Beam with orbital angular momentum

5.2.1 Numerical study of the formation of helical phase fronts

Coherent light firstly with plane phase front moving along the z axis is considered. It is assumed that the phase front at far field is strictly planar and a simplifying approximation is considered. Show in Figure 5.1, 3 discrete plane phase front which is spaced with a λ=775nm at the neighbourhood of focus plane. Here the laser beam is collimated with waist of 18 μm. in the case.

Next let us suppose $\Delta\ (r,\theta)$ is applied by a reflective SLM where r is measured from the beam centre and θ is the azimuthal angle. The domain of coordinates is given $r \in [0, R]$ and $\theta \in [0, 2\pi]$. The phase front is modulated to a spatial structure, which is given as

$$\varphi(r,\theta,z) = \varphi_0 + \Delta \quad (5.1)$$

Our main interest is the Δ is a spiral shift and $\theta \in [0, 2\pi]$. In addition,

$$z = \left(a_0 + \frac{m}{2\pi}\right) \quad (5.2)$$

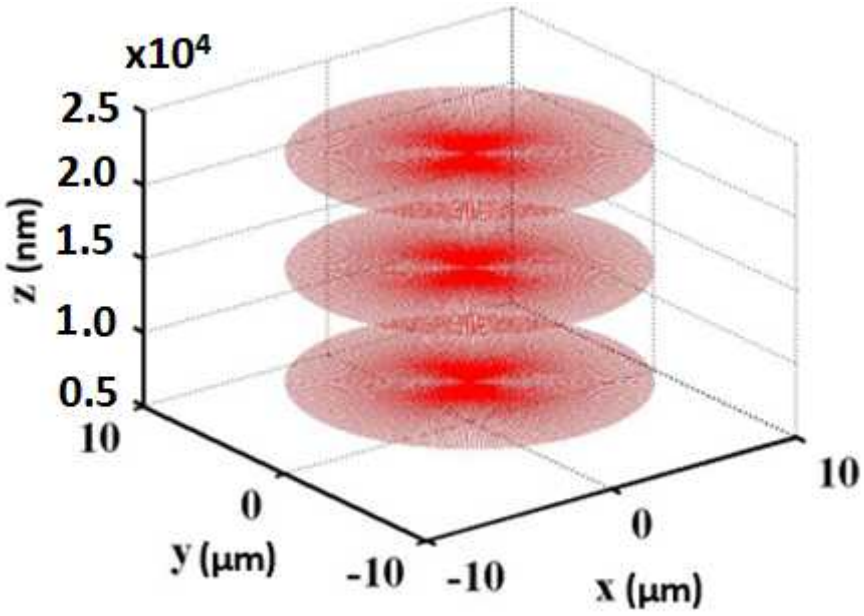

Figure 5.1. 3 plane-phase fronts (m=0) space with λ=775.

and

$$\Delta = \frac{\theta}{2\pi} \quad (5.3)$$

where a_0 is the start point of simulation. The ramp rate of spiral thread is a constant and then the phase change of a tread grows linearly with the angle θ, thus creating a helical path. The require phase change, Δ , for light with a wavelength of λ is 2π. The phase profile $\Delta z(\theta)$ is a triangle-wave profile.

A vortex (m=3) has a spiral structure with 3 spiral threads, shown in Figure 5.2. To generate OAM number (m>3), providing that the number of spiral threads equals to the OAM, is to configure the phase change profile $\Delta z(\theta)$ as a saw tooth profile with the number of periods equal to $3 \times m$. By this method, every thread ramp imprints an azimuthally dependant phase change of 2π in an optical period λ. The MATLAB codes to demonstrate a laser beam with orbital angular momentum are presented in Appendix 1.

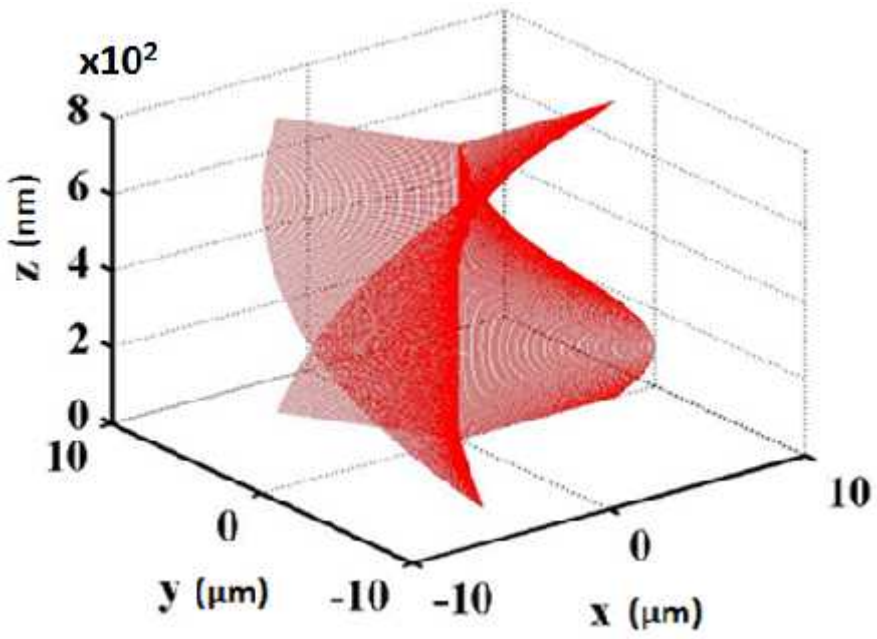

Figure 5.2. A vortex front with 3 spiral treads (m=3) over a period (λ).

5.2.2 Numerical study of intensity profile of laser beam with OAM

It has been discussed in Chapter 2 – theories and literature review. For optical vortex with integer m, the beams are centroid with a phase singularity, leading to a donut-like 2D intensity profile. Optical vortex carries orbital angular momentum (OAM) quantised to topological charge m. The electric field amplitude of optical vortex can be described theoretically by

$$E(r,m,\phi) = E_0\left(\frac{1}{\sqrt{m!}}\right)\left(\frac{\sqrt{2}}{\omega_0}r\right)^m \exp(-r/\omega_0)\exp(\pm i\quad) \quad (5.4)$$ [93].

where r is measured from the beam centre, m is the topological charge and ϕ is the azimuthal angle. Hence, intensity is given by

$$I(r,m,\phi) = E^*E = I(r,m) \quad (5.5)$$

as the complex spiral phase cancels. Setting m=0 gives the expected Gaussian intensity profiles. Plots of the Gaussian and vortex beam intensity profiles with $m_{2\omega} =$ 0, 2 and 4 based on the equation above were calculated. These profiles are shown in Figure 5.3 and consistent with those observed on Spyricon camera.

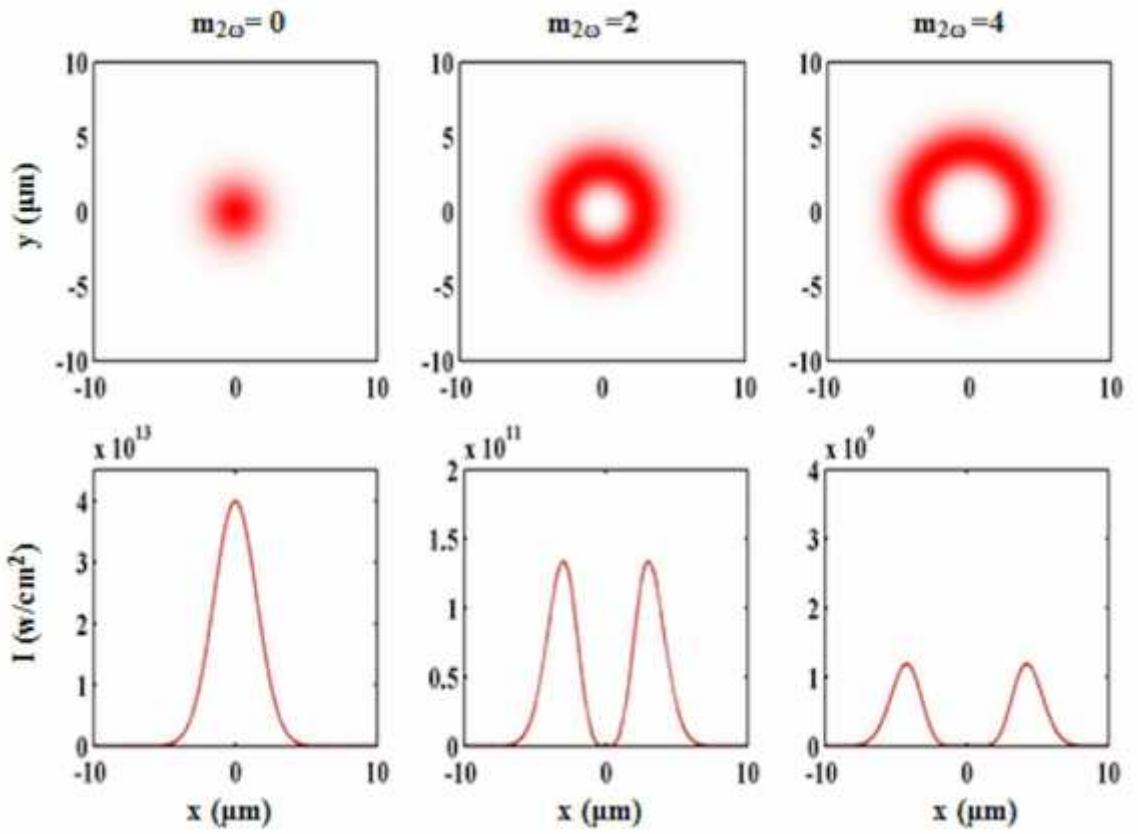

Figure 5.3. Calculated intensity distributions for Gaussian and Vortex beams (W/cm^2) when a 1μJ/ 170fs pulse at 387.5nm is focused with a 50mm lens.

Furthermore, $P = 2\pi \int |a|^2 r$. The following is the derivation process of the laser power. For simplification, the a_0^2 is ignored.

$$P = \frac{2\pi}{m!} \int r \left(\frac{2r^2}{r_0^2}\right)^m e^{\left(\frac{2r^2}{r_0^2}\right)} d = \frac{2\pi}{m!} \int r \left(\frac{2r^2}{r_0^2}\right)^m e^{\left(\frac{2r^2}{r_0^2}\right)} d\left[\left(\frac{\sqrt{2}r}{r_0}\right)\frac{r_0}{\sqrt{2}}\right].$$

r_0 is the beam waist. Here, $\frac{\sqrt{2}r}{r_0} = x$,

$$P = \frac{2\pi}{m!} \cdot \frac{r_0^2}{2} \int x \cdot x^{2m} \exp(-2x) d = \frac{2\pi}{m!} \cdot \frac{r_0^2}{2} \cdot \frac{1}{2} \int x^{2m} \exp(-2x) dx^2 \quad (5.6)$$

Similarly regard x^2 as s,

$$P = \frac{\pi r_0^2}{2m!} \int s^{m+1-1} e^{(-s)} d = \frac{\pi r_0^2}{2m!} \cdot m! = \frac{\pi r_0^2}{2} \quad (5.7)$$

From the above equations, we can see that the laser power remains a fixed value, a_0, the same r0. If the maximum amplitude filed value is wanted, just take the derivative of Equation 5.6 and ignore the coefficient of the equation, we can obtain

$$\frac{d\ (r)}{d} = \left(\frac{\sqrt{2}}{r_0}\right)^m \left[m r^{m-1} e^{\ } \left(-\frac{r^2}{r_0{}^2}\right) + r^m e^{\ } \left(-\frac{r^2}{r_0{}^2}\right)\left(-\frac{2r}{r_0{}^2}\right)\right] = \frac{m}{r} - \frac{2r}{r_0{}^2} = 0$$

Therefore, we can get the maximum point

$$r_m = r_0\sqrt{\frac{m}{2}} \quad (5.8)$$

Substituting this equation in Equation 5.6, we can get the maximum amplitude value

$$P_m \quad = a_0 \frac{1}{\sqrt{m!}} m^{\frac{m}{2}} \exp\left(-\frac{m}{2}\right) \quad (5.9).$$

Referring to the simulating results, it suggests that laser beam will get a donut intensity profile with a singularity in the centre. The higher order, m number, leads to a larger radius which expect to exert larger mechanical torque.

5.2.3 Harmonic orbital angular momentum conversion

Conservation of OAM during harmonic conversion infers that hence when $m_{2\omega}$ is integer, the LG ring mode was observed. A concept schematic is shown in Figure 5.4. Different Z-plane images, shown in Figure 5.5 (a) - (h), of the intensity distributions were observed on a Spyricon camera for the Gaussian and spiral beams with integer and fractional m. A thin film pick-off (*10*%) combined with a *750*mm focal length lens provided observation of the mode at the focus plane of the lens. This is satisfactorily shown to be the case in (c, f, g, h). In contrast, cylindrical symmetrical is broken with a reversed C shape, presented in Figure (b, d). The non-uniform around the rings comes from slight wavefront aberration most likely due to interference from the phase jumps in the CGH near *0* and 2π and beam astigmatism, apparently in (a). Note that images have been rescaled to fit.

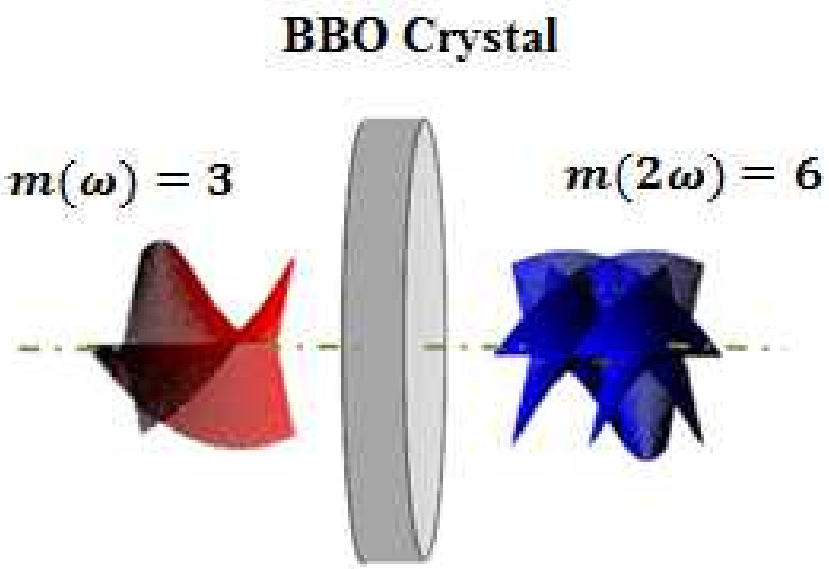

Figure 5.4. Optical vortex (m=3) exhibits helical wavefront.

The effect of adding OAM on focused intensity distribution was first investigated at 387.5nm through micro-structuring of a polished steel sample with an f = 150mm focal length lens. By setting m_{ω}^{775} = *0.3, 0.5, 0.7* and 1.0, the observed patterns structured at 387.5nm on the polished metal surface are shown in Figure 5.7. If OAM is conserved, then after frequency doubling, $m_{2\omega}^{387.5} = 2m_{\omega}^{775}$ and only when $m_{2\omega}^{387.5}$ is integral would we expect to see the LG ring structure.

Referring to Figure 5.8, ring structures when $m_{2\omega}^{387.5}$ = *1, 2* whereas, for $m_{2\omega}^{387.5}$ = *0.6* and *1.4*, this is not the case. This simple experiment with low levels of OAM supports conservation of OAM during SHG, yielding to

$$m_{2\omega} = 2m_{\omega} \quad (2.18).$$

However, there clearly remains some residual wavefront aberration on the beam, likely due to the known slight astigmatism of the output laser beam and phase discontinuity of the 0-2π transition in the CGH. When $m_{2\omega}^{387.5}$ is integral, the expected LG ring mode appears, supporting conservation of OAM during harmonic conversion, peak energy=~*4.8*μJ, exposure time=*0.1*s.

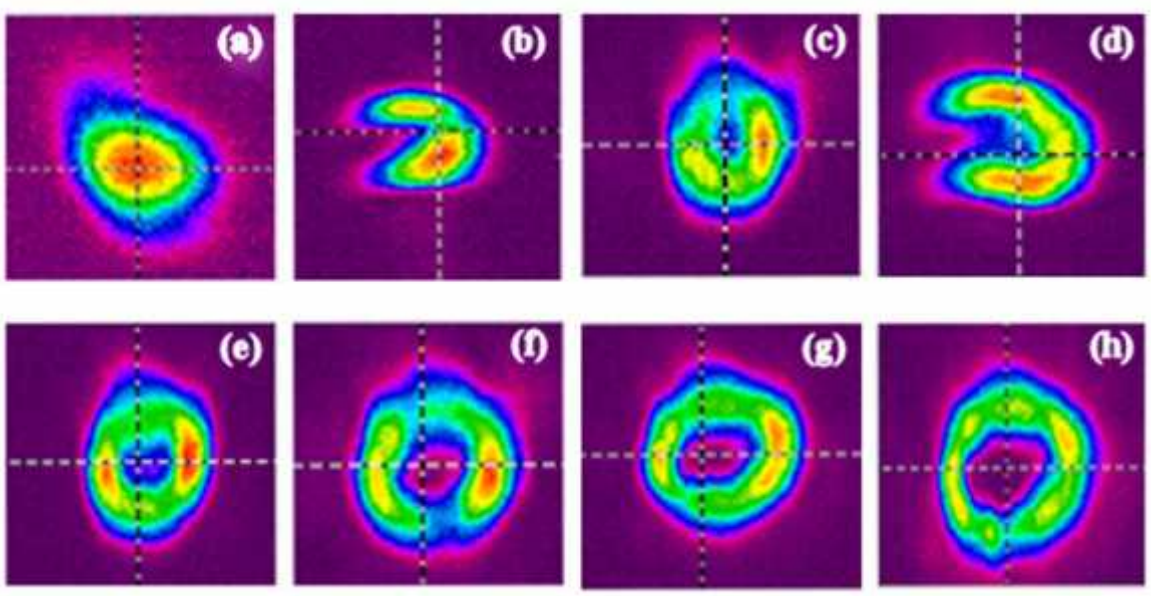

Figure 5.5. Far field intensity distribution observed at *387.5* nm on Spricon camera. Ring structures are clear when $m_{2\omega}$ are integer, indicating conversion of angular momentum during SHG.

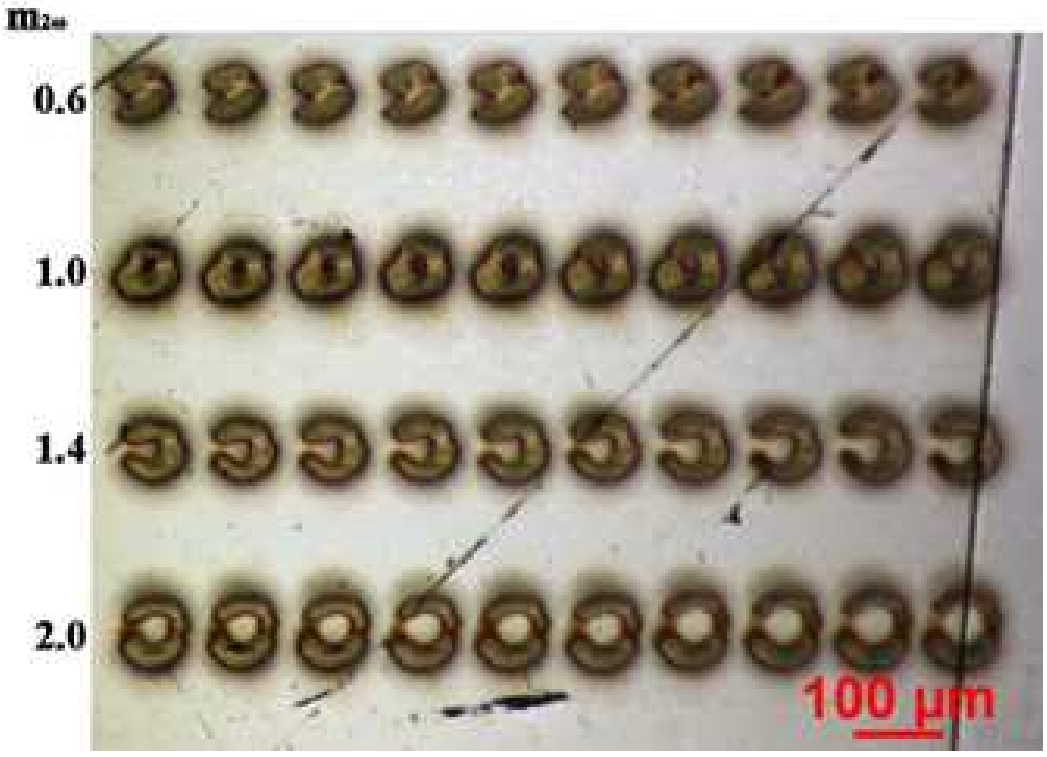

Figure 5.6. Optical micrograph of steel surface ablation (N=100 pulses/spot) at the focal plane of a 150mm focal length lens using spiral beam with $m_{2\omega}^{387.5}$ = *0.6, 1.0, 1.4, 2.0.*

5.2.4 Machining

The setup for surface structuring on stainless steel substrate (S/S 321) using laser beam with OAM is shown in Figure 5.7. The incident light (λ_{775}) is modulated by a LCOS SLM become a cylindrical vortex beam with OAM number varied from *1, 2, 3…*to *8*. After frequency doubling, the OAM number become an even series varied from *2, 4…*to *16*. The focusing optics is a microscopic lens (THORLABS LMU-20X-NUV) which has an effective NA *~0.4* for λ_{387nm}. Peak power is 150 ± 1 mW. Exposure time is 30 ± 0.001 s, which is controlled using a mechanical shutter (NEWPORT 846 HP). Stainless steel substrate is mounted on a 3-axis motion control stage (Aerotech AC3200). By the motion in z or y direction of substrate, laser machining can be engaged along the vertical direction (z) or horizontal direction (y). By the motion in x direction, the focus plane can be shifted from near side to far side and vice versa.

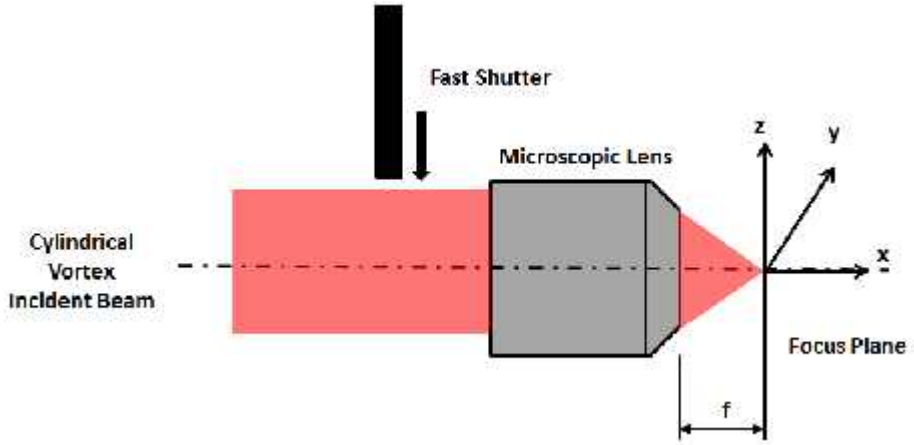

Figure 5.7. Focusing of a cylindrical femtosecond laser beam with orbital angular momentum.

Figure 5.8 presents the microscopic results of surface machining using femtosecond vortex beam. Each rows from left to right regard the substrate surface moving 5μm forward in x direction from near side to far side and passed the focus plane. Each columns regard to a OAM number. The column which is enclosed with blue square regards the pattern on focus plane.

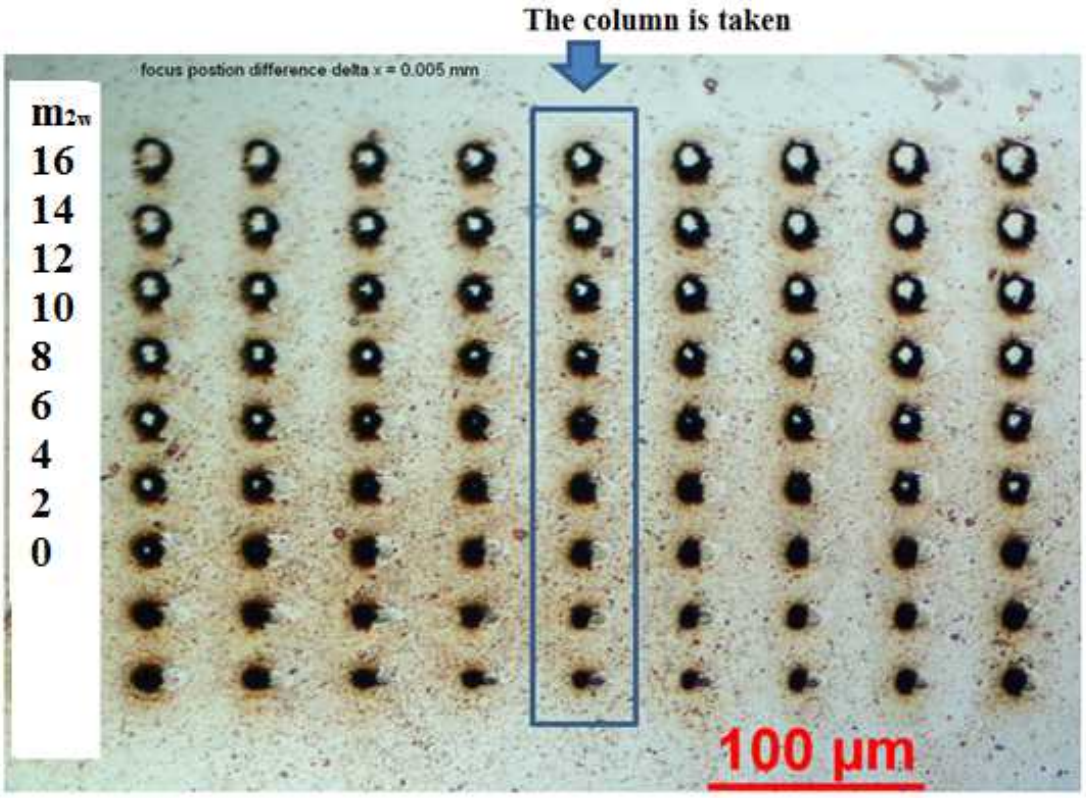

Figure 5.8. m = *0,2,4,6,8,10,12,14* and *16*. Material – stainless steel (S/S 321). Microscopic lens ~ 0.4 NA at λ_{387}. Ep =150±1mW, Exposure time 30s.

Figure 5.9 presents both of simulating results and machining results. The simulating results comes from calculation using Eq. (5.8)

$$r_m = r_0\sqrt{\frac{m}{2}} \quad .$$

The r_0 is ~ 11.2 which is radius of focus spot of a Gaussian beam, measured in Figure 5.8. The fitting line (dash line) of simulating results exhibit a large deviation, especially in higher order mode (m>4), from experimental result (solid line). Experimental sample spot can be still fitted with exponential function however the index is lower to 0.2.

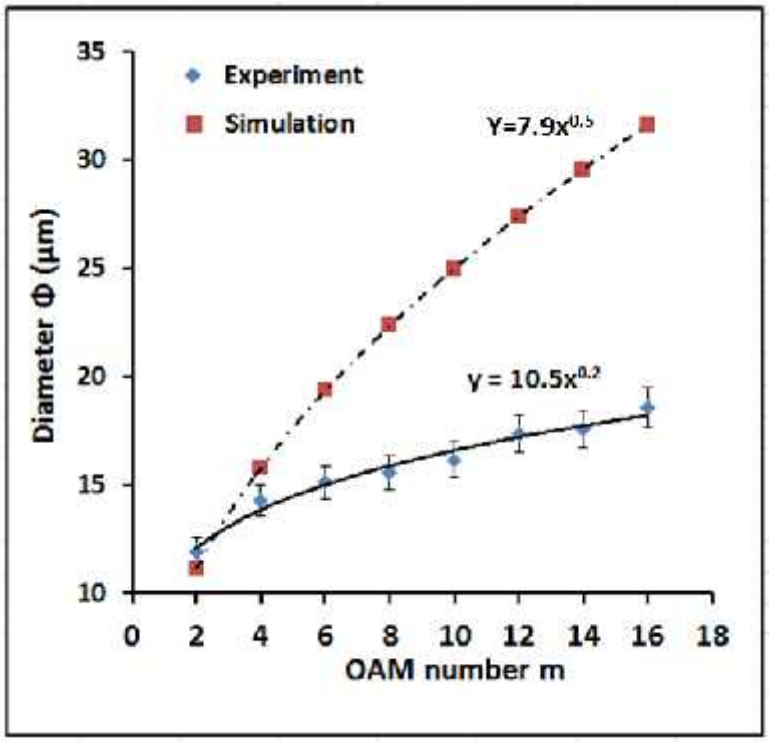

Figure 5.9. Large deviation regarding to m> 4 suggests high-order components were removed in second harmonic generation and the decrease of effective NA number.

When m> 0, the collimated beam become a defocusing beam in front of BBO crystal. The defocusing will lead to two problems. High order components are blocked by the physical aperture size of second harmonic generation (SHG) optics. The second problem is the decrease of effective NA number.

It is observed that the diameter of all ring modes is varied to focus plane and OAM number. It easy to understand that ring with large radius can exert more mechanical torque on a target. If using a ring mode off focus plane, it can be expected to drive a single particle with more torque however in the case of material twisting there is more material contained in exposure area. The result suggests in twisting processing, focus-plane processing and a lens with high NA are preferred.

5.3 Femtosecond vector beam

Figure 5.10 schematically demonstrate vector-beam generation. An advanced optics, called as S waveplate, is used to spatially tailor optical vector field, generating fs vector beam with plane wave front [227]. Rotating the S-waveplate to angles (θ) within the range of ±90° can generate radial (0°) and azimuthal (90°) and tailored spiral (intermediate angle) polarization.

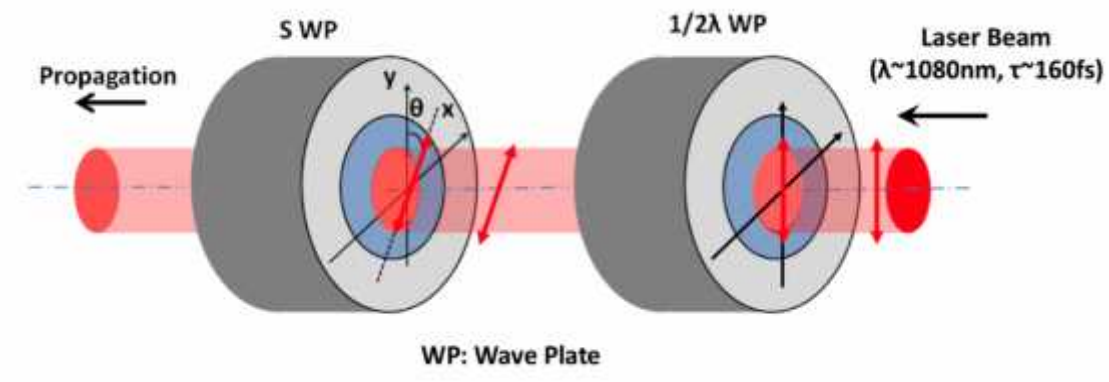

Figure 5.10. Schematic presents the generation of vector beam using S-waveplate. A half waveplate is used to rotate incident linear polarization 45° in clockwise.

The generated vector beam can be considered as partially linear-polarized light which is a fraction of total light in term of degree of polarization. The polarization modulation of the S waveplate was investigated with the experimental set-up shown in Figure 5.10. The laser beam with vertical linear polarization was rotated to the s waveplate with a ½ λ waveplate. The S-waveplate can convert linear polarization to AP and RP.

The vector beam was then analysed by a Glan laser analyser. The transmitted components were measured with a peak energy sensor. The figure 5.12 shows the variation trend of two polarization state: horizontal linear polarization (|H>) and vertical linear polarization (|V>). There is *45*î change between the points of two interact points or peak/valley points. It is notable that corresponding to the peak/valley spot is highly linear with degree freedom.

$$P = \frac{I_m - I_m}{I_m + I_m} \sim 1.$$

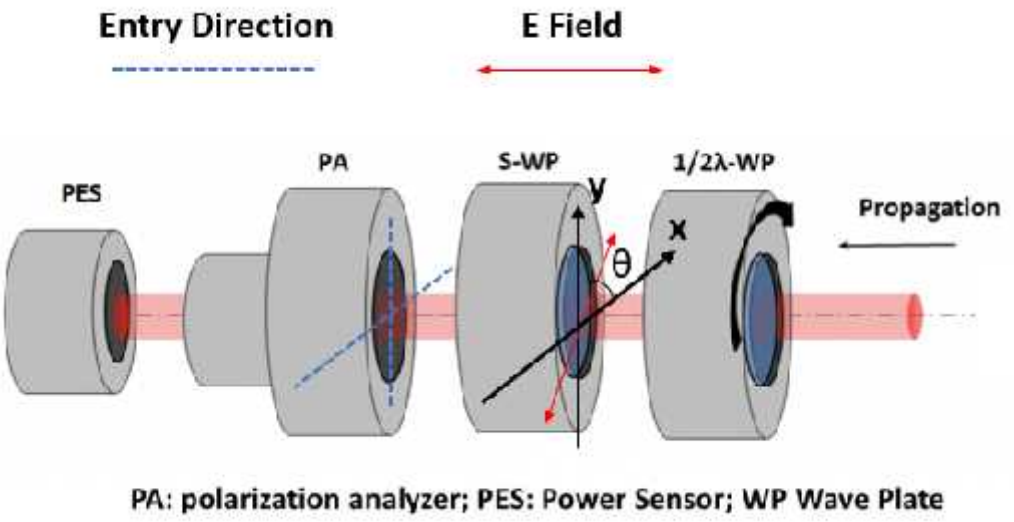

Figure 5.11. Optical set-up used to analysis polarization purity of vector beams generated by S wave plate. The entry direction of PA is put in horizontal or vertical directions.

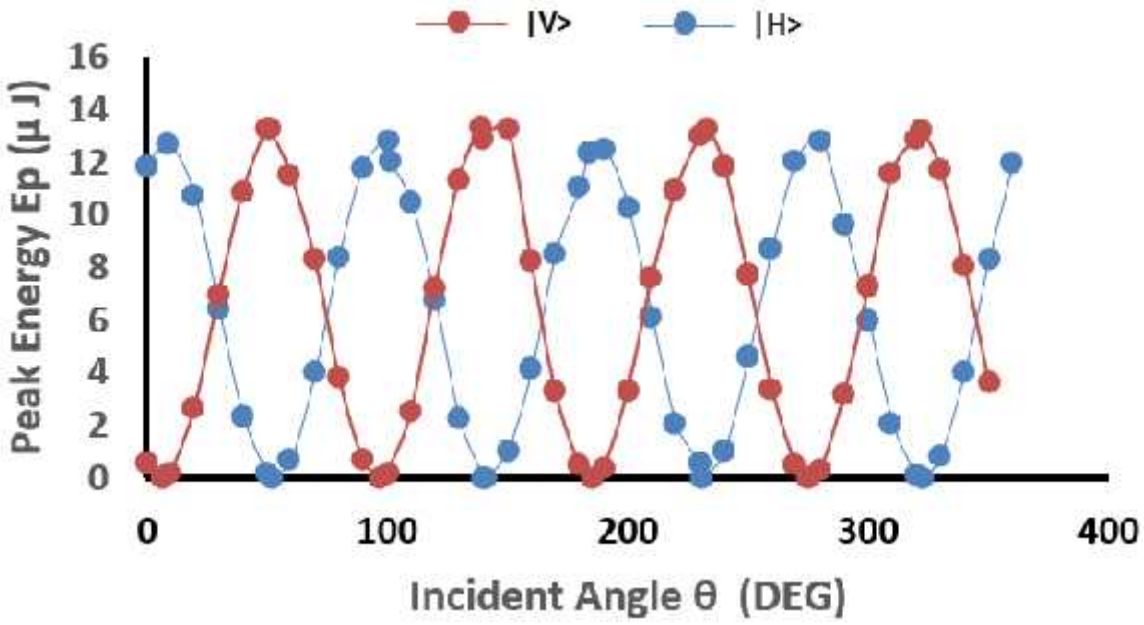

Figure 5.12. Linear polarization purity of vector beam generated by S wave plate regarding to incident angle ranged from *0º* to *360º*.

Where I_m and I_m refer to the intensity of the light transmitted through the Glan laser polarizer when the ½ λ waveplate is rotated through a full range of 360 degree. These patterns also confirm the linear polarization purity to be excellent. Polarization state of output beam are azimuthal and radial when incident angle of ½ λ wave plate is at *22.5º, 67.5º… 337.5º*, instead of linear polarization when the incident angle is *0º, 45º…360º*.

In addition, a beam profiling system was set up to study the vector beam. Figure 5.12 presents the system. A fused silica glass is reflected a focused sampled beam into a CCD camera. The focusing optics is a fused silica singlet lens with focus length 300 mm. The incident angle is close to Brewster angel ($\beta \approx 56°$) and only the s-polarised light is reflected [228].

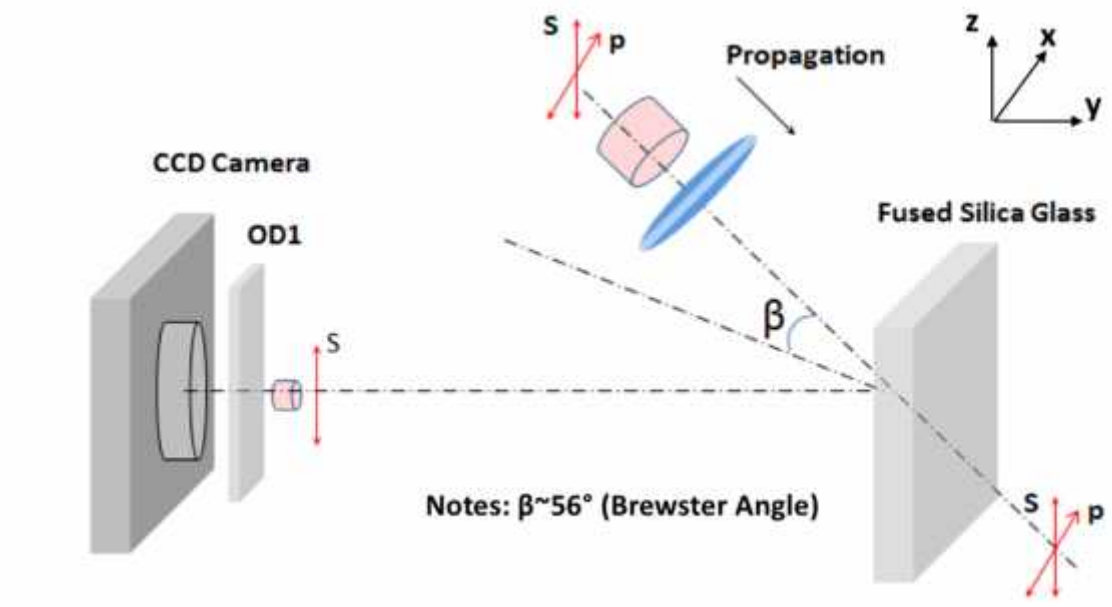

Figure 5.13. Schematic presents only S-polarized light was profiled by a CCD camera.

Figure 5.14 shows the measured intensity profiles when translating the CCD camera in the vicinity of the lens focal plane. These RP and AP beams have a symetrical double-lobe intensity profile as only the s-polarised light is profiled. It is noteable that there is a polarization singularity in the centroid. The profile has an approximately elliptical shape with the long axis of the ellipse dependent on the incident polarization, i.e. vertical (a) or horizontal (b) when the incident beam is radially or azimuthally polarized respectively.

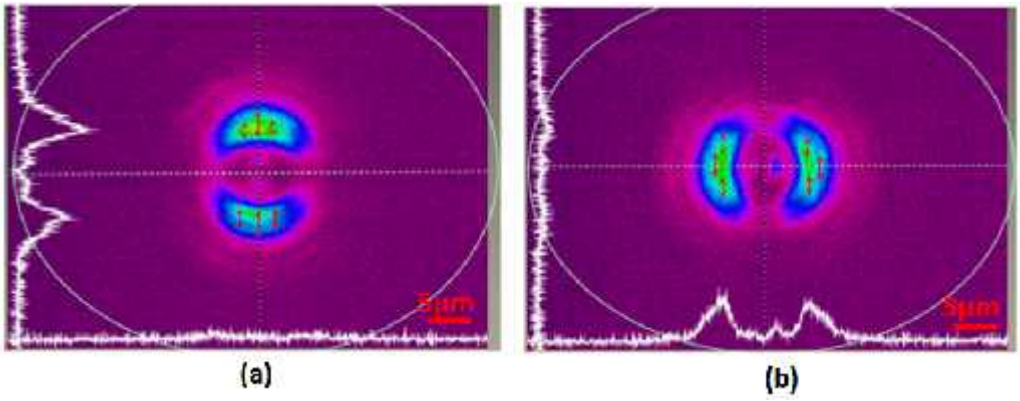

Figure 5.14. Near-field intensity profiles for focused vector beams with radial (a) and azimuthal polarizations (b).

LIPSS structures with annual, radial and spiral patterns are produced. Figure 5.15 shows optical microscopies of LIPSS patterns on the ablation spots structured with AP and RP beams in neighbouring of focal plane. The LIPPS, which have an annual structure with a pitch Λ~1μm maintains their orientation. Radial polarization produces circular LIPSS and azimuthal polarization produces radial LIPSS, entirely consistent with tailored polarization.

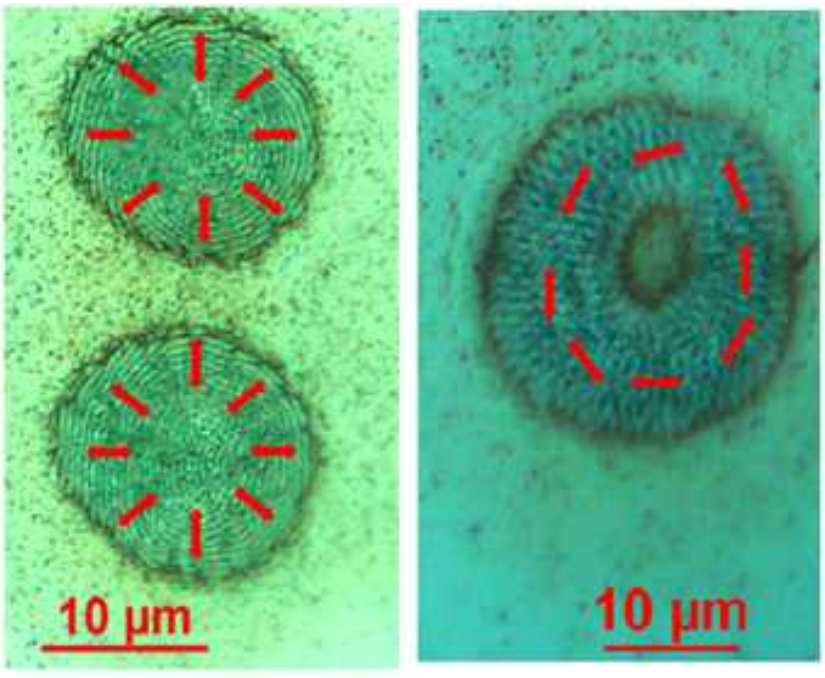

Figure 5.15. Optical images of LIPPS formation with the RP and AP beams when substrate translated through the focal plane.

The intermediate angle between -90° and 90 ° produced spiral microstructure. The spatial distribution of polarization is treated as orthogonal polarization state of azimuthal and radial constructing spiral vector fields.

Figure 5.16 (a) and (b) present LIPSS structure ($\theta = \pm 45°$) and exhibit the fits around edge and inner area to these spirals are satisfying to [195]

$$r(\phi) = ae^{k} \quad (2.22).$$

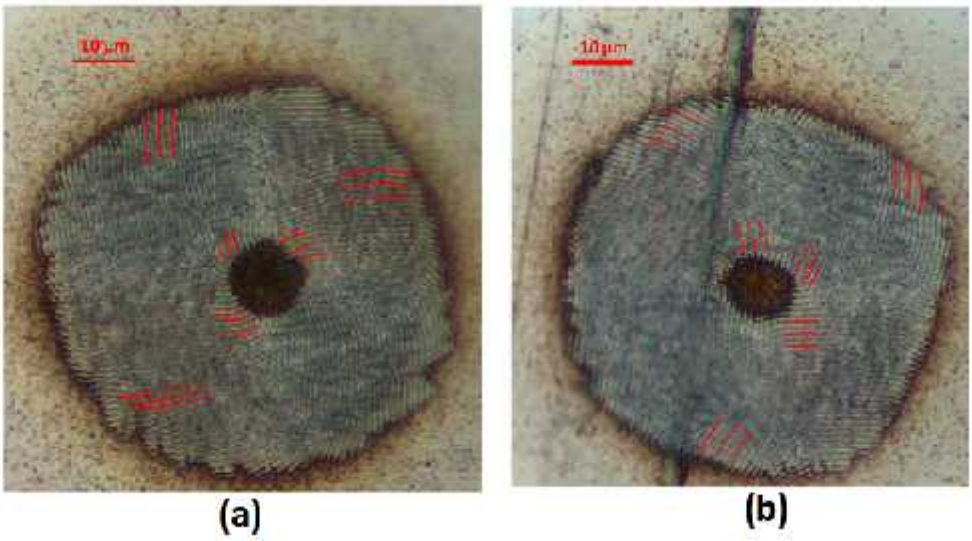

Figure 5.16. (a) -45° and (b) +45°. Microscopic image of Plasmonic patterns structured with spiral vector fields when θ = -45° (a) and +45° (b) and 0.5 mm above focal plane.

5.4 Bulky modification in PMP using vortex beam

5.4.1 Effects of OAM on filamentation in PMP at low NA

Filamentary modifications inscribed with Laguerre-Gaussian beams carrying OAM with are shown in Figure 5.17. The helical beams focusing from the right clearly show evidence of converging ring like cross sections, whose diameter, as expected, increases linearly with m, most evident in the case of $m_{2\omega}$=2. The Gaussian beam filament (top) is shown for comparison showing self-guidance propagation.

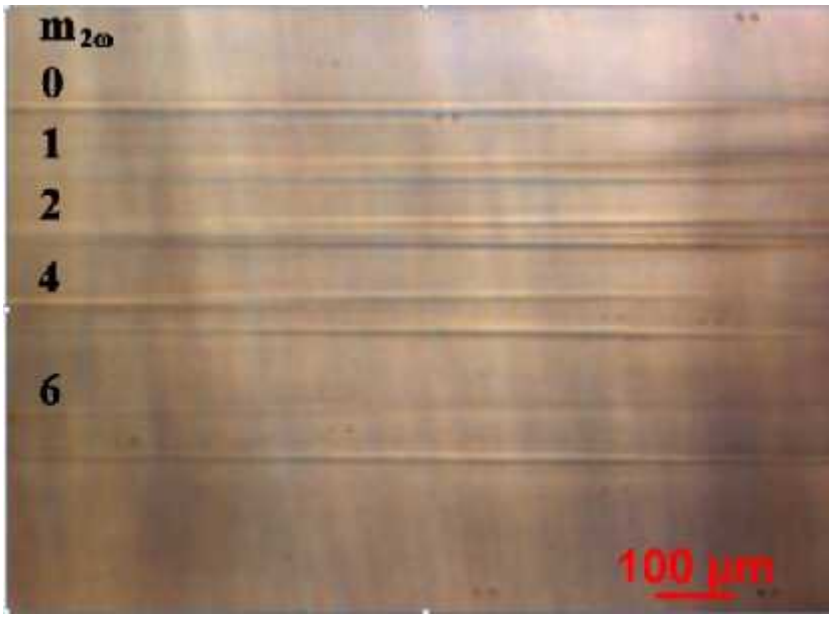

Figure 5.17. Low NA transverse inscription at λ = 387.5nm with spiral beams carrying OAM, $m_{2\omega}^{387.5}$ = 1, 2, 4, 6 with constant pulse energy E_p = 2μJ.

5.4.2 Low NA inscription with spiral beams carrying both OAM and SAM

For interests to know the relevance of SAM (S) and OAM (m) in the light-matter interaction, the addition of spin angular momentum (S = ±1) to beams with topological charge $m_{2\omega}$ = 0, ±2 were investigated. Figure 5.18 shows filamentary cross sections observed at low NA with linearly and circularly polarised Gaussian and LG beams. Total angular momentum therefore ranges from 0 to ±3h/π per photon. Linearly polarised filaments always start nearer the laser source, and as topological charge m increases, these recede inside the material. The circularly polarised filaments start deeper in the material for each OAM state with no difference between right and left hand polarisations. Hence, in this regime, no coupling between OAM and SAM is observed. The stronger coupling with linear polarisation, however, is likely a consequence of self-focusing (SF), dependent on the third order susceptibility $\chi^{(3)}$ which has two components with linear but only one with circular polarisation [229]. It was previously observed such an effect in PMMA but only with polarised Gaussian beams by Ye and his co-workers in 2013 while not published. To the author knowledge, this is the first observation of filamentation in a pure polymer with polarised spiral beam

Table 5.1: Processing parameters of low NA inscription.

Ep	~0.7μJ
Polarization	linear, circular
Scan Speed	1 mm/s
$m_{2\omega}^{387.5}$	0, ±2
J	0, ±1, ±2, ±3

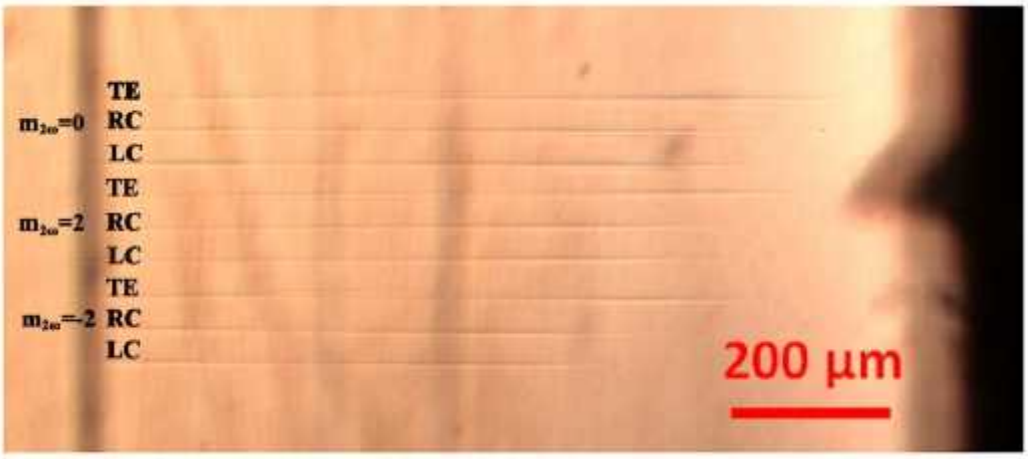

TE: Linear polarization with transverse electric field, RC: right chirality circular polarization, LC: left chirality circular polarization.

Figure 5.18. Optical image of low NA filamentary in side view. There is no effect of coupling between OAM and SAM (RCP and LCP) at low NA but linearly polarised states (TE) couple stronger than circular (RCP and LCP), consistent with third order susceptibility higher with linear than circular polarisation.

Figure 5.19 indicates an identical super-continuum spectrum observed in PMP, generated in this case using spiral beam with $m_{2\omega} = 4$ and extending from *340-500* nm. The intensity modulation either side of the laser wavelength *387.5*nm arises because the dielectric coating reflectivity varies outside of its design bandwidth centred at 387.5 nm (*45*î) in this geometry.

Detailed spectra collected with increasing $m_{2\omega}$ are shown in Figure 5.20. Note the significant broadening of the peak at *387.5*nm to around $4nm_{FWHM}$ and the broad anti-Stokes continuum peaking around *360* nm. The SC signal reduces throughout as topological charge $m_{2\omega}$ in increased from 2 to 8. The inset shows the detailed SC signal measured on the anti-Stokes side from *350-370*nm with background subtracted.

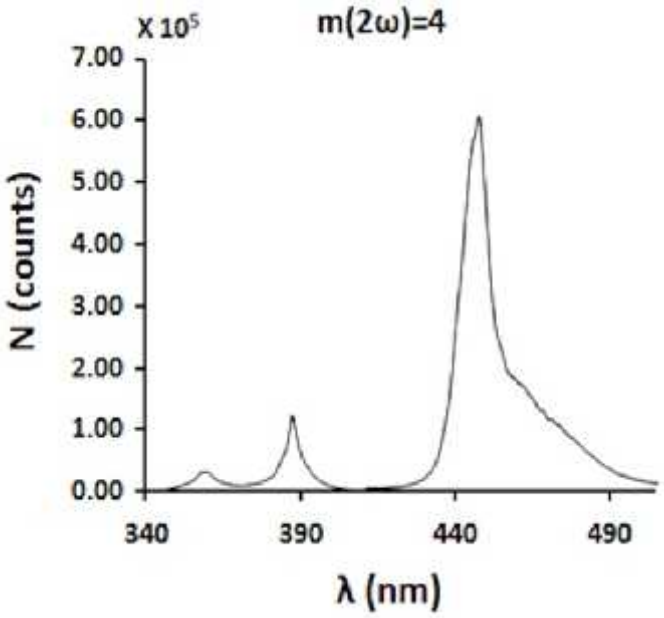

Figure 5.19. Typical SC spectrum (bluish continuum) excited at λ = 387nm covering the NUV to the visible with $m_{2\omega} = 4$.

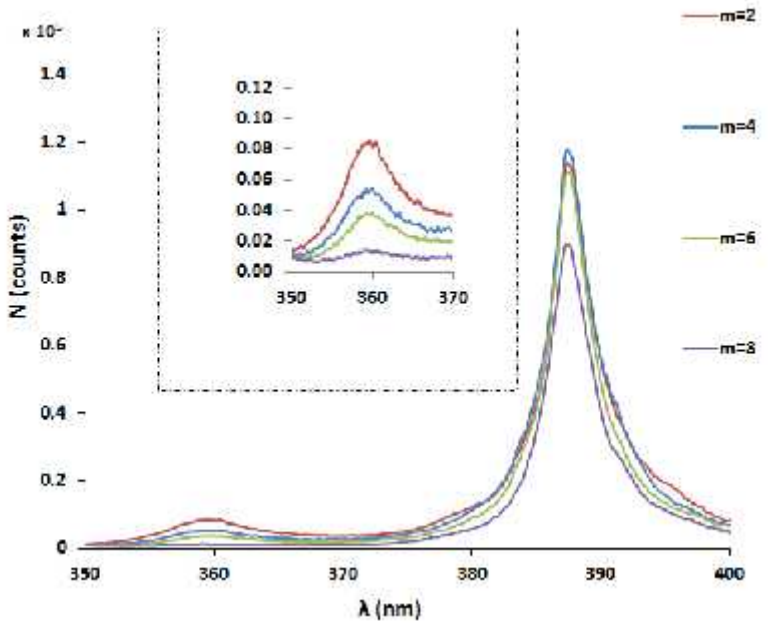

Figure 5.20. SC spectra for spiral beams with $2 \leq m_{2\omega} \leq 8$ over 350-400nm and expanded detail showing that the Anti-Stokes (and Stokes) intensity reduces with increasing $m_{2\omega}$, consistent with critical power rising with $m_{2\omega}$.

Integrated signals are plotted against topological charge $m_{2\omega}$ in Figure 5.26, showing a linear fit to topological charge $m_{2\omega}$. The threshold for SF of LG beams carrying OAM is expected to scale as $P_{th}^{m} = 2\sqrt{3}\ m\ P_{th}^{0}$ where P_{th}^{0} is the threshold for the Gaussian beam [201]. The fit here supports the linear scaling predict, however, the observed scaling factor is not 3.46 but 1.88 and the lower than expected theoretical scaling factor. The lower scaling factor is likelihood due to reduction of spectral signal when high OAM number is applied. In high OAM number case, reflective laser beam from SLM becomes more diffractive. The diffractive beam will lead to loss of laser energy. The observed anti-Stokes continuum, integrated over 350-380nm is shown with topological charge $m_{2\omega}$ in Figure 5.28. This reduces linearly and with $m_{2\omega}$ supporting the fact that increases linearly with $P_{c.}$ These show a difference in coupling due to polarisation dependent self-focusing, independent of the total angular momentum, orbital plus spin.

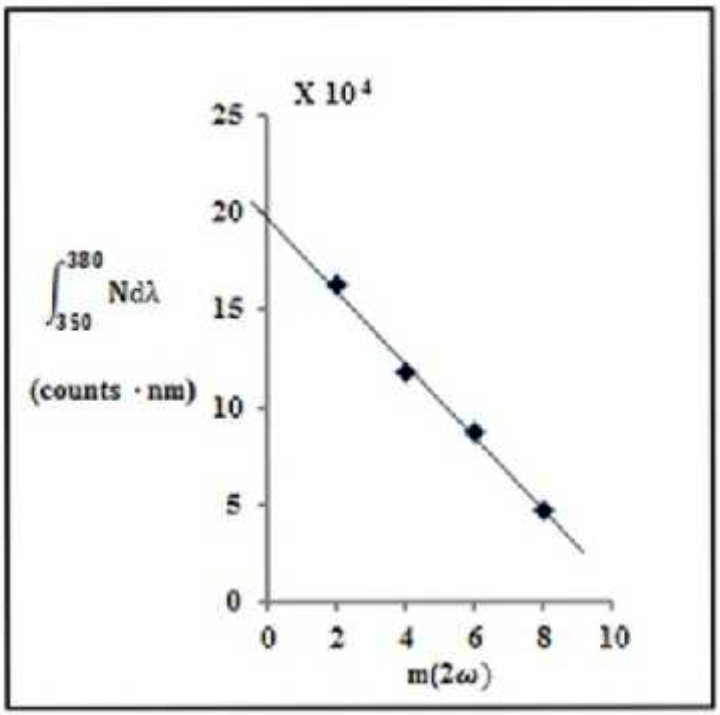

Figure 5.21. Near threshold integrated continuum signal over *350-380*nm for linear polarized spiral beams with $m_{2\omega}$ = 2,4,6,8. Linear scaling is clear indicating that critical power rises linearly with $m_{2\omega}$, showing a difference in coupling due to polarisation dependent self-focusing, independent of the total angular momentum, orbital plus spin.

5.4.3 High-NA inscription with high intensity spiral beams carrying OAM

In high-NA focusing inscription, super continuum cannot ignite. Figure 5.22 shows the optical image observed side view of ring structures inscribed in PMP a microscopic objective (Thorlabs - LMU-20X-NUV) with vortex beam. Focus distance below surface ~400µm. The converging ring cross section due to the LG mode is now apparent ahead of the focal plane and one gets the impression of a twist in the structure at the focal plane. The full convergence angle here is $\theta_{m=2}$ ~4.1°.

Table 5.2: Processing parameters of transverse scan with low pulse energy.

N.A.	0.4
Ep	$0.15 \leq E_p \leq 0.4\mu J$
$m_{2\omega}$[387]	2
Scan Speed	1 mm/s
Polarization	linear

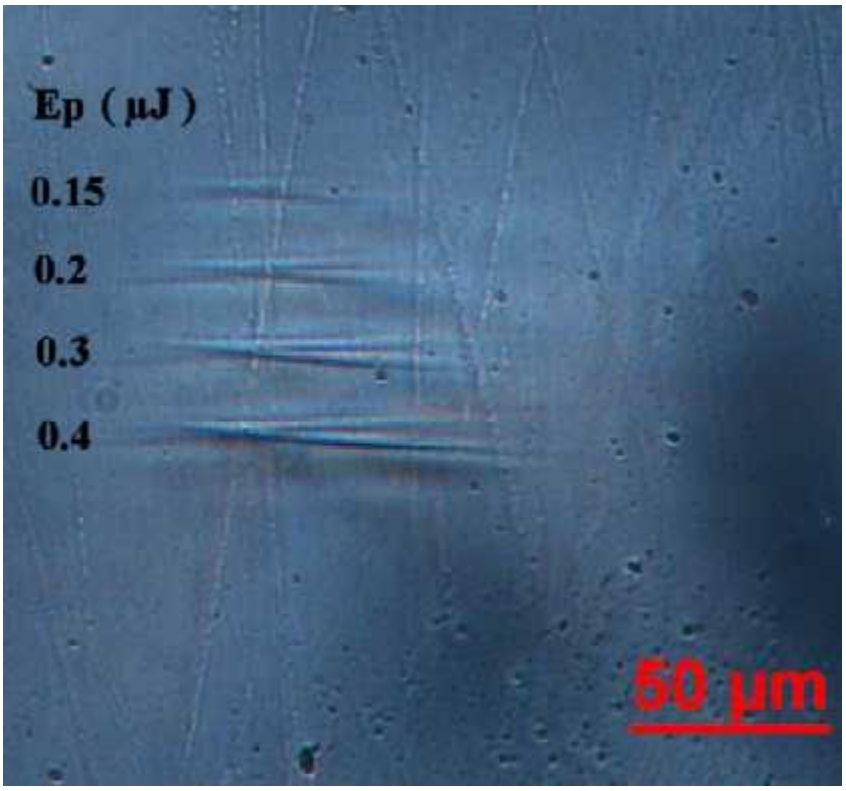

Figure 5.22. Transmission optical image of observed side view of ring structures inscribed transversely in PMP. Focus distance below surface ~400µm.

With higher pulse energies, much more complex filamentary structures were observed, resulting in a series of converging, filamentary modifications which develop further as pulse energy increased. Figure 5.23 shows inscription structure using transverse scan. Beyond the focus or minimum diameter, the light does not propagate more than 200µm, showing evidence of re-focusing phenomena. Maximum convergence angle here is θ ~7.9°. In a Kerr medium, beams carrying OAM can collapse into individual filaments with number $n \leq m_{2\omega}$ [230] which might also explain the complex incident structure. Note that the inner filaments appear close to the optic axis.

Table 5.3: Processing parameters of transverse scan with high pulse energy

N.A.	0.4
Ep	$1 \leq E_p \leq 5\mu J$
$m_{2\omega}$[387]	10
Scan Speed	1 mm/s
Polarization	linear

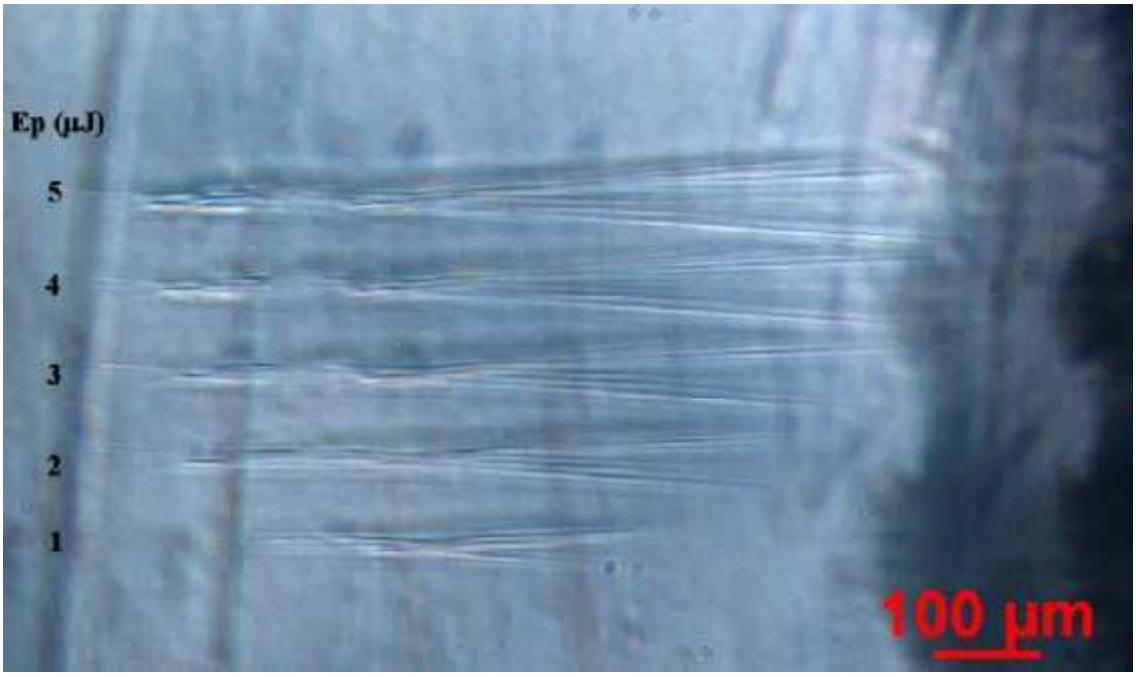

Figure 5.23. Complex filamentation with twisted beam carrying high OAM, $m_{2\omega}$ =10 when varying pulse energy from 1-5µJ

Modified cross sections along the optic axis show multiple filaments, when $m_{2\omega}$ = 6, Figure 5.24(a). As one approaches the focal plane, there is a clear counter-clockwise rotation of these filaments as one approaches the focal plane, (b). This rotation is a likely a consequence of the rotating wavefront associated with the OAM.

Table 5.4: Processing parameters of spotted exposure with NA ~0.4

NA	0.4
Ep	~0.1 µJ
$m_{2\omega}^{387}$	10
Exposure time	30ms
Polarization	linear

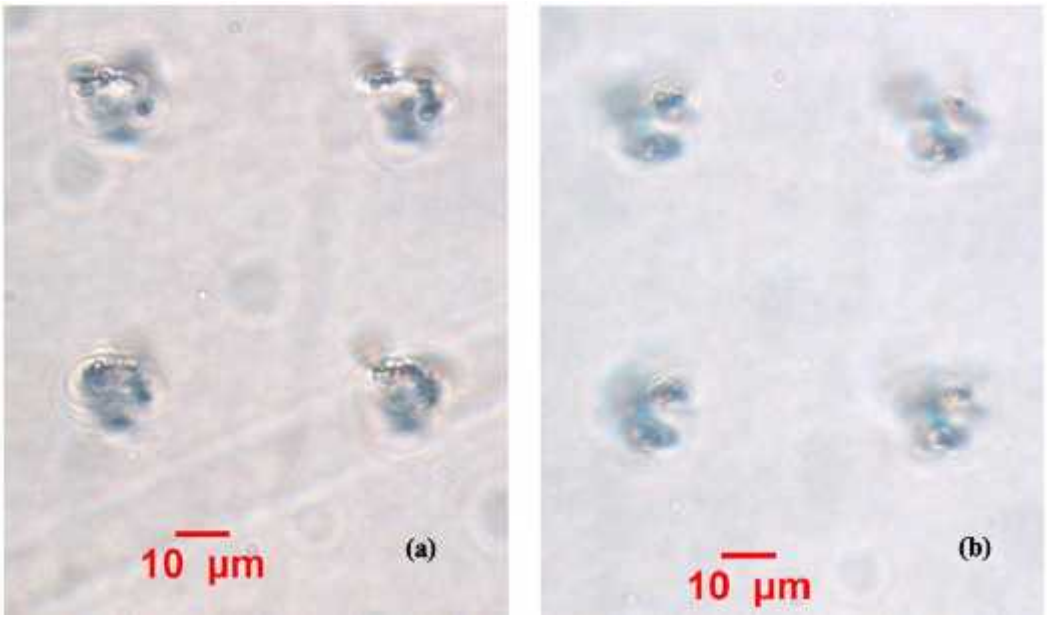

Figure 5.24. (a) Cross sections along optic axis of the filamentary modification in exposed PMP at 0.4NA showing multiple filaments near focus (b) rotation of the two strongest filaments counter-clockwise with increasing depth, relative to (a).

With NA increased further to *0.7*, PMP was exposed just below the surface with the spiral beam, $m_{2\omega}$ = 10 while also varying pulse energy. An optical image (transmission) of the modified cross- section along the optic axis is shown in Figure 5.25(a). Pulse energy was varied from *0.3-0.5*µJ while exposure time was set at 50ms. At E_p =*0.3*µJ, light guiding can be observed at the centre with central core *1.5-2*µm diameter whereas, at *0.5* µJ, there is

evidence of several guiding regions, 22(b), and surrounded by a series of rings due to diffraction.

Table 5.5: Processing parameters of spotted exposure with NA~0.7

N.A.	0.7
Ep	0.3-0.5 µJ
$m_{2\omega}$[387]	10
Exposure time	~ 50ms
Polarization	linear

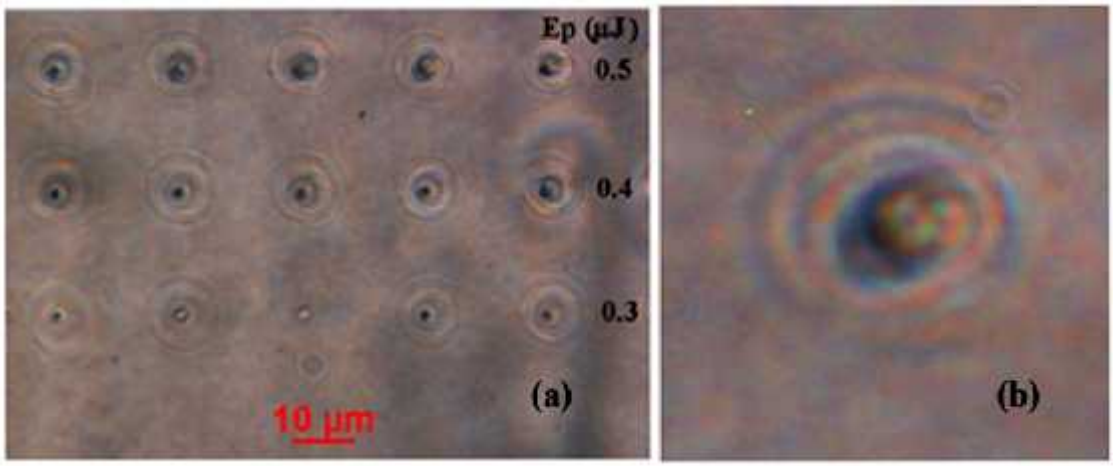

Figure 5.25. (a) Microscope image of modification cross section in PMP with OAM beams, $m_{2\omega}$ =10 while varying pulse energy from *0.3-0.5*µJ, exposure time = *50*ms, NA =*0.7*, (b) expanded image from (a) with E_P = *0.5* µJ showing multiple guiding regions. Surrounding rings are due to WL diffraction around the core.

At the highest NA = *0.7*, longitudinal "waveguides" were also inscribed and results shown in Figure 5.23. However, there is some optical breakdown in these due to the relatively long pulse length. The first thing to notice is that there is a clear difference in inscribed structures when reversing the wavefront helicity. The structures written with $m_{2\omega}$ = 10, shown in Figure 5.27(a), are round while inscribed structures with $m_{2\omega}$ = -10 interestingly show a twisted structure with a clockwise spiral not apparent with the opposite vorticity with m=+10. During absorption of light carrying OAM, angular momentum is conserved so that OAM transfer to the substrate results in a torque experienced by the atoms of the material [231]. If sufficiently strong, this torque could twist and displace material during exposure. Such OAM transfer has

been well demonstrated in the case of optical tweezers rotating micro-particles around the central vortex axis [89]. Here, at high NA with pulses able to break down the material, strong absorption can be expected as the plasma density rises beyond critical density, $n_e > 10^{21}$ cm^{-3} where the optical field of the incoming pulses can be strongly attenuated. As the melting point of this polymer is only *240*°C, rotation of the polymer material is quite possible. However, changing helicity should also reverse this effect but not apparent here.

Table 5.6: Processing parameters of longitudinal inscription

N.A.	0.7
Ep	0.5 µJ
$m_{2\omega}$[387]	±10
Scan Speed	0.5 mm/s
Polarization	linear

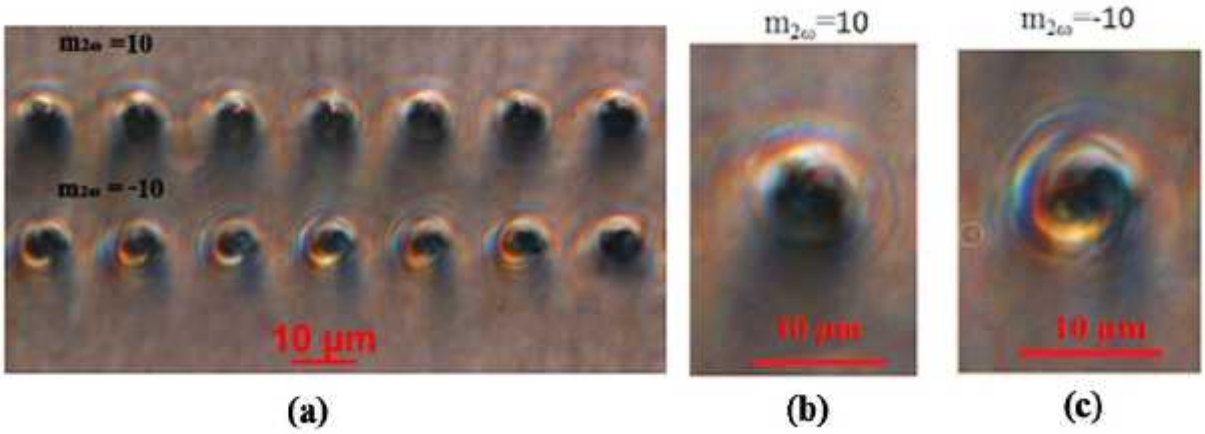

Figure 5.26. (a) Optical image (transmission) of micro-structures inscribed longitudinally along optic axis when $m_{2\omega} = \pm 10$, and longitudinal scan speed was 0.5mm/sec, (b) expanded structure from (a) with $m_{2\omega} = 10$, (c) expanded structure from (a) with $m_{2\omega} = -10$. The structure with $m_{2\omega} = -10$ shows a clockwise spiral, not apparent with the opposite helicity in (b).

Such a reversible twisting effect in a solid has been observed previously during CW laser exposure at *532*nm on the surface of an azo-benzene doped thin film polymer when exposed to spiral beams carrying OAM, m = ±10 and described as light induced spiral mass transport [112]. There, the spiral is clearly clockwise for m = -10 and confirmed beautifully with AFM images of the surface relief. The explanation of this effect, which reversed with helicity, did not appeal to OAM transfer but was explained in terms of interference of the transverse (Ex,

Ey) and longitudinal (Ez) electric field components, the latter appearing for very high NA > 1 focusing of spiral beams. The asymmetry observed here is likely due to residual wavefront aberrations with high OAM and incident beam which has astigmatism [89].

5.5 Summary

The numerical study of optical vortex yields 3-dimentsional spiral phase front. It was suggested the mechanical torque coming from the tangential component of line momentum which is normal to spiral phase front. The intensity profile of optical vortex in neighbourhood of focus has a LG pattern with radius given by $r_m = r_0\sqrt{\frac{m}{2}}$. The experimental results of stainless steel shows great deviation when high order OAM number are applied. It was suggested that the enlarging beam size are blocked by the aperture size of BBO optics.

Electric fields of 1064nm output wavelength from an OPA were manipulated to radial/azimuthal polarization and superposition states using a nano-structured waveplate. Characterized polarization is observed and shows the coherence quality of OPA beam.

Filamentary modifications using spiral phase beams carrying Optical Angular Momentum (OAM) is also investigated at *387.5*nm, observing the continuum created with increasing topological charge m. The anti-stokes signal, integrated over the region *350-370*nm drops in a linear fashion with increasing m, showing that critical power for these OAM states increases linearly with m and expected theoretically but scales as $1.88m_{2\omega}$ not $2\sqrt{3}m_{2\omega}$. Low NA filamentation with spiral beams having both linear and circular polarisations was observed for the first time in PMP. These show a difference in coupling due to polarisation dependent self-focusing, independent of the total angular momentum, orbital plus spin.

With high states of OAM, and high intensity, complex micro-structures are observed, converging to the focus were observed which can collapse to multiple filaments. The effect of rotation on the wavefront appears, resulting in rotated filamentary structures. At NA=0.7 and $m_{2\omega}$ = ±10, inscription cross sections show an asymmetry due to residual phase distortions when using such high OAM on a beam with a degree of astigmatism. While $m_{2\omega}$ = -10 shows a clockwise spiral, which could arise during OAM transfer to the material during strong absorption, this is not observed clearly for $m_{2\omega}$ = 10 due to asymmetry caused by wavefront distortions.

Chapter 6

250W ultrafast pulse (ps) handling with a spatial light modulator

6.1 Introduction

This chapter focuses on high-power tests at average laser power P >100W on liquid-cooled LCOS SLMs. Two SLM (Hamamatsu X-13139-03) operated at λ=1064nm, are investigated. A picosecond (τ~2ps) laser (Edge Wave) which can provide NIR (λ=1064nm) laser beam with average power maximum to 400W and repetition rate from 10kHz - 3MHz. The specific parameters of SLM devices, the laser system and SLMs have been introduced in Chapter 3.

6.2 Experimental Characterization

6.2.1 Thermal tests

Schematic of experimental set-up for high power thermal tests of cooled SLM (Hamamatsu X13139-03) is shown in Figure 6.1. The raw laser beam was expanded ×4, and reflected at low angle from the SLM to the power meter. A thermal camera (FLIR SC660) was positioned to detect heat radiated from the SLM chip and enclosure. The output beam located above an optical table was directed downwards by a 90° turning periscope which brought the beam to required level for the SLM. The beam was then expanded in a telescope (x4, f1=-50mm, f2=200mm, AR coated) before reflecting from the SLM at low angle of incident (AOI) < 10° and directed to an air-cooled power meter (Gentec UP55G-500F-H12), rated for 500W. A calibrated thermal camera (model FLIR SC660, sensitive from 8µm-15µm) was initially placed on a tripod at a distance of ~1m from the SLM and later brought closer to within ~0.4m for higher resolution images. It was possible also to take real time videos with this camera.

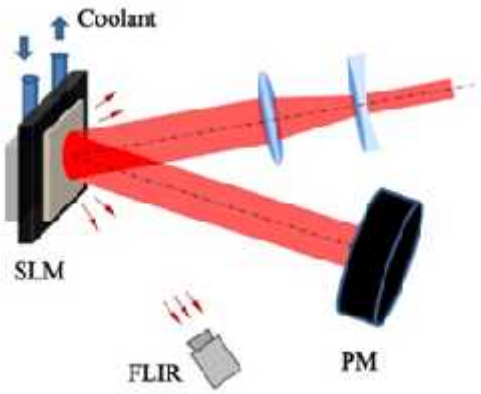

Figure 6.1.
Schematic of experimental set-up for high power thermal tests of cooled SLM (Hamamatsu X13139-03).

The two SLMs tested, -01 and -02, Hamamatsu X-13139-03, have Silicon substrate and fused silica front window with cooling assembly. The SLM product is designed for working in room temperature (~25°). The SLMs are exposure with high average power picosecond pulses were carried out using an FLIR camera to characterize thermal response. The infrared emissivity (ε) for Silicon and fused silica is respectively 0.73 and 0.93 [232], but it is observed that ε only played minor roles on absolute temperature measured. Figure 6.2 presents the temperature rise with exposure for device 1, has demonstrating a highly linear response with exposure power up to 140W. Device reflectivity R is quoted to be 0.97 by Hamamatsu. The thermal response coefficient is,

$$m_{\mathrm{U}} = \frac{T_m - T_r}{F_m} = 0.041°\mathrm{C/W}$$

which shows the SLM, device-01 has excellent thermal performance over this range for high average power picosecond pulses at 404Hz repetition rate. This test was done in the morning and the room temperature was 17°C.

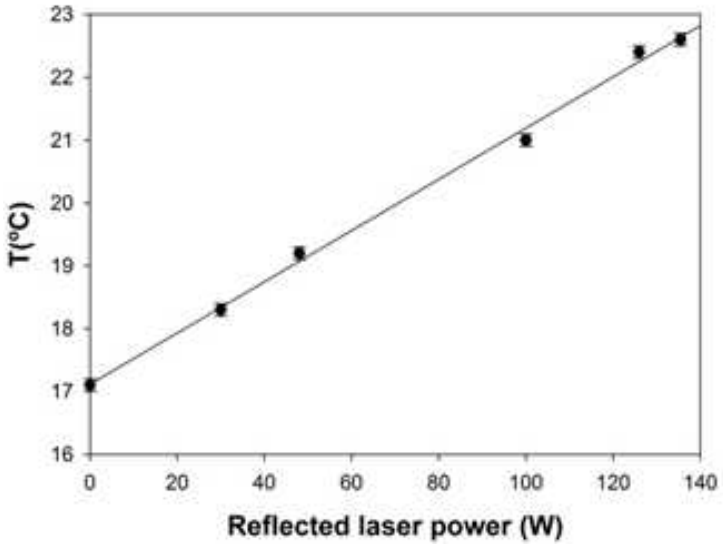

Figure 6.2. Measured temperature variation of device -01 to incident picosecond pulses with repetition of 404 kHz and up to 140W average power. Measured thermal response coefficient (m_0) is 0.041°C/W. Errors represent 1σ and fit is least squares with high confidence, R=0.99.

Figure 6.3 presents the measured temperature of device 02 response to power ranging from 50W to 215W average power. Ambient temperature was now T_0 = 21.8°C with a thermal response slope m_{02} = 0.026°C/W, a maximum exposure of 220W and temperature rise of only 5°C. This is a remarkable performance. The cooling efficiency of device -02 is 1.6 times higher than device -01. As device reflectivity R = 0.97 by Hamamatsu, the incident average power is 226W.

$$m_{02} = \frac{T_m - T_r}{P_m} = 0.026°\text{C/W}$$

The two linear responses relationship and further $\frac{d^2T}{dP^2} = 0$ implies that the effective absorption coefficient $\alpha$is a constant in the power range with effective LCOS chip cooling.

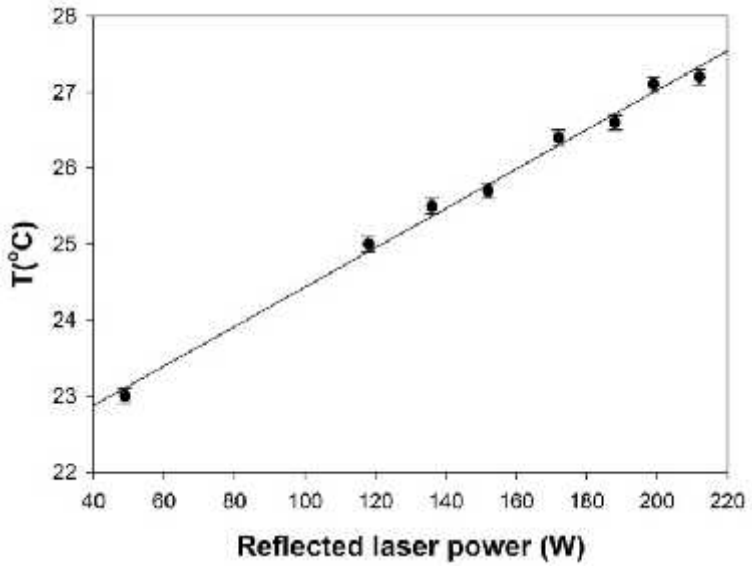

Figure 6.3. Measured temperature variation of device 02 response to incident picosecond pulses with repetition of 1MHz. Measured thermal response coefficient (m_0) is 0.026°C/W, significantly lower than device -01. Errors represent 1σ and fit is least squares with high confidence, R = 0.99.

A set of colour-coded thermal images corresponding to incident power range 0-220W are illustrated in figure 6.4 for SLM device -02. The laser beam centre is aligned to the centre of SLM, which shows higher temperature in 6.4 (b-f). In 3(e) at 215W, the centre of the chip is white, showing hot spot and a few degrees higher than the rest of the chip. It was concluded that a high power exposure combined with efficient cooling caused a temperature slope across the chip. When the 220W exposure was cut off, the measured chip temperature dropped promptly to ambient in 1-2 seconds. The prompt cooling temperature also indicates high thermal diffusion efficiency. The thermal diffusion efficiency is much higher devices without cooling. According to our previous work on Hamamatsu X-10468-04 (532nm) at ~8W exposure with a Gaussian beam showed a temperature rise ΔT ~2° or a thermal response of ~0.25°C/W. The performance is 10 times poorer than device -02. Note in figure 6.4 that the enclosure round the front window also showed a temperature rise, caused by vertically scattered light from the laser. As this is painted matt black, a few degrees rise was observed.

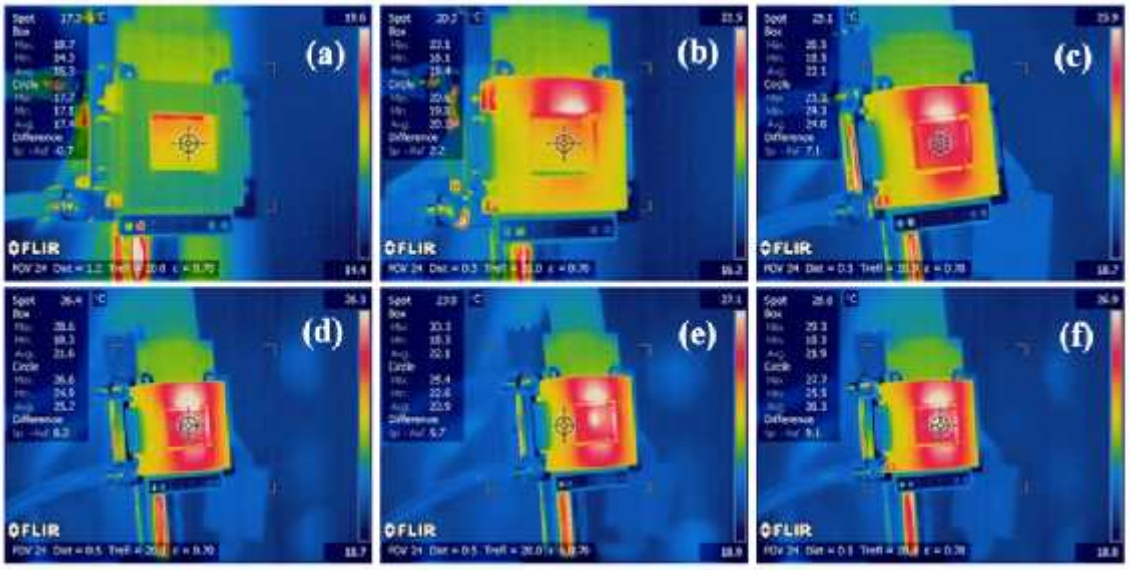

Figure 6.4. Infrared image of device 2 with increasing incident average power (a) P = 0, (b) $\langle P \rangle$ = 44W, (c) $\langle P \rangle$ = 118W, (d) $\langle P \rangle$ = 172W (e) $\langle P \rangle$ =215W, showing evidence of laser spot near the centre of chip, (f) $\langle P \rangle$ = 215W showing spot temperature T = 26.6°C. Note that there was some off axis low intensity scatter from the laser beam reaching the surrounding enclosure (matt black) hence showing a slight temperature rise above and below on this highly absorbing surface. Room temperature is ~ 20°.

6.2.2 Phase response

The phase response of the cooled SLM was investigated with the experimental set-up shown in Figure 6.5. The laser output was expanded x3 and linear polarisation rotated to on the SLM with a half wave plate (Altechna 2-CPW-TZ0-L2-1064). The SLM director was horizontal. A series of CGH's with grey level GL = 0-255(8bit) were applied using *"displayCombinedHologram U8"*, illustrated in Figure 6.6, so that the SLM now behaved as a variable waveplate (introducing a phase delay between the vertical and horizontal electric field components) hence reflected elliptical polarisations. By placing a quarter waveplate (Altechna 2-CPW-TF0-L4-1064) with fast axis at, reflected elliptical polarisation was re-converted to linear polarisation whose rotation axis depended linearly on the applied grey level CGH. This linear polarisation was then analysed by a thin film polarizer (TFP, Altechna 2-HC45TPF-1064-0254). The transmitted and reflected components were measured with air

cooled power meters, Gentec UP55G-500F-H12 (500W) and Gentec UP55N-300F-H12-DO (300W) respectively. The polarisation optics, which are ion beam coated have ultralow low absorption and ultrahigh damage thresholds, quoted as Fth > 20Jcm-2, single pulse with ns pulses [233].

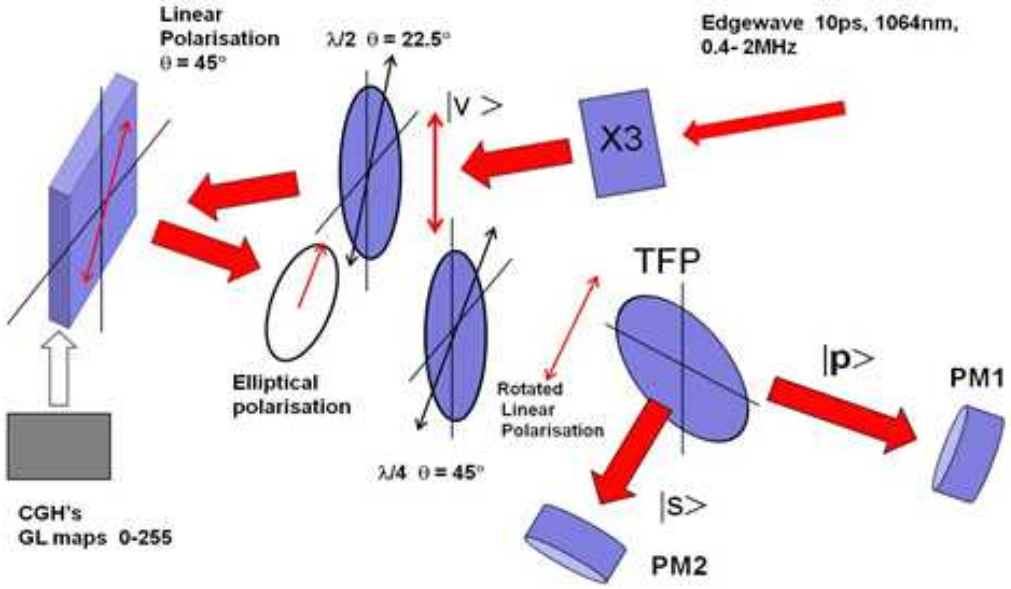

Figure 6.5. Optical set-up used to determine phase response of cooled SLM u polarisation modulation induced by Grey Level (GL) phase i applied to the SLM.

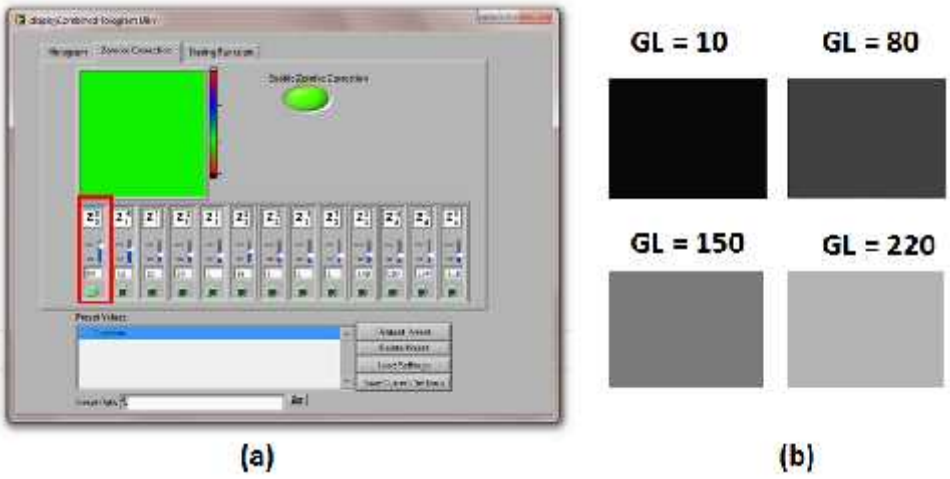

Figure 6.6. Grey-level (GL) adjustment using *"displayCombinedHologram U8"*.

The incident linear polarisation, after reflection from the SLM is right circularly polarised,

$$|R\rangle = \begin{bmatrix} 1 \\ -i \end{bmatrix} \quad (6.1)\ [117]$$

with phase difference $\phi = -\frac{\pi}{2}$ between electric field components. Using the Jones matrix for a $\frac{\lambda}{4}$ plate tilted at $\theta = 45°$ the resulting polarisation after traversing the $\frac{\lambda}{4}$ plate is given by

$$|\Psi\rangle = \begin{bmatrix} 1 & i \\ i & 1 \end{bmatrix} \begin{bmatrix} 1 \\ -i \end{bmatrix} = \begin{bmatrix} 2 \\ 0 \end{bmatrix} = 2 \begin{bmatrix} 1 \\ 0 \end{bmatrix} = 2\,|x\rangle \quad (6.2)\ [124]$$

which is linearly polarised in the horizontal direction while the effect on left circularly polarised

$$|L\rangle = \begin{bmatrix} 1 \\ i \end{bmatrix} \quad (6.3)$$

with phase difference $\phi = \pi/2$ yields vertically linearly polarised light, $|Y\rangle$. Hence, linear polarisation is rotated though an angle $\Delta\phi = \pi/2$ while the phase difference between the orthogonal states $|R\rangle$ and $|L\rangle$, $\Delta\phi = \pi$.

The rotation angle of linear polarisation after the waveplate is thus given

$$\Delta\theta = \Delta\phi/2. \quad (6.4)$$

If the linear polarisation now makes an angle θ with respect to the transmission axis of the polariser, which is horizontal, the transmitted (reflected) amplitude is given by

$$E_0 \cos\theta (E_0 \sin\theta) \quad (6.5)$$

while the transmitted (reflected) intensities are given by

$$I_0 \cos^2\theta (I_0 \sin^2\theta). \quad (6.6)$$

The transmitted (reflected) powers are hence given by $P_0 \cos^2\theta (P_0 \sin^2\theta)$, where P_0 is the incident power and ϕ is the phase applied to the SLM. This function has two maxima over 2π radian. This simple theoretical analysis assumes that the incident laser is highly linearly polarised (>100:1) and that the TFP has a high contrast, which is indeed the case, stated to be T_p / T_s > 1000:1 with wavefront error < λ/8 in the visible [234]. The blazing function of the SLM, supplied with Hamamatsu software is linear, so that $\varphi \propto G$.

The phase response for device-01 are illustrated in Figure 6.4 and Figure 6.5. The data are fit to 6th order regression polynomials. The sum of the measured laser powers (transmitted, P_1 and reflected, P_2 through polariser) by the two devices is indicated in Table 6.1.

Table 6.1: Totally reflected power

Device No.	PM_1+PM_2 (Watt)					
-01	7.5	21.8	37.8	78.8	91.1	132.5
-02	2.6	26.2	60.9	109	160	196

The laser powers (P_1 + P_2) are stable, and the error bars show one standard deviation. At lowest power, the power changes dependent on grey level (GL) are nearly sinusoidal functions and the sum of total powers are close to constant. The crossing points of P_1 and P_2 indicate the reflected polarizations are circular while the points at valley/peak indicate the polarizations are highly linear. There is a π phase change between the crossing points or peak/valley points.

Device 01 was mainly investigated phase response to power below 100W. The results show this identical phase response, provided laser powers are lower than 132 W. When the measured power is 91.1W, shown in Figure 6.4(e), the deviation from identical phase response starts to exhibit. In Figure 6.4(f) and Figure 6.5(e, f), the phase changes do not exhibit a π phase change. It is notable that in Figure 6.4(f) corresponding to 132.5 W the peak/valley spot is still highly linear with degree freedom

$$P = \frac{I_m - I_m}{I_m + I_m} = 0.93$$

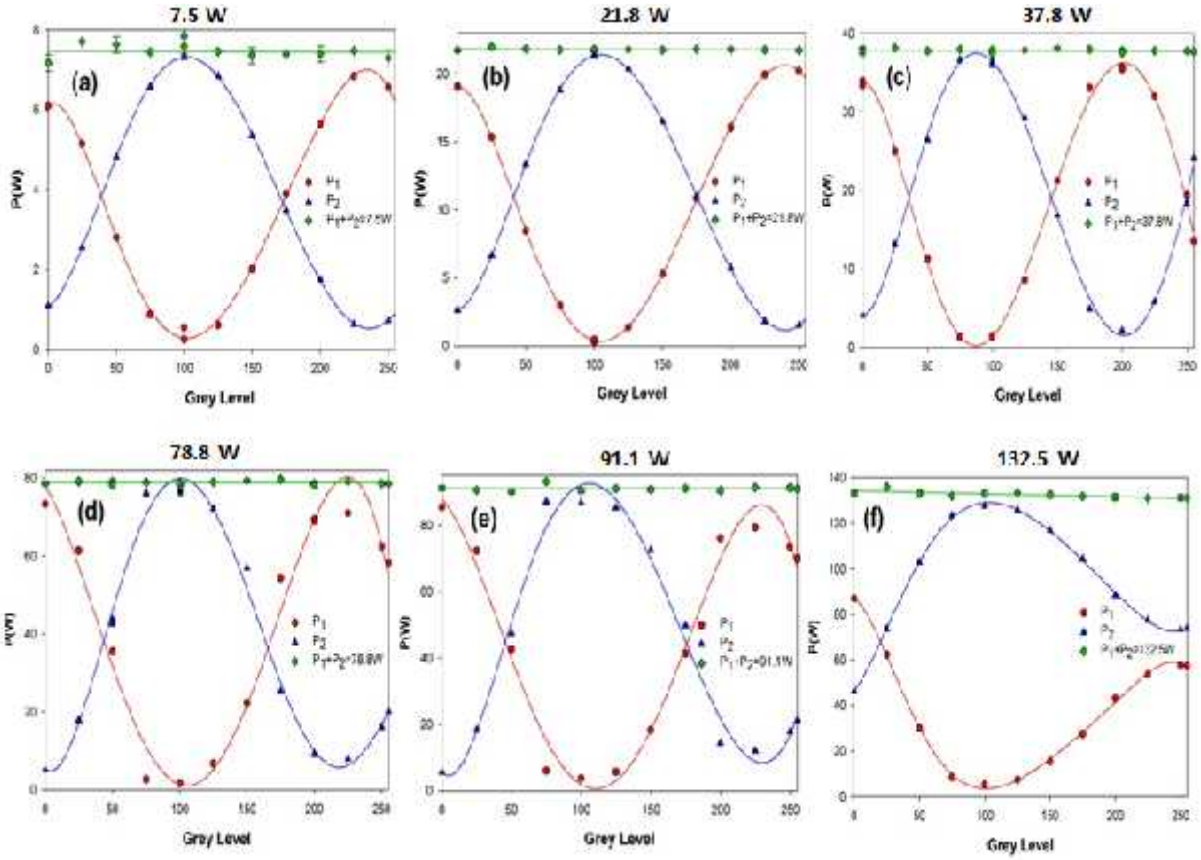

Figure 6.7. Phase changes of Device-01 response to incident power less than 132.5W. The phase response is stable up to average power $\langle P \rangle$ = 37.8W but begins to deviate slightly above 80W while a significant deviation occurs at 132.5W, reaching just over a π phase shift instead of the desired 2π.

This sign that the device still works functionally and the liquid crystal layer is not under stress. In addition, the test for device 1 is continued in nearly one and a half hours. The test for device 2 is continued in several hours and 45min in which the peak power is higher than 160W. It can be concluded that the SLM can work well for heavy-duty tasks.

Device 2 was mainly assessed the phase response to higher power. The same identical phase response trend when the power is up to 109W. the phase change can achieve 2π, shown in Figure 6.5(d). At 109W, the degree of polarization

$$P = \frac{I_m \quad - I_m}{I_m \quad + I_m} = 0.9$$

while at 160W and 190W, P dropped to 0.75 and 0.64. The drop was probably led by the temperature slope gradient across the chips, which was discussed in last section and evidences were shown in infrared images (Figure 6.4). The deviation of 2π phase changes indicates wavefront error across the chip. A correction field could be used to fix the error. The two devices were tested for extended periods at high average power. The work performance kept well. In addition, the device was tested in extreme high power (220W). There wasn't obvious and irreversible damage found on the device. The phase response characteristic kept similarly in the testing.

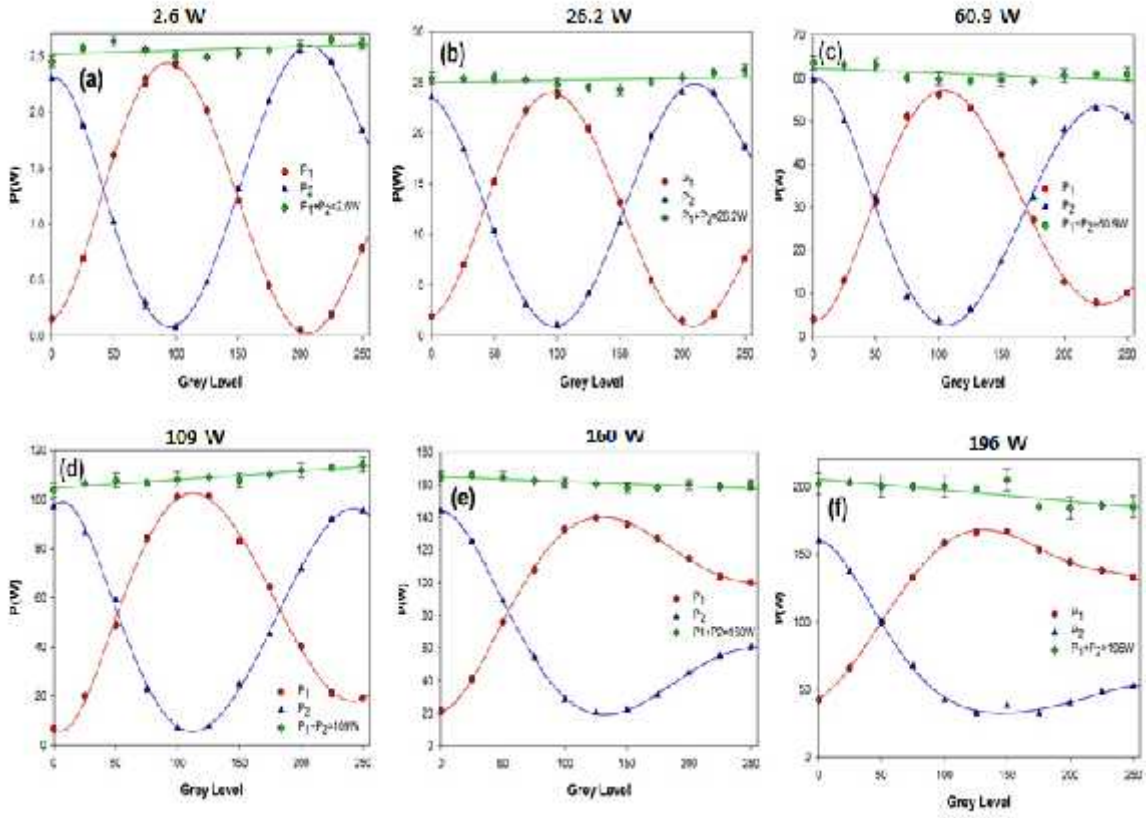

Figure 6.8. Phase modulation of Device-02. The phase response can engage 2π change which is satisfactory at laser power up to $\langle P \rangle$ = 109W but begins to deviate at 160W and above, reaching just over a π phase shift instead of the desired 2π.

6.3 Modelling of observed thermal and phase response

6.3.1 Infrastructure of a liquid-cooled SLM

The thermal-dynamic features of designs and materials are protected. Figure 6.9 illustrate infrastructure of the SLM. Most of heat could be drained out the device by the water cooled copper via CMOS chip and a ceramic plate. The ceramic plate is made of AlN which has thermal conductivity of 150 $Wm^{-1}K^{-1}$ [235].

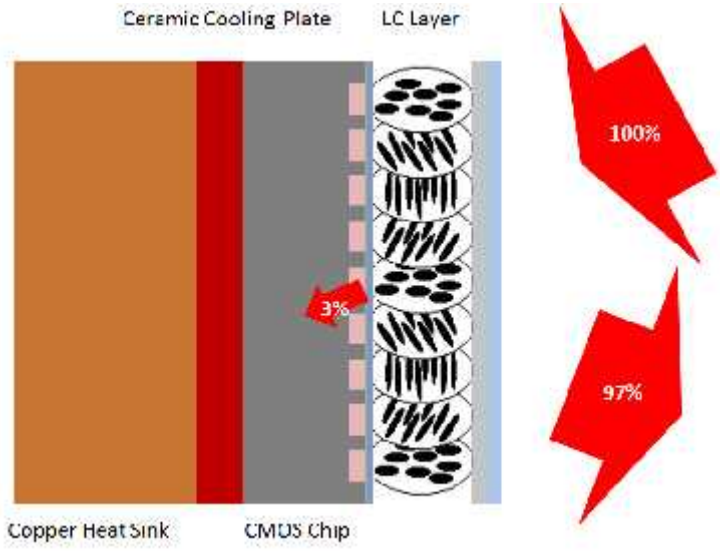

Figure 6.9. Schematic of a liquid-cooled LCOS SLM. Inset illustrates the schematic of the incident of picosecond pulses and LC layer. Temperature response on silicon substrate and phase response with temperature are modelled.

Firstly, the average power $\langle P \rangle$ of incident laser beam is 220W. The absorption of front widow and LC layers are negligible. The reflectivity of the dielectric coating is 97%. Then the laser heat source on silicon substrate is assumed to be a spot with 10mm $1/e^2$ diameter and Gaussian distribution. Surrounding temperature was 293°K.

The front window is probably made of fused silica which is nearly completely transparent to light with λ at 1064nm, and absorption rate α_f^1 is $1 \times 10^{-5}\,cm^{-1}$ [236]. After a 10s exposure to laser beam with average power <P> = 220W, the temperature rise ΔT ~ 3.6×10^{-3} °C. Thus the absorption is negligible.

The know properties of the liquid crystal layer is limited. Key properties, such as LC birefringence, temperature responses and nematic-isotropic transition range, are unclear. Lack of knowledge may reduce the model accuracy. The liquid crystal is organic material, usually containing hydrocarbon end groups and Benzene rings. The absorption coefficient (α_5) of benzene, density (ρ) and specific heat (C) are respectively $\sim 4 \times 10^{-4}$ cm^{-1}, ~1gcm^{-3} and ~2.4$Jg^{-1}K^{-1}$ [237]. In addition, it is assumed at 1064nm, the absorption coefficient α_L^1 is reasonably at the same magnitude with a number of 1×10^{-3} cm^{-1}. Thickness layer of LC is ~ 2μm. Then the absorbed power $\langle P_A \rangle = (1 - e^{-\alpha})\langle P_C \rangle \sim 4 \times 10^{-5}$W, which is likely lead to a temperate rise ΔT ~0.4°C, which is minor. In real circumstances, the absorption coefficient might be higher.

6.3.2 Simulated thermal response

In order to investigate which element of SLM is the major source of the observed temperature rise during Gaussian-beam exposure. It assumes that nonlinear effect is negligible. Therefor the incident beam assumedly comes from a CW laser. A thermal model was used in COMSOL Multi-Physics software which contains the relevant physical properties such as density, heat capacity, for element material, including: silicon chip, ceramic plat and copper sink. The numerical approach is the 3D heat diffusion equation with optimised mesh sizes from 1-3mm. The temperature response of silicon front surface, Si-ceramic boundary and ceramic-copper boundary, are simulated.

Firstly, the response trends without water cooling were simulated and the result is shown in figure 6.10. The system, as expected, does not come to thermal equilibrium. The boundary temperature rises 2°C in the first 3 seconds then continuously increases at a linear rate of 0.024°C/sec.

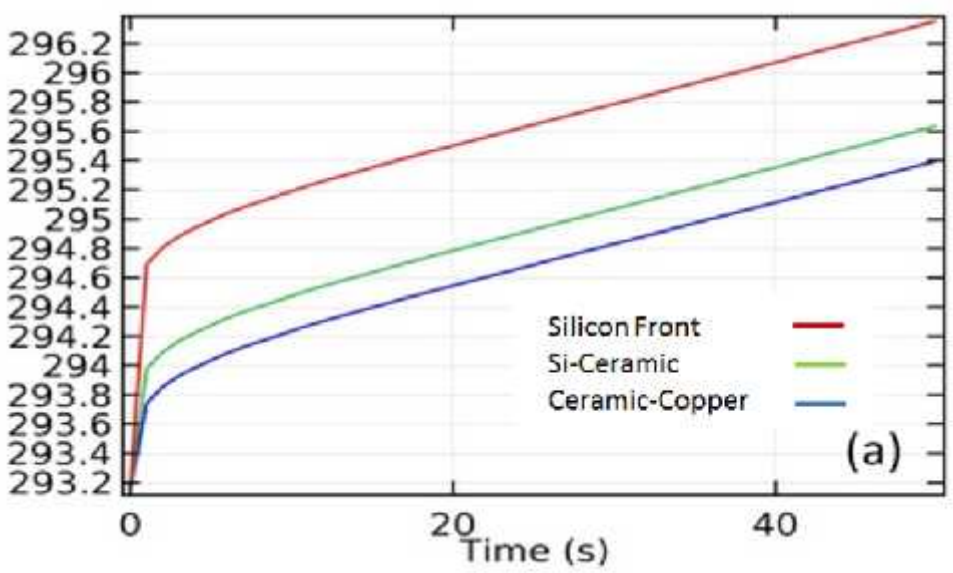

Figure 6.10. Thermal response as boundaries without water-cooling function.

Secondly, response trends with water cooling presents in figure 6.8 which demonstrating that thermal equilibrium is reached after approximately 20 seconds. All trends increase rapidly in the first few seconds and gradually level on. At the silicon front surface, the highest rises at ΔT =2°C. When comparing to experimental result (figure 6.3), the simulating ΔT is lower by a factor of 2.5. Although there is deviation, the simulating results suggest the rising temperature observed in experiment comes from the irradiation absorption in silicon chip.

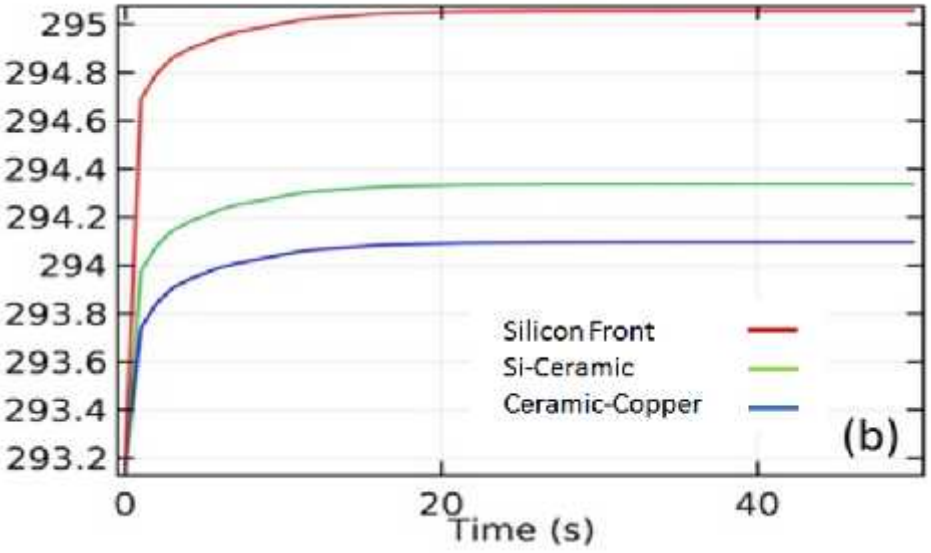

Figure 6.11 Thermal response as boundaries with water-cooling function.

The simulated temperature response of silicon with absorbed power (<P> = 0-10W) is shown in figure 6.12. The rising temperature has a linear relationship exposure power, which is in agreement with experimental observation, (figure 6.3).

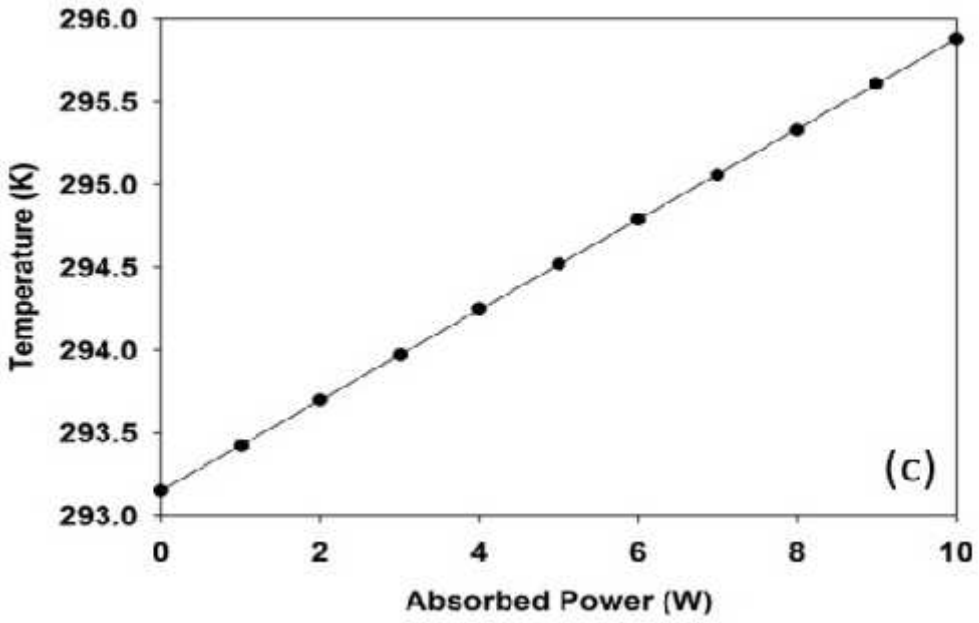

Figure 6.12. Thermal responses of silicon (centre) with absorbed power, ranged from 0 – 10W.

Figure 6.13 presents the simulated temperature distribution across the silicon chip. The incident laser power is 63, 220 and 370W while absorption power is 1.9, 6.6 and 11.1W. Symmetrical patterns indicate the same thermal gradient across the chip which was observed using FLIR camera (figure 6.4).

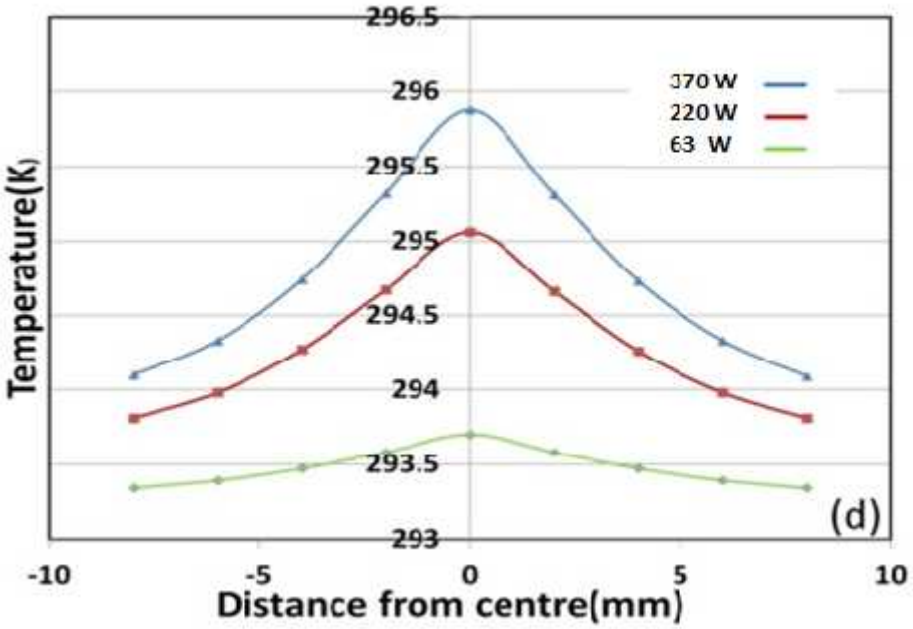

Figure 6.13. Simulated temperature profile at silicon front surface when thermal equilibrium is built.

Thermal modelling of the SLM structure (with and without water cooling) was carried out. This model predicted that during laser exposure, the silicon chip comes to thermal equilibrium only when the SLM was water cooled, reaching 2°C above ambient compared to 5°C rise with <P>=220W exposure (<P>=7W absorbed). The expected chip temperature rises linearly with exposure in accord with observations and in particular, a temperature gradient develps at higher average power above 120W. Allowing for photo-absorption in the organci LC layer, an estimated 0.4°C additional temperature rise could be expected. Combing these two estimates, a 2.5°C rise is within a factor of two of the observed temperture rise.

The thermal response time of the coolded SLMs was approximately 1-2s, observed with the thermal cameral which cutting off the laser power at <P>=220W, supporting the very efficient heat removal from the siicon chip and consistant with the predicted response time from thermal modelling. As device reflectivigty is 97%, then the absorbed power $<P_{abs}>$ ~7W thermal load was removed efficiently at <P> =220W incident laser power.

6.3.3 Phase-response simulation

The thermal-diffusing model supports the view that absorption in silicon is a major of the observed temperature rise during laser exposure of the SLM. It is well known that nematic liquid crystal (LC) has birefringence properties. T_{NI} is a transition temperature (T_{NI}) at which nematic liquid crystal becomes isotropic, leading to degrade of birefringence. The optical thickness of the LC layer is Δn , in which L and Δn are respective thickness and birefringence. The light first travels to the reflecting layer and then reflects outward, in the process, total phase change (ϕ) of the LC layer adding to the light is given by

$$\phi = (4\pi/\lambda)\Delta n \quad (6.7).$$

And then, the phase response to temperature variation is given by,

$$\frac{\partial}{\partial} = (4\pi/\lambda)\left[L\frac{\partial(\Delta n)}{\partial} + \Delta n\frac{\partial}{\partial}\right] \quad (6.8)$$

It is reasonable assumed that the thickness (L) is a constant and not variant to temperature change. Consequently, the second term of equation (6.8) become 0 and the equation is simplified to

$$\frac{\partial}{\partial} = (4\pi/\lambda)\left(\frac{\partial(\Delta n)}{\partial}\right) \quad (6.9).$$

In Peng and his co-works work (2015), Δn could be represented by an empirical equation

$$\Delta n = \Delta n_{\mathbb{C}}(1 - T/T_N)^{\beta} \quad (6.10)$$

Δn_0 is an extrapolated value at 0°K. T is temperature variable. T_{NI} is the critical temperature of nematic-isotropic transition and T_{IN} is typically higher than 60°C. The index β is the orientation order parameter ranged in $0.1 < \beta < 0.3$. According to equation (6.10), it is seen that LC birefringence goes down with the rise of temperature. That means the drop of phase change with rising temperature. But the drop trend is gradual apart from at the transition temperature T_{NI} where Δn suddenly become zero.

$$\frac{\partial}{\partial} = (4\pi/\lambda)\Delta n_{\mathbb{C}}\beta(1 - T/T_N)^{\beta-1}/T_N \quad (6.11)$$

If setting T = 293°K, T_{NI} = 333°K and Δn = 0.30 with β = 0.19, then Δn_0 = 0.45 (0°K), the phase chang ($\frac{\partial}{\partial}$) is 0.01π rad/°K. Hence with a temperature change ΔT= 5°C from room temperature 288°K to 293°K, the phase change (δ) is -0.05π which is only 0.025λ of

1064nm. The phase response corresponds to an effective change in $\delta = \frac{\lambda}{4\Delta n} = 0.88\mu m$, as the LC layer effective thickness is given by $L = \lambda/2\Delta n$. The thickness change might be due to temperature gradient which was observed in the experiment because the temperature gradient may distort the chip mechanical structure.

The beam is modelled as the sum of three concentric areas due to the temperature gradient which is the peak in the centre and reducing towards the edges. The varying thickness affects the phase response so that, the phase delay in central area become more different from inner to outer. In the experiments, this phase delay is represented as a rotation of the linear polarization (see section 6.2.2) and thus the polarization direction varies in the three areas. The component of the polarization, $P_t = P_i \cos^2\theta$, is allowed to transmit is parallel to the polarizer's transmission axis. θ is the angle of the linear polarization to the transmission angle. Because each concentric area have a distinct uniform θ, the laser power transmitted from the central area and remaining two concentric areas around the centre P_{t1}, P_{t2} and P_{t3} will be phase shifted by varying degrees. The normalized transmitted power is the sum of all three components.

Figure 6.14 presents the resulting expected phase change. (a) compares the trend of the calculating normalized power using pure $\cos^2\theta$ function is excellent satisfied to experimental result over 0 - 2π in the case of low incident average power, <P> = 26.2W. (b) illustrate the phase change of the average power case where <P> = 160W. Two trends are reasonable fit. The comparisons suggest the source of drop of maximum Δn corresponding to incident average power comes from thickness variation of LC layer due to the developing of thermal gradient.

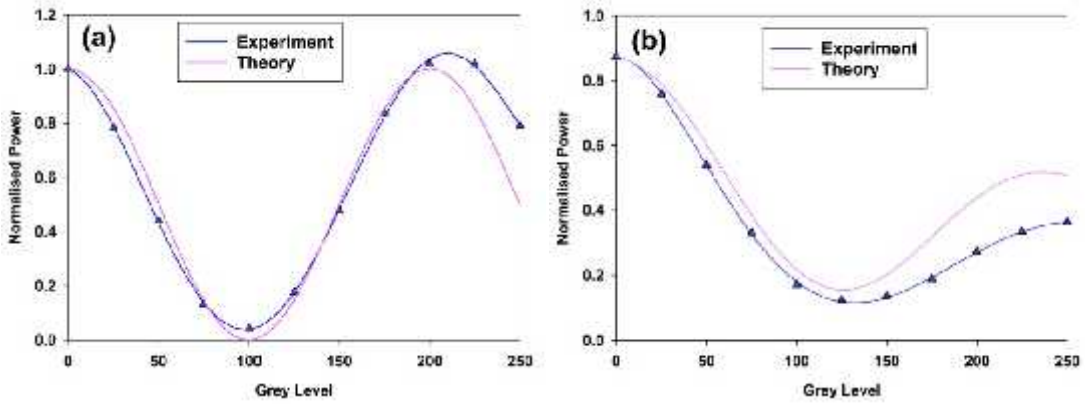

Figure 6.14. Normalized transmitted power and compared to experiment at <P> = 26.2W (a) and at <P> = 160W (b).

6.4 Laser-micromachining results

High speed periodic surface micro-structuring is an important application of parallel-beam processing technology. In the application, a spatial light modulator is used to generate multi-spot pattern in focus plane. In previous sessions, the phase response to laser power W is measured via the investigation of polarization modulation in horizontal direction although parallel-beam processing depends on phase modulation. A good demonstration of using SLM to generate diffractive spots and measure the first order diffraction efficiency and uniformity which could be more instant to understand work performance of SLM under strong exposure to ultrafast pulses and get a solution to beat phase errors.

6.4.1 Parallel beam laser surface processing at $\langle P \rangle \leq 25$W

Phase CGHs can allow efficient use of the high power laser through diffractive splitting parallel beam. Micro-processing was carried out at a range of powers. Stainless steel substrates (60 x 60 x 3mm) with polish surface were used to assess the machining quality.

CGHs for 3-spot pattern (± 1 and zero order) were generated using non-iterative lens and gratings algorithm. Figure 6 are microscopic images of the surface ablated results. For Figure 6.15(a), the processing parameters: repetition rate, average power and scan speed are respectively set to 10 kHz, 2W and 250mms^{-1}. Widths of the 3 ablated tracks are approximately equal, varied from 80 to 100μm, which indicates intensity is distributed evenly in the three orders with peak power ~70μJ per beam. Figure 6.15(b) indicates the zero order

machined at 1000 mm/s with 25W/404kHz. Pulse energy E ~21 μJ and fluence F ~ 0.85Jcm^{-2}. Because the hatching space was set at 460 μm, a pair of ±1st orders are overlapped, seen as asymmetrical pattern.

Table 6.2: Processing parameters (P ≤25W)

Repetition Rate	Average Power	Scan Speed	Fluence (per pulse and per beam)	Hatch Space	Overlap Rate
10kHz	2W	250 mm/s	2.8 J/cm^{-2}	250 μm	25/spot
404kHz	25W	1000 mm/s	0.85 J/cm^{-2}	460 μm	255/spot

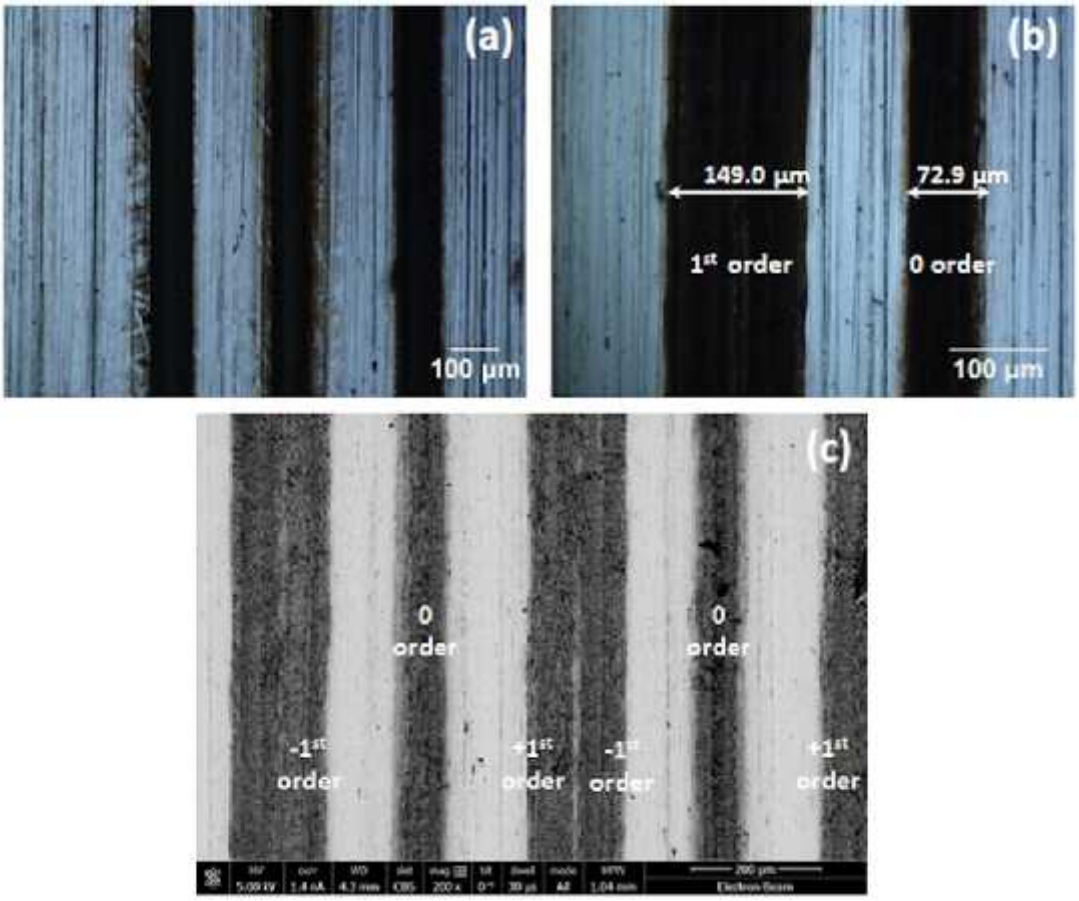

Figure 6.15. (a) Optical micrograph of three parallel tracks (±1st order and 0th order) machined at 2W, 10 kHz and 250 mm/s. (b) Optical micrograph of 3 spot processing with 25W/404kHz exposure with 1000 mms^{-1} scan speed and offset hatch spacing of 460μm, overlapping the ±1st orders. (c) SEM image of the stainless-steel machining in (b) clearly showing the overlapping ±1st orders and zero order in between.

The parallel 3-spots machines were used for surface texturing via laser induced periodic surface structures (LIPSS) [238] and [239]. The period of these structures is close to 1064 nm which is incident wavelength. Figure 6.16(a) shows the result of large area parallel beam surface texturing (3 spots) at 25W average power, 404kHz and 3000 mm/s. The surface dispersion phenomena under illumination of white light show these periodic surface textures. The colour differences are due to the slight change in viewing angles of the camera lens. The effective pattern rate is ~8cm^2/s. Figure 6.16(b) indicates LIPPS is perpendicular to electric field and Figure 6.16(c) shows micro and nanostructures of LIPPs. High order mode of LIPSS structure [240].

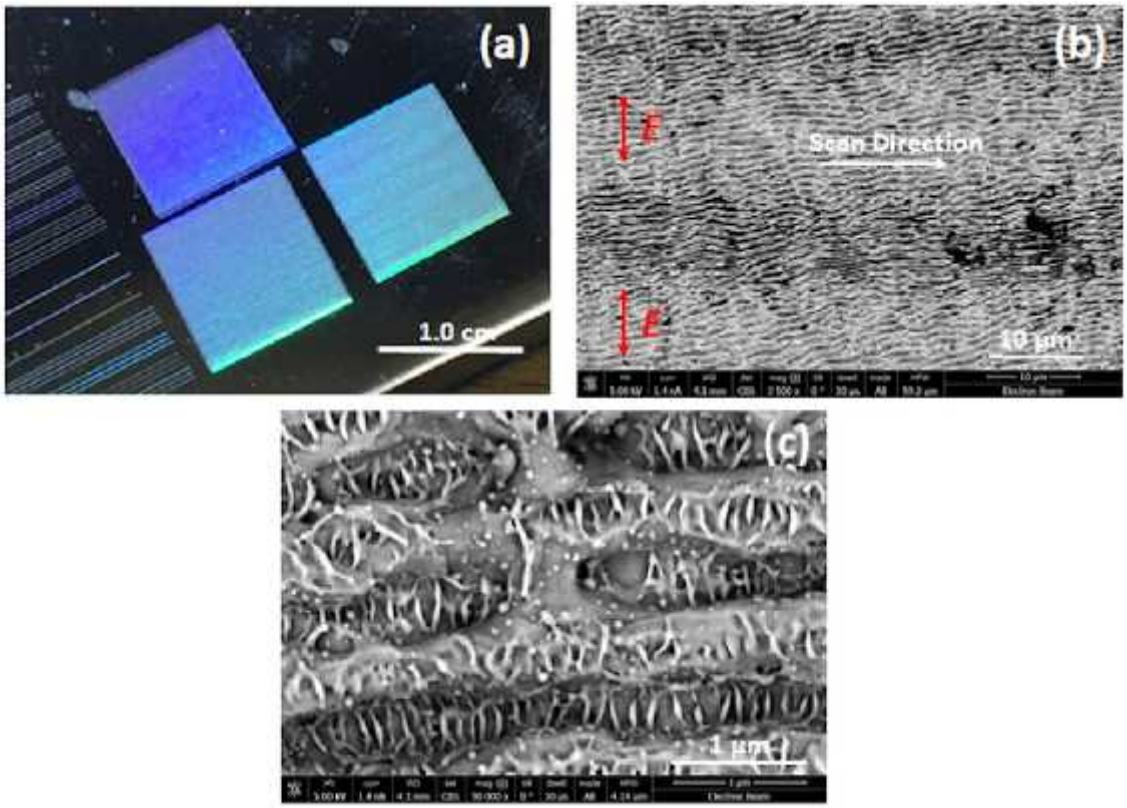

Figure 6.16. (a) Macroscopic image of surface texturing (1cm^2) on a stainless steel sample using diffractive 3-spot patterns. Laser exposure was 25W, 404 kHz with 3 m/s scan speed, minimizing pulse overlap. (b) SEM image indicates LIPSS with 1-µm periodicity (c) High resolution SEM image showing nanostructures within the LIPSSs.

6.4.2 High power processing at $\langle P \rangle$ >100W

In high power cases, the results are shown in Figure 6.17 there are 3×3 squares. The CGH used is same to the case of low power. Hence the asymmetric pattern for 25 W is still apparent the case. It is concluded that the 3-spot CGH is still effective for the power level. With processing of 160W and 50 scans, the surface was oxidized.

Table 6.3: Processing parameters (P ≥ 100)

Repetition Rate	Average Power	Scan Speed	Over Scan	Overlap Rate
1MHz	120W	280 mm/s	1, 5, 10	25/spot
1MHz	120W	1000 mm/s	2, 10 , 20	255/spot
404kHz	160W	1000 mm/s	1,5, 50	85/spot

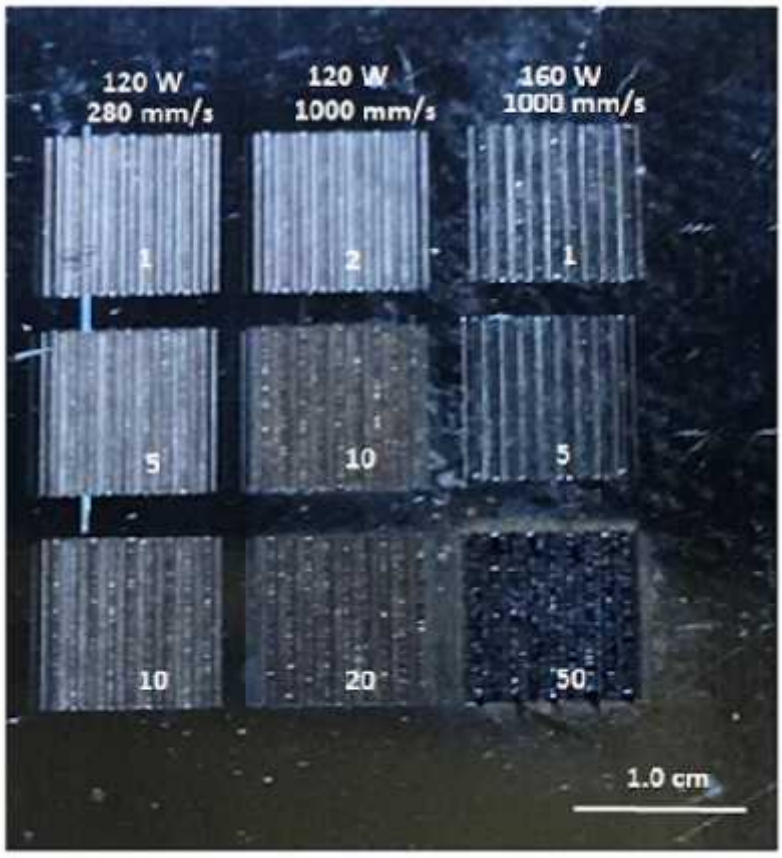

Figure 6.17. Macroscopic image of three beam parallel processing. The asymmetrical pattern persists.

Figure 6.18(a) presents an SEM of machining at 160W, 1MHz, 3 m/s and 1 scan. The similar results of low power cases confirm that even in extreme exposure condition, the SLM still worked well. Optical energy can effectively diffract by the CGH. Figure 6.18(b) presents the machinery results of ±1st order. LIPSSs can be seen at the edges with less exposure.

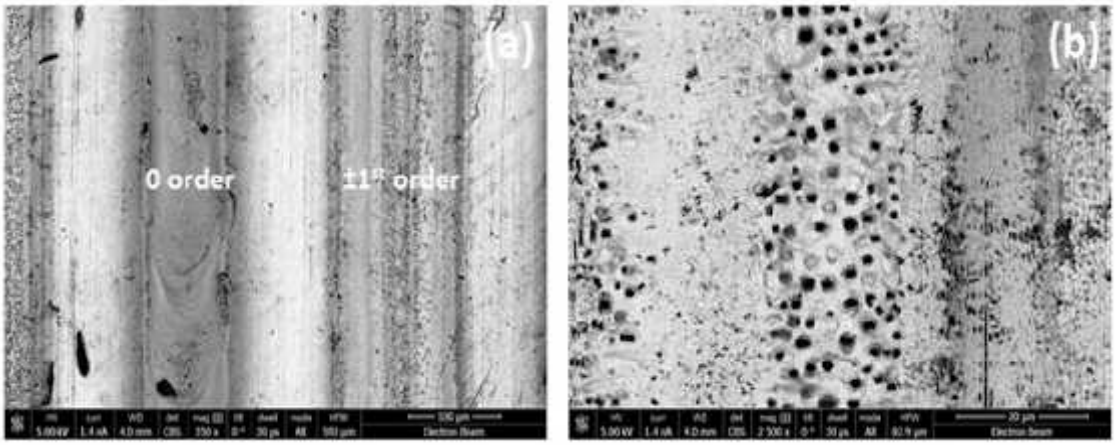

Figure 6.18. SEM images of parallel processing with 3 spots at 160W, 3000 mm/s and 1 scan. (a) is similar to asymmetrical pattern of low power cases. (b) The overlap of ±1st orders.

6.4.3 More complex phase CGH's

In the further step, a pattern to generate 11 spots in focus plane was investigated. The designated M pattern constitutes of 11 spots, shown in Figure 6.19(a). (b) is the complex phase image which is the inverse Fourier transforms without iterative method (Lens and Grating Algorithm). ~2W irradiation is diffracted in far field, shown in (c), is evenly distributed. This intensity profile was attained by placing a screen behind lens 1 of the 4f system. The diffraction optical intensity on first order is higher than 90%.

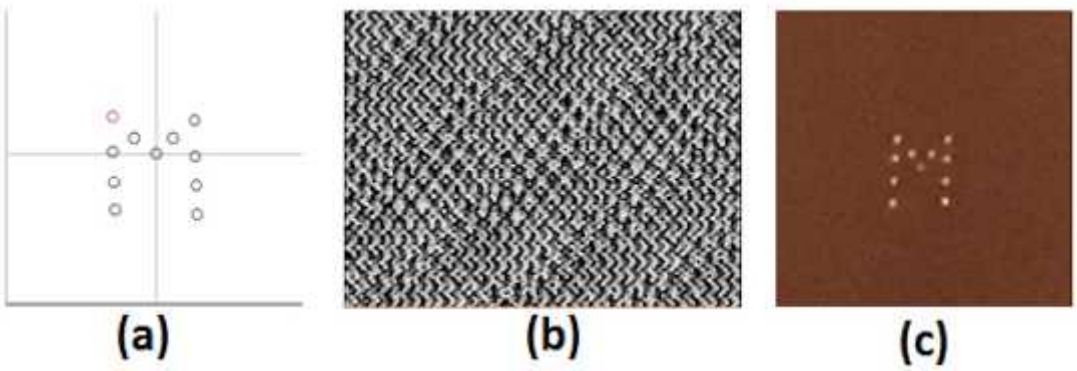

Figure 6.19. (a) Spot pattern set representing the letter M (b) resulting complex phase CGH created by the lens and gratings algorithm (b) observed intensity pattern at far field, showing even distribution.

Figure 6.20 shows the machining results using drill functions with repletion rate 2MHz. Uniform pattern can observed at power level of 90, 120 and 160W. The diffraction efficiency at first order was approximately 70%. At 250 W, the diffraction efficiency shows a drop, shown in (d). The majority of intensity is at the zero order. The drop indicates chip start to work at poor performance with the grey level phase CGH. The tails of each drill spot comes from the deceleration of scanning operation. If using a fast shutter to control exposure after scan spot point on the process position, this tail could be eliminated.

Table 6.4: Diffraction efficiency

Series	Average Power (W)	Exposure (ms)	Diffraction efficiency (η)
(a)	90 W	30	~70%
(b)	120 W	30	~70%
(c)	160 W	10	~70%
(d)	250 W	10	<50%

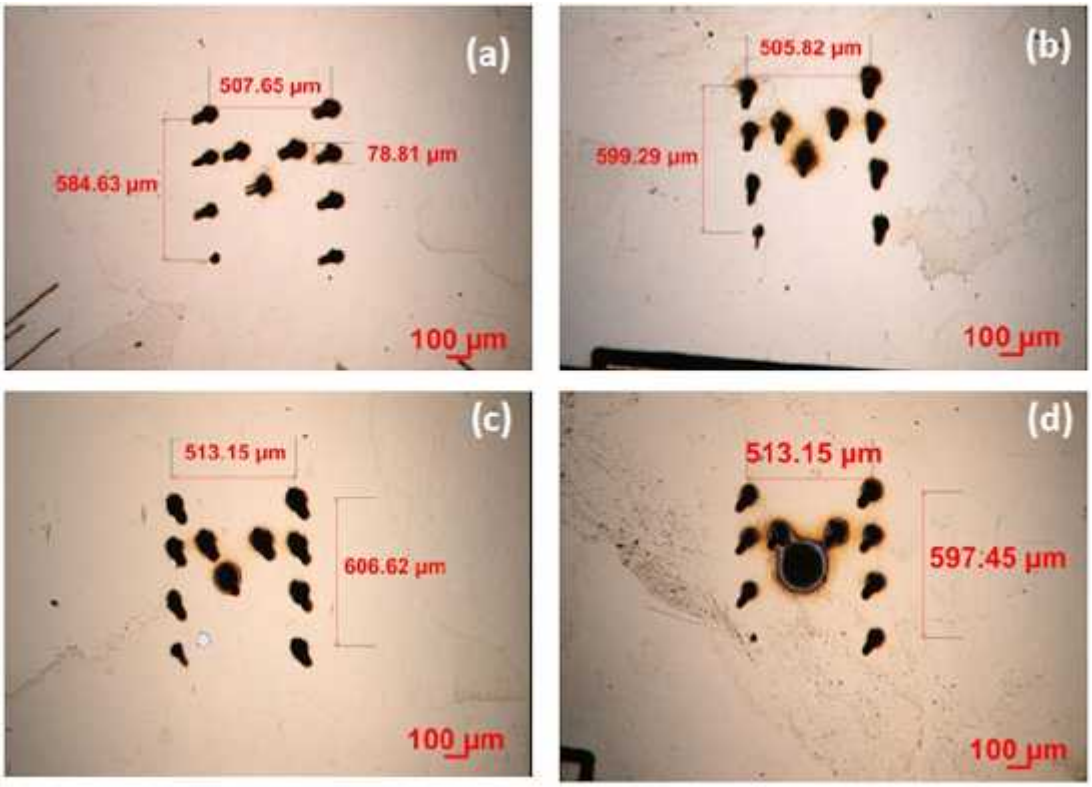

Figure 6.20. Optical images of surface patterning (letter "M") on polished brass plate with increasing laser powers. (a) <P> = 90W, 30ms, (b)<P> = 120W, 30ms, (c) <P> = 60W, 10ms, (d) <P> =250W, 10ms. Diffraction efficiency drops above <P> = 120W as expected.

6.4.4 High speed surface micro-structuring

Thin film micro-structuring is an increasingly important area for ultrafast lasers. Figure 6.21 shows clean, thin film patterning of flexible Al/PET with 97W/404kHz and a near uniform 9 spot pattern. Scan speed was 20m/sec with complete removal of the film without thermal damage to the PET. As the lines were 50um wide, the total film removal rate was therefore 90cm^2/sec. with ~ 50% pulse overlap and fluence F ~ 0.4J/cm^2. Spot separation was 0.5mm so that each line set is 4mm wide.

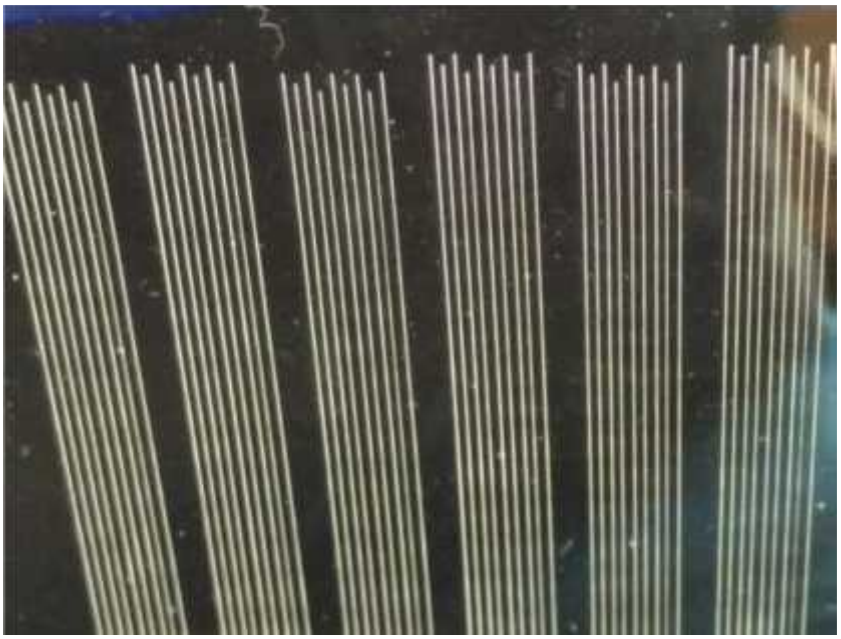

Figure 6.21. Thin film patterning of flexible Al/PET with 97W/404kHz using 9-spot parallel processing with ~ 50% pulse overlap and fluence F ~ 0.4J/cm^2. The total removal rate was 90cm^2/s.

6.5 Discussion and summary

SLMs are important devices for science and industry. The ability of high average and power handling can bring great benefits to application in many fields. In 2010, Beck and his coworkers demonstrated the first cooled devices at Herriot Watt University. It is a Holoeye (LRC-2500) which is attached to a large cooper block [204]. The commercial product was designed for exposure to 1-2W/cm^2 and maximum to 3W intensity. This work is a significant progress to the previous efforts of Beck et al [210] and more recently, Klerks and Eifal [171]. It is different from previous work. The tests are engaged using powerful picosecond pulses. The thermal response time was assessed using FLIR camera. It is observed that the response characteristic shows highly linear to laser power with small gradients of 0.041°C/W (-01) and 0.026°C/W (-02) respectively. To the author knowledge, this is the first report experimental results. The loaded power is 3.7 times higher than that of Klerks and Eifal's work [241]. The difference in the thermal characteristics of the two test devices is likely due to a difference in thermal handling design, proprietary to Hamamatsu. A clear temperature gradient appears across the chip at laser power above <P> =120W exposure, highlighting the efficient axial heat removal. The temperature variation (ΔT) of device 02 was measured to 0.5°C

corresponding to 260W input, posing no threat to the viability of the LC layer or silicon substrate.

Using polarization modulation via SLM incorporated with ¼ waveplate and thin film polarizer (TFP) to critically assess the phase variation generated by elevating exposure level is a practicable approach. In this work, the trends of phase response on the device 01 and 02 were measured by this approach. The elevating exposure covers a range to 180 W while the devices 02 are tested in extreme condition, maximum to 220W. It was observed that the two devices can engage 2 π phase changes with controlling of grey level in the condition of P<109W. In the range of 109W to 160W, the controllable phase change is greater than π. In further range, the maximum phase change became less than π. The limitation of phase modulation is likely due to thickness variation which is caused by the harping temperature slope across the section along with evacuating exposure. The built-up temperature slopes were determined by thermal camera images. This thickness variation also can change the polarization state of reflected lights. Using the approach of polarization-modulation can confirm the characteristic phase response. It was observed that the degree of polarization P at peak/valley points is varied to evacuating exposure. For low-level exposure the polarization of reflected lights can be high linearly polarized. In contrast for high level exposure, the polarization states only remain in elliptical polarized because the limitation of phase changes. It is suggested that the remained elliptical polarization is caused by the thickness of variation built up by the temperature slope, hence for the spatial errors. But the remained elliptical polarization also can due to de-polarization of reflected light which is beyond the field of this study.

This work provides experimental evidences of surface texturing results. One of the SLMs (Device 02) was used to engage parallel processing on metal substrate. The handling beam power covered 25-160W and create LIPSS structures with high speed. The production rate for 25W on stainless steel substrate was at $8cm^2s^{-1}$, which can create high quality products. The production for 160W on stainless steel substrate was presented as well. In high power level, the diffraction efficiency to $\pm1^{st}$ order was demonstrated using 11-spot diffractive pattern. The diffraction efficiency dropped along with the evacuating exposure. Below 160W, the diffraction efficiency is higher than 70%. At 250W/10ms, the diffraction efficiency although dropped significantly, the 11 pattern was still remained. The significant drop implies other mechanism may play majority role on the instantaneous response at the extreme condition.

A continuous high power test was held on device 02. The test lasted 45 minutes and 15 minutes respectively for 160W and 220W. There was not degradation observed. The total time for the usage of high power level lasts several hours, compared with 2 hour test by 60W by Klerks and Eifal [241]. It is concluded that the devices will not be permanently damaged when laser power is at the testing range and can work at the level continuously. If there would have any absorption defect, the liquid crystal should have thermally damage soon. Considering the power threshold for irreversible damages for these devices, several mechanisms are possible. High peak energy of ultrafast pulses with fluence $F > 0.5J/cm^2$ could damage the dielectric coating of the front windows of the SLMs. The multi-absorption nonlinear effects may play roles and create absorption defect in the liquid crystal. It is known that the SLMs are designed to handle $I > 20GW/cm^2$. Nonlinear absorption and surface plasmon resonance have less chance to cause damage. For linear absorption of optical energy the light of 1064 nm can penetrate silicon substrate a few millimetres with attenuation coefficient 10 cm^{-1} [211]. The thickness of silicon is 0.5 mm, hence for 40% of penetration components will be absorbed by the attached cooling metal block. Here, if the work of Beck and his co-workers is considered there was not permanent damage for doubling average power, the testing devices (Hamamatsu X13139-03) should be higher than 440W. But the phase distortion problem should be considered. For example, Dammann gratings or spatial correction field are the solutions.

Chapter 7

Conclusions and recommendations for future work

This thesis has studied the nonlinear femtosecond inscription inside the transparent polymers, PMMA and PMP then multi-photon reduction of silver ions to atoms in a PVA/silica composite. The effect of altering Polarization and wavefront have been explored by numerical and advanced experimental approaches. In addition, this work has investigated the phase-and-thermal response of a LCOS SLM with liquid-cooling, able to handle high average power, picosecond laser pulses at multi-hundred Watt level without damage. Conclusions drawn from each investigation are as follows.

1. Inscription of PMMA. Low NA (~0.08), NIR (λ=775nm), fs pulses ((τ~170fs) were used to generate supercontinuum spectra. With rising pulse energy and both linear and circular polarization $|V\rangle(T)$, $|H\rangle(T)$, and $|R\rangle$, the critical power for supercontinuum generation, also the threshold for self-focusing, were found. It is observed that filamentary modification is polarization-dependent, stronger with linear than circular polarization, consistent with the theoretical predictions. Threshold energy $E_{th,}$ for TE and RC are respectively ~0.51μJ and ~0.69μJ at 387.5nm (170fs) in PMMA and hence the ratio of the critical peak powers is $(P_{cr,circ}/P_{cr,linTE}) = 1.35 \pm 0.08$, close to the theoretical result of 1.5 predicted by Boyd [21].

2. Inscription of PMP. Femtosecond laser inscription in Poly (methyl Pentene) in the NUV at $\lambda = 387.5$nm, at visible wavelengths $550 \leq \lambda \leq 700$nm has been carried out. Low NA ~0.08 inscription at all wavelengths resulted in a correspondingly low refractive index modulation, $\Delta n \sim 1 \times 10^{-4}$ while higher NA ~0.4 inscription at $\lambda = 387.5$nm resulted in an order of magnitude increase in refractive index modulation, $\Delta n \sim 2.3 \times 10^{-3}$. Volume Bragg Gratings inscribed at 387.5nm with 200 lines/mm showed a first order diffraction efficiency $\eta_1 = 68.5\%$, however, diffraction efficiency was limited by observed scatter due to some residual material breakdown at pulse length $\tau_p = 180$fs, creating a low intensity background between orders. The critical power for self-focusing in PMP at 387.5nm, estimated from the threshold for supercontinuum was found to be $P_c^{387} = 2.2$MW (0.4μJ/180fs) inferring that the non-

linear refractive index of PMP at 387nm is $n_2^{387} = 2\times10^{-16}cm^2W^{-1}$ and hence third order susceptibility $\chi^{(3)}$ ~ susceptibility $\chi^{(3)}_{387}$ ~1.1×10^{-14}esu.

3. Fs laser direct write silver doped PVA-silica hybrid. NUV, fs exposure of a silver doped PVA-silica composite resulted in silver ion reduction via MPI in the bulk material. Material mechanical properties become better via the addition of PVA in the sol-gel silica. The photoionisation of PVA likely catalyses the transition from silver ion to atoms. The optical energy is well confined within filamentation. Via 3-photon absorption, both PVA and silica are probably ionized to provide free electrons, splitting chemical bonds. The nearly perfect fit of SAR peak at pulse energy E = *0.26«J* coincides with Mie's theory indicating that silver nanoparticles start to form, at this threshold energy. The study suggests the viability of 3D conducting metal circuits embed in Ag doped dielectric insulators.

4. **Twisted structures generated by vortex beams.** Filamentary modifications using spiral phase beams carrying Optical Angular Momentum (OAM) is also investigated at 387.5nm, observing the continuum created with increasing topological charge m. The anti-stokes signal, integrated over the region 350-370nm drops in a linear fashion with increasing m, showing that critical power for these OAM states increases linearly with m and expected theoretically but scales as $1.88m_{2\omega}$ and not $2\sqrt{3}m_{2\omega}$ [219]. Low NA filamentation with spiral beams having both linear and circular polarisations was observed for the first time in PMP. These show a difference in coupling due to polarisation dependent self-focusing, independent of the total angular momentum, orbital plus spin. Absorption of photons carrying high levels of OAM can generate a torque on the surrounding material, which has been investigated here. With high states of OAM, and high intensity, complex micro-structures are observed, converging to the focus which can collapse to multiple filaments. The effect of rotation on the wavefront appears, resulting in rotated filamentary structures. At NA = 0.7 and $m_{2\omega}$ = ±10, inscription cross sections show an asymmetry due to residual phase distortions when using such high OAM on a beam with a degree of astigmatism. While $m_{2\omega}$ = -10 shows a clockwise spiral, which could arise during OAM transfer to the material during strong absorption, this is not observed clearly for $m_{2\omega}$ = 10 due to asymmetry caused by wavefront distortions.

5. Vector-beam generation using 1064nm fs pulses (OPA) method. Ultrahigh intensity femtosecond pulses with complex 2D vector fields (radial and azimuthal) were generated by combining a tuneable OPA at 1064nm and a nanostructured S-waveplate. The experiments of polarization purity confirmed the optical field is tailored with high quality. When passing through a polariser, beam profiles with two-lobes are demonstrated, rotated by 90°. Characterized polarization is observed and shows the coherence quality of OPA beam. These vector beams are used to machine surface LIPSS patters on polished steel substrates (radial and azimuthal patterns). LIPPS patterns develop at right angles to the corresponding to the polarization states. The beam mode in neighbourhood of focus plane has a LG intensity distribution with a polarization singularity in the centre. Clean logarithmic spiral micro-structures were observed when the transmission axis of S-waveplate is rotated ±45° to the linear polarization. The spiral structures were previously predicted [196] superposition of azimuthal and radial electric field components. In addition, the magnetic field is parallel to these spiral trends. Femtosecond pulses with spiral electric fields might be used in particle acceleration. Other applications of spiral field distribution are expected. The spiral vector field could be used as a new channel for multiplexing communications. The identical spiral microstructure can be used to encode information, recorded by micro-machining on a mould tool then moulding pattern on to a medium.

6. Characterization of thermal effects on liquid coolant spatial light modulator. Cooled SLM's (type Hamamatsu X-13139-03) were exposed to high average power ultrafast NIR, 10ps pulse at up to 260W without damage. This power level is 4.2 times higher than previous work [203]. A temperature rise of 5°C with 220W exposure was observed on the best device and a temperature gradient developed across the CMOS chip. The phase modulation achieved of 2π radian with up to P = 130 W. When the average power is higher than 220W, the modulation drops to just over π radian, still a remarkable performance. The reduction in phase response is due to the thickness variation built up by the temperature gradient across the liquid crystal chip which is confirmed by FLIR camera images and modeled theoretically. In addition, high average power parallel beam surface micro-machining was demonstrated on Metals and on thin film Al/PET using appropriate phase only CGH's. With 100W average power, we achieved high quality (4 spot) ablation at a rate of $4mm^3$/second on stainless steel and patterned thin film Al/PET with 9 parallel spots. at a rate of $80cm^2$/sec. These experimental micro-machining rates are some of the highest reported to date while the

thermal and phase measurements with average power are the first reported at such high powers. Handling such high average and powers with SLM devices has great industrial significance. Incorporated with optimized CGH's, the zero order beam, if sufficiently energetic, could be evenly split to many thousands of spots to create extreme parallel processing [220], increasing production efficiency massively. Of course, this technique can also be used for other engineering and scientific application, such as optical vortex and optical tweezers.

It is believed that the novel optical and thermal results presented here provide on ultrafast laser-materials micro-structuring with phase only spatial light modulators technique are important for future scientific and industrial applications of this technology. A few recommendations for future research have arisen, these are:

1. Refractive-index modification in bulk single-crystal Sapphire with femtosecond pulse train. Sapphire is hard and environmentally stable material, which is a promised material suitable to produce high-value diffractive optics. But there are challenges. Sapphire has a high bandgap (*10.8*eV) and a very high thermal conductivity. These properties lead to the difficulty MPI and defeats thermal accumulation. Initial experimental trials have started with a femtosecond system (RegA) eg at the Photon Science Institute of University of Manchester. The laser can be tuned to performance (1μJ @ 800 nm) pulse energies and 150 fs pulse lengths. At best performance, it can be optimised to 2-3μJ and 110 fs which helps induce MPI. An infrared ultrafast harmonic generation system and NL BBO crystal can provide pulses at 400 nm. The repetition rate is variable from 10-250 kHz. The focusing device is a microscopic objective (Nikon Plan Fluo LWO 20x10 NA ~ 0.46). With scan speed of 0.1mm/s and repetition rate is 250 kHz. Modification within bulk Sapphire was successful producing single layer VBG's with first order diffraction efficiency of 15%, an encouraging result. Hence, 100fs pulses with high repetition rates can change refractive index within Sapphire for creating photonic components.

2. Inscription of Zinc Selenide. Writing 3-dimentional refractive-index structures in Zinc Selenide has great engineering interests. Zinc Selenide is transparent from 500nm to 18μm, a tremendous transmission band hence mid-infrared light can be used to produce inscribed diffractive optics or simply a lens. The most important is that is Zinc Selenide is attractive

host material for solid-state infrared lasers. Cr^{2+}: ZnSe has enormous gain bandwidth which gives the availability to generate infrared pulses with extreme short duration in a few cycles. The mode-locked implementation using Cr^{2+}: ZnSe (850 nm FWHM) to generate sub 100fs pulses was reported in previous works [174]. In addition, using Er-doped fiber laser (CW, λ=1.16μm) to pump multi-crystalline Cr^{2+}: ZnSe can generate femtosecond frequency combs with a central wavelength λ = 2.45 μm [221]. Femtosecond frequency combs can provide higher resolution for optical interferometer and precise spectroscopy. In addition, the comb is used to harness the phase of the electric field in such attosecond pulses. The poly-crystalline material has great potential to produce the compact and cost-effective mid-infrared devices when doped. However, focusing inside ZnSe with fs pulses for Δn inscription is extremely difficult due to its very high NL response, creating strong electron plasma which defocuses converging wavefronts. Longer pulselengths and non-Gaussian, LG modes may be useful here in reducing the effect of plasma generation.

3. Average laser power exceeding 400W handling using liquid cooled SLM. It was speculated that exposure at average laser power exceeding 400W will not be problematic but clearly, phase variations due to the temperature gradient on these devices needs to be addressed and if possible, eliminated by further improved thermal engineering. If the temperature gradient could be removed by further improved thermal cooling, then it may be possible to achieve the full 2π phase response at <P> above 200W. Ultimately, testing these devices with both ultrahigh peak intensities exceeding P_{peak} = 50GWcm^{-2} combined with multi hundred Watt average powers would be highly desirable. Scientific applications such as NL filamentation in air for control of lightning discharges may be possible [222] where dynamic control of phase, polarisation and orbital angular momentum of ultrahigh peak power pulses at high repetition rate would be beneficial. Future expansion of industrial applications in ultrahigh throughput laser marking, patterning and machining are likely when high power laser sources are combined with polygon scanners able to achieve scan speeds on a substrate s > 200ms^{-1}. When combined with a high energy, high average power laser system and optimised CGHs creating uniform or variable intensity spots massively parallel-beam laser micro-structuring for industrial applications will be possible.

References

1 R. Alfano and S. Shapiro, "Emission in the region 4000 to 7000 Å via four-photon coupling in glass," Phys. Rev. Lett. **24,** 584 (1970).

2 F. Shimizu, "Frequency broadening in liquids by a short light pulse," Phys. Rev. Lett. **19,** 1097 (1967).

3 P. Corkum, C. Rolland, and T. Srinivasan-Rao, "Supercontinuum generation in gases," Phys. Rev. Lett. **57,** 2268 (1986).

4 E. Nibbering, P. Curley, G. Grillon, B. Prade, M. Franco, F. Salin, and A. Mysyrowicz, "Conical emission from self-guided femtosecond pulses in air," Opt. Lett. **21,** 62-64 (1996).

5 K. M. Davis, K. Miura, N. Sugimoto, and K. Hirao, "Writing waveguides in glass with a femtosecond laser," Opt. Lett. **21,** 1729-1731 (1996).

6 H. Mochizuki, W. Watanabe, R. Ezoe, T. Tamaki, Y. Ozeki, K. Itoh, M. Kasuya, K. Matsuda, and S. Hirono, "Density characterization of femtosecond laser modification in polymers

7 A. Baum, P. J. Scully, W. Perrie, D. Jones, R. Issac, and D. A. Jaroszynski, "Pulse-duration dependency of femtosecond laser refractive index modification in poly (methyl methacrylate)," Opt. Lett. **33,** 651-653 (2008).

8 E. J. J. Samuel and S. Mohan, "FTIR and FT Raman spectra and analysis of poly (4-methyl-1-pentene)," Spectrochimica Acta Part A: Molecular and Biomolecular Spectroscopy **60,** 19-24 (2004).

9 J. D. Lytle, G. W. Wilkerson, and J. G. Jaramillo, "Wideband optical transmission properties of seven thermoplastics," Appl. Opt. **18,** 1842-1846 (1979).

10 J. Qiu, K. Miura, and K. Hirao, "Three-dimensional optical memory using glasses as a recording medium through a multi-photon absorption process," Japanese journal of applied physics **37,** 2263 (1998).

11 S. Wackerow, G. Seifert, and A. Abdolvand, "Homogenous silver-doped nanocomposite glass," Optical Materials Express **1,** 1224-1231 (2011).

12 M. Padgett and R. Bowman, "Tweezers with a twist," Nature Photonics **5,** 343-348 (2011).

13 A. Ambrosio, L. Marrucci, F. Borbone, A. Roviello, and P. Maddalena, "Light-induced spiral mass transport in azo-polymer films under vortex-beam illumination," Nature communications **3,** 989 (2012).

14 V. Lauer, "New approach to optical diffraction tomography yielding a vector equation of diffraction tomography and a novel tomographic microscope," J. Microsc. **205,** 165-176 (2002).

15 G. Sinclair, J. Leach, P. Jordan, G. Gibson, E. Yao, Z. J. Laczik, M. J. Padgett, and J. Courtial, "Interactive application in holographic optical tweezers of a multi-plane Gerchberg-Saxton algorithm for three-dimensional light shaping," Optics Express **12,** 1665-1670 (2004).

16 Y. I. Salamin and C. H. Keitel, "Electron acceleration by a tightly focused laser beam," Phys. Rev. Lett. **88,** 095005 (2002).

17 D. J. McKnight, D. G. Vass, and R. M. Sillitto, "Development of a spatial light modulator: a randomly addressed liquid-crystal-over-nMOS array," Appl. Opt. **28,** 4757-4762 (1989).

18 D. J. McKnight, K. M. Johnson, and R. A. Serati, "256× 256 liquid-crystal-on-silicon spatial light modulator," Appl. Opt. **33,** 2775-2784 (1994).

19 G. D. Love, "Wave-front correction and production of Zernike modes with a liquid-crystal spatial light modulator," Appl. Opt. **36,** 1517-1524 (1997).

20 A. S. Ostrovsky, C. Rickenstorff-Parrao, and V. Arrizón, "Generation of the “perfect” optical vortex using a liquid-crystal spatial light modulator," Opt. Lett. **38,** 534-536 (2013).

21 A. M. Yao and M. J. Padgett, "Orbital angular momentum: origins, behavior and applications," Advances in Optics and Photonics **3,** 161-204 (2011).

22 J. Ouyang, W. Perrie, O. Allegre, T. Heil, Y. Jin, E. Fearon, D. Eckford, S. Edwardson, and G. Dearden, "Tailored optical vector fields for ultrashort-pulse laser induced complex surface plasmon structuring," Optics express **23,** 12562-12572 (2015)

23 Y. Jin, O. Allegre, W. Perrie, K. Abrams, J. Ouyang, E. Fearon, S. Edwardson, and G. Dearden, "Dynamic modulation of spatially structured polarization fields for real-time control of ultrafast laser-material interactions," Optics express **21,** 25333-25343 (2013).

24 H. Mochizuki, W. Watanabe, R. Ezoe, T. Tamaki, Y. Ozeki, K. Itoh, M. Kasuya, K. Matsuda, and S. Hirono, "Density characterization of femtosecond laser modification in polymers," Appl. Phys. Lett. **92,** 091120 (2008).

25 H. Mochizuki, W. Watanabe, R. Ezoe, T. Tamaki, Y. Ozeki, K. Itoh, M. Kasuya, K. Matsuda, and S. Hirono, "Density characterization of femtosecond laser modification in polymers," Appl. Phys. Lett. **92,** 091120 (2008).

26 B. Dorin, G. Zhu, P. Parkinson, W. Perrie, M. Benyezzar, and P. Scully, "Characterization of a silica-PVA hybrid for high density and stable silver dissolution," Mater. Chem. Phys. **177,** 19-24 (2016)

27 https://www.trumpf-scientific-lasers.com

28 T. Klerks and S. Eifel, “Flexible beam shaping system for next generation of process developments in laser micro-machining”, 9th International conference on Photonic technologies, LANE 2016 (Industrial paper)

29 A. Couairon, L. Sudrie, M. Franco, B. Prade, and A. Mysyrowicz, "Filamentation and damage in fused silica induced by tightly focused femtosecond laser pulses," Physical Review B **71,** 125435 (2005).

30 K. Itoh, W. Watanabe, and Y. Ozeki, "Nonlinear ultrafast focal-point optics for microscopic imaging, manipulation, and machining," Proc IEEE **97,** 1011-1030 (2009).

31 R. Boyd, "Nonlinear Optics 3rd edn (New York: Academic)," 161-183 (2008).

32 G. Zverev and V. Pashkov, "Self-focusing of laser radiation in solid dielectrics," Sov.Phys.—JETP **30,** 616-621 (1970).

33 A. Brodeur, C. Chien, F. Ilkov, S. Chin, O. Kosareva, and V. Kandidov, "Moving focus in the propagation of ultrashort laser pulses in air," Opt. Lett. **22,** 304-306 (1997).

34 G. K. Wong, S. G. Murdoch, R. Leonhardt, and J. D. Harvey, "Widely-tunable high-conversion-efficiency chi (3) parametric oscillator," in *Optical Internet, 2007 and the 2007 32nd Australian Conference on Optical Fibre Technology. COIN-ACOFT 2007. Joint International Conference on,* Anonymous (IEEE, 2007), pp. 1-3.

35 R. Noskov, A. Krasnok, and Y. S. Kivshar, "Nonlinear metal–dielectric nanoantennas for light switching and routing," New Journal of Physics **14,** 093005 (2012).

36 J. García-Merino, C. Mercado-Zúñiga, C. Martínez-González, C. Torres-SanMiguel, J. Vargas-García, and C. Torres-Torres, "Magneto-conductive encryption assisted by third-order nonlinear optical effects in carbon/metal nanohybrids," Materials Research Express **4,** 035601 (2017).

37 R. Hellwarth, "Third-order optical susceptibilities of liquids and solids," Progress in Quantum Electronics **5,** 1-68 (1977).

38 Boyd R W and Fischer G L, Nonlinear optical materials *Encyclopedia of materials*; Science and technology (Oxford: Elsevier) pp6237-44 (2001).

39 A. Couairon and A. Mysyrowicz, "Femtosecond filamentation in transparent media," Physics reports **441,** 47-189 (2007)

40 B. Buchalter and G. R. Meredith, "Third-order optical susceptibility of glasses determined by third harmonic generation," Appl. Opt. **21,** 3221-3224 (1982).

41 F. D’Amore, M. Lanata, S. M. Pietralunga, M. C. Gallazzi, and G. Zerbi, "Enhancement of PMMA nonlinear optical properties by means of a quinoid molecule," Optical Materials **24,** 661-665 (2004).

42 U. Gubler and C. Bosshard, "Optical third-harmonic generation of fused silica in gas atmosphere: Absolute value of the third-order nonlinear optical susceptibility χ (3)," Physical Review B **61,** 10702 (2000).

43 J. C. Phillips and J. Van Vechten, "Nonlinear optical susceptibilities of covalent crystals," Physical Review **183,** 709 (1969).

44 C. B. Schaffer, A. Brodeur, J. F. García, and E. Mazur, "Micromachining bulk glass by use of femtosecond laser pulses with nanojoule energy," Opt. Lett. **26,** 93-95 (2001)

45 M. Lenzner, J. Krüger, S. Sartania, Z. Cheng, C. Spielmann, G. Mourou, W. Kautek, and F. Krausz, "Femtosecond optical breakdown in dielectrics," Phys. Rev. Lett. **80,** 4076 (1998).

46 A. Baum, P. J. Scully, W. Perrie, D. Jones, R. Issac, and D. A. Jaroszynski, "Pulse-duration dependency of femtosecond laser refractive index modification in poly (methyl methacrylate)," Opt. Lett. **33,** 651-653 (2008)

47 A. Q. Wu, I. H. Chowdhury, and X. Xu, "Femtosecond laser absorption in fused silica: Numerical and experimental investigation," Physical Review B **72,** 085128 (2005).

48 W. Luo, S. Ismail-Beigi, M. L. Cohen, and S. G. Louie, "Quasiparticle band structure of ZnS and ZnSe," Physical Review B **66,** 195215 (2002).

49 www.goodfellow.com/E/Sapphire.html

50 L. Keldysh, "Ionization in the field of a strong electromagnetic wave," Sov.Phys.JETP **20,** 1307-1314 (1965).

51 S. C. Jones, P. Braunlich, R. T. Casper, X. Shen, and P. Kelly, "Recent progress on laser-induced modifications and intrinsic bulk damage of wide-gap optical materials," Optical Engineering **28,** 281039-281039-(1989).

52 N. Nguyen, A. Saliminia, W. Liu, S. Chin, and R. Vallée, "Optical breakdown versus filamentation in fused silica by use of femtosecond infrared laser pulses," Opt. Lett. **28,** 1591-1593 (2003).

53 D. Du, X. Liu, G. Korn, J. Squier, and G. Mourou, "Laser-induced breakdown by impact ionization in SiO2 with pulse widths from 7 ns to 150 fs," Appl. Phys. Lett. **64,** 3071-3073 (1994).

54 A. Ruehl, M. J. Martin, K. C. Cossel, L. Chen, H. McKay, B. Thomas, C. Benko, L. Dong, J. M. Dudley, and M. E. Fermann, "Ultrabroadband coherent supercontinuum frequency comb," Physical Review A **84,** 011806 (2011).

55 G. Genty, S. Coen, and J. M. Dudley, "Fiber supercontinuum sources," JOSA B **24,** 1771-1785 (2007).

56 K. Lindfors, T. Kalkbrenner, P. Stoller, and V. Sandoghdar, "Detection and spectroscopy of gold nanoparticles using supercontinuum white light

confocal microscopy," Phys. Rev. Lett. **93,** 037401 (2004).

57 A. F. Fercher, W. Drexler, C. K. Hitzenberger, and T. Lasser, "Optical coherence tomography-principles and applications," Reports on progress in physics **66,** 239 (2003).

58 R. Alfano and S. Shapiro, "Emission in the region 4000 to 7000 Å via four-photon coupling in glass," Phys. Rev. Lett. **24,** 584 (1970).

59 E. Riedle, M. Beutter, S. Lochbrunner, J. Piel, S. Schenkl, S. Spörlein, and W. Zinth, "Generation of 10 to 50 fs pulses tunable through all of the visible and the NIR," Appl. Phy. B **71,** 457-465 (2000).

60 N. Il'Ichev, V. Koroblin, V. Korshunov, A. Malyntin, T. Okroashvili, and P. Paining, "Superbroadening of the spectrum of ultrashort pulses in liquids and glasses," JETP Lett. **15,** 133-135 (1972).

61 E. Nibbering, P. Curley, G. Grillon, B. Prade, M. Franco, F. Salin, and A. Mysyrowicz, "Conical emission from self-guided femtosecond pulses in air," Opt. Lett. **21,** 62-64 (1996).

62 R. Y. Chiao, E. Garmire, and C. H. Townes, "Self-trapping of optical beams," Phys. Rev. Lett. **13,** 479 (1964).

63 N. Bondarenko, I. Eremina, and V. Talanov, "Broadening of Spectrum in Self Focusing of Light in Crystals," Soviet Journal of Experimental and Theoretical Physics Letters **12,** 85 (1970).

64 W. Werncke, A. Lau, M. Pfeiffer, K. Lenz, H. Weigmann, and C. Thuy, "An anomalous frequency broadening in water," Opt. Commun. **4,** 413-415 (1972).

65 N. Bloembergen, "Role of cracks, pores, and absorbing inclusions on laser induced damage threshold at surfaces of transparent dielectrics," Appl. Opt. **12,** 661-664 (1973).

66 A. Brodeur and S. Chin, "Band-gap dependence of the ultrafast white-light continuum," Phys. Rev. Lett. **80,** 4406 (1998).

67 A. Brodeur and S. Chin, "Ultrafast white-light continuum generation and self-focusing in transparent condensed media," JOSA B **16,** 637-650 (1999).

68 Y. Dong, C. Zorman, and P. Molian, "Femtosecond pulsed laser micromachining of single crystalline 3C–SiC structures based on a laser-induced defect-activation process," J Micromech Microengineering **13,** 680 (2003).

69 T. Kurobori, K. Kawamura, M. Hirano, and H. Hosono, "Simultaneous fabrication of laser-active colour centres and permanent micrograting in lithium fluoride by a single femtosecond pulse," Journal of Physics: Condensed Matter **15,** L399 (2003).

70 N. Nguyen, A. Saliminia, S. Chin, and R. Vallée, "Control of femtosecond laser written waveguides in silica glass," Applied Physics B **85,** 145-148 (2006).

71 J. Morikawa, A. Orie, T. Hashimoto, and S. Juodkazis, "Thermal and optical properties of femtosecond-laser-structured PMMA," Appl. Phys. A **101,** 27-31 (2010).

72 G. Cerullo, R. Osellame, S. Taccheo, M. Marangoni, D. Polli, R. Ramponi, P. Laporta, and S. De Silvestri, "Femtosecond micromachining of symmetric waveguides at 1.5 μm by astigmatic beam focusing," Opt. Lett. 27, 1938-1940 (2002).

73 K. Yamada, W. Watanabe, T. Toma, K. Itoh, and J. Nishii, "In situ observation of photoinduced refractive-index changes in filaments formed in glasses by femtosecond laser pulses," Opt. Lett. **26,** 19-21 (2001).

74 J. W. Chan, T. Huser, S. Risbud, and D. Krol, "Structural changes in fused silica after exposure to focused femtosecond laser pulses," Opt. Lett. **26,** 1726-1728 (2001).

75 C. B. Schaffer, A. Brodeur, and E. Mazur, "Laser-induced breakdown and damage in bulk transparent materials induced by tightly focused femtosecond laser pulses," Measurement Science and Technology **12,** 1784 (2001).

76 P. Saeta, J. Wang, Y. Siegal, N. Bloembergen, and E. Mazur, "Ultrafast electronic disordering during femtosecond laser melting of GaAs," Phys. Rev. Lett. **67,** 1023 (1991).

77 A. Baum, P. J. Scully, M. Basanta, C. P. Thomas, P. R. Fielden, N. J. Goddard, W. Perrie, and P. R. Chalker, "Photochemistry of refractive index structures in poly (methyl methacrylate) by femtosecond laser irradiation," Opt. Lett. **32,** 190-192 (2007).

78 A. Baum, P. J. Scully, W. Perrie, D. Jones, R. Issac, and D. A. Jaroszynski, "Pulse-duration dependency of femtosecond laser refractive index modification in poly (methyl methacrylate)," Opt. Lett. **33,** 651-653 (2008).

79 S. Wackerow, G. Seifert, and A. Abdolvand, "Homogenous silver-doped nanocomposite glass," Optical Materials Express **1,** 1224-1231 (2011).

80 J. Qiu, K. Miura, and K. Hirao, "Three-dimensional optical memory using glasses as a recording medium through a multi-photon absorption process," Japanese journal of applied physics **37,** 2263 (1998).

81 T. R. Jensen, M. D. Malinsky, C. L. Haynes, and R. P. Van Duyne, "Nanosphere lithography: tunable localized surface plasmon resonance spectra of silver nanoparticles," The Journal of Physical Chemistry B **104,** 10549-10556 (2000).

82 A. Stalmashonak, G. Seifert, and H. Graener, "Spectral range extension of laser-induced dichroism in composite glass with silver nanoparticles," Journal of Optics A: Pure and Applied Optics **11,** 065001 (2009).

83 A. N. Ananth, S. K. Daniel, T. A. Sironmani, and S. Umapathi, "PVA and BSA stabilized silver nanoparticles based surface–enhanced plasmon resonance probes for protein detection," Colloids and Surfaces B: Biointerfaces **85,** 138-144 (2011).

84 A. Stalmashonak, A. Abdolvand, and G. Seifert, "Metal-glass nanocomposite for optical storage of information," Appl. Phys. Lett. **99,** 201904 (2011).

85 T. Südmeyer, C. Kränkel, C. Baer, O. Heckl, C. Saraceno, M. Golling, R. Peters, K. Petermann, G. Huber, and U. Keller, "High-power ultrafast thin disk laser oscillators and their potential for sub-100-femtosecond pulse generation," Applied Physics B **97,** 281 (2009).

86 S. Guenther, M. Koestler, O. Schulz, and B. Spengler, "Laser spot size and laser power dependence of ion formation in high resolution MALDI imaging," International Journal of Mass Spectrometry **294,** 7-15 (2010).

87 A. Schliesser, N. Picqué, and T. W. Hänsch, "Mid-infrared frequency combs," Nature Photonics **6,** 440 (2012).

88 M. R. Dennis, K. O'Holleran, and M. J. Padgett, "Singular optics: optical vortices and polarization singularities," Progress in Optics **53,** 293-363 (2009).

89 A. M. Yao and M. J. Padgett, "Orbital angular momentum: origins, behavior and applications," Advances in Optics and Photonics **3,** 161-204 (2011).

90 M. Harris, C. Hill, and J. Vaughan, "Optical helices and spiral interference fringes," Opt. Commun. **106,** 161-166 (1994).

91 M. R. Dennis, K. O'Holleran, and M. J. Padgett, "Singular optics: optical vortices and polarization singularities," Progress in Optics **53,** 293-363 (2009).

92 T. Yusufu, Y. Tokizane, M. Yamada, K. Miyamoto, and T. Omatsu, "Tunable 2-μm optical vortex parametric oscillator," Optics Express **20,** 23666-23675 (2012).

93 L. Ju, T. Huang, K. Xiao, G. Wu, S. Yang, R. Li, Y. Yang, T. Long, H. Zhang, and S. Wu, "Controlling multiple filaments by relativistic optical vortex beams in plasmas," Physical Review E **94,** 033202 (2016).

94 M. Andersen, C. Ryu, P. Cladé, V. Natarajan, A. Vaziri, K. Helmerson, and W. D. Phillips, "Quantized rotation of atoms from photons with orbital angular momentum," Phys. Rev. Lett. **97,** 170406 (2006).

95 W. Jiang, Q. Chen, Y. Zhang, and G. Guo, "Computation of topological charges of optical vortices via nondegenerate four-wave mixing,"

Physical Review A **74,** 043811 (2006).

96 R. Fickler, R. Lapkiewicz, W. N. Plick, M. Krenn, C. Schaeff, S. Ramelow, and A. Zeilinger, "Quantum entanglement of high angular momenta," Science **338,** 640-643 (2012).

97 R. A. Bartels, A. Paul, H. Green, H. C. Kapteyn, M. M. Murnane, S. Backus, I. P. Christov, Y. Liu, D. Attwood, and C. Jacobsen, "Generation of spatially coherent light at extreme ultraviolet wavelengths," Science **297,** 376-378 (2002).

98 A. S. Desyatnikov, L. Torner, and Y. S. Kivshar, "Optical vortices and vortex solitons," arXiv preprint nlin/0501026 (2005).

99 A. M. Yao and M. J. Padgett, "Orbital angular momentum: origins, behavior and applications," Advances in Optics and Photonics **3,** 161-204 (2011).

100 J. Courtial, K. Dholakia, L. Allen, and M. Padgett, "Second-harmonic generation and the conservation of orbital angular momentum with high-order Laguerre-Gaussian modes," Physical Review A **56,** 4193 (1997).

101 P. Miao, Z. Zhang, J. Sun, W. Walasik, S. Longhi, N. M. Litchinitser, and L. Feng, "Orbital angular momentum microlaser," Science **353,** 464-467 (2016).

102 G. Swartzlander Jr and C. T. Law, "Optical vortex solitons observed in Kerr nonlinear media," Phys. Rev. Lett. **69,** 2503 (1992).

103 K. E. Strecker, G. B. Partridge, A. G. Truscott, and R. G. Hulet, "Formation and propagation of matter-wave soliton trains," Nature **417,** 150-153 (2002).

104 D. Mihalache, D. Mazilu, L. Crasovan, I. Towers, A. Buryak, B. A. Malomed, L. Torner, J. Torres, and F. Lederer, "Stable spinning optical solitons in three dimensions," Phys. Rev. Lett. **88,** 073902 (2002).

105 J. R. Salgueiro, A. H. Carlsson, E. Ostrovskaya, and Y. Kivshar, "Second-harmonic generation in vortex-induced waveguides," Opt. Lett. **29,** 593-595 (2004).

106 G. Swartzlander Jr and C. T. Law, "Optical vortex solitons observed in Kerr nonlinear media," Phys. Rev. Lett. **69,** 2503 (1992).

107 W. J. Firth and D. V. Skryabin, "Optical solitons carrying orbital angular momentum," Phys. Rev. Lett. **79,** 2450 (1997).

108 D. V. Skryabin and W. J. Firth, "Dynamics of self-trapped beams with phase dislocation in saturable Kerr and quadratic nonlinear media," Physical Review E **58,** 3916 (1998).

109 M. Berry and M. Dennis, "Polarization singularities in isotropic random vector waves," in *Proceedings of the Royal Society of London A: Mathematical, Physical and Engineering Sciences*, Anonymous (The

Royal Society, 2001), pp. 141-155.

110 V. Yannopapas, "Photonic analog of a spin-polarized system with Rashba spin-orbit coupling," Physical Review B **83,** 113101 (2011).

111 S. Li, L. Kong, Z. Ren, Y. Li, C. Tu, and H. Wang, "Managing orbital angular momentum in second-harmonic generation," Physical Review A **88,** 035801 (2013).

112 A. Ambrosio, L. Marrucci, F. Borbone, A. Roviello, and P. Maddalena, "Light-induced spiral mass transport in azo-polymer films under vortex-beam illumination," Nature communications **3,** 989 (2012).

113 M. Padgett and R. Bowman, "Tweezers with a twist," Nature Photonics **5,** 343-348 (2011).

114 H. Toyota, K. Takahara, M. Okano, T. Yotsuya, and H. Kikuta, "Fabrication of microcone array for antireflection structured surface using metal dotted pattern," Japanese Journal of Applied Physics **40,** L747 (2001).

115 D. Barada, G. Juman, I. Yoshida, K. Miyamoto, S. Kawata, S. Ohno, and T. Omatsu, "Constructive spin-orbital angular momentum coupling can twist materials to create spiral structures in optical vortex illumination," Appl. Phys. Lett. **108,** 051108 (2016).

116 https://physics.anu.edu.au/laser/research/processing.php

117 M. Stalder and M. Schadt, "Polarization converters based on liquid crystal devices," Molecular Crystals and Liquid Crystals **282,** 343-353 (1996).

118 B. Spekto, A. Normatov and J. Shamir, 2008. Singular beam microscopy. Applied optics, 47(4), pp.A78-A87.

119 Y. Kozawa and S. Sato, 2010. Optical trapping of micrometer-sized dielectric particles by cylindrical vector beams. Optics Express, 18(10), pp.10828-10833.

120 Y.I.Salamin, and C.H. Keitel, 2002. Electron acceleration by a tightly focused laser beam. Physical review letters, 88(9), p.095005.

121 G. Machavariani, Y. Lumer, I. Moshe, A. Meir, and S. Jackel, "Efficient extracavity generation of radially and azimuthally polarized beams," Opt. Lett. **32,** 1468-1470 (2007).

122 A. Couairon, "Dynamics of femtosecond filamentation from saturation of self-focusing laser pulses," Physical Review A **68,** 015801 (2003).

123 J.M. Guay, A. Villafranca, F. Baset, K. Popov, L. Ramunno and V.R. Bhardwaj, 2012. Polarization-dependent femtosecond laser ablation of poly-methyl methacrylate. New Journal of Physics, 14(8), p.085010.

124 G.R. Fowles, 1975. Introduction to modern optics. Courier Corporation.

125 H. Kleinpoppen, Constituents of Matter, Atoms, Molecules, Nuclei and Particles, p142, Ed. Bergmann/Schaefer, Copyright Walter de Gruyer, Berlin, New York (1997),Berlin, Germany … Rev. Lett. 97(23), 237403 (2006). 13.

126 L. Bergé, S. Skupin, F. Lederer, G. Méjean, J. Yu, J. Kasparian, E. Salmon, J. Wolf, M. Rodriguez, and L. Wöste, "Multiple filamentation of terawatt laser pulses in air," Phys. Rev. Lett. **92,** 225002 (2004).

127 F. H. Faisal, "Multiple absorption of laser photons by atoms," Journal of Physics B: Atomic and Molecular Physics **6,** L89 (1973).

128 P. Monson and W. McClain, "Polarization Dependence of the Two-Photon Absorption of Tumbling Molecules with Application to Liquid 1-Chloronaphthalene and Benzene," J. Chem. Phys. 53, 29-37 (1970).

129 T. R. Bader and A. Gold, "Polarization dependence of two-photon absorption in solids," Physical Review **171,** 997 (1968)

130 W. Gawelda, D. Puerto, J. Siegel, A. Ferrer, Ruiz De La Cruz, A, H. Fernandez, and J. Solis, "Ultrafast imaging of transient electronic plasmas produced in conditions of femtosecond waveguide writing in dielectrics," Appl. Phys. Lett. **93,** 121109 (2008).

131 R.W. Boyd and G. L. Fischer G L, Nonlinear Optics 3rd edn (Burlington, MA: Academic) Chapter 4, pp207-52.

132 Temnov, K. Sokolowski-Tinten, P. Zhou, A. El-Khamhawy, and D. Von Der Linde, "Multiphoton ionization in dielectrics: comparison of circular and linear polarization," Phys. Rev. Lett. **97,** 237403 (2006).

133 H. Reiss, "Spectrum of atomic electrons ionised by an intense field," Journal of Physics B: Atomic and Molecular Physics **20,** L79 (1987).

134 H. Carman Jr and R. Compton, "High-order multiphoton ionization photoelectron spectroscopy of nitric oxide," J. Chem. Phys. 90, 1307-1312 (1989).

135 S. Nolte, G. Kamlage, F. Korte, T. Bauer, T. Wagner, A. Ostendorf, C. Fallnich and H. Welling, 2000. Microstructuring with femtosecond lasers. Advanced Engineering Materials, 2(1-2), pp.23-27.

136 A. Weber and E. Ivers-Tiffée, 2004. Materials and concepts for solid oxide fuel cells (SOFCs) in stationary and mobile applications. Journal of Power Sources, 127(1-2), pp.273-283.

137 M. Meier, V. Romano, V. and T. Feurer, 2007. Material processing with pulsed radially and azimuthally polarized laser radiation. Applied Physics A, 86(3), pp.329-334.

138 J. Ouyang, W. Perrie, O.J. Allegre, T. Heil, Y.Jin, E. Fearon, D. Eckford, S.P. Edwardson and G. Dearden, 2015. Tailored optical vector fields for ultrashort-pulse laser induced complex surface plasmon structuring. Optics Express, 23(10), pp.12562-12572.

139 J. Bonse, A. Rosenfeld, and J. Krüger, "On the role of surface plasmon polaritons in the formation of laser-induced periodic surface structures upon irradiation of silicon by femtosecond-laser pulses," J. Appl. Phys. **106,** 104910 (2009).

140 F. Garrelie, J. Colombier, F. Pigeon, S. Tonchev, N. Faure, M. Bounhalli, S. Reynaud, and O. Parriaux, "Evidence of surface plasmon resonance in ultrafast laser-induced ripples," Optics express **19,** 9035-9043 (2011).

141 Y. Shimotsuma, P. G. Kazansky, J. Qiu, and K. Hirao, "Self-organized nanogratings in glass irradiated by ultrashort light pulses," Phys. Rev. Lett. **91,** 247405 (2003).

142 D. Du, X. Liu, G. Korn, J. Squier, and G. Mourou, "Laser induced breakdown by impact ionization in SiO2 with pulse widths from 7 ns to 150 fs," Appl. Phys. Lett. **64,** 3071-3073 (1994).

143 A. Baum, P. J. Scully, W. Perrie, D. Jones, R. Issac, and D. A. Jaroszynski, "Pulse-duration dependency of femtosecond laser refractive index modification in poly (methyl methacrylate)," Opt. Lett. **33,** 651-653 (2008).

144 C. B. Schaffer, J. F. García, and E. Mazur, "Bulk heating of transparent materials using a high-repetition-rate femtosecond laser," Applied Physics A **76,** 351-354 (2003).

145 D. Von der Linde and H. Schüler, "Breakdown threshold and plasma formation in femtosecond laser–solid interaction," JOSA B **13,** 216-222 (1996).

146 J. B. Ashcom, R. R. Gattass, C. B. Schaffer, and E. Mazur, "Numerical aperture dependence of damage and supercontinuum generation from femtosecond laser pulses in bulk fused silica," JOSA B **23,** 2317-2322 (2006).

147 E. Glezer, M. Milosavljevic, L. Huang, R. Finlay, T. Her, J. P. Callan, and E. Mazur, "Three-dimensional optical storage inside transparent materials," Opt. Lett. **21,** 2023-2025 (1996).

148 C. B. Schaffer, A. Brodeur, and E. Mazur, "Laser-induced breakdown and damage in bulk transparent materials induced by tightly focused femtosecond laser pulses," Measurement Science and Technology **12,** 1784 (2001).

149 K. Miura, J. Qiu, H. Inouye, T. Mitsuyu, and K. Hirao, "Photowritten optical waveguides in various glasses with ultrashort pulse laser," Appl. Phys. Lett. **71,** 3329-3331 (1997).

150 S. Sowa, W. Watanabe, T. Tamaki, J. Nishii, and K. Itoh, "Symmetric waveguides in poly (methyl methacrylate) fabricated by femtosecond laser pulses," Optics Express **14,** 291-297 (2006).

151 A. Okhrimchuk, V. Mezentsev, A. Shestakov, and I. Bennion, "Low loss depressed cladding waveguide inscribed in YAG: Nd single crystal by femtosecond laser pulses," Optics express **20,** 3832-3843 (2012).

152 F. Chen and J. Aldana, "Optical waveguides in crystalline dielectric materials produced by femtosecond-laser micromachining," Laser & Photonics Reviews **8,** 251-275 (2014).

153 G. Martin and R. Hellwarth, "Infrared-to-optical image conversion by Bragg reflection from thermally induced index gratings," Appl. Phys. Lett. **34,** 371-373 (1979).

154 S. C. Barden, J. A. Arns, W. S. Colburn, and J. B. Williams, "Volume-phase holographic gratings and the efficiency of three simple volume-phase holographic gratings," Publications of the Astronomical Society of the Pacific **112,** 809 (2000).

155 S. Blais-Ouellette, O. Daigle, and K. Taylor, "The imaging Bragg tunable filter: a new path to integral field spectroscopy and narrow band imaging," in *Ground-based and Airborne Instrumentation for Astronomy*, Anonymous (International Society for Optics and Photonics, 2006), pp. 62695H.

156 D. Strickland and G. Mourou, "Compression of amplified chirped optical pulses," Opt. Commun. **55,** 447-449 (1985).

157 B. W. Atherton and M. K. Reed, "Pre-chirped fiber transport of 800 nm 100 fs pulses," in *Proc. SPIE*, Anonymous (, 1998), pp. 22-25.

158 H. Kogelnik, "The Bell System Technical Journal," Volume **48,** 2909-2947 (1969)

159 S. Kawata and Y. Kawata, "Three-dimensional optical data storage using photochromic materials," Chem. Rev. **100,** 1777-1788 (2000).

160 M. Masuda, K. Sugioka, Y. Cheng, T. Hongo, K. Shihoyama, H. Takai, I. Miyamoto, and K. Midorikawa, "Direct fabrication of freely movable microplate inside photosensitive glass by femtosecond laser for lab-on-chip application," Appl. Phys. A **78,** 1029-1032 (2004).

161 H. Ma, A. Jen, and L. R. Dalton, "Polymer-based optical waveguides: materials, processing, and devices," Adv Mater **14,** 1339-1365 (2002).

162 K. Miura, J. Qiu, S. Fujiwara, S. Sakaguchi, and K. Hirao, "Three-dimensional optical memory with rewriteable and ultrahigh density using the valence-state change of samarium ions," Appl. Phys. Lett. **80,** 2263-2265 (2002).

163 S. Fedotov, R. Drevinskas, S. Lotarev, A. Lipatiev, M. Beresna, A. Čerkauskaitė, V. Sigaev, and P. Kazansky, "Direct writing of birefringent elements by ultrafast laser nanostructuring in multicomponent glass," Appl. Phys. Lett. **108,** 071905 (2016).

164 J. Rapp, C. Glumann, F. Dausinger and H. Hügel, 1995. Laser welding of aluminium lightweight materials: problems, solutions, readiness for application. Optical and Quantum Electronics, 27(12), pp.1203-1211.

165 K. Choi, J. Kim, Y. Lee, and H. Kim, "ITO/Ag/ITO multilayer films for the application of a very low resistance transparent electrode," Thin Solid Films **341,** 152-155 (1999).

166 www.hamamatsu.com

167 Y. Jin, O. Allegre, W. Perrie, K. Abrams, J. Ouyang, E. Fearon, S. Edwardson, and G. Dearden, "Dynamic modulation of spatially structured polarization fields for real-time control of ultrafast laser-material interactions," Optics express **21,** 25333-25343 (2013).

168 J. A. Davis, D. E. McNamara, D. M. Cottrell, and T. Sonehara, "Two-dimensional polarization encoding with a phase-only liquid-crystal spatial light modulator," Appl. Opt. **39,** 1549-1554 (2000).

169 N. Mukohzaka, N. Yoshida, H. Toyoda, Y. Kobayashi, and T. Hara, "Diffraction efficiency analysis of a parallel-aligned nematic-liquid-crystal spatial light modulator," Appl. Opt. **33,** 2804-2811 (1994).

170 R.J.Beck, J.P. Parry, W.N. MacPherson, A. Waddie, N.J.Weston, J.D. Shephard, and D.P. Hand, D.P., 2010. Application of cooled spatial light modulator for high power nanosecond laser micromachining. Optics express, 18(16), pp.17059-17065.

171 T. Klerks and S. Eifal, “Flexible beam shaping system for next generation of process developments in laser micro-machining”, 9th International conference on Photonic technologies, LANE 2016 (Industrial paper)

172 J. R. Leger, D. Chen, and Z. Wang, "Diffractive optical element for mode shaping of a Nd: YAG laser," Opt. Lett. **19,** 108-110 (1994).

173 C. Giles, V. Aksyuk, B. Barber, R. Ruel, L. Stulz, and D. Bishop, "A silicon MEMS optical switch attenuator and its use in lightwave subsystems," IEEE Journal of selected topics in quantum electronics **5,** 18-25 (1999).

174 K. J. Mitchell, S. Turtaev, M. J.Padgett, T. Cizmar and D. J. Phillips, “High speed spatial control of the intensity, phase and polarisation of vector beams using digital micro-mirror device” Optics Express, 24(25), 29269-29282 (2016)

175 J. Kato, N. Takeyasu, Y. Adachi, H. Sun, and S. Kawata, "Multiple-spot parallel processing for laser micronanofabrication," Appl. Phys. Lett. **86,** 044102 (2005).

176 A. M. Weiner, "Femtosecond pulse shaping using spatial light modulators," Rev. Sci. Instrum. **71,** 1929-1960 (2000).

177 G. Sinclair, J. Leach, P. Jordan, G. Gibson, E. Yao, Z. J. Laczik, M. J. Padgett, and J. Courtial, "Interactive application in holographic optical tweezers of a multi-plane Gerchberg-Saxton algorithm for three-dimensional light shaping," Optics Express **12,** 1665-1670 (2004).

178 X. Xun, X. Chang, and R. W. Cohn, "System for demonstrating arbitrary multi-spot beam steering from spatial light modulators," Optics express **12,** 260-268 (2004).

179 Z. Kuang, D. Liu, W. Perrie, S. Edwardson, M. Sharp, E. Fearon, G. Dearden, and K. Watkins, "Fast parallel diffractive multi-beam femtosecond laser surface micro-structuring," Appl. Surf. Sci. **255,** 6582-6588 (2009).

180 D. Liu, Z. Kuang, W. Perrie, P. Scully, A. Baum, S. Edwardson, E. Fearon, G. Dearden, and K. Watkins, "High-speed uniform parallel 3D refractive index micro-structuring of poly (methyl methacrylate) for volume phase gratings," Appl. Phy. B **101,** 817-823 (2010).

181 L. Ye, W. Perrie, O. Allegre, Y. Jin, Z. Kuang, P. Scully, E. Fearon, D. Eckford, S. Edwardson, and G. Dearden, "NUV femtosecond laser inscription of volume Bragg gratings in poly (methyl) methacrylate with linear and circular polarizations," Laser Physics **23,** 126004 (2013).

182 J. A. Davis, D. E. McNamara, D. M. Cottrell, and T. Sonehara, "Two-dimensional polarization encoding with a phase-only liquid-crystal spatial light modulator," Appl. Opt. **39,** 1549-1554 (2000).

183 H. Kong and J. Jang, "Antibacterial properties of novel poly (methyl methacrylate) nanofiber containing silver nanoparticles," Langmuir **24,** 2051-2056 (2008).

184 H. Zhang, I. Hussain, M. Brust, M. F. Butler, S. P. Rannard, and A. I. Cooper, "Aligned two-and three-dimensional structures by directional freezing of polymers and nanoparticles," Nature materials **4,** 787-793 (2005).

185 A. Dan, B. Satpati, P. Satyam, and D. Chakravorty, "Diodelike behavior in glass–metal nanocomposites," J. Appl. Phys. **93,** 4794-4800 (2003).

186 Sarkar, D.K., Cloutier, F. and El Khakani, M.A., 2005. Electrical switching in sol–gel derived Ag–Si O 2 nanocomposite thin films. *Journal of applied physics*, *97*(8), p.084302.

187 J. Almeida, L. De Boni, W. Avansi, C. Ribeiro, E. Longo, A. C. Hernandes, and C. R. Mendonça, "Generation of copper nanoparticles induced by fs-laser irradiation in borosilicate glass," Optics express **20,** 15106-15113 (2012).

188 H. El Hamzaoui, R. Bernard, A. Chahadih, F. Chassagneux, L. Bois, B. Capoen, and M. Bouazaoui, "Continuous laser irradiation under ambient conditions: a simple way for the space-selective growth of gold

nanoparticles inside a silica monolith," Mater. Res. Bull. **46,** 1530-1533 (2011).

189 K. Berg, A. Berger, and H. Hofmeister, "Small silver particles in glass surface layers produced by sodium-silver ion exchange—their concentration and size depth profile," Zeitschrift für Physik D Atoms, Molecules and Clusters **20,** 309-311 (1991).

190 A. Kuznetsov, V. Tikhomirov, M. Shestakov, and V. Moshchalkov, "Ag nanocluster functionalized glasses for efficient photonic conversion in light sources, solar cells and flexible screen monitors," Nanoscale **5,** 10065-10075 (2013).

191 H. Zhang, I. Hussain, M. Brust, M. F. Butler, S. P. Rannard, and A. I. Cooper, "Aligned two-and three-dimensional structures by directional freezing of polymers and nanoparticles," Nature materials **4,** 787-793 (2005).

192 A. L. Wu, Planar interconnect for integrated circuits (1986).

193 G. Seifert, M. Kaempfe, K. Berg, and H. Graener, "Production of “dichroitic” diffraction gratings in glasses containing silver nanoparticles via particle deformation with ultrashort laser pulses," Appl. Phy. B **73,** 355-359 (2001).

194 A. Stalmashonak, A. Podlipensky, G. Seifert, and H. Graener, "Intensity-driven, laser induced transformation of Ag nanospheres to anisotropic shapes," Appl. Phy. B **94,** 459-465 (2009).

195 R. Kuladeep, L. Jyothi, S. Chakradhar, and D. N. Rao, "Fabrication of metal nanostructures in a polymer matrix using femtosecond laser writing technique," Optical Engineering **53,** 071823-071823 (2014).

196 H. Nakamura and Y. Maeda, Laser sintering powder, method for producing structure, apparatus for producing structure (2014).

197 W. Wu, A. DeConinck, and J. A. Lewis, "Omnidirectional printing of 3D microvascular networks," Adv Mater **23,** (2011).

198 S. Kang, K. Vora, and E. Mazur, "One-step direct-laser metal writing of sub-100 nm 3D silver nanostructures in a gelatin matrix," Nanotechnology **26,** 121001 (2015).

199 E. N. Boulos and N. Kreidl, "Structure and properties of silver borate glasses," J Am Ceram Soc **54,** 368-375 (1971).

200 S. Wackerow, G. Seifert, and A. Abdolvand, "Homogenous silver-doped nanocomposite glass," Optical Materials Express **1,** 1224-1231 (2011).

201 M. Bellec, A. Royon, K. Bourhis, J. Choi, B. Bousquet, M. Treguer, T. Cardinal, T., J.J. Videau, M. Richardson and L. Canioni, 2010. 3D patterning at the nanoscale of fluorescent emitters in glass. The Journal of Physical Chemistry C, 114(37), pp.15584-15588.

202 A. Babapour, O. Akhavan, R. Azimirad, and A. Moshfegh, "Physical characteristics of heat-treated nano-silvers dispersed in sol–gel silica matrix," Nanotechnology **17,** 763 (2006).

203 P. Innocenzi, M. Abdirashid, and M. Guglielmi, "Structure and properties of sol-gel coatings from methyltriethoxysilane and tetraethoxysilane," J. Sol Gel Sci. Technol. **3,** 47-55 (1994).

204 H. Haus, K. Tamura, L. Nelson, and E. Ippen, "Stretched-pulse additive pulse mode-locking in fiber ring lasers: theory and experiment," IEEE J. Quant. Electron. **31,** 591-598 (1995).

205 G. A. Mourou, C. Barty, and M. D. Perry, Ultrahigh-intensity laser: physics of the extreme on a tabletop (1997).

206 A. Babapour, O. Akhavan, R. Azimirad, and A. Moshfegh, "Physical characteristics of heat-treated nano-silvers dispersed in sol–gel silica matrix," Nanotechnology **17,** 763 (2006).

207 C. J. Brinker and G. W. Scherer, *Sol-gel science: the physics and chemistry of sol-gel processing* (Academic press, 2013).

208 Photonics, R.P., Pulse Front Tilt.

209 F. Mok, J. Diep, H. Liu, and D. Psaltis, "Real-time computer-generated hologram by means of liquid-crystal television spatial light modulator," Opt. Lett. **11,** 748-750 (1986).

210 Y. Roichman, B. Sun, Y. Roichman, J. Amato-Grill, and DG Grier, Phys. Rev. Lett. 100, 013602 (2008). SUN et al. PHYSICAL REVIEW E 80, 010401(R) (2009) …

211 Y. Jin, O. Allegre, W. Perrie, K. Abrams, J. Ouyang, E. Fearon, S. Edwardson, and G. Dearden, "Dynamic modulation of spatially structured polarization fields for real-time control of ultrafast laser-material interactions," Optics express **21,** 25333-25343 (2013).

212 F. Shimizu, "Frequency broadening in liquids by a short light pulse," Phys. Rev. Lett. **19,** 1097 (1967).

213 L. Ye, W. Perrie, O. Allegre, Y. Jin, Z. Kuang, P. Scully, E. Fearon, D. Eckford, S. Edwardson, and G. Dearden, "NUV femtosecond laser inscription of volume Bragg gratings in poly (methyl) methacrylate with linear and circular polarizations," Laser Physics **23,** 126004 (2013).

214 A. Brodeur, C. Chien, F. Ilkov, S. Chin, O. Kosareva, and V. Kandidov, "Moving focus in the propagation of ultrashort laser pulses in air," Opt. Lett. **22,** 304-306 (1997).

215 C. B. Schaffer, A. Brodeur, and E. Mazur, "Laser-induced breakdown and damage in bulk transparent materials induced by tightly focused femtosecond laser pulses," Measurement Science and Technology **12,** 1784 (2001).

216 L. Sudrie, A. Couairon, M. Franco, B. Lamouroux, B. Prade, S. Tzortzakis, and A. Mysyrowicz, "Femtosecond laser-induced damage and filamentary propagation in fused silica," Phys. Rev. Lett. **89,** 186601 (2002).

217 G. Zverev and V. Pashkov, "Self-focusing of laser radiation in solid dielectrics," Sov.Phys.—JETP **30,** 616-621 (1970).

218 H. Mochizuki, W. Watanabe, R. Ezoe, T. Tamaki, Y. Ozeki, K. Itoh, M. Kasuya, K. Matsuda, and S. Hirono, "Density characterization of femtosecond laser modification in polymers," Appl. Phys. Lett. **92,** 091120 (2008).

219 https://www.mitsuichemicals.com/tpx.htm

220 E. J. J. Samuel and S. Mohan, "FTIR and FT Raman spectra and analysis of poly (4-methyl-1-pentene)," Spectrochimica Acta Part A: Molecular and Biomolecular Spectroscopy **60,** 19-24 (2004).

221 E.J. J. Samuel and S. Mohan, 2004. FTIR and FT Raman spectra and analysis of poly (4-methyl-1-pentene). Spectrochimica Acta Part A: Molecular and Biomolecular Spectroscopy, 60(1-2), pp.19-24.

222 J. Morikawa, A. Orie, T. Hashimoto, and S. Juodkazis, "Thermal and optical properties of femtosecond-laser-structured PMMA," Appl. Phys. A **101,** 27-31 (2010).

223 S. Juodkazis, Y. Nishi, H. Misawa, V. Mizeikis, O. Schecker, R. Waitz, P. Leiderer, and E. Scheer, "Optical transmission and laser structuring of silicon membranes," Optics express **17,** 15308-15317 (2009).

224 S. Sowa, W. Watanabe, T. Tamaki, J. Nishii, and K. Itoh, "Symmetric waveguides in poly (methyl methacrylate) fabricated by femtosecond laser pulses," Optics Express **14,** 291-297 (2006).

225 V. Amendola, S. Scaramuzza, F. Carraro, and E. Cattaruzza, "Formation of alloy nanoparticles by laser ablation of Au/Fe multilayer films in liquid environment," J. Colloid Interface Sci. **489,** 18-27 (2017).

226 A. Stalmashonak, G. Seifert, and H. Graener, "Spectral range extension of laser-induced dichroism in composite glass with silver nanoparticles," Journal of Optics A: Pure and Applied Optics **11,** 065001 (2009).

227 C. Maurer, A. Jesacher, S. Fürhapter, S. Bernet, and M. Ritsch-Marte, "Tailoring of arbitrary optical vector beams," New Journal of Physics **9,** 78 (2007).

228 G. R. Fowles, *Introduction to modern optics* (Courier Corporation, 1975) p47.

229 B. Ilan, G. Fibich, and G. Papanicolaou, "Self-focusing with fourth-order dispersion," SIAM J Appl Math **62,** 1437-1462 (2002).

230 M. Soskin and M. Vasnetsov, "Singular optics," Progress in optics **42,** 219-276 (2001).

231 J. E. Curtis and D. G. Grier, "Structure of optical vortices," Phys. Rev. Lett. **90,** 133901 (2003).

232 N. M. Ravindra, B. Sopori, O. H. Gokce, S. X. Cheng, A. Shenoy, L. Jin, S. Aberdrabbo and Y. Chang, “Emissivity measurements and modelling of Silicon-Related Materials:An Overview” International Journal of Thermophysics Vol. 22, No.5, (Sep.2001)

233 http://www.altechna.com

234 J. J. J. Kaakkunen, P. Laakso, and V. Kujanpää, “Adaptive multibeam laser cutting of thin steel sheets with fiber laser using spatial light modulator, Journal of Laser Applications 26, 032008 (2014)

235 W. Jiajun and Y. Xiao-Su, "Effects of interfacial thermal barrier resistance and particle shape and size on the thermal conductivity of AlN/PI composites," Composites Sci. Technol. **64,** 1623-1628 (2004).

236 N. Nguyen, A. Saliminia, S. Chin, and R. Vallée, "Control of femtosecond laser written waveguides in silica glass," Applied Physics B **85,** 145-148 (2006).

237 H.Cabrera, A.Marcano and Y.Castellanos “Absorption coefficients of nearly transparent liquids measured using thermal lens spectrometry”, Condensed Matter Physics Vol. 9, No 2(46), pp. 385–389 (2006).

238 B Tan and K Venkatakrishnan, “A femtosecond laser-induced periodical surface structure on crystalline silicon” J. Micromech. Microeng. (2006) 16 1080.

239 F. Garrelie, J. P. Colombier, F. Pigeon, S. Tonchev, N. Faure, M. Bounhalli, S. Reynaud, and O. Parriaux, “Evidence of surface plasmon resonance in ultrafast laser-induced ripples” Optics Express, Vol. 19, Issue 10, pp. 9035-9043, (2011).

240 A. Borowiec and H. Haugen, "Subwavelength ripple formation on the surfaces of compound semiconductors irradiated with femtosecond laser pulses," Appl. Phys. Lett. **82,** 4462-4464 (2003).

241 R. J. Beck, J. P. Parry, W. N. MacPherson, A. Waddie, N. J. Weston, J.D. Shephard, and D. P Hand, “Application of cooled spatial light modulator for high power nanosecond laser micromachining” Optics Express, Vol. 18, Issue 16, pp. 17059-17065 (2010)

242 D. Dai, J. Wang, and Y. Shi, "Silicon mode (de) multiplexer enabling high capacity photonic networks-on-chip with a single-wavelength-carrier light," Opt. Lett. **38,** 1422-1424 (2013).

Appendix 1

Optical-vortex simulation in MatLab environment

Plot a 3 planes of m=0 over 3λ. Calculate the gradient of z using linear function which is assumed as ψ=kz. Display the 3 planes indicating 3 sections with same ψ.

```
Clear;close;
m=1; n=1; g=0;
axis on;
while m<=256;
    n=1;
    g=(1/256)*m;
   while n<=80;
     x(n)=(0.1*(n-1))*cos((2*pi/256)*(m-1));
     y(n)=(0.1*(n-1))*sin((2*pi/256)*(m-1));
     z(n)=7.75;
     plot3 (x(n),y(n),z(n),'Color',[1,0,0]);
     hold on; n=n+1;
   end
    m=m+1;
end
m=1; n=1; g=0;
while m<=256;
   n=1;
   g=(1/256)*m;
   while n<=80;
     x(n)=(0.1*(n-1))*cos((2*pi/256)*(m-1));
     y(n)=(0.1*(n-1))*sin((2*pi/256)*(m-1));
     z(n)=7.75;
     plot3 (x(n),y(n),z(n),'Color',[1,0,0]);
     hold on;
     n=n+1;
   end
    m=m+1;
end
m=1; n=1; g=0;
```

```
while m<=256;
   n=1; g=(1/256)*m;
   while n<=80;
     x(n)=(0.1*(n-1))*cos((2*pi/256)*(m-1));
     y(n)=(0.1*(n-1))*sin((2*pi/256)*(m-1));
     z(n)=15.5;
     plot3 (x(n),y(n),z(n),'Color',[1,0,0]);
     hold on;
     n=n+1;
   end
  m=m+1;
end
m=1; n=1; g=0;
while m<=256;
   n=1;
   g=(1/256)*m;
   while n<=80;
     x(n)=(0.1*(n-1))*cos((2*pi/256)*(m-1));
     y(n)=(0.1*(n-1))*sin((2*pi/256)*(m-1));
     z(n)=23.25;
     plot3 (x(n),y(n),z(n),'Color',[1,0,0]);
     hold on;
     n=n+1;
   end
    m=m+1;
end
xlabel('x'); ylabel('y'); zlabel('z');
n=n+1;
grid on;
```

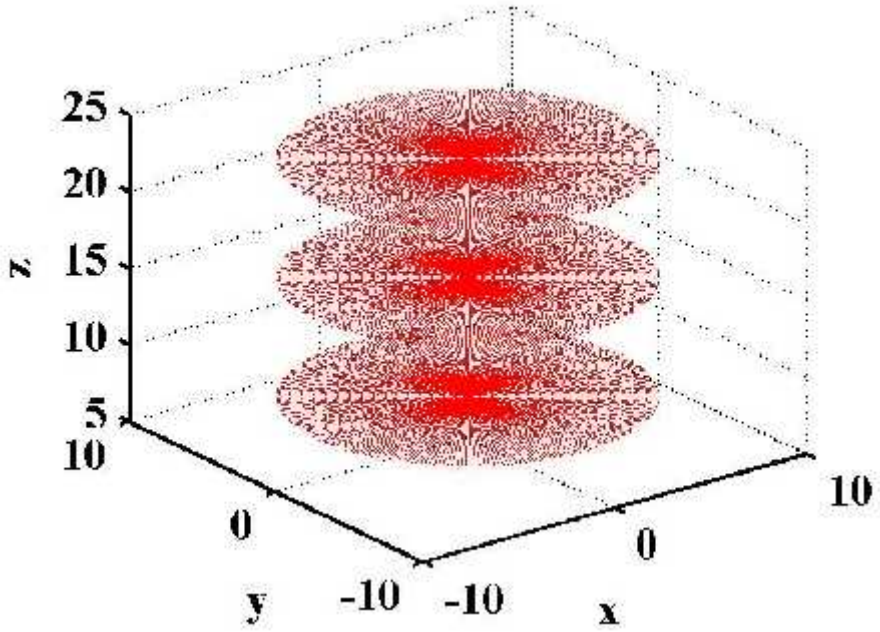

.

Plot a 3 threshold spiral vortex front (m=3) over a λ. Calculate the gradient of X-Y is assumed as a constant.

```
clear; close;
m=1; n=1;g=0;
while m<=256;
   n=1;
    g=(1/256)*m;
   while n<=80;
     x(n)=(0.1*(n-1))*cos((2*pi/256)*(m-
1)/3);
     y(n)=(0.1*(n-1))*sin((2*pi/256)*(m-
1)/3);
     z(n)=7.75-(7.75/256)*(m-1);
     plot3 (x(n),y(n),z(n),'Color',[1,0,0]);
     hold on;
     n=n+1;
   end
    m=m+1;
end
m=1;
while m<=256;
   n=1;
   g=(1/256)*m;
   while n<=80;
     x(n)=(0.1*(n-
1))*cos(2*pi/3+(2*pi/256)*(m-1)/3);
     y(n)=(0.1*(n-
1))*sin(2*pi/3+(2*pi/256)*(m-1)/3);
     z(n)=7.75-(7.75/256)*(m-1);
     plot3 (x(n),y(n),z(n),'Color',[1,0,0]);
     hold on;
     n=n+1;
   end
   m=m+1;
end
m=1;
while m<=256;
   n=1;
    g=(1/256)*m;
   while n<=80;
     x(n)=(0.1*(n-
1))*cos(4*pi/3+(2*pi/256)*(m-1)/3);
     y(n)=(0.1*(n-
1))*sin(4*pi/3+(2*pi/256)*(m-1)/3);
     z(n)=7.75-(7.75/256)*(m-1);
     plot3 (x(n),y(n),z(n),'Color',[1,0,0]);
     hold on;
     n=n+1;
   end
   m=m+1;
end
xlabel('x'); ylabel('y'); zlabel('z');
n=n+1;
grid on; axis on;
```

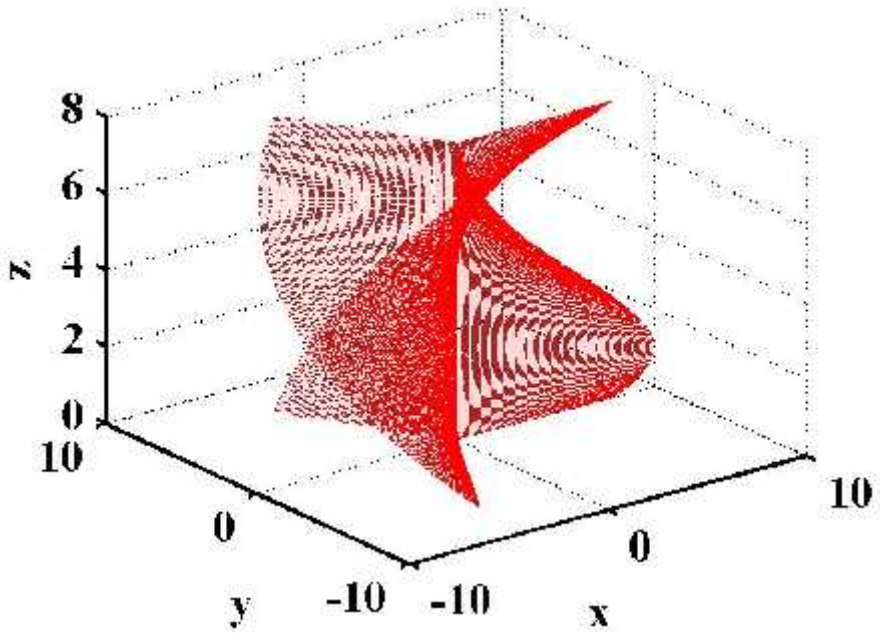

Variant Zernike correction coefficient (Z_0^0) and dynamic display rotated wavefront. The dynamic demonstration is referred in a GIF file in CD disk.

```
colormap(hsv);
filename = 'test_m3.gif';
for k=1:1:30
view(30+18*(k-1),30)
    M(k)=getframe;
    frame=getframe;
    im = frame2im(frame);
    [imind,cm] = rgb2ind(im,256);
    if k == 1;
    imwrite(imind,cm,filename,'gif', 'Loopcount',inf);
    else
        imwrite(imind,cm,filename,'gif','WriteMode','append');
    end
end
movie(M,20);
colormap(hsv);
 filename = 'test_m6.gif';
for k=1:1:30
    view(30-18*(k-1),30)
    M(k)=getframe;
    frame=getframe;
    im = frame2im(frame);
    [imind,cm] = rgb2ind(im,256);
    if k == 1;
        imwrite(imind,cm,filename,'gif', 'Loopcount',inf);
    else
        imwrite(imind,cm,filename,'gif','WriteMode','append');
    end
end
movie(M,20);
```

Plot an intensity distribution of m=4. Calculate the gradient of X-Y is

$$P = \frac{2\pi}{m!}\int r\left(\frac{2r^2}{r_0{}^2}\right)^m e^{\left(\frac{2r^2}{r_0{}^2}\right)} d = \frac{2\pi}{m!}\int r\left(\frac{2r^2}{r_0{}^2}\right)^m e^{\left(\frac{2r^2}{r_0{}^2}\right)} d\left[\left(\frac{\sqrt{2}r}{r_0}\right)\frac{r_0}{\sqrt{2}}\right].$$

Here regard, $\frac{\sqrt{2}r}{r_0} = x$.

```
clear all;
i=sqrt(-1); t=0;
r0=3;
E0=sqrt(4e13);
m=4; theta=pi;
for r=0:0.02:20
 t=t+1;
 % radius r=5um
 p=2*r^2/r0^2;
 E=E0*(1/sqrt(factorial(m)))*
 (sqrt(2)*abs(r)/r0^2)^m *
 exp(-r^2/r0^2)*exp(i*m*theta);

 EC=conj(E);
 I(t)=E*EC;
end

Imax=max(I);
t=0;
```

```
for r=0:0.02:20
t=t+1;
c=1-I(t)/Imax;

theta2=-pi:pi/100:pi;
x=r*cos(theta2);
y=sqrt(r^2-x.^2);
plot(x,y,'Color',[1,c,c]);
hold on
theta2=pi:pi/100:2*pi;
x=r*cos(theta2);
y=-sqrt(r^2-x.^2);
plot(x,y,'Color',[1,c,c]);
hold on
axis([-10 10 -10 10]);
end
```

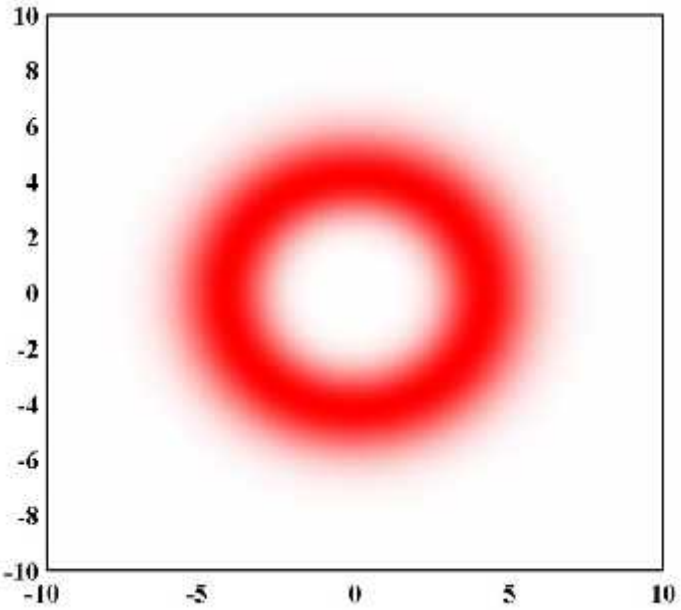

Plot an aspect profile of vortex beam with m=4.

```
clear all;
i=sqrt(-1); t=0;
r0=3;
E0=sqrt(4e13);
m=4;
theta=pi;
for x=-10:0.1:10
  t=t+1;
  E=E0*(1/sqrt(factorial(m)))*(sqrt(2)*abs(x)/r0^2)^m * exp(-
(abs(x))^2/r0^2)*exp(i*m*theta);
  I(t)=E*conj(E);
end
t=0; x=-10:0.1:10;
plot(x,I,'r-');
hold on; axis on;
axis([-10 10 0 0.4e10]);
```

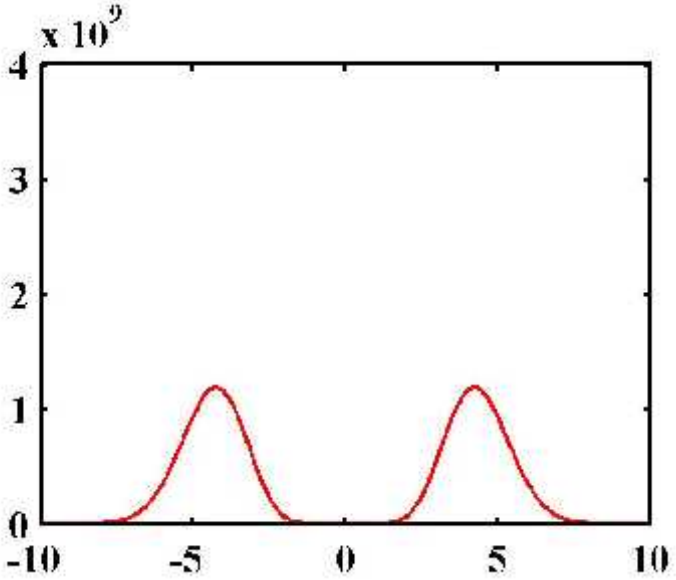

Appendix 2

Spatial-light-modulating method developing in LabVIEW environment

Spatial Light Modulator: Hamamatsu X10468-02 (λ = 775 nm, repletion rate 60 Hz)

Software Development Environment: LabVIEW Development System 6.0

Objective Software Kit: Blue Tweezer

A2.1 Rotation Vortex Phase Front

Motivation:

A spatial light modulator can modulate light lively. It would be interested to create an animating CGH to add rotation on a vortex beam. To the author's knowledge, few researches have been done on the method.

Solution:

1. Add a Boolean button and a text filed on VI "*interface*" in order to switch rotation "on/off" and control rotation speed respectively. The two components are illustrated in Figure A2.1.
2. Add a global numerical variable *"rotation speed"* as a buffer to store speed coefficient.
3. Go to the Block Diagram *"Zernike Correction"*.
4. Connect the Global Variable *"rotation speed"* to the terminal of a multiplier in Block Diagram *"Zernike Correction"*, shown in Figure A2.2.
5. By the method, an animating CGH is created. Figure 2.3 shows 4 consequent screenshots, showing the pursued dynamic effect.

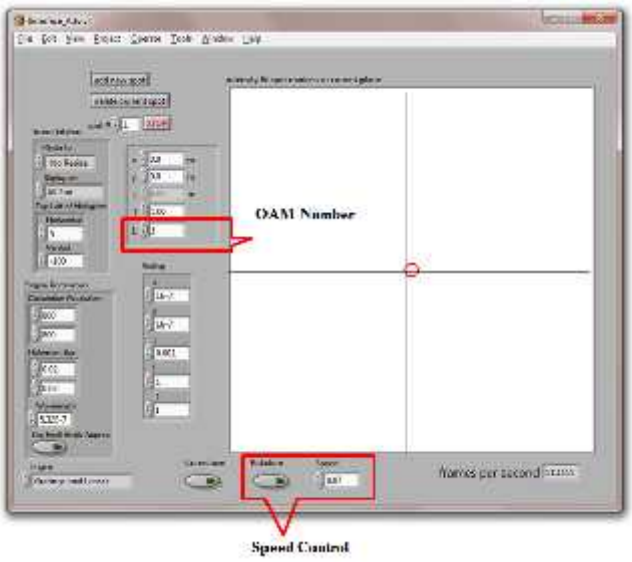

Figure A2.1: Two functional components are added on VI "*interface*", in which the two components are marked out by red rectangular.

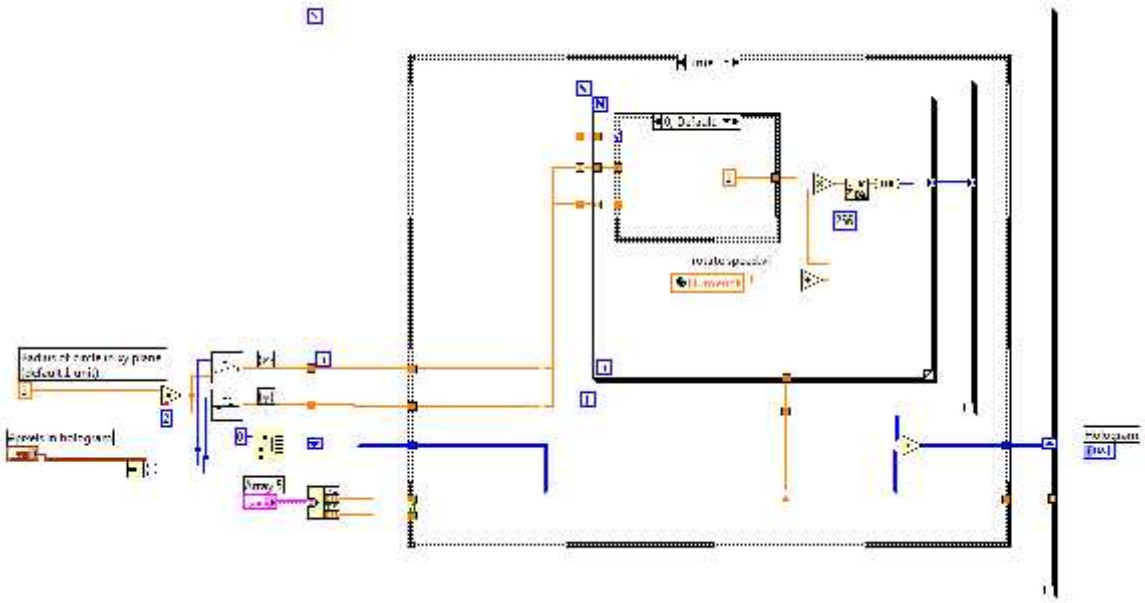

Figure A2.2: Block Diagram *"Zernike Correction"*

Figure A2.3 Consequent screenshot of CGHs, generated in LabVIEW environment.

A2.2 Movable Correction Field

Problem:

The original control panel (BLUETWEEZER interface) was designed to allow users to shift CGH along vertical or horizontal directions. It is notable that the shifts are also applied on correction-field background. The insufficient function yields much more troubles to keep two centroids to be coincident. The background however must be kept on the centroid of SLM.

Solution:

The problem is resolved by operating separate shifts of two CGHs to compensate the off-axis with respect to the centroid of laser beam and background.

Usage:

This app-upgrade work provides more convenience without manual adjustment of optic devices. While specifically designed to generate vortex beam, it can be used to any application in which CGHs (computed generated holograms) have a symmetrical pattern, such as Bessel beam, cylindrical lens and Zernike correction.

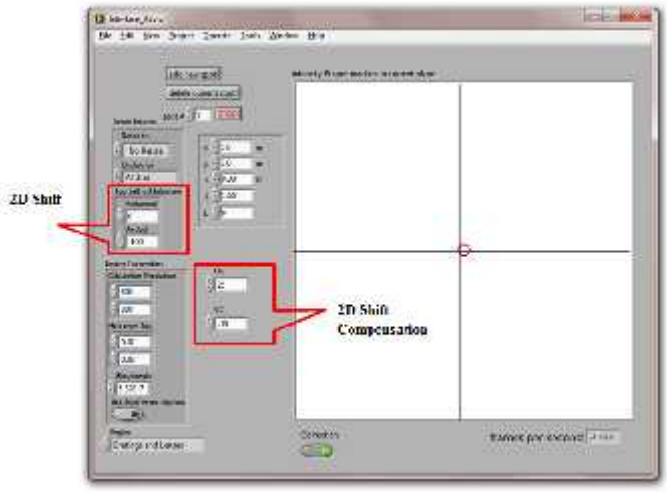

Figure A2.4: Two functional components are added on VI "*interface*", in which the two components are marked out by red rectangular.

.

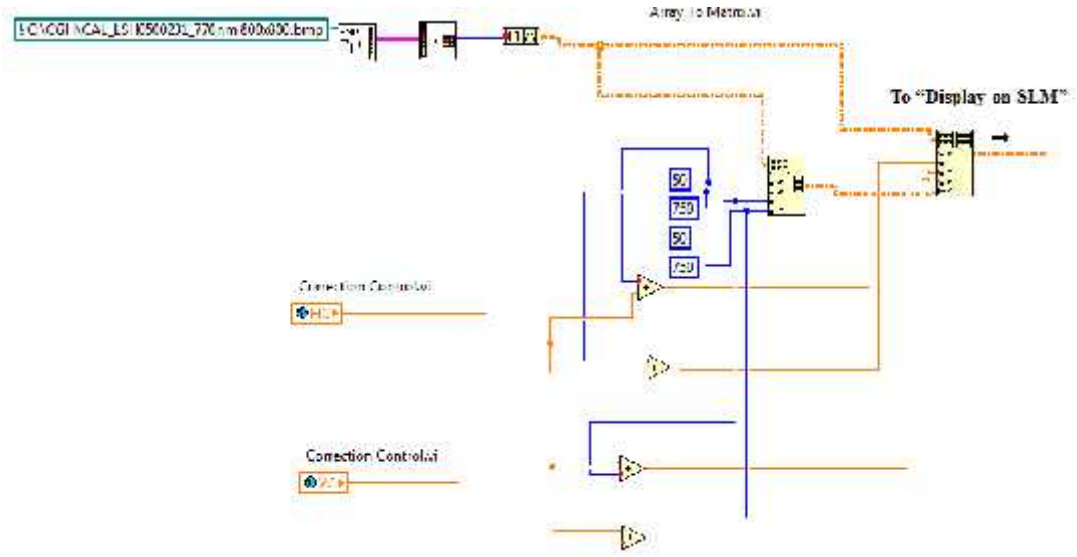

Figure A2.5: Block Diagram *"interface"*

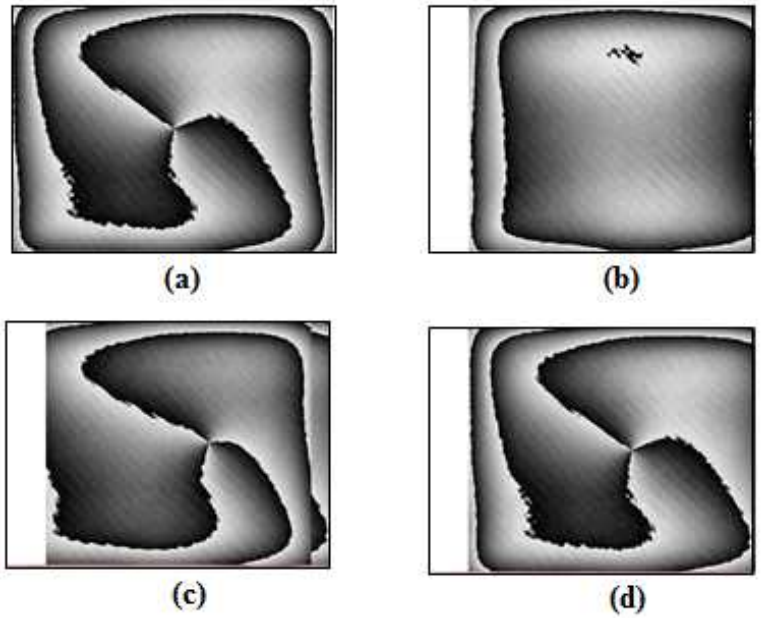

Figure A2.6: Demonstration of compensation of correction-field movement.

Appendix 3

Laser sources, optics and investigated materials

TABLE A3.1: ULTRAFAST COHERENT LIGHT SOURCES

SOURCE	τ	f_{rep}	λ	I_{max}	Notes:
CLARK MXR CPA 2010	170 fs	1Khz	775nm	1 W	Ti-Sapphire
TOPAS C	160 fs	1Khz	200nn -1500 nm	~0.2 W	OPA
HIGH Q	5 ps	5Khz	1064 nm	5 W	Nd-YAG
INNOSLAB	5 ps	2 MHz	1064 nm	300 W	Diode-pumped and turn key
REGA	140 fs	10Khz	800 nm	0.1 W	Nd: Van

TABLE A3.2: BIREFRINGENCE OPTICS

OPTICS	MFR	SPC	USAGE
½ WAVEPLATES 1#	THORLABS	(10RP-780) 1st Order	polarization modulation.
½ WAVEPLATES 2#	-	1064 nm	Intensity attenuation
¼ WAVEPLATE 1	NEWPORT	775 nm	Polarization effect, spin and OAM coupling
¼ WAVEPLATE 2#	-	1064 nm	Vector beam generation
¼ WAVEPLATE 2	CVI	QWPO-400-06-2-R10	Polarization effect
S- WAVEPLATE	-	1064 nm	Vector beam generation
GLAN-LASER POLARIZER	New Port	BBAR coated 10GL0AR.16	Attenuation, polarization purifying.

TABLE A3.3: RETROREFLECTOR OPTICS

OPTICS	MFR	SPC	USAGE
DIELECTRIC COATING MIRRORS	SLS Optics Ltd.	355 mm, 25 mm DIA	NUV Inscription
DIELECTRIC COATING MIRRORS	SLS Optics Ltd.	355 mm, 50 mm DIA	NUV Inscription
DIELECTRIC COATING MIRROR	SLS Optics Ltd.	NIR/775 nm 25mm DIA	NIR Inscription
ALUMINIUM COATING MIRROR	THORLABS	Φ 25.4 mm, UV enhanced	Inscription, vector beam, SC signal reflecting
SILVER COATING MIRROR	THORLABS	Φ 25.4 mm,	SC signal reflecting

TABLE A3.4: EXCUTION DEVICE

DEVICES	MER	SPC	USAGE
CNC STAGE	AEROTECH	3 axis air-bearing linear motion	internal inscription
SCAN HEAD	SCANLAB	Digital Interfaced (RTCS SL200)	SLM testing
NUMERICAL SHUTTER #1	NEWPORT	-	Internal Inscription

TABLE A 3.5: LASER POWER METER

POWER METER	DETECTOR	RANGE	USAGE
COHERENCE FIELDMASTER	Thermopile	100 µW to >5 kW	Cavity and bench alignment
GENTEC UP55G-500F-H1	Silicon and air cooled	100 µW to >500W	SLM testing
COHERENT LM1/FIELDMASTER	Thermopile	100 µW to >5 kW	VBG diffraction

TABLE A3.6: INVESTIGATED MATERIALS

MATERIALS	MER	SORT	USAGE
PMMA	VISTA OPTICS	polymer	inscription
PMP	GOODFELLOW	polymer	inscription
KAPTYN	-	polymer	surface twisting
SILICA-PVA HYBRIDS	*	composite	internal fabrication
SAPPHIRE	-	dielectric	inscription
ZNSE	CRYSTRAN	poly crystalline	inscription
SUS316	-	metal alloy	plasmon structuring
TITANIUM	-	metal alloy	plasmon structuring
BRASS ON STEEL	-	metal alloy	plasmon structuring, parallel processing
RHODAMINE 6G	LAMBDAPHYSIK	laser dye	internal twist

(* TEOS, silver nitride and PVA are provided by Sigma-Aldrich.)

Transmittance spectra of several polymer materials and Glass

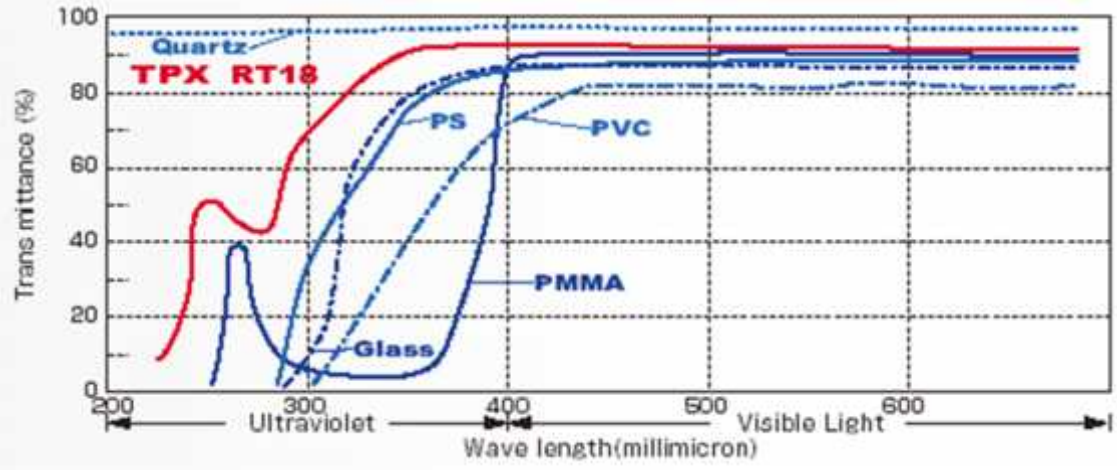

Notes: this figure is courtesy to MITSU CHEMICAL AMERICA, retrieved (14/05/2018) from https://www.mitsuichemicals.com/tpx_cha.htm

Transmittance spectrum of ZnSe

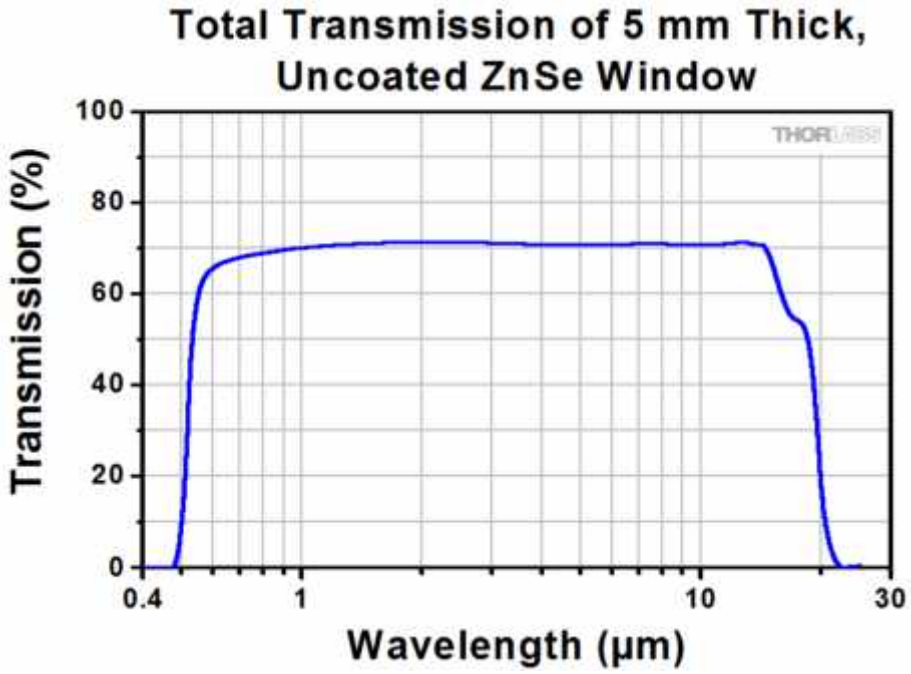

Notes: this figure is courtesy to THORLABS, retrieved (14/05/2018) from http://www.thorlabs.com

Transmittance spectrum of Sapphire

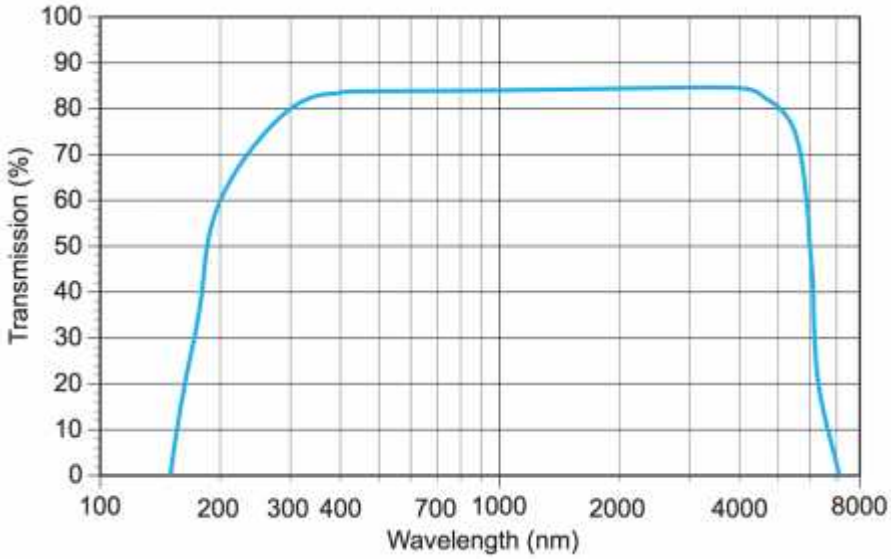

Notes: this figure is courtesy to ESCO optics, retrieved (14/05/2018) from https://escooptics.com on 14/05/2018